

May 2019

Analysis of FRP-Wrapped Concrete Piles in Integral Abutment Bridges Subjected to Axial and Cyclic Lateral Loads

Hassan Mohammed Magbool
University of Wisconsin-Milwaukee

Follow this and additional works at: <https://dc.uwm.edu/etd>



Part of the [Civil Engineering Commons](#)

Recommended Citation

Magbool, Hassan Mohammed, "Analysis of FRP-Wrapped Concrete Piles in Integral Abutment Bridges Subjected to Axial and Cyclic Lateral Loads" (2019). *Theses and Dissertations*. 2096.
<https://dc.uwm.edu/etd/2096>

This Dissertation is brought to you for free and open access by UWM Digital Commons. It has been accepted for inclusion in Theses and Dissertations by an authorized administrator of UWM Digital Commons. For more information, please contact open-access@uwm.edu.

ANALYSIS OF FRP-WRAPPED CONCRETE PILES IN INTEGRAL ABUTMENT
BRIDGES SUBJECTED TO AXIAL AND CYCLIC LATERAL LOADS

by

Hassan Mohammed Magbool

A Dissertation Submitted in
Partial Fulfillment of the
Requirements for the Degree of

Doctor of Philosophy
in Engineering

at

The University of Wisconsin-Milwaukee

May 2019

ABSTRACT

ANALYSIS OF FRP-WRAPPED CONCRETE PILES IN INTEGRAL ABUTMENT BRIDGES SUBJECTED TO AXIAL AND CYCLIC LATERAL LOADS

by

Hassan Mohammed Magbool

The University of Wisconsin-Milwaukee, 2019
Under the Supervision of Professor Habib Tabatabai

The long-term maintenance problems associated with expansion joints, which are used to accommodate bridge movements in conventional bridges, have been the primary motivation for the use of integral abutment (jointless) bridges. These bridges rely on the interaction between the structure and the surrounding soil to accommodate bridge movements without the use of any expansion joints on the bridge superstructure. As the bridge superstructure expands and contracts due to seasonal thermal and other strains, relatively large forces can develop in the pile near the pile-cap interface. These reversible moment and shear forces can lead to localized damage near the top of the pile. Steel piles are the most commonly used type of piles in integral abutment bridges. However, concrete piles are preferred in some regions of the United State as well as other countries due to economic factors and soil conditions. Concrete piles are susceptible to cracking and spalling at the pile/pile cap interface and that has limited their use in integral abutment bridges.

This study was aimed at determining the behavior and performance parameters in integral abutment bridges that are supported by concrete piles and evaluating the effect of carbon fiber reinforced polymer composites in mitigating the expected localized damage in these piles. To achieve these objectives, a comprehensive review of literature was first

conducted. Two sets of analytical models were prepared using the ABAQUS finite element program to analyze prestressed concrete piles in integral abutment bridges with or without localized FRP reinforcement at the interface between the pile and the pile cap. The effectiveness and accuracy of the finite element models were verified using three sets of available experimental data. Also, a comprehensive parametric study was conducted to understand and compare the influence of various parameters on the behavior of the bridge and the pile.

Empirical equations were developed to estimate the pile displacement and the abutment rotation based on the span length, the height of the abutment and the girder displacement. Results indicate that the use of carbon fiber reinforced polymer composite wraps can substantially reduce damage at the pile-abutment interface. However, the magnitude of shear and movement forces imposed by the pile on the abutment and bridge superstructure increase as a result of the reduction in damage. Estimates of these forces for various bridge span lengths and soil conditions are provided. A set of design recommendations are provided for the application of concrete piles in integral abutment bridges using CFRP composites in retrofit cases or in new bridges construction.

TABLE OF CONTENTS

ABSTRACT.....	ii
TABLE OF CONTENTS	iv
LIST OF FIGURES	ix
LIST OF TABLES	xxvii
ACKNOWLEDGMENTS	xxxi
1 INTRODUCTION.....	1
1.1 Background	1
1.2 Problem Statement.....	6
1.3 Objectives.....	7
1.4 Scope of Work	8
2 LITERATURE REVIEW	11
2.1 Integral Bridges.....	11
2.1.1 Types of Load Applied to Integral Bridges	13
2.1.1.1 <u>Shrinkage and Creep</u>	13
2.1.1.2 <u>Temperature Gradient</u>	14
2.1.1.3 <u>Differential Settlement</u>	14
2.1.1.4 <u>Earth Pressure</u>	14
2.1.2 Integral Abutments	15
2.1.3 States Practice.....	16
2.1.3.1 <u>Consideration of integral abutment bridges</u>	18
2.1.4 Piles	21

2.1.4.1.1	<i>Steel Piles</i>	21
2.1.4.1.2	<i>Concrete Piles</i>	23
2.1.5	Behavior of Piles under Lateral Movement.....	25
2.1.6	The Effect of Bridge-Soil Interactions on the Behavior of Piles Supporting Integral Abutments.....	26
2.1.6.1	Lateral Stiffness of Soil-Pile System	29
2.1.6.1.1	<i>Cohesive Soils</i>	29
2.1.6.1.2	<i>Cohesionless Soils</i>	31
2.1.6.2	Lateral Strength of Soil-Pile System.....	32
2.1.6.2.1	<i>Cohesive Soils</i>	32
2.1.6.2.2	<i>Cohesionless Soils</i>	33
2.1.7	Prestressed Concrete Piles in Seismic Regions	34
2.1.8	Curvature Ductility	37
2.1.9	Target Curvature Demand	37
2.1.10	Relationship between Displacement and Curvature Ductility Factor	39
2.1.11	Pile Tests for Integral Abutment Bridges	40
2.1.11.1	Laboratory Tests	41
2.1.11.1.1	<i>Arsoy et al.</i>	41
2.1.11.1.2	<i>Kamel et al.</i>	42
2.1.11.1.3	<i>Tabatabai et al.</i>	44
2.1.11.2	Field Tests.....	47
2.1.11.2.1	<i>Burdette et al.</i>	47
2.2	Confinement	48

2.2.1	Steel	48
2.2.2	FRP	49
2.2.2.1	FRP Properties and applications	49
2.2.2.2	FRP Strengthening Columns Subjected to Seismic Loads	50
3	DEVELOPMENT OF FINITE ELEMENT MODELS.....	52
3.1	Introduction to ABAQUS.....	52
3.2	Material properties and models.....	52
3.2.1	Concrete.....	52
3.2.1.1	Smearred Crack (SC)	53
3.2.1.2	Concrete Damage Plasticity (CDP)	53
3.2.2	Soil.....	58
3.2.3	Reinforcement	61
3.2.3.1	Steel Reinforcement.....	61
3.2.3.2	FRP External Wraps	64
3.3	Meshing.....	65
3.4	Physical Models.....	66
3.4.1	General model.....	67
3.4.2	Localized pile-pile cap model:	68
3.5	Verification Models.....	69
3.5.1	<i>Verification model 1: Tabatabai et al. (1999)</i>	70
3.5.2	<i>Verification model 2: Choi et al. (2015)</i>	80
3.5.3	<i>Verification model 3: Soil-Pile interaction test – Burdette et al. (2004)</i>	85
3.6	Parametric Study	88

4	NUMERICAL STUDY AND RESULTS	90
4.1	General Model	90
4.1.1	Geometry	93
4.1.2	Boundary Conditions and Application of Displacements	95
4.1.3	Meshing	96
4.1.4	Analysis Procedures	97
4.1.5	Results	98
4.1.5.1	Rotations	99
4.1.5.2	Displacements.....	111
4.1.5.3	Curvature.....	114
4.1.5.4	Point of Inflection POI.....	119
4.2	Localized Model	123
4.2.1	Transverse displacement of POI (Δ_m)	126
4.2.2	Geometry and Model Assembly	131
4.2.3	Mesh Sensitivity	132
4.2.4	Analysis Procedures	135
4.2.5	Results	137
4.2.5.1	Lateral (shear) load on the Piles.....	138
4.2.5.2	The effect of CFRP on Control of Damage	149
4.3	Development of Empirical Equations	156
5	SUMMARY AND CONCLUSIONS	164
5.1	Design Recommendations	168
5.2	Recommendations for Future Study	169

REFERENCES.....	170
Appendix A: Girders Details For The General Model	178
Appendix B: General Model Results For All Cases Studied.....	179
Appendix C: Localized Model Results: Lateral (Shear) Load vs. Displacement Δ_m....	197
Appendix D: Localized Model Results: Damage Indicators for $\Delta_g = \pm 50.8$ mm (± 2 in)	215
CURRICULUM VITAE.....	269

LIST OF FIGURES

Figure 1: Typical components of an integral abutment bridge (Moulton, GangaRao and Halvorsen 1985).....	2
Figure 2: Bridges Types (Abendroth and Greimann 2005).	13
Figure 3: Integral Abutment Schematic (Fanous, et al. 2010).....	16
Figure 4: Graphical representation of states specifically considering integral/semi-integral bridges (green) (Tabatabai, Magbool, et al. 2017).....	18
Figure 5: Deflected shape and bending moment distribution of a laterally loaded fixed head pile a). First yield limit state b). Second yield limit state c). Ultimate limit state (Song, Chai and Hale 2004).....	29
Figure 6: Subgrade coefficient of cohesionless soil (Song, Chai and Hale 2004).....	31
Figure 7: Ultimate soil pressure distribution for laterally loaded fixed head piles in cohesive soils (Song, Chai and Hale 2004).	33
Figure 8: Ultimate soil pressure distribution for laterally loaded fixed head piles in cohesionless soil (Song, Chai and Hale 2004).....	34
Figure 9: Cross section of prestressed concrete piles (Fanous, et al. 2010).	35
Figure 10: Prestressed concrete pile square cross section (Clatrans 2006).	36
Figure 11: Idealized lateral force-displacement response of fixed head piles (Song, Chai and Hale 2004).....	40
Figure 12: Proposed concrete pile-abutment joint (Kamel, et al. 1996).....	43
Figure 13: Schematic of prestressed concrete piles test setup (Tabatabai and Oesterle 1999).	45
Figure 14: Test setup (Burdette, Howard and Tidwell, et al. 2004).	48

Figure 15: Effective confinement areas in circular, square and rectangular columns (Parvin and Brighton 2014).	50
Figure 16: Concrete damage plasticity modified stress-strain curve (ABAQUS 2015)...	54
Figure 17: Actual and modified stress-strain curves for the steel strands (60 ksi vs. 270 ksi).....	64
Figure 18: Two layers of CFRP (both on hoop orientation).....	65
Figure 19: Deflected shape and bending moment of lateral loaded fixed head pile (adapted from (Song, Chai and Hale 2004)).....	67
Figure 20: General model	68
Figure 21: Localized model	69
Figure 22: Design details for prestressed concrete pile (Tabatabai and Oesterle 1999)...	71
Figure 23: Pile cap details (Tabatabai and Oesterle 1999).	72
Figure 24: Pile cap cross section (Tabatabai and Oesterle 1999).	72
Figure 25: Schematic of prestressed concrete pile test setup (Tabatabai and Oesterle 1999).	73
Figure 26: Model's assembly and boundary conditions.	74
Figure 27: Vertical load vs. vertical displacement $\pm 16\text{mm}$ (± 0.63 in).	75
Figure 28: Tension plastic strain (PEEQT).....	76
Figure 29: Tension damage.....	76
Figure 30: Compression plastic Strain (PEEQ)	77
Figure 31: Compression damage.	77
Figure 32: Stresses in reinforcing steel.....	78
Figure 33: Concrete spalling damage during lab test (Tabatabai and Oesterle 1999).	79

Figure 34: Predicted damage from FE model.	79
Figure 35: Test setup (Choi, et al. 2015).	81
Figure 36: Model’s assembly and boundary conditions.	83
Figure 37: Experimental vertical load vs. vertical displacement (Choi, et al. 2015).....	84
Figure 38: FE model vertical load vs. vertical displacement.....	84
Figure 39: Test setup (Burdette, Howard and Tidwell, et al. 2004).	86
Figure 40: Front view shows the displacement at 25.4 mm (1 in).....	87
Figure 41: Top view shows the displacement at 25.4 mm (1in).....	87
Figure 42: Load vs. displacement of view cycles of field test (Burdette, Howard and Tidwell, et al. 2004).....	88
Figure 43: Load vs. displacement of first two cycles of FEM.....	88
Figure 44: General model.	91
Figure 45: Pile details.	92
Figure 46: Soil part.	93
Figure 47: Abutment, pile and girder as one part.	94
Figure 48: Steel reinforcing cage for the pile (half model).	94
Figure 49: CFRP wrap (half model).	95
Figure 50: Boundary Conditions.....	96
Figure 51: The mesh at the location of interest.....	97
Figure 52: The maximum pull in the pull cycle with +50.8 mm (+2 in).	98
Figure 53: The maximum push in the push cycle -50.8 mm (-2 in).	98
Figure 54: A schematic showing the results reported in this study.	99

Figure 55: The deflected shape of the low rotational stiffness model, $\Delta_g = +50.8$ mm (+2 in), exaggerated.....	100
Figure 56: The deflected shape of the medium rotational stiffness model, $\Delta_g = +50.8$ mm (+2 in), exaggerated.....	100
Figure 57: The deflected shape of the high rotational stiffness model, $\Delta_g = +50.8$ mm (+2 in), exaggerated.....	100
Figure 58: The rotations at the abutment (θ_A), pile (θ_p), and POI (θ_{pi}) for: control, short span, pulling away from backfill, +50.8 mm (+2 in) cases.	105
Figure 59: The rotations at the abutment (θ_A), pile (θ_p), and POI (θ_{pi}) for: CFRP, short span, pulling away from backfill, +50.8 mm (+2 in) cases.	105
Figure 60: The rotations at the abutment (θ_A), pile (θ_p), and POI (θ_{pi}) for: control, medium span, pulling away from backfill, +50.8 mm (+2 in) cases.	106
Figure 61: The rotations at the abutment (θ_A), pile (θ_p), and POI (θ_{pi}) for: CFRP, medium span, pulling away from backfill, +50.8 mm (+2 in) cases.	106
Figure 62: The rotations at the abutment (θ_A), pile (θ_p), and POI (θ_{pi}) for: control, long span, pulling away from backfill, +50.8 mm (+2 in) cases.	107
Figure 63: The rotations at the abutment (θ_A), pile (θ_p), and POI (θ_{pi}) for: CFRP, long span, pulling away from backfill, +50.8 mm (+2 in) cases.	107
Figure 64: θ_p vs. Δ_g for: control, pulling away from backfill, short span.....	108
Figure 65: θ_p vs. Δ_g for: CFRP, pulling away from backfill, short span.....	108
Figure 66: θ_p vs. Δ_g for: control, pulling away from backfill, medium span.....	109
Figure 67: θ_p vs. Δ_g for: CFRP, pulling away from backfill, medium span.	109
Figure 68: θ_p vs. Δ_g for: control, pulling away from backfill, long span.....	110

Figure 69: θ_p vs. Δ_g for: CFRP, pulling away from backfill, medium span.	110
Figure 70: Deflection along the pile in control, medium sand, short span.	114
Figure 71: Calculation of curvature along the pile.	115
Figure 72: Curvature demand along the pile for: control, medium sand, short span, pulling away from backfill.....	116
Figure 73: Curvature demand along the pile for: control vs. CFRP, medium sand, short span, pulling away from backfill.	116
Figure 74: Curvature demand along the pile for all types of, medium span, pulling away from backfill, $\Delta_g = +50.8$ mm (+ 2in).....	117
Figure 75: Curvature demand along the pile for all types of, long span, pulling away from backfill, $\Delta_g = +50.8$ mm (+2 in).....	117
Figure 76: Curvature demand for: control (no CFRP), stiff clay, long span, pulling away from backfill.....	118
Figure 77: Curvature demand for: CFRP, sand dense, short span, pulling away from backfill.	118
Figure 78: The curvature along the pile showing (L_{pi}) decreased at 50.8mm (2in) displacement in control model.	122
Figure 79: The curvature along the pile showing (L_{pi}) increased at 50.8mm (2in) displacement with the use of CFRP.	122
Figure 80: A schematic of the localized model showing the pile to the POI and the pile's cap.	123
Figure 81: The localized model displacement (Δ_m).	128
Figure 82: Pile-pile cap assembly and boundary condition.	132

Figure 83: Three different models: (a) Control (b) Retrofit (c) ECFRP.....	132
Figure 84: Load-displacement results from the localized models with three different mesh sizes.....	133
Figure 85: The tensile plastic strains for the different mesh sizes (a) 40mm	134
Figure 86: Load-displacement curves using L_{pi} for dense sand vs. L_{pi-avg}	137
Figure 87: Load-displacement curves using L_{pi} for soft clay vs. L_{pi-avg}	137
Figure 88: Lateral load vs. displacement for medium sand, control, and medium span case.....	139
Figure 89: Lateral load vs. displacement for medium sand, CFRP, and medium span case.	139
Figure 90: Lateral load vs. displacement for medium sand, ECFRP, and medium span case.....	139
Figure 91: Lateral load vs. displacement for medium clay, control, and medium span case.....	140
Figure 92: Lateral load vs. displacement for medium clay, CFRP, and medium span case.	140
Figure 93: Lateral load vs. displacement for medium clay, ECFRP, and medium span case.....	140
Figure 94: Lateral load vs. Displacement for: medium sand, all types of confinement, medium span cases.....	143
Figure 95: Lateral load vs. Displacement for: medium clay, all types of confinement, medium span cases.....	144

Figure 96: Lateral load vs. Displacement of all types for: control, all types of, medium span cases.....	144
Figure 97: Lateral load vs. Displacement of all types for: CFRP, all types of, medium span cases.....	145
Figure 98: Lateral load vs. Displacement of all types for: ECFRP, all types of, medium span cases.....	145
Figure 99: Lateral load vs. Displacement for: control, medium sand, all different span lengths.....	146
Figure 100: Lateral load vs. Displacement for: CFRP, medium sand, all different span lengths.....	147
Figure 101: Lateral load vs. Displacement for: ECFRP, medium sand, all different span lengths.....	147
Figure 102: Lateral load vs. Displacement for: control, medium clay, all different span lengths.....	148
Figure 103: Lateral load vs. Displacement for: CFRP, medium clay, all different span lengths.....	148
Figure 104: Lateral load vs. Displacement for: ECFRP, medium clay, all different span lengths.....	149
Figure 105: Tensile plastic strain: control, sand medium, medium span.....	151
Figure 106: Tensile plastic strain: CFRP, sand medium, medium span.....	151
Figure 107: Tensile plastic strain: ECFRP, sand medium, medium span.....	151
Figure 108: Tensile damage: control, medium sand, medium span.....	152
Figure 109: Tensile damage: CFRP, medium sand, medium span.....	152

Figure 110: Tensile damage: ECFRP, medium sand, medium span.....	152
Figure 111: Tensile plastic strain: control, medium clay, medium span.	153
Figure 112: Tensile damage: control, medium clay, medium span.	153
Figure 113: Tensile plastic strain: control, sand medium, short span.....	154
Figure 114: Tensile plastic strain: control, sand medium, medium span.....	154
Figure 115: Tensile plastic strain: control, sand medium, long span.....	154
Figure 116: Tensile damage: control, medium sand, short span.....	155
Figure 117: Tensile damage: control, medium sand, medium span.	155
Figure 118: Tensile damage: control, medium sand, long span.	155
Figure 119: $(\theta_A H_A/\Delta_g)$ vs. (Δ_p/Δ_g) for short span, all Δ_g	157
Figure 120: $(\theta_A H_A/\Delta_g)$ vs. (Δ_p/Δ_g) for medium span, all Δ_g	157
Figure 121: $(\theta_A H_A/\Delta_g)$ vs. (Δ_p/Δ_g) for long span, all Δ_g	158
Figure 122: The slope for $(\Delta_p/\Delta_g)_e$ equation	159
Figure 123: The intercept for $(\Delta_p/\Delta_g)_e$ equation.....	159
Figure 124: FE (Δ_p/Δ_g) vs. estimated $(\Delta_p/\Delta_g)_e$	159
Figure 125: The rotation at the abutment (θ_A) for different girder, $\Delta_g= +50.8\text{mm}$ (+2 in).	160
Figure 126: The rotation at the abutment (θ_A) for sands.....	161
Figure 127: The rotation at the abutment (θ_A) for clays.	161
Figure 128: FE (θ_A) vs. estimated (θ_A) for sand.	163
Figure 129: FE (θ_A) vs. estimated (θ_A) for clay.	163
Figure 130: Displacements of pile and girder.....	167
Figure C - 1: Lateral load vs. displacement Δ_m : control, dense sand, short span.	197

Figure C - 2: Lateral load vs. displacement Δ_m : CFRP, dense sand, short span..... 197

Figure C - 3: Lateral load vs. displacement Δ_m : ECFRP, dense sand, short span. 197

Figure C - 4: Lateral load vs. displacement Δ_m : control, medium sand, short span. 198

Figure C - 5: Lateral load vs. displacement Δ_m : CFRP, medium sand, short span..... 198

Figure C - 6: Lateral load vs. displacement Δ_m : ECFRP, medium sand, short span. 198

Figure C - 7: Lateral load vs. displacement Δ_m : control, loose sand, short span..... 199

Figure C - 8: Lateral load vs. displacement Δ_m : CFRP, loose sand, short span. 199

Figure C - 9: Lateral load vs. displacement Δ_m : ECFRP, loose sand, short span. 199

Figure C - 10: Lateral load vs. displacement Δ_m : control, stiff clay, short span..... 200

Figure C - 11: Lateral load vs. displacement Δ_m : CFRP, stiff clay, short span. 200

Figure C - 12: Lateral load vs. displacement Δ_m : ECFRP, stiff clay, short span..... 200

Figure C - 13: Lateral load vs. displacement Δ_m : control, medium clay, short span..... 201

Figure C - 14: Lateral load vs. displacement Δ_m : CFRP, medium clay, short span. 201

Figure C - 15: Lateral load vs. displacement Δ_m : ECFRP, medium clay, short span. 201

Figure C - 16: Lateral load vs. displacement Δ_m : control, soft clay, short span. 202

Figure C - 17: Lateral load vs. displacement Δ_m : CFRP, soft clay, short span..... 202

Figure C - 18: Lateral load vs. displacement Δ_m : ECFRP, soft clay, short span. 202

Figure C - 19: Lateral load vs. displacement Δ_m : control, dense sand, medium span. ... 203

Figure C - 20: Lateral load vs. displacement Δ_m : CFRP, dense sand, medium span..... 203

Figure C - 21: Lateral load vs. displacement Δ_m : ECFRP, dense sand, medium span. .. 203

Figure C - 22: Lateral load vs. displacement Δ_m : control, medium sand, medium span. 204

Figure C - 23: Lateral load vs. displacement Δ_m : CFRP, medium sand, medium span.. 204

Figure C - 24: Lateral load vs. displacement Δ_m : ECFRP, medium sand, medium span.
..... 204

Figure C - 25: Lateral load vs. displacement Δ_m : control, loose sand, medium span. 205

Figure C - 26: Lateral load vs. displacement Δ_m : CFRP, loose sand, medium span. 205

Figure C - 27: Lateral load vs. displacement Δ_m : ECFRP, loose sand, medium span. 205

Figure C - 28: Lateral load vs. displacement Δ_m : control, stiff clay, medium span. 206

Figure C - 29: Lateral load vs. displacement Δ_m : CFRP, stiff clay, medium span. 206

Figure C - 30: Lateral load vs. displacement Δ_m : ECFRP, stiff clay, medium span. 206

Figure C - 31: Lateral load vs. displacement Δ_m : control, medium clay, medium span. 207

Figure C - 32: Lateral load vs. displacement Δ_m : CFRP, medium clay, medium span. . 207

Figure C - 33: Lateral load vs. displacement Δ_m : ECFRP, medium clay, medium span. 207

Figure C - 34: Lateral load vs. displacement Δ_m : control, soft clay, medium span. 208

Figure C - 35: Lateral load vs. displacement Δ_m : CFRP, soft clay, medium span. 208

Figure C - 36: Lateral load vs. displacement Δ_m : ECFRP, soft clay, medium span. 208

Figure C - 37: Lateral load vs. displacement Δ_m : control, dense sand, long span. 209

Figure C - 38: Lateral load vs. displacement Δ_m : CFRP, dense sand, long span. 209

Figure C - 39: Lateral load vs. displacement Δ_m : ECFRP, dense sand, long span. 209

Figure C - 40: Lateral load vs. displacement Δ_m : control, medium sand, long span. 210

Figure C - 41: Lateral load vs. displacement Δ_m : CFRP, medium sand, long span. 210

Figure C - 42: Lateral load vs. displacement Δ_m : ECFRP, medium sand, long span. 210

Figure C - 43: Lateral load vs. displacement Δ_m : control, loose sand, long span. 211

Figure C - 44: Lateral load vs. displacement Δ_m : CFRP, loose sand, long span. 211

Figure C - 45: Lateral load vs. displacement Δ_m : ECFRP, loose sand, long span. 211

Figure C - 46: Lateral load vs. displacement Δ_m : control, stiff clay, long span.	212
Figure C - 47: Lateral load vs. displacement Δ_m : CFRP, stiff clay, long span.	212
Figure C - 48: Lateral load vs. displacement Δ_m : ECFRP, stiff clay, long span.....	212
Figure C - 49: Lateral load vs. displacement Δ_m : control, medium clay, long span.....	213
Figure C - 50: Lateral load vs. displacement Δ_m : CFRP, medium clay, long span.	213
Figure C - 51: Lateral load vs. displacement Δ_m : ECFRP, medium clay, long span.....	213
Figure C - 52: Lateral load vs. displacement Δ_m : control, soft clay, long span.....	214
Figure C - 53: Lateral load vs. displacement Δ_m : CFRP, soft clay, long span.	214
Figure C - 54: Lateral load vs. displacement Δ_m : ECFRP, soft clay, long span.	214
Figure D - 1: Tensile plastic strain: control, dense sand, short span.	215
Figure D - 2: Tensile plastic strain: CFRP, dense sand, short span.	215
Figure D - 3: Tensile plastic strain: ECFRP, dense sand, short span.....	215
Figure D - 4: Tensile damage: control, dense sand, short span.	216
Figure D - 5: Tensile damage: CFRP, dense sand, short span.....	216
Figure D - 6: Tensile damage: ECFRP, dense sand, short span.	216
Figure D - 7: Stiffness degradation: control, dense sand, short span.....	217
Figure D - 8: Stiffness degradation: CFRP, dense sand, short span.	217
Figure D - 9: Stiffness degradation: ECFRP, dense sand, short span.....	217
Figure D - 10: Tensile plastic strain: control, medium sand, short span.	218
Figure D - 11: Tensile plastic strain: CFRP, medium sand, short span.....	218
Figure D - 12: Tensile plastic strain: ECFRP, medium sand, short span.....	218
Figure D - 13: Tensile damage: control, medium sand, short span.	219
Figure D - 14: Tensile damage: CFRP, medium sand, short span.....	219

Figure D - 15: Tensile damage: ECFRP, medium sand, short span.	219
Figure D - 16: Stiffness degradation: control, medium sand, short span.....	220
Figure D - 17: Stiffness degradation: CFRP, medium sand, short span.	220
Figure D - 18: Stiffness degradation: ECFRP, medium sand, short span.....	220
Figure D - 19: Tensile plastic strain: control, loose sand, short span.	221
Figure D - 20: Tensile plastic strain: CFRP, loose sand, short span.....	221
Figure D - 21: Tensile plastic strain: ECFRP, loose sand, short span.	221
Figure D - 22: Tensile damage: control, loose sand, short span.	222
Figure D - 23: Tensile damage: CFRP, loose sand, short span.....	222
Figure D - 24: Tensile damage: ECFRP, loose sand, short span.	222
Figure D - 25: Stiffness degradation: control, loose sand, short span.	223
Figure D - 26: Stiffness degradation: CFRP, loose sand, short span.....	223
Figure D - 27: Stiffness degradation: ECFRP, loose sand, short span.	223
Figure D - 28: Tensile plastic strain: control, stiff clay, short span.....	224
Figure D - 29: Tensile plastic strain: CFRP, stiff clay, short span.	224
Figure D - 30: Tensile plastic strain: ECFRP, stiff clay, short span.	224
Figure D - 31: Tensile damage: control, stiff clay, short span.....	225
Figure D - 32: Tensile damage: CFRP, stiff clay, short span.	225
Figure D - 33: Tensile damage: ECFRP, stiff clay, short span.....	225
Figure D - 34: Stiffness degradation: control, stiff clay, short span.	226
Figure D - 35: Stiffness degradation: CFRP, stiff clay, short span.....	226
Figure D - 36: Stiffness degradation: ECFRP, stiff clay, short span.	226
Figure D - 37: Tensile plastic strain: control, medium clay, short span.	227

Figure D - 38: Tensile plastic strain: CFRP, medium clay, short span.....	227
Figure D - 39: Tensile plastic strain: ECFRP, medium clay, short span.	227
Figure D - 40: Tensile damage: control, medium clay, short span.	228
Figure D - 41: Tensile damage: CFRP, medium clay, short span.....	228
Figure D - 42: Tensile damage: ECFRP, medium clay, short span.	228
Figure D - 43: Stiffness degradation: control, medium clay, short span.	229
Figure D - 44: Stiffness degradation: CFRP, medium clay, short span.	229
Figure D - 45: Stiffness degradation: ECFRP, medium clay, short span.	229
Figure D - 46: Tensile plastic strain: control, soft clay, short span.	230
Figure D - 47: Tensile plastic strain: CFRP, soft clay, short span.....	230
Figure D - 48: Tensile plastic strain: ECFRP, soft clay, short span.	230
Figure D - 49: Tensile damage: control, soft clay, short span.	231
Figure D - 50: Tensile damage: CFRP, soft clay, short span.....	231
Figure D - 51: Tensile damage: ECFRP, soft clay, short span.	231
Figure D - 52: Stiffness degradation: control, soft clay, short span.	232
Figure D - 53: Stiffness degradation: CFRP, soft clay, short span.	232
Figure D - 54: Stiffness degradation: ECFRP, soft clay, short span.....	232
Figure D - 55: Tensile plastic strain: control, dense sand, medium span.	233
Figure D - 56: Tensile plastic strain: CFRP, dense sand, medium span.....	233
Figure D - 57: Tensile plastic strain: ECFRP, dense sand, medium span.	233
Figure D - 58: Tensile damage: control, dense sand, medium span.	234
Figure D - 59: Tensile damage: CFRP, dense sand, medium span.....	234
Figure D - 60: Tensile damage: ECFRP, dense sand, medium span.	234

Figure D - 61: Stiffness degradation: control, dense sand, medium span.....	235
Figure D - 62: Stiffness degradation: CFRP, dense sand, medium span.	235
Figure D - 63: Stiffness degradation: ECFRP, dense sand, medium span.....	235
Figure D - 64: Tensile plastic strain: control, medium sand, medium span.	236
Figure D - 65: Tensile plastic strain: CFRP, medium sand, medium span.	236
Figure D - 66: Tensile plastic strain: ECFRP, medium sand, medium span.	236
Figure D - 67: Tensile damage: control, medium sand, medium span.	237
Figure D - 68: Tensile damage: CFRP, medium sand, medium span.	237
Figure D - 69: Tensile damage: ECFRP, medium sand, medium span.	237
Figure D - 70: Stiffness degradation: control, medium sand, medium span.....	238
Figure D - 71: Stiffness degradation: CFRP, medium sand, medium span.	238
Figure D - 72: Stiffness degradation: ECFRP, medium sand, medium span.....	238
Figure D - 73: Tensile plastic strain: control, loose sand, medium span.	239
Figure D - 74: Tensile plastic strain: CFRP, loose sand, medium span.....	239
Figure D - 75: Tensile plastic strain: ECFRP, loose sand, medium span.	239
Figure D - 76: Tensile damage: control, loose sand, medium span.	240
Figure D - 77: Tensile damage: CFRP, loose sand, medium span.	240
Figure D - 78: Tensile damage: ECFRP, loose sand, medium span.	240
Figure D - 79: Stiffness degradation: control, loose sand, medium span.	241
Figure D - 80: Stiffness degradation: CFRP, loose sand, medium span.....	241
Figure D - 81: Stiffness degradation: ECFRP, loose sand, medium span.	241
Figure D - 82: Tensile plastic strain: control, stiff clay, medium span.....	242
Figure D - 83: Tensile plastic strain: CFRP, stiff clay, medium span.	242

Figure D - 84: Tensile plastic strain: ECFRP, stiff clay, medium span.....	242
Figure D - 85: Tensile damage: control, stiff clay, medium span.....	243
Figure D - 86: Tensile damage: CFRP, stiff clay, medium span.	243
Figure D - 87: Tensile damage: ECFRP, stiff clay, medium span.....	243
Figure D - 88: Stiffness degradation: control, stiff clay, medium span.....	244
Figure D - 89: Stiffness degradation: CFRP, stiff clay, medium span.	244
Figure D - 90: Stiffness degradation: ECFRP, stiff clay, medium span.	244
Figure D - 91: Tensile plastic strain: control, medium clay, medium span.	245
Figure D - 92: Tensile plastic strain: CFRP, medium clay, medium span.....	245
Figure D - 93: Tensile plastic strain: ECFRP, medium clay, medium span.	245
Figure D - 94: Tensile damage: control, medium clay, medium span.	246
Figure D - 95: Tensile damage: CFRP, medium clay, medium span.	246
Figure D - 96: Tensile damage: ECFRP, medium clay, medium span.	246
Figure D - 97: Stiffness degradation: control, medium clay, medium span.	247
Figure D - 98: Stiffness degradation: CFRP, medium clay, medium span.....	247
Figure D - 99: Stiffness degradation: ECFRP, medium clay, medium span.	247
Figure D - 100: Tensile plastic strain: control, soft clay, medium span.	248
Figure D - 101: Tensile plastic strain: CFRP, soft clay, medium span.....	248
Figure D - 102: Tensile plastic strain: ECFRP, soft clay, medium span.	248
Figure D - 103: Tensile damage: control, soft clay, medium span.	249
Figure D - 104: Tensile damage: CFRP, soft clay, medium span.....	249
Figure D - 105: Tensile damage: ECFRP, soft clay, medium span.	249
Figure D - 106: Stiffness degradation: control, soft clay, medium span.	250

Figure D - 107: Stiffness degradation: CFRP, soft clay, medium span.	250
Figure D - 108: Stiffness degradation: ECFRP, soft clay, medium span.	250
Figure D - 109: Tensile plastic strain: control, dense sand, long span.	251
Figure D - 110: Tensile plastic strain: CFRP, dense sand, long span.	251
Figure D - 111: Tensile plastic strain: ECFRP, dense sand, long span.	251
Figure D - 112: Tensile damage: control, dense sand, long span.	252
Figure D - 113: Tensile damage: CFRP, dense sand, long span.	252
Figure D - 114: Tensile damage: ECFRP, dense sand, long span.	252
Figure D - 115: Stiffness degradation: control, dense sand, long span.	253
Figure D - 116: Stiffness degradation: CFRP, dense sand, long span.	253
Figure D - 117: Stiffness degradation: ECFRP, dense sand, long span.	253
Figure D - 118: Tensile plastic strain: control, medium sand, long span.	254
Figure D - 119: Tensile plastic strain: CFRP, medium sand, long span.	254
Figure D - 120: Tensile plastic strain: ECFRP, medium sand, long span.	254
Figure D - 121: Tensile damage: control, medium sand, long span.	255
Figure D - 122: Tensile damage: CFRP, medium sand, long span.	255
Figure D - 123: Tensile damage: ECFRP, medium sand, long span.	255
Figure D - 124: Stiffness degradation: control, medium sand, long span.	256
Figure D - 125: Stiffness degradation: CFRP, medium sand, long span.	256
Figure D - 126: Stiffness degradation: ECFRP, medium sand, long span.	256
Figure D - 127: Tensile plastic strain: control, loose sand, long span.	257
Figure D - 128: Tensile plastic strain: CFRP, loose sand, long span.	257
Figure D - 129: Tensile plastic strain: ECFRP, loose sand, long span.	257

Figure D - 130: Tensile damage: control, loose sand, long span.....	258
Figure D - 131: Tensile damage: CFRP, loose sand, long span.	258
Figure D - 132: Tensile damage: ECFRP, loose sand, long span.	258
Figure D - 133: Stiffness degradation: control, loose sand, long span.	259
Figure D - 134: Stiffness degradation: CFRP, loose sand, long span.	259
Figure D - 135: Stiffness degradation: ECFRP, loose sand, long span.	259
Figure D - 136: Tensile plastic strain: control, stiff clay, long span.....	260
Figure D - 137: Tensile plastic strain: CFRP, stiff clay, long span.	260
Figure D - 138: Tensile plastic strain: ECFRP, stiff clay, long span.....	260
Figure D - 139: Tensile damage: control, stiff clay, long span.....	261
Figure D - 140: Tensile damage: CFRP, stiff clay, long span.	261
Figure D - 141: Tensile damage: ECFRP, stiff clay, long span.....	261
Figure D - 142: Stiffness degradation: control, stiff clay, long span.	262
Figure D - 143: Stiffness degradation: CFRP, stiff clay, long span.	262
Figure D - 144: Stiffness degradation: ECFRP, stiff clay, long span.	262
Figure D - 145: Tensile plastic strain: control, medium clay, long span.	263
Figure D - 146: Tensile plastic strain: CFRP, medium clay, long span.....	263
Figure D - 147: Tensile plastic strain: ECFRP, medium clay, long span.	263
Figure D - 148: Tensile damage: control, medium clay, long span.....	264
Figure D - 149: Tensile damage: CFRP, medium clay, long span.	264
Figure D - 150: Tensile damage: ECFRP, medium clay, long span.	264
Figure D - 151: Stiffness degradation: control, medium clay, long span.	265
Figure D - 152: Stiffness degradation: CFRP, medium clay, long span.	265

Figure D - 153: Stiffness degradation: ECFRP, medium clay, long span. 265

Figure D - 154: Tensile plastic strain: control, soft clay, long span. 266

Figure D - 155: Tensile plastic strain: CFRP, soft clay, long span..... 266

Figure D - 156: Tensile plastic strain: ECFRP, soft clay, long span. 266

Figure D - 157: Tensile damage: control, soft clay, long span. 267

Figure D - 158: Tensile damage: CFRP, soft clay, long span..... 267

Figure D - 159: Tensile damage: ECFRP, soft clay, long span. 267

Figure D - 160: Stiffness degradation: control, soft clay, long span. 268

Figure D - 161: Stiffness degradation: CFRP, soft clay, long span..... 268

Figure D - 162: Stiffness degradation: ECFRP, soft clay, long span. 268

LIST OF TABLES

Table 1: Maximum permissible length of steel and concrete Integral Abutment Bridges (Tabatabai, Magbool, et al. 2017).....	20
Table 2: Pile types for integral abutment bridges (Tabatabai, Magbool, et al. 2017).	21
Table 3: Steel pile orientation in integral abutment bridges (Tabatabai, Magbool, et al. 2017).	22
Table 4: Minimum embedment length of pile into pile cap (Tabatabai, Magbool, et al. 2017).	22
Table 5: Summary of curvature demands estimated for piles in the field during past earthquakes (Fanous, et al. 2010).	38
Table 6: Summary of curvature capacities reported for prestressed concrete piles used in seismic regions (Fanous, et al. 2010).....	38
Table 7: Concrete damage plasticity general parameters (ABAQUS 2015).	56
Table 8: Concrete compression hardening (Tyau 2009).....	56
Table 9: Concrete Compression damage (Tyau 2009).	57
Table 10: Concrete tension stiffening (Tyau 2009).	57
Table 11: Concrete tension damage (Tyau 2009).....	58
Table 12: Sands properties (Allen and Meade 1988, Das, et al. 1999, Monley and Wu 1993).	59
Table 13: Clay proprieties (Monley and Wu 1993, Allen and Meade 1988, Das, et al. 1999).	60
Table 14: Soil's friction coefficient and (Das, et al. 1999).	61
Table 15: Mechanical properties of CFRP (American Concrete Institute 2008).....	65

Table 16: Cross-sectional properties of prestressed concrete pile (Tabatabai and Oesterle 1999).	71
Table 17: Concrete properties (Tabatabai and Oesterle 1999).	74
Table 18: Reinforcing Steel properties (Tyau 2009).	74
Table 19: Mechanical properties of column reinforcement (Choi, et al. 2015).....	80
Table 20: Mechanical properties of fibers (Choi, et al. 2015).	81
Table 21: Steel 414 MPa (60ksi) stress vs. plastic strains Data (Barker and Puckett 2006).	82
Table 22: Equivalent girder dimensions, moment of inertia, and pile loads for various span lengths.....	93
Table 23: Models dimensions based on span lengths.	94
Table 24: Number of elements used in different models.	97
Table 25: The recorded rotations in all control cases-pulling away from the backfill. ..	101
Table 26: The recorded rotations in all control cases-pushing against backfill.....	102
Table 27: The recorded rotations in all CFRP cases-pulling away from backfill.....	103
Table 28: The recorded rotations in all CFRP cases-pushing against backfill.	104
Table 29: Δ_p of all cases (control, pulling away from backfill).	112
Table 30: Δ_p of all cases (control, pushing against backfill).	112
Table 31: Δ_p of all cases (CFRP, pulling away from backfill).	113
Table 32: Δ_p of all cases (CFRP, pushing against backfill).	113
Table 33: L_{pi} for the control cases (pulling away from backfill)	120
Table 34: L_{pi} for the control cases (pushing against backfill).....	120
Table 35: L_{pi} for the CFRP cases (pulling away from backfill).....	121

Table 36: L_{pi} for the CFRP cases (pushing against backfill)	121
Table 37: Δ_{pi} for the control cases (pulling away from backfill)	124
Table 38: Δ_{pi} for the control cases (pushing against backfill)	124
Table 39: Δ_{pi} for the CFRP cases (pulling away from backfill)	125
Table 40: Δ_{pi} for the CFRP cases (pushing against backfill)	125
Table 41: Average L_{pi} values for all control cases.....	126
Table 42: Average L_{pi} for all CFRP cases.	127
Table 43: Δ_m for the control cases (pulling away from backfill)	129
Table 44: Δ_m for the control cases (pushing against backfill)	130
Table 45: Δ_m for the CFRP cases (pulling away from backfill)	130
Table 46: Δ_m for the CFRP cases (pushing against backfill)	131
Table 47: Control model (elements number vs. analysis time).	133
Table 48: L_{pi-avg} for all control cases.....	136
Table 49: L_{pi-avg} for all CFRP cases.	136
Table 50: Average L_{pi-avg} for all control cases.	136
Table 51: Average L_{pi-avg} for all CFRP cases.....	136
Table 52: Maximum lateral force at the fifth cycle - control.....	141
Table 53: Maximum lateral force at the fifth cycle - CFRP	141
Table 54: Maximum lateral force at the fifth cycle - ECFRP.....	141
Table 55: Control piles calculated moment.	142
Table 56: CFRP piles calculated moment.....	142
Table 57: ECFRP piles calculated moment.	142
Table 58: The maximum strains in steel at the pile-abutment interface.	156

Table 59: The regression parameters for sand.	162
Table 60: The regression parameters for clay.	162
Table A - 1: General model girder details.	178
Table B - 1: General model results: control, short span, $\Delta_g = \pm 12.7$ mm (± 0.5 in).....	179
Table B - 2: General model results: control, short span, $\Delta_g = \pm 25.4$ mm (± 1 in).....	180
Table B - 3: General model results: control, short span, $\Delta_g = \pm 50.8$ mm (± 2 in).....	181
Table B - 4: General model results: CFRP, short span, $\Delta_g = \pm 12.7$ mm (± 0.5 in)	182
Table B - 5: General model results: CFRP, short span, $\Delta_g = \pm 25.4$ mm (± 1 in)	183
Table B - 6: General model results: CFRP, short span, $\Delta_g = \pm 50.8$ mm (± 2 in)	184
Table B - 7: General model results: control, medium span, $\Delta_g = \pm 12.7$ mm (± 0.5 in)....	185
Table B - 8: General model results: control, medium span, $\Delta_g = \pm 25.4$ mm (± 1 in).....	186
Table B - 9: General model results: control, medium span, $\Delta_g = \pm 50.8$ mm (± 2 in).....	187
Table B - 10: General model results: CFRP, medium span, $\Delta_g = \pm 12.7$ mm (± 0.5 in) ...	188
Table B - 11: General model results: CFRP, medium span, $\Delta_g = \pm 25.4$ mm (± 1 in)	189
Table B - 12: General model results: CFRP, medium span, $\Delta_g = \pm 50.8$ mm (± 2 in)	190
Table B - 13: General model results: control, long span, $\Delta_g = \pm 12.7$ mm (± 0.5 in).....	191
Table B - 14: General model results: control, long span, $\Delta_g = \pm 25.4$ mm (± 1 in).....	192
Table B - 15: General model results: control, long span, $\Delta_g = \pm 50.8$ mm (± 2 in).....	193
Table B - 16: General model results: CFRP, long span, $\Delta_g = \pm 12.7$ mm (± 0.5 in)	194
Table B - 17: General model results: CFRP, long span, $\Delta_g = \pm 25.4$ mm (± 1 in)	195
Table B - 18: General model results: CFRP, long span, $\Delta_g = \pm 50.8$ mm (± 2 in)	196

ACKNOWLEDGMENTS

This work would not have been possible without the help and support of many people. I would like first to thank my academic advisor, Professor Habib Tabatabai, for his endless support and help through to its completion. The number of times I turned to Professor Tabatabai for guidance cannot be counted, and he always gave willingly of his time and experience to get me over the rough spots.

I would like also to thank Professor Adeeb Rahman, Professor Hani Titi, Professor Konstantin Sobolev, and Professor Benjamin Church who served on my committee and provided valuable suggestions and time.

Also, I would like to thank my family for their endless support especially my parents and my wife. Thank you for all the support and belief in me.

I would like to thank Jazan University for their financial support throughout my PhD study.

1 INTRODUCTION

1.1 Background

Enhancing durability and reliability of bridge structures is an important concern (Nabizadeh, Tabatabai and Tabatabai 2018, Tabatabai and Nabizadeh 2018, Tabatabai, Nabizadeh and Tabatabai 2018). Conventional bridges constructed with steel and concrete girders require expansion joints and bearings at piers and abutments to accommodate displacements that are generated due to thermal movement and other inelastic strains. The major problem with these joints and bearings is their relatively high cost of long-term maintenance and repairs associated with their failures. The joints can be damaged by snow plows and heavy trucks. The rubber components could also leak and allow deicing salts to reach various superstructure and substructure elements. Runoff containing deicing salts can lead to long-term deterioration. Bearings may often freeze and restrict movement. So, the use of expansion joints and bearings in conventional bridges to accommodate thermal movements contribute to maintenance problems, instead of solving them (Burdette, Howard, et al. 2005).

Integral bridges rely on the interaction between the structure and its surrounding soil to accommodate the longitudinal contraction or expansion movements without the use of any expansion joints on the bridge itself. Integral bridges can have one or more spans, and their superstructure is sometimes cast integrally with the substructure. Integral abutments are typically supported on a single row of piles to better facilitate movement. The piers for integral abutment bridges can be constructed either integrally or non-integrally with the superstructure (Wasserman and Walker 1996).

To accommodate thermal expansion or contraction, an approach slab and a sleeper slab are commonly used in integral abutment bridges. To prevent pavement buckling, or bulging, an expansion joint is typically used at the end of the approach slab. At this location, the consequences of a failure of the joint including infiltration of runoff are far less unfavorable compared to having the joint on the bridge. A typical integral abutment bridge is shown schematically in Figure 1.

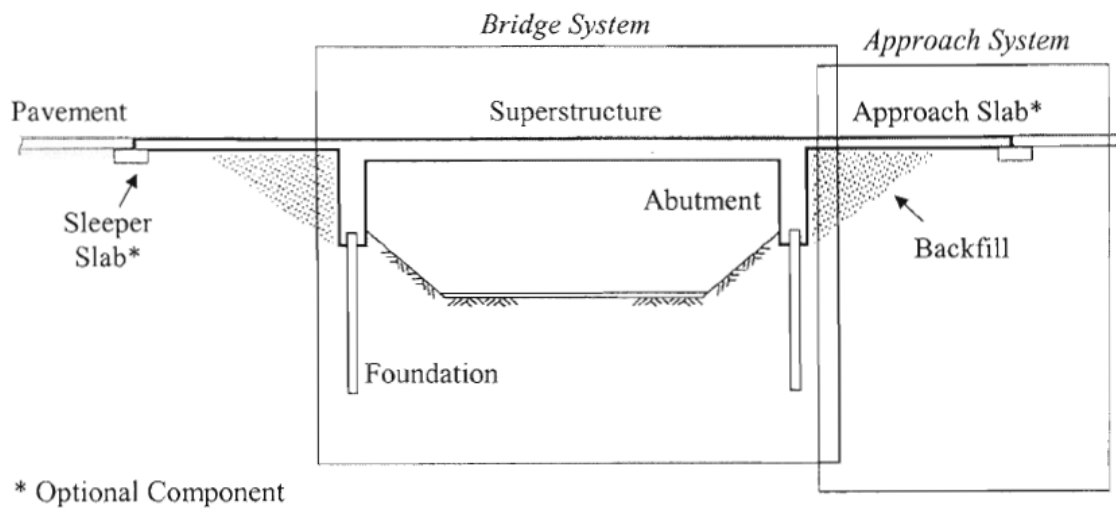


Figure 1: Typical components of an integral abutment bridge (Moulton, GangaRao and Halvorsen 1985).

Integral abutment bridges are favored over jointed bridges for several reasons. Due to the elimination of expansion joints, integral bridges are expected to have reduced short- and long-term maintenance cost. Moreover, the construction process is simplified, and battered piles are not needed. Integral bridges are expected to have better seismic performance because the superstructure is cast integrally with the foundation resulting in greater structural redundancy (Moulton, GangaRao and Halvorsen 1985). In continuous integral bridges, the weight of the abutments can help prevent uplift of the girder and the ratio of end-span to interior-span for girders cast integrally with abutments can be

decreased (Burdette, Howard, et al. 2005).

When constructing integral abutment bridges, steel H-piles are most frequently used, mainly due to the unique stress and flexibility requirements of the abutments (Burdette, Howard, et al. 2004). In addition to steel H-piles, concrete filled steel pipe piles and prestressed concrete piles have also been used. The basic design approach for integral bridges is to build flexibility in the integral abutments to allow movement. Therefore, steel piles have been perceived to offer a better solution by the majority of states in the US.

The behavior of integral abutment piles has been extensively studied, both in the laboratory and in the field. While earlier investigations of the behavior of integral abutment piles had been primarily focused on field studies of integral abutment bridges and tests on driven piles, laboratory studies of integral abutment piles, using either full-size or scaled-down models have also been performed (Shah 2007). Most of the experimental studies involve the use of steel H-piles. However, a study performed by Tabatabai et al. (1999) reported results of laboratory tests on prestressed concrete piles and H-piles. Arsoy, Duncan, and Barker dealt with the utilization of steel pipe piles and prestressed concrete piles (Mistry 2005). Greimann et al. (1988) performed full-scale model tests on integral abutments with prestressed concrete piles. It was reported that horizontal abutment movements larger than 13 mm (0.5 in) would cause the steel piles to yield (Greimann and Wolde-Tinsae 1988). Jorgenson (1981) pointed out that, for a maximum measured movement of the abutment equivalent to 50 mm (1.96 in), the stress at the top of the steel pile was calculated to be adequate to commence yielding in the steel, but not sufficient to form a plastic hinge (Jorgenson 1981).

Considering the results mentioned above, it is clear that the abutment movement associated with the expansion of the bridge may cause yielding of the steel pile at its interface with the pile cap. The recurring movements that would be expected to occur over the lifespan of a bridge would cause repetitive back-and-forth movements including reversals of tensile and compressive yielding stresses at the interface of the steel pile with the pile cap. Consequently, there have been concerns regarding the capability of the steel pile to uphold these inelastic strain reversals without compromising its load-carrying capacity (Tabatabai, Oesterle and Lawson 1999, Oesterle, et al. 1999).

When prestressed concrete piles are used in integral abutments, cracking and spalling of concrete can occur at the interface with the pile cap due to repetitive back-and-forth movements. This issue is further complicated by the fact that prestressed concrete piles are typically embedded in the concrete cap for a distance of 1220 mm (2 ft) or less. The greatest moment in this region of the pile is anticipated to occur at the bottom of the cap. The embedded strands may slip due to bond failure since the embedment distance is far shorter than the theoretical development length of the strand (Tabatabai, Oesterle and Lawson 1999).

Tests have been performed to evaluate the performance and limitations of steel and prestressed concrete piles in bridges with integral abutments (Tabatabai, Oesterle and Lawson 1999). The piles under the integral abutments must be engineered to accommodate cyclic movements due to temperature changes as well as creep and shrinkage strains while maintaining the capacity to resist vertical dead and live loads. The results of laboratory tests performed on steel and prestressed concrete pile specimens were summarized as follows (Tabatabai, Oesterle and Lawson 1999):

- “Local distortion (buckling) could occur during the cyclic movement of the steel pile. However, these cyclic movements did not cause major damage or loss of axial load-carrying capacity of the steel pile during the tests.
- The cyclic displacement tests showed that the prestressed concrete pile specimen was also able to sustain the loads. However, the amount of damage (cracking and spalling) caused was considered to be unacceptable.”

In prestressed concrete piles, the maximum displacement limits must be kept at lower values (compared to steel piles) unless extra steps are taken to manage cracking in the interface with the cap (Tabatabai, Oesterle and Lawson 1999). Pile-cap connections would have important influence on the pile’s curvature demand. For example, piles with fixed head connection will be under large curvature demand due to the fact that it will be subjected to many cyclic lateral loads like seismic load. Since pile failure under seismic loads has been reported and post-earthquake inspection may be difficult, damage assessments on piles are very important to ensure bridge safety (Song, Chai and Hale 2004).

Fiber Reinforced Polymer (FRP) composites have the potential to substantially enhance the integrity, ductility and strength of precast concrete piles at the interface with pile caps in integral abutment bridges. FRP wraps are widely used to repair and retrofit various concrete structural elements, especially in seismic areas and marine structures. Their lightweight, high strength and resistance to chemicals offer important benefits (Rajan and Mullins 2007). In its fabric form, the FRP can accommodate members with various shapes. The ability to change fiber direction allows optimized design options. FRP applications are particularly suited for emergency repairs where damage can be

multi-directional and rapid repairs are crucial (Rajan and Mullins 2007).

Because of their high strength and stiffness-to-weight ratio as well as corrosion and fatigue resistance, FRP systems have increased use in civil infrastructure systems. FRP wraps increase ultimate strength and ductility of reinforced concrete columns. Because of the immediate need for the seismic upgrade of existing reinforced concrete columns, most of the research efforts in the FRP field focus on the ductility of columns in seismic application (Cheng, Sotelino and Chen 2004).

1.2 Problem Statement

Although the most common pile used in integral abutment bridges is the steel H pile, some in the United State and other countries prefer using concrete piles due to local economic factors and soil conditions. The problem associated with steel piles in integral abutments undergoing cyclic lateral movement is the possible yielding and local buckling at the pile head and concern regarding the ability of the steel pile to sustain these inelastic strains without compromising its load-carrying capacity (Tabatabai, Oesterle and Lawson 1999, Greimann, Wolde-Tinsae and Yang 1983, Jorgenson 1981). On the other hand, concrete piles under repetitive back-and-forth movements would be expected to crack and spall at the interface with the pile cap (Tabatabai, Oesterle and Lawson 1999). Earlier study by Tabatabai et al. (1999) included a cyclic lateral movement test of a prestressed concrete pile under axial load. Results showed that the lateral cyclic movement due to bridge expansion and contraction could result in multiple cracks at the pile-pile cap interface. The results showed that the prestressed concrete pile could sustain the axial and transverse loads during cyclic lateral movement test, but the extent of damage to the pile

near the interface with the cap was considered unacceptable (Tabatabai, Oesterle and Lawson 1999).

Therefore, there is a need to develop procedures to address and minimize the damage in concrete piles at the interface with the pile cap in integral abutment bridges. In this study, the use of FRP composite wraps are proposed and studied to enhance the performance of prestressed concrete piles in integral bridges.

1.3 Objectives

The primary objectives of this research are highlighted and listed below:

1. Determine the performance parameters in integral abutment bridges supported by concrete piles.
2. Understand the behavior of concrete pile at the interface with the pile cap in integral abutment bridges with or without external FRP reinforcement.
3. Evaluate the effect of soil and soil-structure interaction on the behavior of concrete pile in integral abutment bridges.
4. Evaluate the effectiveness of localized FRP external reinforcement in enhancing the strength and ductility of reinforced concrete piles in integral abutment bridges.
5. Evaluate the performance and structural response of concrete piles in integral abutment bridges.

To achieve these objectives, a comprehensive literature review was conducted to obtain the latest information on the topics related to this study. Also, analytical models were prepared using the ABAQUS finite element program to analyze reinforced concrete piles under bridge integral abutments with or without localized FRP reinforcement at the interface between the pile and the pile cap. This included a parametric study of the

superstructure-abutment-soil-pile system to assess the effect of bridge superstructure movement on the forces and movements in the pile. Subsequently, detailed localized models of the pile/abutment were generated to study the effects of FRP wraps on the behavior of the pile. The effectiveness and accuracy of finite element models were verified using experimental data in the literature. This included a pile-pile cap load test, and an FRP-wrapped column test under cyclic deformations. Based on detailed analysis of the results, a set of design recommendations are made.

1.4 Scope of Work

The scope of work for this research can be summarized as follows:

1. Development of nonlinear FE models for integral abutments utilizing prestressed concrete piles with and without FRP external reinforcement.

The ABAQUS finite element program was utilized in this study to develop a generalized model of the structure including the abutment, pile, and the superstructure for three different span lengths. In addition, a localized model focusing on the pile-abutment zone was generated based on the results of the general model.

2. Verification of FE models.

To verify the basic FE modeling techniques used, several verification cases (models) were considered. These models were selected to verify the responses of concrete and FRP. The data used in the verification models were:

- A test by Tabatabai et al. (1999) as a verification model for the reinforced concrete pile under axial load and cyclic transverse displacement.

- A test by Choi et al. (2015) (seismic retrofit of reinforced concrete columns) to verify the response of a FRP-wrapped concrete column subjected to axial and cyclic lateral loads.
- A test by Burdette et al. (2004) as a verification model for a soil-pile system under cyclic lateral loads.

3. Parametric study.

The parametric study performed using the general model involved six different types of soil (three sands and three clays), two types of confinement (control [without FRP] and FRP [two layers of FRP]), three different span lengths (short or 15.25 m [50 ft], medium or 30.5 m [100 ft], and long or 45.75 m [150 ft]), and three different ranges of displacement imposed at centroid of the composite girders (± 12.7 mm [± 0.5 in], ± 25.4 mm [± 1 in], and ± 50.8 mm [± 2 in]).

The parametric study was performed using the localized model, and involved different pile depths to the point of inflection as well as different displacements imposed at the point of inflection. These cases represented different type of soils, different rotational stiffnesses of the girder (span lengths), and different imposed displacement. The parameters for the localized model were determined using the results of the general model. .

4. Evaluation of the numerical results.

The following tasks were performed:

- Determine the response parameters for the integral abutments supported by concrete piles in various soil conditions.

- Assess the effect of FRP on the shear and moment in the pile at the pile-abutment interface.
 - Assess the effect of FRP on mitigating the expected pile damage at the interface with the abutment.
5. Design recommendations.

After evaluating the numerical results, the performance and structural response of concrete piles in integral abutment bridges (with or without FRP reinforcement) are examined, and design recommendations are provided.

2 LITERATURE REVIEW

2.1 Integral Bridges

Safe, economical, and aesthetic design are important considerations in any bridge design project. Another important consideration that deserves special attention at the time of initial design is the long-term maintenance cost. Since the 1950s, most bridges were designed with expansion joints at the ends of each span. These systems tend to not perform as intended over the long term because of the direct and indirect effects of the expansion joints on the durability of the bridge. This issue is a primary motivation for the use of integral bridges (semi-integral or fully integral bridges) (Arsoy, Barker and Duncan 1999). Economically, one of the most important factors in bridge design is the maintenance cost, and the elimination of these expansion joints could help to reduce maintenance costs (Mistry 2005).

Integral abutment bridges have abutments that are constructed integrally with the superstructure (girders and deck), while conventional (non-integral) bridges utilize an expansion joint that allows relative movement between the abutment and the bridge superstructure. Figure 2 shows examples of a single-span integral abutment (jointless) as well as a conventional jointed bridge. The non-integral (jointed) bridge in Figure 2a has an abutment that is typically supported with both vertical and battered piles. On the other hand, the integral abutment bridge shown in Figure 2b has vertical piles only. The vertical piles associated with integral abutment bridges offer enhanced flexibility to accommodate the longitudinal bridge movements due to temperature changes, creep, and shrinkage (Abendroth and Greimann 2005).

Evaluating the forces and displacements that are induced in the abutment and its piles is an important consideration in jointless bridges. The ductility requirements for abutment piles due to longitudinal and transverse movements should also be considered. Additional strains and stresses would be induced in the bridge elements due to thermal contraction and expansion of the bridge, as well as creep and shrinkage of concrete. Movement of the abutment towards the soil backfill behind the abutment would generate pressures on the abutment backwall and induce forces in the supporting piles. The passive pressure from the soil and the horizontal reactions from the piles would induce axial forces, shear forces, and bending moments in the bridge superstructure elements (Abendroth and Greimann 2005).

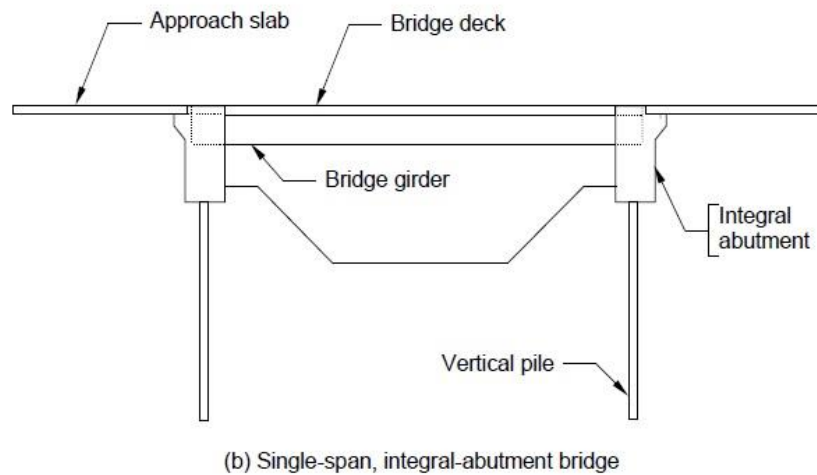
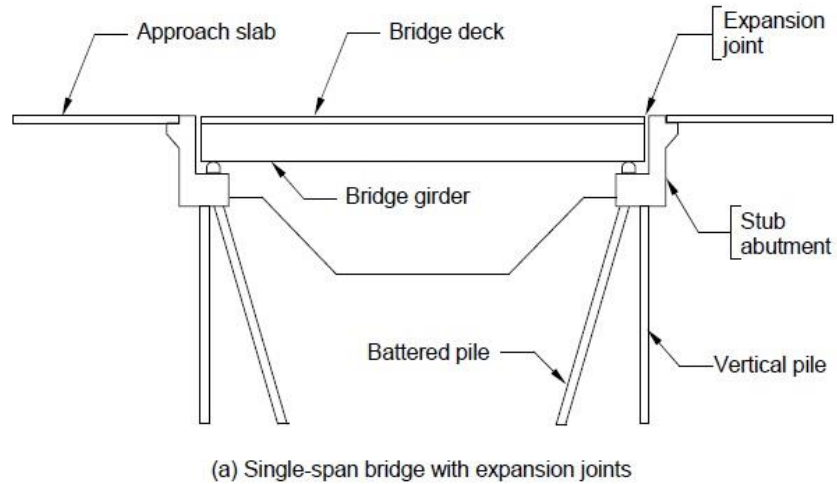


Figure 2: Bridges Types (Abendroth and Greimann 2005).

2.1.1 Types of Load Applied to Integral Bridges

The loads applied on the abutments include not only primary loads (dead and live loads), but also, secondary forces that are generated because of creep, shrinkage, temperature variations (including gradients), and differential settlements. Both primary and secondary loads must be considered in the design of integral abutment bridges (Arsoy, Barker and Duncan 1999).

2.1.1.1 Shrinkage and Creep

Shrinkage and creep can induce forces in various elements of bridges. Shrinkage

of the deck concrete could induce moments on single span and continuous girders. Creep and shrinkage effects are time dependent with shrinkage and creep decreasing with time. Creep and shrinkage can result in inward movement and rotation of integral abutments (Arsoy, Barker and Duncan 1999, Burke 1993).

2.1.1.2 Temperature Gradient

The variation of temperature along the height of a bridge girder can create secondary continuity moments in continuous beams and can generate restraint stresses within a cross section when the temperature gradient is nonlinear. The moment induced by thermal gradients can be calculated using procedures described by Tabatabai et al. (1999). The movements and curvature changes resulting from the gradients can introduce movements and rotations in integral abutments.

2.1.1.3 Differential Settlement

Differential settlements can also induce secondary bending moments in continuous bridges. Settlement of piers would cause positive moments in interior supports, while settlement in abutments of multiple-span bridges would cause negative moments at interior supports (Burke, Integral and Semi-Integral Bridges 2009).

2.1.1.4 Earth Pressure

Earth pressure can be as low as the minimum active pressure or as high as maximum passive pressure based on the amount of displacement of the abutment due to change of temperature. A simple procedure to calculate earth pressure, such as Rankine and Coulomb are preferred by the designers (Arsoy, Barker and Duncan 1999). These calculations are conservative and are in reasonably good agreement with experiments.

However, in the design procedures for short integral bridges, neglecting the effect of earth pressure may be acceptable. (Arsoy, Barker and Duncan 1999).

A survey conducted by Maruri et al. (2004) indicated that 59% of the state DOTs account for passive earth pressure when designing integral abutments (Maruri and Petro 2004). However, some state DOTs (such as Illinois DOT) account for vertical loads only. North Dakota DOT uses a specified pressure to account for various loads (passive pressure, thermal, creep and shrinkage loads). Moreover, Iowa DOT uses a model developed by Greimann and Abendroth at Iowa State University that does not consider passive or active pressure. Thirty-three percent (33%) of the responding states account for creep effects when designing integral abutment bridges, while a few states indicated that they did not account for creep movements (Maruri and Petro 2004).

2.1.2 Integral Abutments

Mr. Henry Derthick, who was once the Engineer of Structures for the Tennessee Department of Transportation (TDOT) expressed his opinion of joints in this way: “The only good joint is no joint.” This view led the State of Tennessee and others to pioneer and adopt designs that minimize joints in bridges (Burdette, Howard, et al. 2005). Consequently, the use of integral abutments have increased substantially, with Tennessee being the national leader in the implementation of designs using integral abutments (Burdette, Howard, et al. 2005). A schematic of an integral abutment is shown in Figure 3.

Various states have used different definitions to describe integral abutments is listed below (Tabatabai, Magbool, et al. 2017):

- Connecticut DOT: Integral abutments are “abutments that are cast integrally with

the superstructure.”

- Delaware DOT: a class of abutments where the superstructure is integrally connected to the abutment and the abutment foundation.
- New York DOT: “in an integral abutment structure, a rigid connection is made between the primary support members of the superstructure and a pile supported substructure by encapsulating the support members into the abutment concrete.”
- Rhode Island DOT: “Integral abutments are abutments which are supported on single row of flexible H-piles and which are rigidly connected to the superstructure.”
- Montana: “Integral Abutment is a flexible abutment without joint between the backwall and pile cap (in cross section, the backwall and pile cap may, in fact, appear as a monolithic rectangle with no apparent cap).”

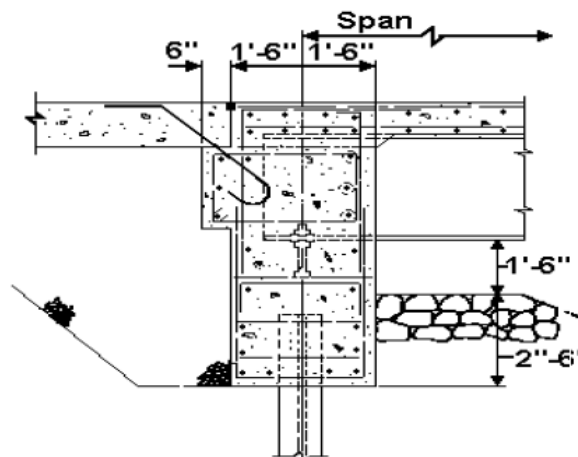


Figure 3: Integral Abutment Schematic (Fanous, et al. 2010).

2.1.3 State Practices

The maximum length of an integral abutment bridge is generally controlled by the maximum longitudinal displacement that the abutment and its piles can sustain. The integral bridge design is usually compatible with short and moderate length bridges.

Some DOTs limit the horizontal movement of piles by allowing construction of bridges with lengths of up to 160 m (500 ft) and 240 m (800 ft) for steel and concrete bridges, respectively (Tabatabai, Magbool, et al. 2017). These lengths, however, have been exceeded. A steel bridge with a total length of 175 m (575 ft) and a concrete bridge with a total length of 360 m (1,175 ft) long have been built (Wasserman and Walker 1996).

The design of integral abutment bridges is not specifically addressed in the U.S. Bridge Design Specifications published by the American Association of State Highway and Transportation Officials (AASHTO) (Tabatabai, Magbool, et al. 2017). Nevertheless, the design and use of such bridges have grown gradually in many states since the 1980s because of issues related to the conventional jointed bridges. As discussed earlier, one of the pioneering states that put forth substantial efforts in designing integral abutment bridges was Tennessee. Moreover, a major research effort sponsored by the U.S. Federal Highway Administration (FHWA) provided comprehensive design recommendations for integral abutment bridges (Oesterle et al. 1999). However, until AASHTO adopts a comprehensive set of design specifications for such bridges, differences in practice from state to state would be expected (Tabatabai, Magbool, et al. 2017).

Tabatabai et al. studied and compared the design criteria and practices being utilized by various states for the design of jointless and integral abutment bridges. In that work, the necessary information was obtained from bridge design manuals that are commonly (but not universally) published online by various state departments of transportation (DOTs) in the United States. Moreover, the authors contacted the states that did not have a published design manual to obtain the necessary information. The

- Superior long-term performance
- Stiffer longitudinal response at abutments

The maximum allowable lengths of steel and concrete integral abutment bridges as indicated by the states in their bridge manuals are shown in Table 1. The average maximum lengths allowed for steel and concrete bridges are 107.5 m (353.3 ft) and 147 m (482.7 ft), respectively. The corresponding standard deviations for maximum length of steel and concrete bridges are 32.3 m (106 ft) and 47.1 m (154.5 ft), respectively (Tabatabai, Magbool, et al. 2017).

Table 1: Maximum permissible length of steel and concrete Integral Abutment Bridges

(Tabatabai, Magbool, et al. 2017).

State	Max. Length-Steel		Max. Length-Concrete	
	ft	m	ft	m
Colorado	640	195	790	241
DC	460	140	460	140
Delaware	400	122	400	122
Idaho	350	107	650	198
Illinois	310	94	410	125
Indiana	500	152	500	152
Iowa	400	122	575	175
Kansas	300	91	500	152
Maine	200	61	330	101
Massachusetts	350	107	600	183
Michigan	300	91	400	122
Minnesota	300	91	300	91
Montana	200	61	200	61
Nevada	150	46	250	76
New Hampshire	300	91	600	183
New Jersey	450	137	450	137
North Carolina	300	91	400	122
North Dakota	400	122	400	122
Ohio	400	122	400	122
Pennsylvania	390	119	590	180
Rhode Island	350	107	600	183
South Carolina	240	73	300	91
Tennessee	500	152	800	243
Vermont	395	120	695	212
Virginia	300	91	500	152
Washington	300	91	450	137

The performance of integral abutment may be affected by the backfill behind the abutment. The results from the survey shows that the majority of state DOTs (69%) require the backfill to be compacted, while 15% do not require compaction. Additionally, some states also require using other compressible materials behind abutment such as

expanded polystyrene (EPS) and lightweight fills in order to reduce and/or control the earth pressures exerted on integral abutments during expansion cycles (Maruri and Petro 2004).

2.1.4 Piles

The most common type of pile used to support integral abutments is the steel H-pile. However, concrete filled steel tubes and prestressed concrete piles have also been used (Arsoy, Barker and Duncan 1999). As shown in Table 2 the majority (59%) of state DOTs prefer using steel H-piles, while 7% use prestressed concrete piles (Tabatabai, Magbool, et al. 2017).

Table 2: Pile types for integral abutment bridges (Tabatabai, Magbool, et al. 2017).

Pile Type	States
HP-Steel	30
Steel Pipe	9
PS Concrete	4
CFSP (concrete filled steel pipe)	5
Not mentioned	10

2.1.4.1.1 *Steel Piles*

Table 3 shows that 57% of state DOTs that consider integral abutment bridges prefer to orient the pile such that bending of the pile would occur about the weak axis (due to longitudinal thermal movements). On the other hand, 14% prefer to orient the pile such that the bending would occur about the strong axis. New York State selects the pile axis orientation based on bridge length as follows:

- “If bridge length is less than 245 feet, orient the pile to bend along the weak axis.”
- “If bridge length is more than 245 feet, orient the pile to bend along the strong axis.”

Oesterle et al. (1999) noted that it is the relative stiffness of the pile to the soil that determines the relative flexibility of the abutment with respect to horizontal movement. A stiffer pile (oriented about the strong axis) would be able to move against the soil more easily (Oesterle, et al. 1999).

State preferences for the embedment length of the pile into pile caps is presented in Table 4. The most common embedment length is 0.46 m to 0.61 m (18 to 24 in) (Tabatabai, Magbool, et al. 2017).

Table 3: Steel pile orientation in integral abutment bridges (Tabatabai, Magbool, et al. 2017).

Orientation (bending axis)	States	Percentage of states considering integral abutment bridges (%)
Weak	21	56.8%
Strong	5	13.5%
Designer Choice	5	13.5%
Not mentioned	6	16.2%
Total	37	100.0%

Table 4: Minimum embedment length of pile into pile cap (Tabatabai, Magbool, et al. 2017).

Embedment Length	States	Percentage of states considering integral abutment bridges (%)
11-12 in (0.28 – 0.30 m)	7	19.4%
18-24 in (0.46 – 0.61 m)	18	50.0%
30-36 in (0.76 – 0.91 m)	3	8.3%
Not mentioned	8	22.3%
Total	36	100.0%

The reduction of pile's vertical load capacity due to horizontal displacement is an important factor in pile design. Usually a pile can fail if the elastic buckling loads are less than generated lateral loads (Greimann and Wolde-Tinsae 1988). The ability of piles to withstand lateral displacement is an important factor in determining the maximum length of integral bridges. To reduce stresses on the piles, predrilled holes have been used

through which the piles would be driven. The predrilled holes filled with loose sand are an alternative that has been adopted in some cases (Greimann and Wolde-Tinsae 1988).

Abendroth et al. (1989) proposed simplified methods to design abutment piles in integral abutment bridges. According to the authors, the deformation capacity of the pile depends not only on the pile flexural stiffness, but also on the soil-pile system's stiffness. The authors used an equivalent cantilever column model for the soil-pile system. They suggested an equation to estimate the equivalent effective cantilever length for fixed-head steel piles as shown below. These methods have been widely accepted and utilized (Tabatabai, Oesterle and Lawson 1999).

$$L_e = 2.4(EI/K_h)^{0.25} \quad (\text{In U.S. units})$$

Where:

L_e = the equivalent cantilever length

E = modulus of elasticity

I = moment of inertia

K_h = horizontal stiffness of the soil.

2.1.4.1.2 Concrete Piles

Concrete piles have relatively high load-carrying capacity and good track record in bridge applications. These piles can be precast (usually prestressed) or cast-in-place in drilled shafts. Cast-in-place concrete piles can be cast in a variety of shapes. The most important benefits are reported to be low cost and suitability for corrosive environments (Fanous, et al. 2010). As discussed earlier, most state DOTs use steel piles for integral bridges. However, steel piles have relatively small cross section (surface area) to depend on skin friction and they can be subjected to corrosion. Therefore, steel piles are

considered beneficial with stiff soil conditions with bedrock that is close to surface. On the other hand, precast concrete piles have larger surface area and larger cross-sectional area (Abendroth , Greimann and LaViolette 2007, Kamel, et al. 1996).

Concrete piles can be cast-in place, composite, or precast. In cast-in-place concrete piles, an augured hole is filled with concrete after a rebar cage is placed. Two different types of composite piles can be used: Concrete filled steel pipes or rolled steel shapes encased in concrete (Fanous, et al. 2010).

The main interest of this study is precast (typically prestressed) concrete piles. This type of concrete pile is manufactured away from site in a plant under controlled conditions. Precast piles must withstand service loads as well as handling and driving forces. Precast concrete piles can be divided into two different types (non-prestressed and prestressed concrete piles) (Fanous, et al. 2010).

The non-prestressed precast concrete piles are reinforced with conventional longitudinal and transvers steel reinforcement. The most common use for this type of pile is in marine environment with the need of deep foundations. The advantages of non-prestressed precast concrete piles are listed below (Fanous, et al. 2010):

- “They can be prefabricated under controlled conditions to maintain good quality construction.”
- “They can be used for structures on land when (hard driving) is not required.”
- “Good corrosion resistance can be attained because the concrete cover provides a high-quality protective layer over the reinforcing steel”.

In precast prestressed concrete piles (PS piles), prestressing strands replace the longitudinal steel reinforcing bars. In addition to the advantages of non-prestressed piles

listed above, PS piles offer the followings benefits (Fanous, et al. 2010):

- There is less potential for cracking during driving;
- There is further protection from corrosion due to reduced cracking or crack widths due to pre-compression.
- The piles can usually be made lighter, longer, and more durable due to prestressing.

2.1.5 Behavior of Piles under Lateral Movement

Piles in integral abutment bridges are subjected to lateral movements as the bridge expands and contracts (Greimann, Yang, et al. 1984). These movements can induce significant stresses in local regions on the pile (Tabatabai, Oesterle and Lawson 1999). Therefore, defining the maximum lateral displacement that can be safely accommodated while carrying the axial load is important in calculating the maximum length of an integral bridge (Greimann, Yang, et al. 1984, Tabatabai, Oesterle and Lawson 1999). Arsoy et al. performed a test simulating 75 years of bridge life on three types of piles; steel H-piles, pipe piles, and prestressed concrete piles. The authors reported that concrete piles were not recommended for integral abutment bridges because, under repeated lateral loads, tension cracks developed and progressively worsened resulting in significantly reduced vertical load capacity. The test was performed without accounting for the soil-pile interaction. Moreover, an axial load was not applied on the prestressed concrete pile test as was done with the steel pile (Arsoy, Duncan and Barker 2002).

Tabatabai et al. performed tests on both steel and prestressed concrete piles and found that prestressed concrete piles tend to develop cracking after relatively small abutment movements (Tabatabai, Oesterle and Lawson 1999). Although both types of

piles were able to resist axial loads under the displacement ranges tested, the extent of cracking at the pile-pile cap interface was unacceptable (Tabatabai, Oesterle and Lawson 1999).

In a project sponsored by the Tennessee Department of Transportation (TDOT), Burdette et al. (2004) tested four prestressed concrete piles in the field. They used 356 mm (14 in) square prestressed concrete piles for the test. The piles were driven into clay for a distance of 36 ft. (11 m). All piles were embedded 304.8 mm (12 in) into the abutment with the strands extended for 0.914 m (3 ft) into the abutment in three tests (Burdette, Howard and Tidwell, et al. 2004). In the fourth test, the strands were cut flush with the top of the pile.

The results of the test showed that when the horizontal displacement at top of the pile reached 25.4 mm (1 in), a crack developed just below the abutment-pile interface. However, during unloading, the prestressing force closed the crack. Also, the authors reported that the reduction in stiffness caused by the localized crack had a small effect on the overall load-deflection behavior. Moreover, cracks that appeared on the abutment were considered minor. The authors investigated the embedment length of strands into the abutment. The results of the test clearly showed resisting moments in the pile with the strands cut off at top of the pile were lower than the other cases where strands were extended into the abutment. This was attributed to slippage of strands (Burdette, Howard and Tidwell, et al. 2004).

2.1.6 The Effect of Bridge-Soil Interactions on the Behavior of Piles

Supporting Integral Abutments

The length of a bridge would change in response to changes in the effective

bridge temperature. The change in length would push and pull the abutments towards and away from the soil behind the abutment (Duncan and Arsoy 2003). Since, the bridge superstructure is much stiffer than the approach fill or the piles supporting the abutments, the bridge displacements would not be influenced significantly by the resistance offered by the soil or piles. Some studies have further concluded that piles supporting integral abutment would also be subjected to the same magnitude of displacement as the bridge superstructure (Duncan and Arsoy 2003). This observation, however, ignores the fact that the rotation of the abutment during superstructure movement could alter (reduce) the displacement demand on the piles when compared to the girder displacement.

Several studies indicate that the interactions between the abutment, the approach fill, and the piles supporting integral bridges is an important factor in determining the maximum length of integral bridges because these interactions could influence the ability of a pile to laterally displace without causing significant distress (Duncan and Arsoy 2003, Song, Chai and Hale 2004, Taheri, Moayed and Nozari 2015, Abdel-Mohti and Khodair 2014).

Using concrete piles with fixed connection to the cap means that the pile head would be restrained against rotation relative to the cap. Piles with fixed connection would be subjected to relatively large curvature demand at the pile/pile-cap connection when cyclic lateral movement is applied. Pile failure under seismic loads had been observed in recent earthquakes (Song, Chai and Hale 2004). Since post-earthquake inspection of piles is difficult, damage assessment of piles is essential to ensure the safety of bridge structure (Song, Chai and Hale 2004).

As a result of the large curvature demand at the pile/pile-cap connection, a plastic

hinge may develop at that area. This plastic hinge would not develop unless the flexural strength (M_u) of the pile is reached at the pile/pile-cap connection (first yield limit state). When the plastic hinge is fully developed, the pile head become free to rotate with further displacement. Moreover, displacements beyond the first yield limit state would increase the bending moment at another location along the pile until a second plastic hinge develop. Both plastic hinges would rotate under any additional displacement until a failure mechanism occurs (ultimate limit state). Figure 5 describes the three stages with the corresponding deflection shape and moment distribution (Song, Chai and Hale 2004). The performance of the fixed head pile depends on the level of inelastic deformation imposed on the pile. Inelastic deformation or curvature demand is linked to the properties of the soil-pile system and to the plastic hinge length on the pile (L_p) (Song, Chai and Hale 2004).

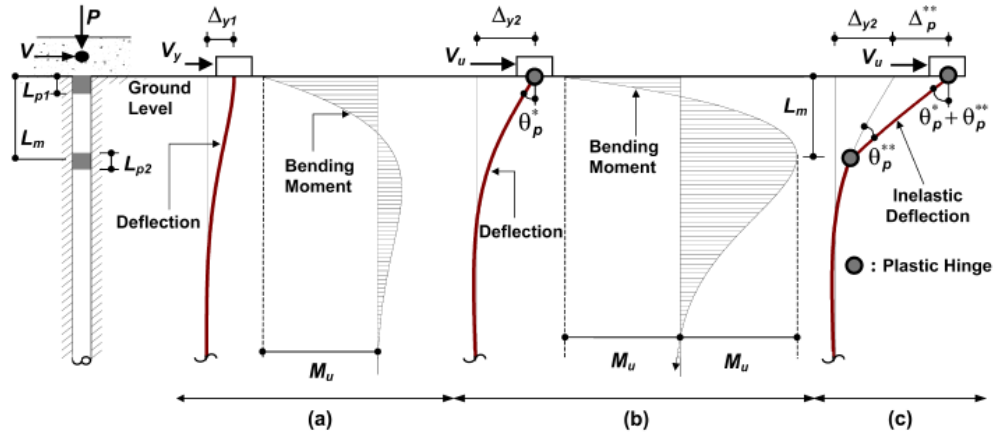


Figure 5: Deflected shape and bending moment distribution of a laterally loaded fixed head pile a). First yield limit state b). Second yield limit state c). Ultimate limit state (Song, Chai and Hale 2004).

2.1.6.1 Lateral Stiffness of Soil-Pile System

Song et al. developed a kinematic model that relates the displacement ductility factor to the curvature ductility factor for different soil conditions. This approach assumes that a laterally loaded soil-pile system can be analyzed as a flexural member supported by an elastic Winkler foundation (soil is replaced by a series of springs that provide a reaction proportional to the lateral deflection) (Song, Chai and Hale 2004).

2.1.6.1.1 Cohesive Soils

In this case, the stiffness of the soil-spring is assumed to be independent of the depth. So, the Winkler foundation will be a constant horizontal subgrade reaction K_h (in units of force/length³) (Song, Chai and Hale 2004).

$$K_h = 67 S_u$$

Where:

S_u = The undrained shear strength of the cohesive soil that can be determined from

field tests or from site classifications in current US building codes.

The lateral stiffness of soil-pile system is (Song, Chai and Hale 2004):

$$K_1 = \frac{V}{\Delta} = \sqrt{2} \frac{EI_e}{R_c^3}$$

Where:

Δ = imposed lateral displacement

V = lateral force required to produce Δ

EI_e = effective flexural rigidity of the pile

R_c = characteristic length of the pile = $\sqrt[4]{EI_e/K_h}$

At the first limit state the lateral deflection Δ_{y1} is equal to:

$$\Delta_{y1} = \frac{M_u R_c^2}{EI_e}$$

Where:

M_u : The ultimate moment capacity

So, by using K_1 and Δ_{y1} the lateral force to cause the formation of first yield limit state can be calculated as:

$$V_y = K_1 \Delta_{y1} = \sqrt{2} \frac{M_u}{R_c}$$

The boundary condition of the pile will essentially change from fixed to hinge just before the development of the first plastic hinge. The reduced lateral stiffness K_2 and the corresponding plastic rotation θ at the ground level are given by:

$$K_2 = \frac{V - V_y}{\Delta - \Delta_{y1}} = \frac{EI_e}{\sqrt{2} R_c^3} \quad \text{for } V > V_y \text{ and } \Delta > \Delta_{y1}$$

$$\theta = \frac{\Delta - \Delta_{y1}}{\sqrt{2} R_c} \quad \text{for } \Delta > \Delta_{y1}$$

2.1.6.1.2 Cohesionless Soils

In this case the stiffness of the soil-spring is modeled to be linearly increasing with the modulus of horizontal subgrade reaction (Song, Chai and Hale 2004).

$$K_1 = \frac{V}{\Delta} = 1.08 \frac{EI_e}{R_n^3}$$

Where:

$$R_n = \text{characteristic length of the pile} = \sqrt[5]{EI_e/n_h}$$

The subgrade coefficient n_h (in units of force/length³) can be estimated from Figure 6 based on the relative density of the soil.

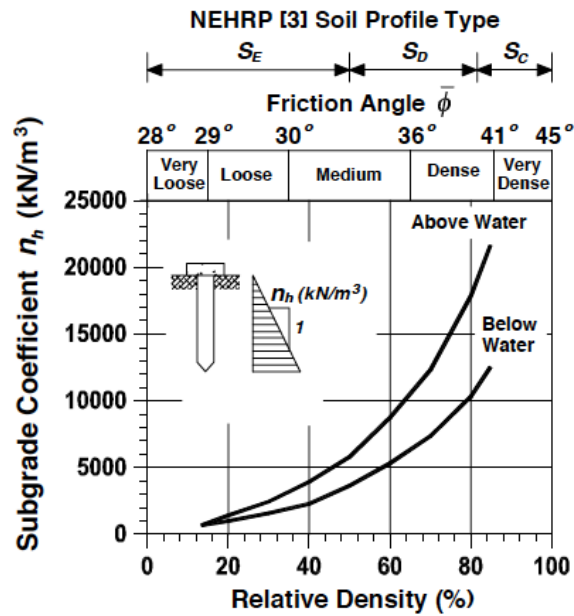


Figure 6: Subgrade coefficient of cohesionless soil (Song, Chai and Hale 2004).

At the first limit state, the lateral deflection Δ_{y1} and the corresponding force at the ground level:

$$\Delta_{y1} = \frac{M_u R_c^2}{EI_e}$$

$$V_y = K_1 \Delta_{y1} = 1.08 \frac{M_u}{R_c}$$

Moreover, the reduced lateral stiffness K_2 and the corresponding plastic rotation θ at the ground level after the first yield limit state can be calculated using (Song, Chai and Hale 2004).

$$K_2 = \frac{V - V_y}{\Delta - \Delta_{y1}} = 0.41 \frac{EI_e}{R_n^3} \quad \text{for } V > V_y \text{ and } \Delta > \Delta_{y1}$$

$$\theta = \frac{2}{3} \frac{\Delta - \Delta_{y1}}{R_n} \quad \text{for } \Delta > \Delta_{y1}$$

2.1.6.2 Lateral Strength of Soil-Pile System

The lateral strength and ductility capacity of a concrete pile with fixed head can be described based on the level of confinement provided for the pile. By assuming that a large pile deflection has occurred and the ultimate soil pressure is mobilized at a depth corresponding to the location of maximum moment in the pile, we can calculate the lateral strength of the pile. So, after the formation of the first plastic hinge, the pile will continue to deflect and the second plastic hinge will develop at a depth associated with the maximum bending moment. Also, depending on the failure mechanism of the, the shape of the pile cross-section, and the friction between the pile surface and surrounding, the magnitude and distribution of the ultimate soil pressure acting on the pile can be determined (Song, Chai and Hale 2004).

2.1.6.2.1 Cohesive Soils

The ultimate soil pressure distribution can be estimated by considering the failure mechanism of the soil around the pile, as suggested by Reese and Van Impe (Reese and Impe 2011). In the upper region, the failure mechanism will be controlled by a sliding soil wedge. Therefore, the soil pressure will increase linearly with depth. While, in the lower region plastic flow would occur and result in a constant ultimate soil pressure as

shown in Figure 7 (Song, Chai and Hale 2004).

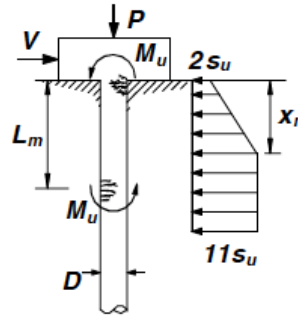


Figure 7: Ultimate soil pressure distribution for laterally loaded fixed head piles in cohesive soils (Song, Chai and Hale 2004).

The ultimate soil pressure distribution for cohesive soils maybe written as (Song, Chai and Hale 2004):

$$P_u(x) = \begin{cases} \left(2 + \frac{9}{\Psi_r} \frac{x}{D}\right), & x \leq x_r \\ 11S_u, & x > x_r \end{cases}$$

Where:

$$x_r = \text{The critical depth, } x_r = \Psi_r D = \frac{9S_u}{\gamma' D + 2\sqrt{2} S_u} D$$

Ψ_r = critical depth coefficient

γ' = effective unit weight of the soil

D= diameter of the pile

2.1.6.2.2 Cohesionless Soils

The ultimate soil pressure on pile in cohesionless soil shown in Figure 8 (Song, Chai and Hale 2004).

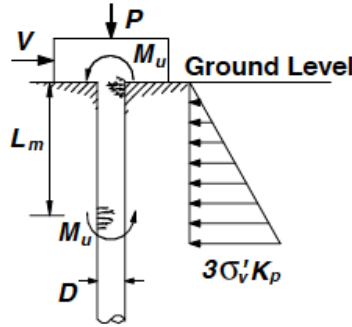


Figure 8: Ultimate soil pressure distribution for laterally loaded fixed head piles in cohesionless soil (Song, Chai and Hale 2004).

$$P_u(x) = 3 \sigma'_v(x) K_p$$

Where:

σ'_v = is the vertical effective overburden stress, $\sigma'_v = \gamma' * x$ x : depth

K_p = is the coefficient of passive soil pressure, $K_p = \frac{(1+\sin\phi)}{(1-\sin\phi)}$

ϕ : friction angle of cohesionless soil

2.1.7 Prestressed Concrete Piles in Seismic Regions

Prestressed concrete piles have been widely used in building structures with different environmental conditions as they have performed well under a variety of loads including lateral loads induced by wind, waves, and earthquakes. There is a variety of prestressed concrete pile cross sections such as square, octagonal and circular (hollow and solid) as shown in Figure 9 (Fanous, et al. 2010).

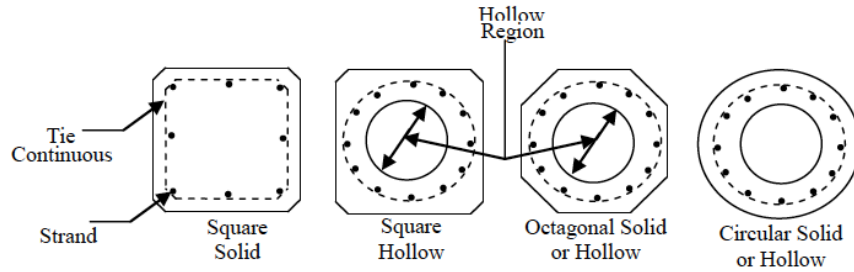
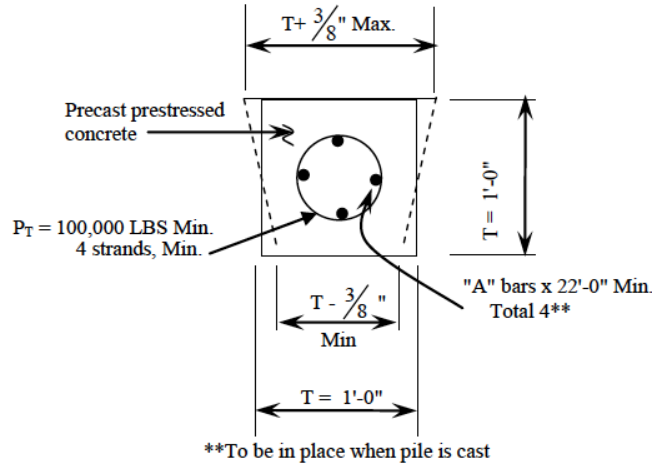
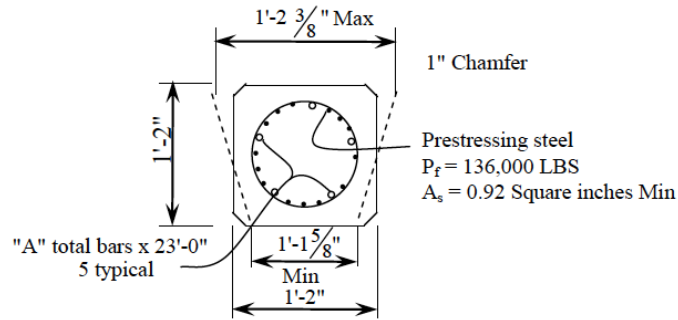


Figure 9: Cross section of prestressed concrete piles (Fanous, et al. 2010).

The most common type of prestressed concrete piles used in seismic regions are solid square and solid octagonal cross sections (Fanous, et al. 2010). 12-, 14-, and 16-in square piles, and 16- and 24-in octagonal piles are the most commonly used (Fanous, et al. 2010). Figure 10 a) and b) specify typical details of the standard piles used for bridge foundations in seismic regions by the California Department of Transportation (Clatrans 2006).



a) 12-in



b) 14-in

Figure 10: Prestressed concrete pile square cross section (Clatrans 2006).

The maximum curvature demand and curvature capacity are important considerations for concrete piles. The maximum curvature demand is the maximum curvature that the pile section may be subjected to under earthquake loading. The curvature capacity is the maximum curvature that a pile can withstand without affecting its capability to withstand the combined axial and flexural actions (Fanous, et al. 2010). Since there is a lack of information about the maximum possible curvature demand for piles in seismic regions, the confinement design for the plastic hinge region can be very challenging.

2.1.8 Curvature Ductility

Curvature demand on a pile will depend on many factors such as axial load, moment demand, material properties, pile/pile cap connection details, in addition to the soil properties around the top of the pile (Fanous, et al. 2010, Song, Chai and Hale 2004). Joen, et al., 1990, stated that the curvature ductility of a pile can be used to define its ability to withstand large cyclic lateral deformation by experiencing post elastic strains in specific regions (plastic hinges), without reducing its lateral load carrying capacity (Joen and Park 1990). The curvature ductility demand in piles would depend on the boundary condition at the pile head and the surrounding soil (Fanous, et al. 2010, Song, Chai and Hale 2004).

2.1.9 Target Curvature Demand

There is limited information available on this topic. Some literature indicates a target curvature ductility demand for piles in the range of 0.0002/in to 0.00152/in (Fanous, et al. 2010). The data summarized in Table 5 shows the curvature demands reported by Fanous et al. at the Iowa State University (Fanous, et al. 2010). On the other hand, the data summarized in Table 6 shows the curvature capacity limits for different piles used in seismic regions. It is noticeable that the maximum capacity shown in Table 6 is 0.00107/in, 40 % lower than the maximum demand of 0.00152/in shown in Table 5 (Fanous, et al. 2010).

Table 5: Summary of curvature demands estimated for piles in the field during past earthquakes (Fanous, et al. 2010).

Topic	Reference	Pile Type	Pile Dimensions (in.)	Type of Loading	Curvature Demand (in ⁻¹)
Analytical model for ductility assessment of fixed-head concrete piles	Song, Chai, Hale-2004	Reinforced concrete (CIDH)	D = 22	Earthquake	0.00132
Analytical model for ductility assessment of fixed-head concrete piles	Song, Chai, Hale-2004	Reinforced concrete (CIDH)	D = 22	Earthquake	0.00145
Damage of piles caused by lateral spreading-back study of three cases	Lin, Tseng, Chiang, Hung-2005	Reinforced concrete	D = 11.8 L* = 393.6	1964 Niigata Earthquake	0.0002
Damage of piles caused by lateral spreading-back study of three cases	Lin, Tseng, Chiang, Hung-2005	Prestressed high strength concrete pile	D = 13.8 L = 906	1995 Kobe Earthquake	0.000381
Damage of piles caused by lateral spreading-back study of three cases	Lin, Tseng, Chiang, Hung-2005	Driven steel pile	D = 24 thickness = 0.07	1964 Niigata Earthquake	0.000432
Field investigation and analysis study of damaged pile foundation during the 2003 Tokachi-Oki earthquake	Koyamada, Miyamoto, Tokimatsu-2005	Prestressed high strength concrete pile	D = 15.7 L = 1122	2003 Tokachi-oki Earthquake	0.00152

L* = length of pile

Table 6: Summary of curvature capacities reported for prestressed concrete piles used in seismic regions (Fanous, et al. 2010).

Topic	Reference	Pile Type	Pile Dimensions (in.)	Type of Loading	Curvature Capacity (in ⁻¹)
Seismic design of prestressed concrete piling	Sheppard, 1980	Square piles	16x16 L = 516	Axially until 600 kips, then monotonically to failure	0.00023
Seismic design of prestressed concrete piling	Sheppard, 1981	Square piles	18x18 L = 516	Axially until 600 kips, then monotonically to failure	0.0002
Seismic design of prestressed concrete piling	Sheppard, 1980	Square piles	12	Axially until 200 kips by post-tensioning, then monotonically to failure	0.00028
Seismic design of prestressed concrete piling	Sheppard, 1980	Square piles	12	Prestressed to induce effect precompression of 700 kips, axially to 300 kips by post-tensioning and cyclically loaded	0.00031
Seismic design of prestressed concrete piling	Sheppard, 1980	Square piles	12	Prestressed to induce effect precompression of 700 kips, axially to 300 kips by post-tensioning and cyclically loaded	0.00107
Seismic performance of precast prestressed concrete piles	Banerjee, Stanton, Hawkins 1987	Octogonal piles	14	Cyclic lateral load tests	0.0008
Seismic performance of precast prestressed concrete piles	Banerjee, Stanton, Hawkins 1987	Octogonal piles	14	Cyclic	0.00081

2.1.10 Relationship between Displacement and Curvature Ductility Factor

In 2004, Song et al. developed a kinematic relationship between the lateral displacement of pile's head and the curvature ductility factor (μ_ϕ). Controlling the curvature demand can limit the local damage in the pile plastic hinge region and thus adequate performance of pile can be controlled. At the second yielding limit state, two plastic hinges will be fully developed. These hinges have different curvature ductility demand that depends on the displacement imposed on the pile. The curvature ductility demand in the critical region can be estimated if a tri-linear force-displacement response is assumed for the lateral response of a fixed head pile as shown in Figure 11. Δ_{y1} and Δ_{y2} correspond to the first and second yield limit states, respectively. A constant lateral force indicates fully plastic response for displacements beyond Δ_{y2} . Δ_u shown in Figure 11 represents the lateral displacement corresponding to the ultimate limit state, and is dependent on the ductility capacity of the plastic hinges. A bilinear elasto-plastic response shown can be another simplification for lateral force-displacement response with the equivalent elasto-plastic yield displacement Δ_y (Song, Chai and Hale 2004).

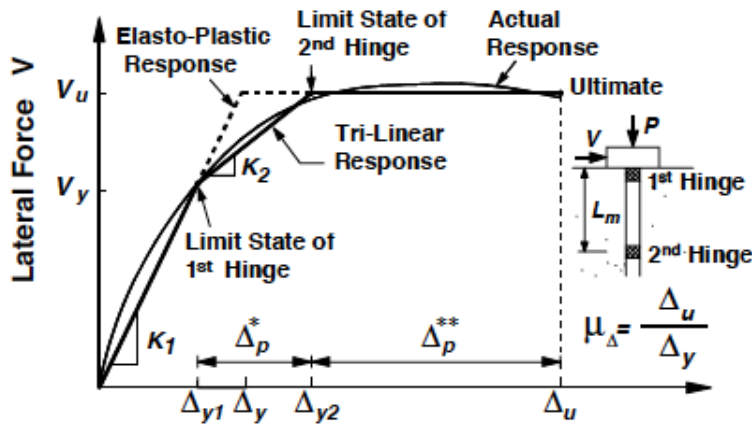


Figure 11: Idealized lateral force-displacement response of fixed head piles (Song, Chai and Hale 2004).

The displacement ductility factor μ_{Δ} is defined as:

$$\mu_{\Delta} = \frac{\Delta_u}{\Delta_y} = \frac{\Delta_{y2}}{\Delta_y} + \frac{\Delta_p^{**}}{\Delta_y}$$

Where:

Δ_p^{**} = Additional plastic displacement from the formation of the second plastic hinge to the ultimate limit state.

The plastic rotation for hinges (θ_p^{**}) is related to the plastic displacement Δ_p^{**} , as shown in Figure 5(c) in section 2.2.5. The lateral displacement of the pile from Δ_{y2} to Δ_u results in the rotation of θ_p^{**} in both plastic hinges (Song, Chai and Hale 2004):

$$\theta_p^{**} = \frac{\Delta_p^{**}}{L_m}$$

Where L_m : is the depth to the second plastic hinge $L_m = L_m^* D$

2.1.11 Pile Tests for Integral Abutment Bridges

As stated earlier, piles in integral abutment must accommodate the horizontal movements without compromising their load carrying capacity. So, it is important to fully

understand the pile behavior and determined the maximum movement that a pile can safely accommodate during the lifetime of integral abutment bridges (Tabatabai, Oesterle and Lawson 1999).

The behavior of integral abutment piles has been studied extensively in the laboratory and field. Field studies on in-service bridges as well as laboratory tests on full-size or scaled model have been performed (Arsoy, Duncan and Barker 2002). However, most such studies have been performed on steel piles.

2.1.11.1 Laboratory Tests

2.1.11.1.1 Arsoy et al.

In this study, cyclic lateral load tests were performed on three types of piles (steel H-pile, pipe pile, and prestressed concrete piles). The test involves simulating 75 years of bridge life by applying over 27,000 displacement cycles. The authors reported that the steel H-piles oriented to bend about the weak axis was the best type of pile to support integral abutment. The steel pipes piles were considered stiffer and would generate more stresses at the pile cap. Also, the concrete piles were not recommended under cyclic load since the developed tension cracks. According to authors, these cracks would reduce the vertical load carrying capacity of the piles. However, the test setup did not account for the soil-pile interaction. Also, axial load was not applied on the prestressed concrete pile during the test. The authors stated that “the application of vertical load would result in further compressive damage of the pile when laterally deflected.”

Therefore, there is a need to study and understand the behavior of concrete piles in integral bridges to reduce damage and improve their performance during displacement cycles (Arsoy, Duncan and Barker 2002).

2.1.11.1.2 Kamel et al.

The main purpose of this study was to determine the possibility of using precast, prestressed concrete piles to support integral abutment bridges. Another objective was to develop the criteria for designing the connection between the pile and the abutment. Three pile-to-pile-cap specimens were tested as cantilevers to find the load-deflection relationship. The purposes of these tests were to understand differences in stiffness between concrete and steel piles in addition to evaluating flexural rigidity and moment-curvature in concrete piles.

The three specimens used in this study included a steel H-pile (10x42) (Specimen 1), a prestressed concrete pile (309 mm [12 in] square with 229 mm [9 in] pitch spiral reinforcement) (Specimen 2), and a prestressed concrete pile (309 mm [12 in] square with 76 mm [3 in] pitch spiral reinforcement) (Specimen 3). Specimen 3 had the standard detail used in Nebraska for (309 mm [12 in] prestressed concrete piles. Also, the concrete pile cap used had an embedded length of 609.6 mm [24 in]).

The results indicated that steel pile had higher ability to accommodate lateral deflection than the concrete piles. According to the authors, the difference was not very significant. Steel pile with a hinged head condition could deflect up to 10.2 mm (0.40 in) in loose sand. On the other hand, under the same conditions, prestressed concrete pile could deflect up to 8.6 mm (0.34 in). Moreover, a lateral force of 34.69 kN (7.8 kips) was needed to deflect the prestressed concrete pile to 8.6 mm (0.34 in) as compared to 22.68 kN (5.1 kips) that was needed to deflect the steel pile to 10.1 mm (0.40 in).

The authors also studied the use of a predrilled hole filled with loose sand in the first 10 ft. (3.05 m) of embedment. The results indicated that the loose sand layer has a

significant effect on the behavior of the pile because the largest moment and deflection occur in this region. So, the types of soil in this region will have a significant effect on the behavior of the pile under lateral loads according to the authors.

Also, in this study, the ability to use a sliding joint for pile/abutment connection was examined. This joint is designed to allow the abutment to slide and rotate over the top of the pile, and facilitate lateral movement. Figure 12 shows a proposed joint detail.

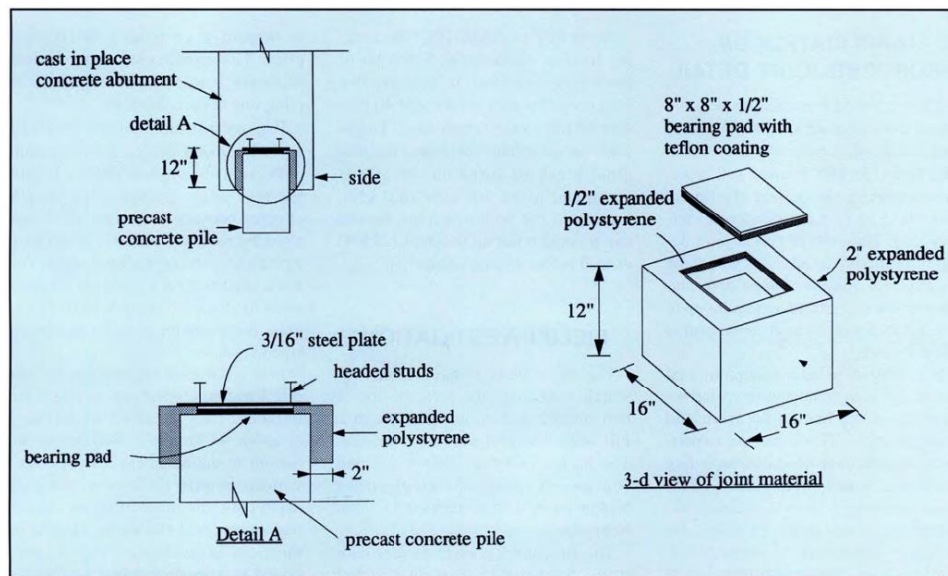


Figure 12: Proposed concrete pile-abutment joint (Kamel, et al. 1996).

To allow the lateral movement against the embedded steel plate that is connected to the cast-in-place concrete abutment by welded studs or reinforcing bars, a bearing pad was used at the top of the pile. This pad had a layer of neoprene coated with a teflon layer. A compressible material such as expanded polystyrene or urethane styrofoam was covering the four sides of the pile top. This compressible material was designed to allow lateral movements. Results indicated that the joint was able to allow lateral movements of about 25.4 mm (1 in) in each direction under sustained vertical loads of up to 400 (kN 90 kips).

The authors recommended the use of concrete pile with modifications at the pile/cap connection. They suggested that the practice of using a predrilled hole filled with loose sand would have a significant effect on the behavior of laterally loaded piles. They reported that the new joint would allow the prestressed concrete pile to deflect for at least 58.4 mm (2.3 in). The authors concluded that the joint would allow concrete piles to be used in concrete or steel integral abutment bridges with lengths of 183.0 m (600ft) and 107.0 m (350 ft), respectively (Kamel, et al. 1996).

2.1.11.1.3 Tabatabai et al.

In a major study sponsored by Federal Highway Administration (FHWA) on jointless, (Tabatabai, Oesterle and Lawson 1999) conducted laboratory tests in two piles (a steel H-pile and a prestressed concrete pile). The piles were embedded 0.610 m (2 ft) into a concrete cap. The 356 mm (14 in) square prestressed concrete pile was manufactured in accordance with Kentucky's standard details.

The prestressed concrete pile test setup on the laboratory floor is presented in Figure 13. The lateral load was applied near the end of the pile. Also, a 400 kN (90 kips) axial load was applied horizontally at the end of the pile.

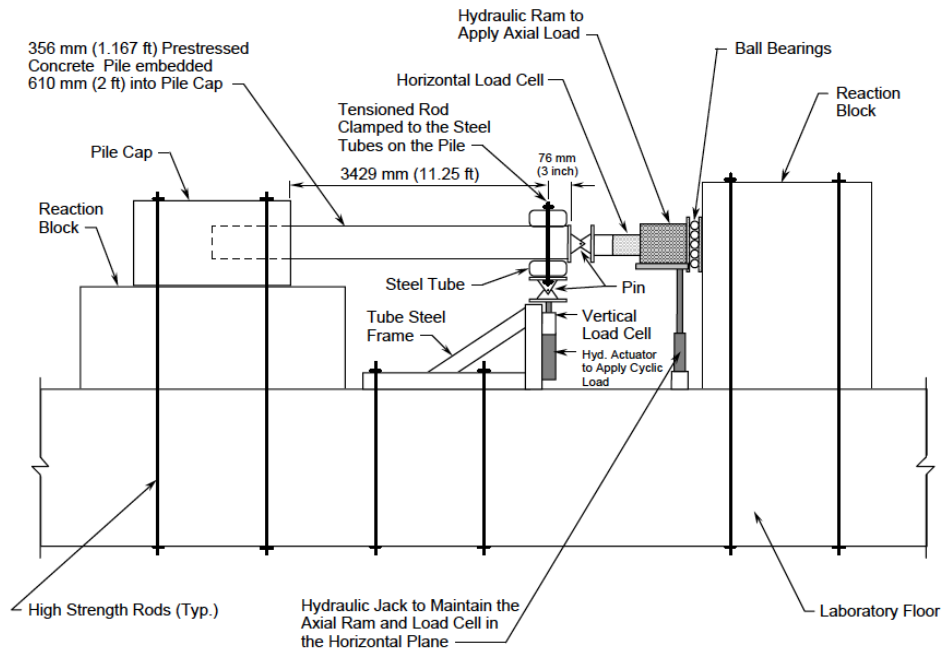


Figure 13: Schematic of prestressed concrete piles test setup (Tabatabai, Oesterle and Lawson 1999).

The end of the pile (away from the cap) was modeled as a hinge. This hinge represented the midpoint or inflection point on an equivalent fixed-fixed beam (equivalent cantilever). This length of the equivalent cantilever was calculated using the following equation (US units) from (Greimann, Abendroth, et al. 1987):

$$L_e = 2.4(EI/K_h)^{0.25}$$

Where:

L_e = equivalent effective cantilever length

E = modulus of elasticity of concrete = 36.5 MPa (5290 kips/in²)

I = moment of inertia = 1,332,000 mm² (3201 in⁴)

K_h = horizontal stiffness of soil = 26.9 MPa/m (100 lbf/in³) (assumed soft soil)

Using all the above values and substitute it into equation:

L_e = 6860 mm (270 in)

Increasing displacement cycles were applied up to the displacement corresponding to the inelastic rotational capacity of a plastic hinge in the pile. The displacement equation used was proposed by (Greimann, Abendroth, et al. 1987). The moment capacity of the pile at the face of the pile cap was used to determine the theoretical failure displacement. The displacement corresponding to the calculated moment capacity of the pile was determined numerically by integrating the moment-curvature relationship over the length of the equivalent cantilever.

The ranges of the displacement for the tests were selected to be 25 percent, 50 percent, and 100 percent of the calculated displacement at theoretical failure with fifty cycles applied at each range. Displacement ranges were ± 16 mm (± 0.63 in), ± 32 mm (± 1.25 in), and ± 64 mm (± 2.50 in).

These tests were designed to evaluate the performance and limitations of steel and prestressed concrete piles in integral abutment bridges. The prestressed concrete pile specimen was able to sustain the applied loads during the cyclic displacement tests. However, the amount of damage observed was not acceptable. Therefore, the authors concluded that the displacement in prestressed concrete piles must be limited to a lower value unless steps are taken to control cracking in the vicinity of the cap. The authors suggested that a flexible pile/abutment connection for precast concrete piles such as the detail recommended by (Kamel, et al. 1996) may be used.

Although, the extent of damage in the prestressed concrete pile was considered not to be acceptable, the prestressed concrete pile specimen was nonetheless able to withstand the loads during the cyclic displacement tests. Therefore, effective methods to control the expected damage are needed using modifications to provide an effective pile-

abutment connection in integral abutment bridges.

2.1.11.2 Field Tests

2.1.11.2.1 Burdette et al.

A project sponsored by the Tennessee Department of Transportation (TDOT) investigated the use of prestressed concrete piles to support integral abutment bridges. Also, the design criteria used by TDOT was evaluated. Four prestressed concrete piles (356 mm [14 in] square) were driven 11 m (36 ft) into undisturbed clay soil. The abutment supported the four piles was 0.914 m (3 ft) deep and 3.05 m (10 ft) wide. The abutment was cast integrally with an abutment slab as shown in Figure 14. By pulling the slab-abutment system horizontally, lateral displacement was imposed on the pile. This lateral displacement would generate moments and shears the pile. To simulate the behavior of an abutment in an actual bridge, the abutment slab was restrained rotation. A number of tests were performed in which displacements displacement of up to 25.5 mm (1.0 in) were imposed on the piles. One of the piles was subjected to 100 cycles of displacement slightly more than 25.4 mm (1.0 in). Moreover, one of the piles was laterally pulled to failure. The tests results show that prestressed concrete piles were suitable for use in integral abutment bridges and that the TDOT design criteria were conservative.

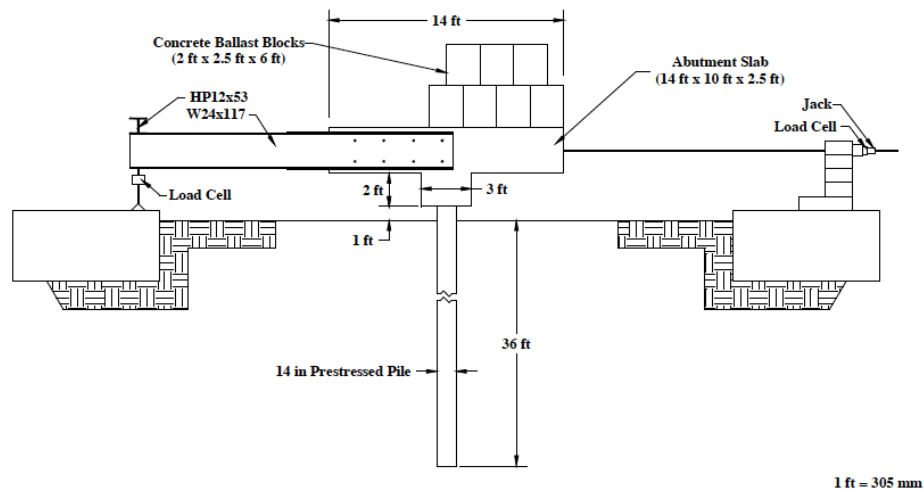


Figure 14: Test setup (Burdette, Howard and Tidwell, et al. 2004).

2.2 Confinement

One approach to reduce and mitigate damage at the top of concrete piles may be to confine the section in a manner similar to reinforced concrete members that are subjected to seismic loads. A discussion of confinement option is provided here.

2.2.1 Steel

A study by Fanous et al. at Iowa State University (Fanous, et al. 2010) resulted in a new equation for the volumetric ratio of transverse reinforcement provides an ultimate curvature capacity of at least (0.00194/in), approximately 27% greater than the maximum curvature demand established from the literature review (0.00152/in) see Table 5 in section 2.2.8. Closely spaced spirals have been provided to improve strength and toughness of the concrete core and to avoid premature buckling of the longitudinal steel reinforcement. The closely-spaced spirals have been used at critical regions including:

- At the pile ends, to prevent bursting and splitting stresses that would be caused by the release of prestress force and during pile driving.

- At the potential plastic hinge regions to ensure adequate curvature capacity.

The volumetric ratio of transverse reinforcement equation proposed by the authors contains a curvature ductility demand term that reportedly ensures a curvature ductility capacity for the pile. The authors suggested using a curvature ductility of at least 18 in high, 12, and 6 in moderate, and low seismic risk areas, respectively (Fanous, et al. 2010).

2.2.2 FRP

Fiber reinforced polymer (FRP) composites consist of high strength fibers embedded in a resin matrix. FRP composites may be made with carbon fibers (CFRP), glass fibers (GFRP), armed fiber, etc (AFRP) (Suh 2006):

2.2.2.1 FRP Properties and applications

FRP materials have been widely used for repaired retrofit of civil structural systems including concrete structure. FRP composites provide a lightweight and high strength choice that offers great flexibility in application in its fabric form (Rajan and Mullins 2007, Suh 2006, Wu 2017). Moreover, FRP is particularly suitable for emergency repairs when damage may be multi-directional and the speed of repair is critically important. In addition, FRP can be bonded to wet concrete surfaces with the use of particular adhesives, so, that has made it economically possible to be used in emergency repairs on sub-structure elements (Rajan and Mullins 2007).

In marine environments, the corrosion of steel reinforcement in piles is one of the biggest factors contributing to the premature deterioration of these piles. Cracking, spalling and delamination of the concrete piles can lead to loss of strength and ductility. The traditional approach to repair corrosion damage in reinforced concrete is the “chip

and patch” method. There are three steps in this method; 1) remove the deteriorated concrete, 2) clean the corroded steel, and 3) apply the patching material. Studies have shown that this method is not durable. As result, FRP-wraps have become alternative method of repairing such piles (Suh 2006). FRP repairs can be quick without the need for heavy equipment. Despite the higher cost of materials, these repairs can be cost effective (Suh 2006, Wu 2017). FRP sheets or encasements have been used to enhance the axial load carrying capacity of the structural member without much increase in the cross-sectional area. Using FRP for confinement of the structural member can result in more ductility and higher load capacity. Figure 15 shows the zones of effectiveness of FRP confinement on different column shapes. The orientation angle of the fibers can be altered in various FRP layers to affect its mechanical properties in different directions. (Parvin and Brighton 2014).

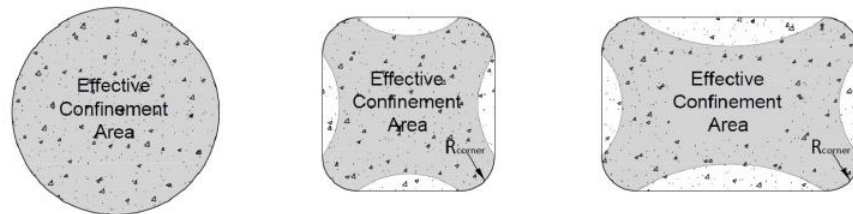


Figure 15: Effective confinement areas in circular, square and rectangular columns (Parvin and Brighton 2014).

2.2.2.2 FRP Strengthening Columns Subjected to Seismic Loads

Several studies have investigated the effects of the length of FRP reinforcement on the plastic hinge region and the drift capacity of concrete columns. The length of plastic hinge is an important parameter since it influences on the extent of damage and the drift capacity. With an increase in FRP reinforcement the sectional curvature capacity can (Parvin and Brighton 2014).

Parvin and Wang (2014) reported that the FRP reinforcement in the potential plastic hinge location improved both strength and ductility capacities. Also, the FRP jacket delayed the degradation of the stiffness of reinforced concrete columns (Parvin and Brighton 2014). The effectiveness of FRP jacketing to retrofit RC columns designed with nonseismic transverse detailing been studied by Lacobucci et al (Lacobucci, Sheikh and Bayrak 2003). Both ductility and energy dissipation capacity improved on a result of FRP jacketing.

FRP also enhances the ductility factor and shear capacity of hollow rectangular bridge columns (Parvin and Brighton 2014).

Choi et al. (2015) performed tests on reinforced concrete columns with and without CFRP at the plastic hinge location. The column wrapped with CFRP exhibited improvements in strength of up to 143% in strength over the control column. Moreover, the CFRP column exhibited three times higher ductility (Choi, et al. 2015). This experiment is one of the verification models that are used in this study to verify the finite element models (section 3.2.2).

3 DEVELOPMENT OF FINITE ELEMENT MODELS

3.1 Introduction to ABAQUS

The finite element method (FEM) is an advanced numerical analysis technique commonly used in engineering fields. The structure is discretized into elements that are connected to each other via nodes. The accuracy of results increases when number of nodes increases and the element size decreases (Fekadu 2010).

ABAQUS is a powerful FEM tool to examine linear and nonlinear (2-D and 3-D) problems in numerous areas. It is capable of addressing the complex problems in this study such as the interaction between the soil and concrete, behavior of FRP composites, and nonlinear response of reinforced concrete structure (including cracking and crushing) (Fekadu 2010).

3.2 Material properties and models

Concrete,, reinforcing steel, prestressing steel, and FRP reinforcement are used in ABAQUS models in this study. In this section, the various materials properties and constitutive models are discussed

3.2.1 Concrete

The nonlinear analysis of reinforced concrete structures is a complicated task because of the potential cracking and crushing of concrete, and the need to consider the interaction between the concrete and the embedded reinforcing steel. Cracking affects the stiffness of the structure, resulting in nonlinear response. The bond between concrete and embedded steel is another important consideration in high-flexural force zones such as the pile/pile cap interface (Jankowiak and Lodygowski 2005, Tyau 2009).

There are two primary methods to model nonlinear reinforced concrete behavior in ABAQUS, Smearred Crack (SC) and Concrete Damage Plasticity (CDP). In both SC and CDP methods, concrete must be defined as a 3-D solid element.

3.2.1.1 Smearred Crack (SC)

The SC model can reduce the stiffness properties of concrete over the areas with stresses exceeding the tensile strength of concrete. This model does not track the individual cracks, but can model the effects of cracks in a distributed way. Moreover, the SC model does not consider compression failure (crushing). Therefore, under conditions when cyclic cracking and crushing can occur, CDP may be a more appropriate model. However, CDP can significantly increase complexity and computational costs while introducing potential convergence issues (Jankowiak and Lodygowski 2005, Tyau 2009).

3.2.1.2 Concrete Damage Plasticity (CDP)

The CDP method uses the experimental stress and strain data to model the extent of damage in concrete elements under tension and compression stresses. In this model, the nonlinear (including post-yield) response of the reinforced concrete member is described including unloading and reloading effects. The model parameters are automatically adjusted to include the effects of damage due to yielding of reinforcement as well as cracking and crushing of concrete. Moreover, in cyclic loading, recovery factors can be identified to account for the strength available after the elements are damaged. These parameters cause the damaged elements to behave differently from the unaffected elements. For example, the suggested ranges of compression and tension recovery values for 5000 psi concrete are 0.85-0.99 and 0.01-0.1, respectively. In cyclic loading, the damage and recovery parameters come into use. In Figure 16 the response

shown in dotted line illustrates the basic compression and tension stress-strain curves. The solid line is a high damage cyclic loading curve (Jankowiak and Lodygowski 2005, Tyau 2009, ABAQUS 2015).

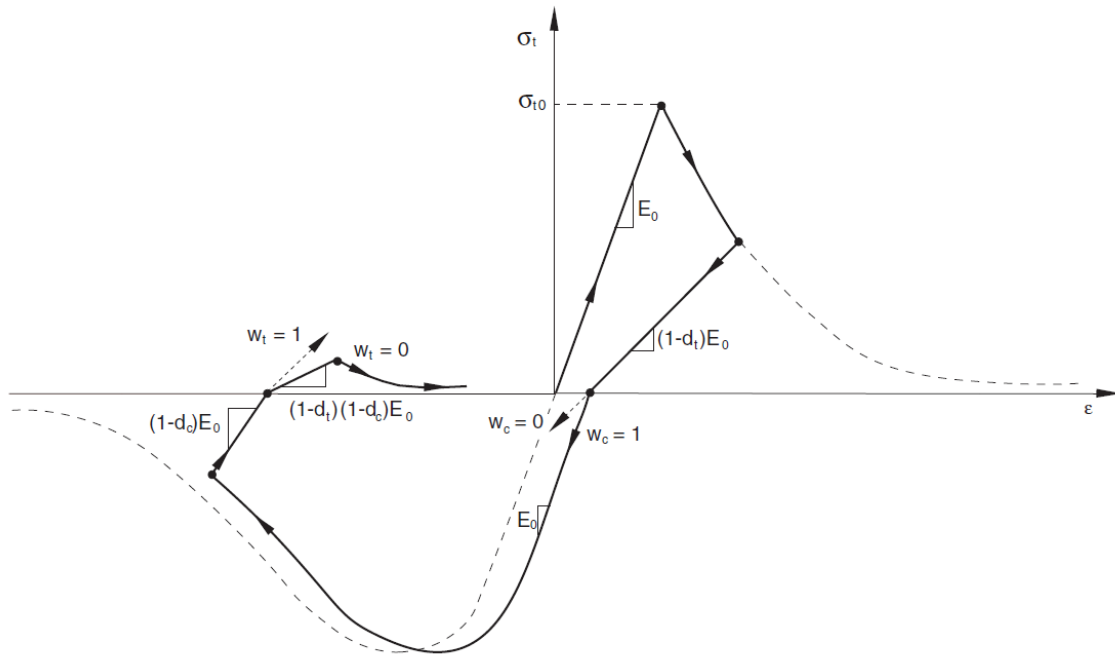


Figure 16: Concrete damage plasticity modified stress-strain curve (ABAQUS 2015).

The parameters in Figure 16 are defined as follows:

E_0 = Modulus of Elasticity of concrete

d_c = compression damage parameter

d_t = tension damage parameter

Damage parameters must range between $0 < d < 1$ to avoid instability. 0 = undamaged and 1 = total loss of strength

W_c = compression recovery factor

W_t = tension recovery factor

Recovery parameters range between $0 \leq W \leq 1$ with 0 indicating zero recoverable strength and 1 means total recovery of the strength when the stress goes from tension to compression to tension again.

In addition to the above information, some parameters related to the yield surface of individual finite concrete elements must be defined. These parameters include dilation angle ψ which is the angle measured in the p-q plane at high confining pressure. Where p is the hydrostatic pressure and q is the Von Mises-equivalent effective stress. Also, the eccentricity of the plastic potential surface (m) is suggested to be set at 0.1 by the ABAQUS user manual, and the ratio of initial biaxial compressive yield stress to initial uniaxial compressive yield stress σ_{b0}/σ_{c0} has a default value of 1.16. The ratio of the second stress invariant on the tensile and compressive meridian (q_t and q_c) is taken as $K_c=2/3$. Lastly, the viscosity parameter μ is used for the visco-plastic regularization of the concrete constitutive equations in ABAQUS, and it has a range between 0.005 and 0.0005 (Yusuf and Aktaş 2015, Jankowiak and Lodygowski 2005, Tyau 2009, ABAQUS 2015).

The general concrete damage plasticity parameters used in this study are presented in Table 7. The stress-strain curve data for the concrete ($f_c' = 5000$ psi) was obtained from Tyau et al. (2009) and they presented in Tables 8 to 11. The element type used to discretize the concrete was eight-node 3-D stress brick element. This element has six degree of freedom at each node to capture deformation and rotation.

Table 7: Concrete damage plasticity general parameters (ABAQUS 2015).

Ψ	m	σ_{c0}/σ_{b0}	K_c	μ
30	0.1	1.16	0.667	0.001

Table 8: Concrete compression hardening (Tyau 2009).

Stress MPa	Crushing strain
15	0
20.2	0.000075
30	0.0001
40.3	0.00015
50	0.00076
40.2	0.00256
20.2	0.00567
5.3	0.01173

Table 9: Concrete Compression damage (Tyau 2009).

Damage value d_c	Strain
0	0
0	0.00007
0	0.00010
0	0.00015
0	0.00076
0.2	0.00256
0.6	0.00568
0.9	0.01173

Table 10: Concrete tension stiffening (Tyau 2009).

Stress MPa	Cracking strain
2.00	0
2.84	0.00003
1.87	0.00016
0.86	0.00028
0.23	0.00068
0.06	0.00109

Table 11: Concrete tension damage (Tyau 2009).

Damage value d_t	Strain
0	0
0	0.00003
0.406	0.00016
0.696	0.00028
0.920	0.00068
0.980	0.00109

3.2.2 Soil

In this study, nonlinear soil models must be used since one of the objectives of is to evaluate the effect of soil and soil-structure interactions on the behavior of concrete piles in integral abutment bridges. As nonlinear material, soils can experience elastic and plastic strains under cyclic loading. ABAQUS provides more than one plasticity models to include soil nonlinearity in the analysis. These include the Mohr-Coulomb plasticity model and the modified Drucker-Prager/Cap model. These models use both elasticity (Hooke's Law) and plasticity theories to describe reversible and irreversible deformation. The Mohr-Coulomb plasticity model has been used widely to describe the nonlinearity of the soil. Therefore, Mohr-Coulomb plasticity model (MCP) is used in this study (Abdel-Mohti and Khodair 2014, Ramachandran 2005, Sushma and Pradeep Kumar 2012). MCP uses the classical Mohr-Coulomb yield Criterion:

$$\tau = c - \sigma \tan \varphi$$

Where:

τ : Shear stress

c : Cohesion

σ : Normal stress

ϕ : Angle of internal friction

In addition to the above parameters, the MCP model require inclusion of the elastic properties of the soil (modulus of elasticity and Poisson's ratio), density, angle of dilation, and cohesive yield stress vs. plastic strain (Taheri, Moayed and Nozari 2015, Ramachandran 2005, Sushma and Pradeep Kumar 2012, ABAQUS 2015).

In this study, three types of sands and clay compaction were used to evaluate the effect of soil and soil-structure interactions on the behavior of concrete piles in integral abutment bridges. The soils properties are described in Table 12 and Table 13.

Table 12: Sands properties (Allen and Meade 1988, Das, et al. 1999, Monley and Wu 1993).

Type of Soil	Sand 95% (Sand-Dense)	Sand 90% (Sand-Medium)	Sand 85% (Sand-Loose)
Modulus of Elasticity Ksi (Mpa)	2.9 (20)	1.9 (13.1)	1.16 (8)
Poisson's Ratio	0.3	0.3	0.3
Angle of internal friction (degrees)	43	38	34.5
Cohesion Ksi (Mpa)	0	0	0
Unit weight (γ) Pcf (Kn/m ³)	128 (20.1)	126 (19.8)	112 (17.6)

Table 13: Clay proprieties (Monley and Wu 1993, Allen and Meade 1988, Das, et al. 1999).

Type of Soil	Clay-Stiff	Clay-Medium	Clay-Soft
Modulus of Elasticity Ksi (MPa)	2.43 (16.75)	2.08 (14.36)	1.74 (11.97)
Poisson's Ratio	0.3	0.4	0.4
Angle of internal friction (degrees)	30	28	24
Cohesion Ksi (MPa)	3.47 (23.9)	2.1 (14.5)	1.74 (12)
Unit weight (γ) Pcf (Kn/m ³)	114.7 (18)	120 (18.9)	112.5 (17.7)

The interaction between soil and pile is an important factor because separation can occur under large displacement. Surface-based contact elements that allow modeling contact between two deformable solid elements were used in this study. In the case of soil-concrete interaction, normal and tangential behavior contact was used with the friction coefficient determined based on the type of soil as shown in Table 14. ABAQUS uses the concept of contact piers with master surface (concrete pile or abutment wall) and slave surface (soil) (Taheri, Moayed and Nozari 2015, ABAQUS 2015). The element type used to model the soil part was eight-node 3-D stress brick element as in concrete part. This element also has ability to capture deformation as well as excess pore pressure (ABAQUS 2015).

Table 14: Soil's friction coefficient and (Das, et al. 1999).

Type of Soil	Friction coefficient
Sand-Dense	0.62
Sand-Medium	0.52
Sand-Loose	0.46
Clay-Stiff	0.38
Clay-Medium	0.35
Clay-Soft	0.3

3.2.3 Reinforcement

ABAQUS provides confinement analysis for three different concrete constitutive models: smeared crack model, brittle cracking model, and concrete damaged plasticity. Each model is designed to provide capability for modeling plain and reinforced concrete.

3.2.3.1 Steel Reinforcement

There are many ways to model reinforcing bar elements In ABAQUS. In all methods, the bar elements are embedded and constrained within the host element (concrete). The concrete element must be defined as 3-D solid element. The steel bar element can be defined as beam, truss or solid element (ABAQUS 2015, Charan and Topdar 2013). Beam, truss and solid elements can be similarly embedded in the concrete as reinforcing steel modeling. Tyau et al. (2009) reported that beam and truss methods were computationally more efficient (Tyau 2009).

Below the yield stress (linear behavior), the reinforcing steel behavior is defined by the modulus of elasticity and poisson's ratio. Beyond the yield stress, the elements will be defined by the metal plasticity parameters (stress-plastic strains relationship) (Conte, Troncone and Vena 2013, Tyau 2009).

As discussed in chapter 2, most prestressed concrete piles are embedded to a depth less than or equal 0.61 m (2 ft) into the pile cap. In this study, the embedment was 0.61 m (2 ft). This embedment is far shorter than the typical development length of prestressing strand. Therefore, it is anticipated that a slip of prestressing strand would occur at relatively small abutment movement. Two methods may be used to model the bond slip. One approach would be to use contact elements and model the bond failure in a detailed manner. However, this approach is computationally expansive and would likely results in convergence issues. The other approach involves using a modified steel bar model proposed by (Braga, et al. 2012, D'Amato, et al. 2012). This simplified model takes into account the bond-slip problem (in cyclic loading) through a modified (simplified) bilinear (elastic-perfectly plastic) stress-slip behavior as shown in Figure 17. It further assumed that the bond slip behavior is linear along the bar. The model was verified using experimental results. This approach proposed by (Braga, et al. 2012, D'Amato, et al. 2012) was therefore used in this study to model bond-slip in the prestressing strand. This approach was implemented using a steel yield stress that was lower than the actual yield strength of prestressing strand. The experimental pile test data provided by Tabatabai et al. (1999) was used to determine an equivalent yield strength of 414 MPa (60 ksi). Therefore, reinforcing bar model models with a yield strength of 414 MPa (60 ksi) were used for both the prestressing strands and other mild steel reinforcement. Furthermore, the strands were not prestressed in FE model. This is due to the fact that shorter embedment length (point of maximum moment being relatively close to the end of strand) and the resulting bond slip at relatively low stress would relieve the prestress at the pile-pile cap interface zone.

The steel bar was designed as 2 nodes linear 3-D truss element. The bar elements have been embedded and constrained within the host element (concrete).

The steel properties and behavior were obtained from the Design of Highway Bridges (Barker and Puckett 2006). The following equations represent the behavior of steel under elastic and plastic portions. Figure 17 shows the actual and modified stress-strain curves for the steel strands.

Elastic Portion

$$f_s = \varepsilon_s E_s \quad 0 \leq \varepsilon_s \leq \varepsilon_y$$

Plastic Portion

$$f_s = f_y \quad \varepsilon_y \leq \varepsilon_s \leq \varepsilon_h$$

Where:

E_s = Steel modulus of elasticity

f_s : steel stress

f_y : yield stress

ε_s : steel strain

ε_y : yield strain

ε_h : hardening strain

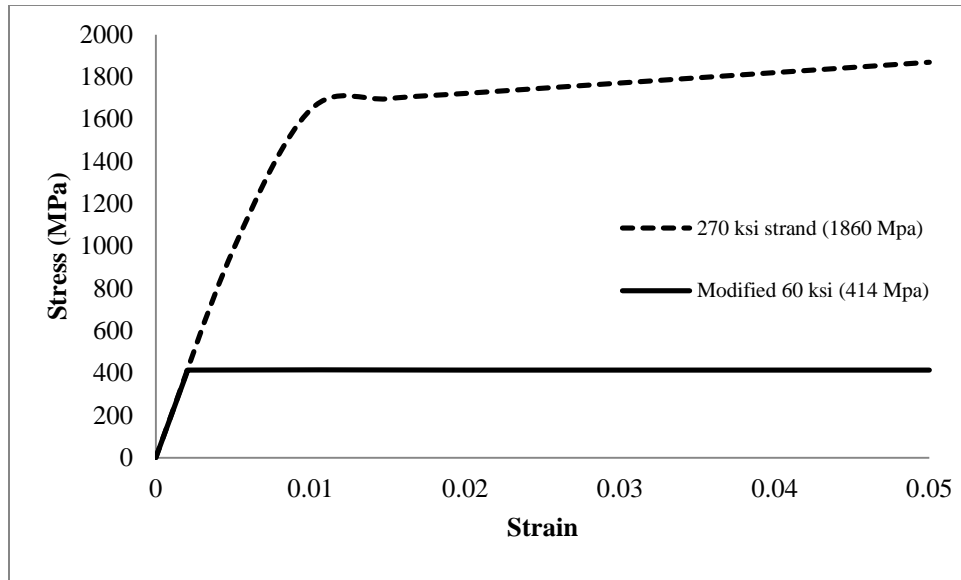


Figure 17: Actual and modified stress-strain curves for the steel strands (60 ksi vs. 270 ksi).

3.2.3.2 FRP External Wraps

One of the main objectives of this study was to evaluate the effectiveness of localized FRP external reinforcement in enhancing the strength and ductility of reinforced concrete piles in integral abutment bridges. FRP was modeled as a multi-layer shell element. Each layer can be designated by its own materials properties, thickness and fiber orientation. Modulus of elasticity must be defined in both fiber directions. Moreover, failure conditions must be defined. As with the, surface-based contact elements were used to connect the FRP elements to concrete elements (using cohesive behavior) (ABAQUS 2015).

In this study, carbon fiber reinforced polymer (CFRP) was used with two layers as shown in Figure 18. Both layers were oriented in hoop direction each layer with 0.33 mm (0.013 in) thickness. The material properties were acquired from American Concrete Institute as one of two systems required for strengthening concrete members as presented

in Table 15. The CFRP material was defined as lamina type of elasticity. Lamina type elasticity requires providing the modulus of elasticity in both fiber directions. As recommended by most references, both fibers assumed to be similar. Furthermore, tensile stress and strain must be defined for the CFRP layers.

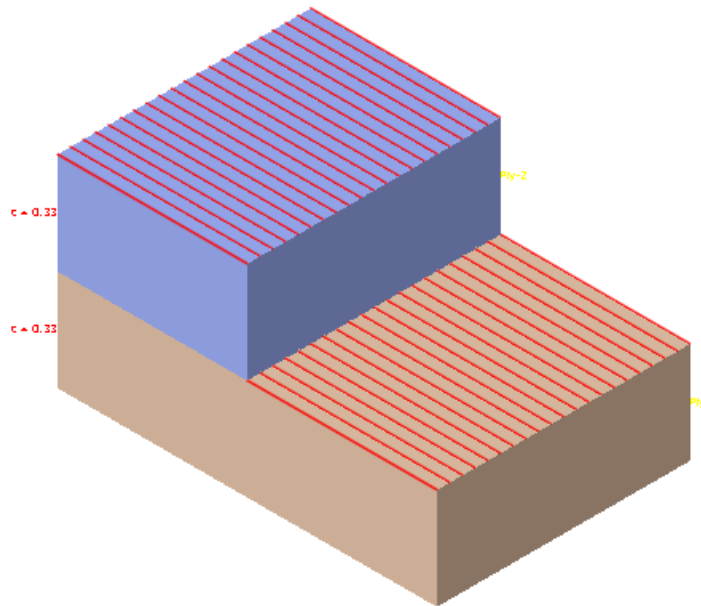


Figure 18: Two layers of CFRP (both on hoop orientation).

Table 15: Mechanical properties of CFRP (American Concrete Institute 2008)

Mechanical Properties	
Thickness	0.013 in (0.33mm)
Tensile Stress	550 ksi (3,792 MPa)
Tensile Strain	1.60%
Modulus of Elasticity	33,000 ksi (227,527 MPa)

3.3 Meshing

Element meshing is an important factor especially for CDP models. As explained previously, the CDP model has a large number of input parameters and any small change

in these parameters may cause changes in the structural behavior. These changes can be reduced by using finer element meshing. Mesh size sensitivity analysis was done to optimize the element size. However, with finer mesh, the model would become computationally expensive.

3.4 Physical Models

In this study, two types of models were studied. First, a general model was used to represent all components of the structure including, pile, abutment and girders. Then, a localized model was used to study the pile-pile cap zone in details. The results of the general model were used to determine the parameters in the local.

The general model was to determine the point of inflection of the pile. Then, a second more refined model was prepared that included the pile cap and a section of the pile from the cap to the point of inflection without modeling the soil.

The point of zero moment or point of inflection (POI) is defined as shown in Figure 19. As shown in Figure 19, the moment diagram between the pile cap and the point of inflection is nearly linear. Therefore, in the localized model, the pile can be modeled to the point of inflection without the soil. This allows a more refined modeling of the plastic hinge zone in the localized model. The point of fixity is located at a depth where the displacement is zero.

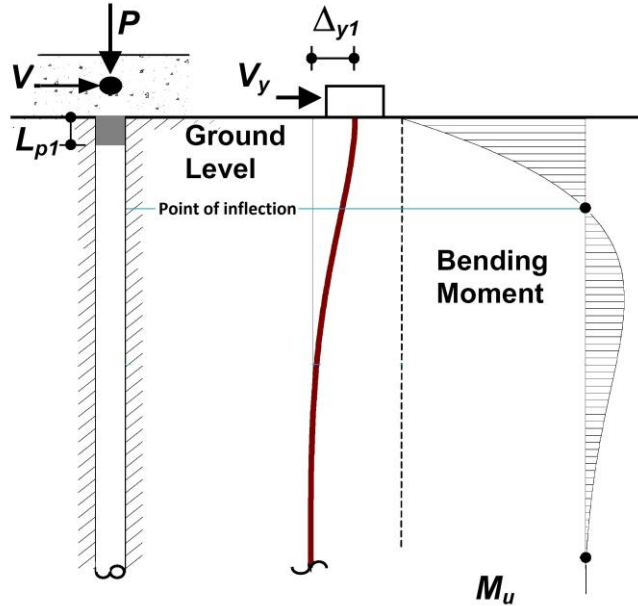


Figure 19: Deflected shape and bending moment of laterally loaded fixed head pile (adapted from (Song, Chai and Hale 2004)).

3.4.1 General model

An overall model of, pile, and a stub abutment was considered. The soil model was nonlinear, while the abutment was considered to be linearly elastic. The pile was modeled using the concrete CDP model. The reinforcement steel included the plastic behavior. The effective stiffness of the superstructure was considered with a fictitious beam model as shown in Figure 20. Three different displacement ranges were imposed at the end of the girder (± 12.7 mm [± 0.5 in]; ± 25.4 mm [± 1 in]; ± 50.8 mm [± 2 in]). The meshing of the concrete pile in this model was less refined than in the subsequent localized model. Various types of, as well as, different span length and corresponding abutment heights were used. The POI was determined for different ranges of soil parameters, pile types, displacement ranges, and superstructure stiffness.

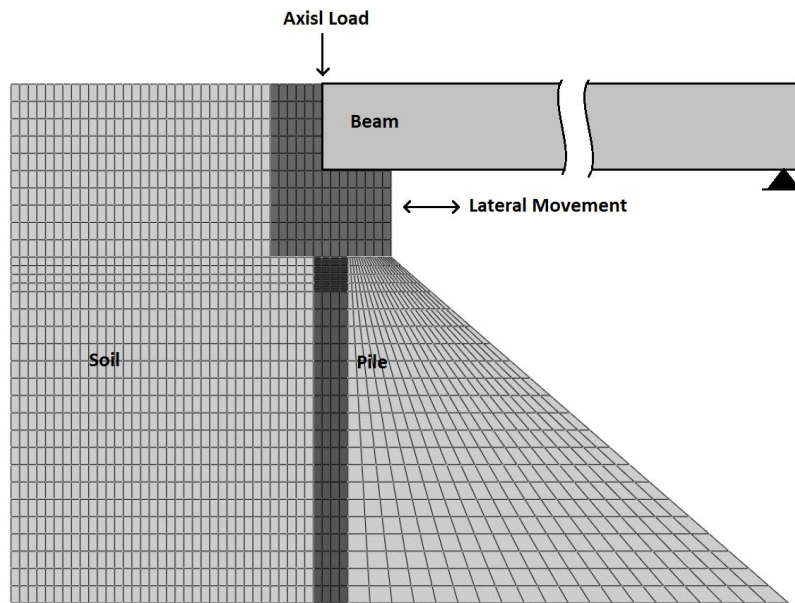


Figure 20: General model

3.4.2 Localized pile-pile cap model:

A model of a pile cap and a partial length of the pile (to POI) were generated as shown in Figure 21. The boundary condition at the POI had a hinged condition (zero moment, with ability to transfer shear). The CDP model was used for both pile and pile cap elements. The plastic hinge zone was finely meshed, and the steel reinforcement bars were modeled as 3-D truss element with elasto-plastic behavior. The plastic hinge zone was extended a distance of 2 times the pile size.

In addition to the control model (without FRP reinforcement), a model with two layers of FRP applied to the pile from the pile cap to a distance of twice the pile size (FRP retrofit). This model would represent cases where FRP was retrofitted on an existing bridge.

A third localized model involved application of FRP that extended into the cap. This can only be done in new construction when FRP can be applied on the pile before casting the pile cap.

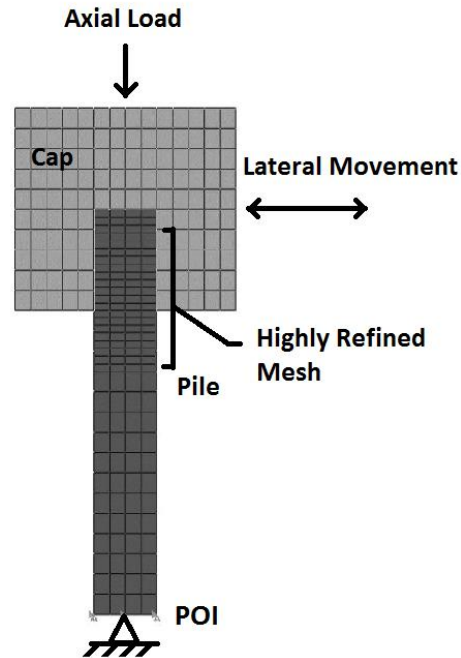


Figure 21: Localized model

3.5 Verification Models

Although the ABAQUS nonlinear finite element program is a powerful and well-established platform, models built in these platforms must be verified experimentally to ensure that they are properly developed. In this thesis, three sets of experimental results from the literature was used to verify the modeling techniques used. These three experiments address; 1) modeling of a concrete pile-pile cap without FRP reinforcement; 2) modeling of a concrete pier column to pier cap connection with FRP external reinforcement; and 3) modeling of the lateral movement of pile in soil. To verify the FE

model, these three sets of experimental results were modeled using ABAQUS. In all these verification models, the concrete element used was a 3D Stress solid element with 8-nodes. The steel reinforcement was 2-nodes 3-D stress truss element. The truss element was embedded in the solid concrete element with full node-to-node constraint.

3.5.1 Verification model 1: Tabatabai et al. (1999)

The pile used in the test was a 356mm (14in) square prestressed concrete pile as shown in Figure 22. The cross sectional and material properties are presented in Table 16. The pile was saw-cut to obtain the needed length of 4115 mm (13.5ft). The saw cut end was embedded a distance of 610mm (2ft) into the pile cap. The concrete pile cap dimensions and reinforcement details are shown in Figure 23 and Figure 24. The test setup is presented in Figure 25. An axial load of 400 kN (90 kips) was applied at the face of the pile. Lateral cyclic displacement was applied. Three different displacement ranges were used;

1. ± 16 mm (± 0.63 in), 50 cycles
2. ± 32 mm (± 1.25 in), 50 cycles
3. ± 64 mm (± 2.5 in), 50 cycles

Experimental results showed extended cracking and spalling of pile concrete at the interface with the pile cap. However, the pile was still able to resist the axial load at significant displacement despite damage at the interface. Tabatabai et al. (1999) concluded that although the load was being resisted, the extent of localized damage to the pile was unacceptable.

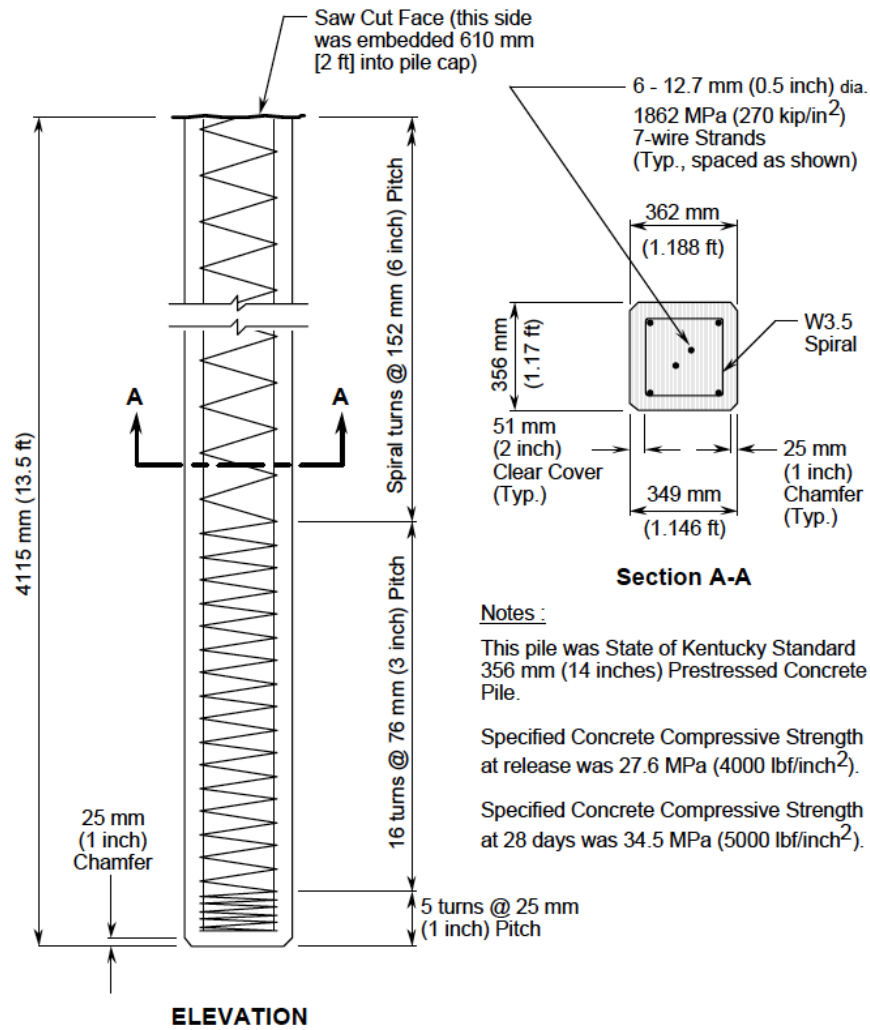


Figure 22: Design details for prestressed concrete pile (Tabatabai, Oesterle and Lawson 1999).

Table 16: Cross-sectional properties of prestressed concrete pile (Tabatabai, Oesterle and Lawson 1999).

Area mm ² (in ²)	I mm ⁴ (in ⁴)	Width mm (in)	Height mm (in)	Average E GPa (kips/in ²)	Average f'c MPa (kips/in ²)	Average ϵ_u (millionths)
125,160 (194.0)	1.295 x 10 ⁹ (3112)	356 (14.0)	356 (14.0)	36.47 (5290)	67.75 (9.83)	2000

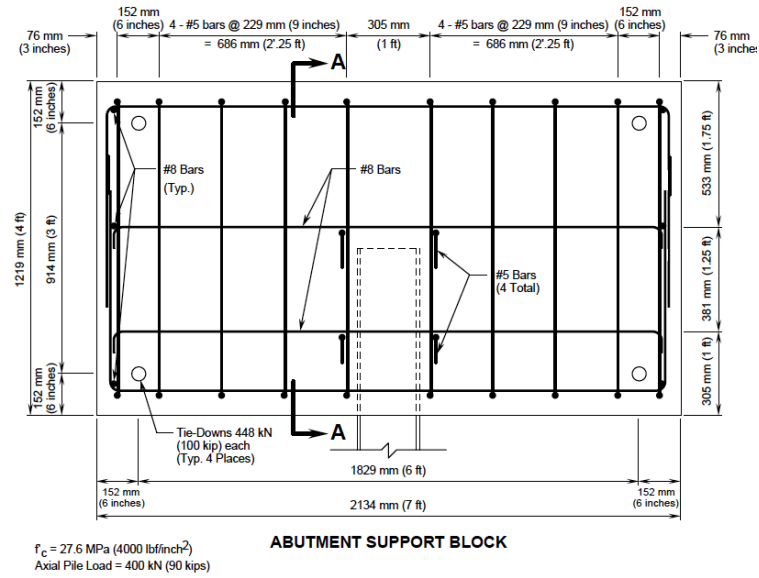


Figure 23: Pile cap details (Tabatabai, Oesterle and Lawson 1999).

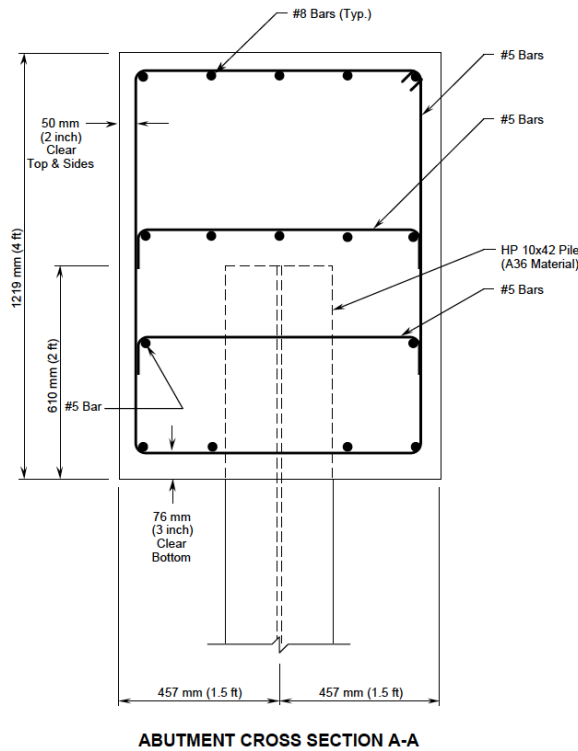


Figure 24: Pile cap cross section (Tabatabai, Oesterle and Lawson 1999).

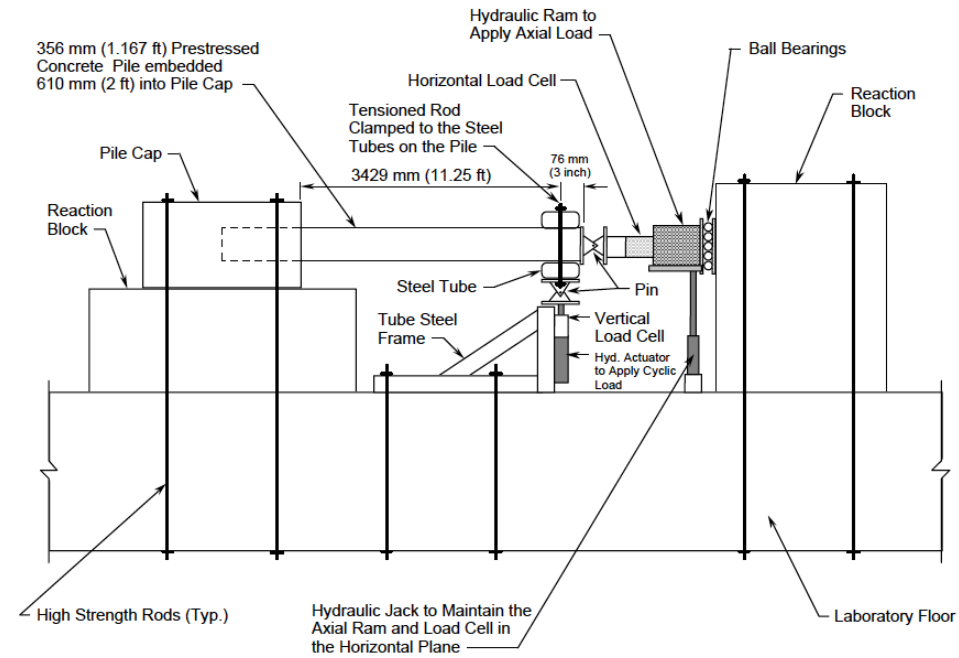


Figure 25: Schematic of prestressed concrete pile test setup (Tabatabai, Oesterle and Lawson 1999).

The general concrete damage plasticity parameters used in the verification model are presented in Table 7 (section. The stress-strain curve data for the concrete (5000 psi) was obtained from Tyau et al. (2009) and they presented in Tables 8 through 11 (section 3.2.1.2). The prestressed steel was modeled using a modified 414 MPa (60 ksi) steel based on the simplified bond-slip model proposed by (Braga, et al. 2012, D'Amato, et al. 2012). The stress-strain curve data used to define steel is shown in Table 21 (section 3.2.3.1). Moreover, Table 17 and Table 18 contain more material properties used for concrete and steel. The FE model assembly and boundary conditions are shown in Figure 26. The top and bottom surfaces of the abutment are fixed from displacing at all three directions.

Table 17: Concrete properties (Tabatabai, Oesterle and Lawson 1999).

Modulus of Elasticity E_c (MPa)	Compressive Strength f'_c (MPa)	Modulus of Rupture f_r (MPa)	Poisson's Ratio ν
36470	67.75	3.13	0.2

Table 18: Reinforcing Steel properties (Tyau 2009).

Steel bar	Area mm^2 (in^2)	Modulus of Elasticity (MPa)	Average Yield Stress (MPa)	Average Ultimate Stress (MPa)
M15 (#5)	200(0.31)	210000	414	720
M25 (#8)	500(0.79)			

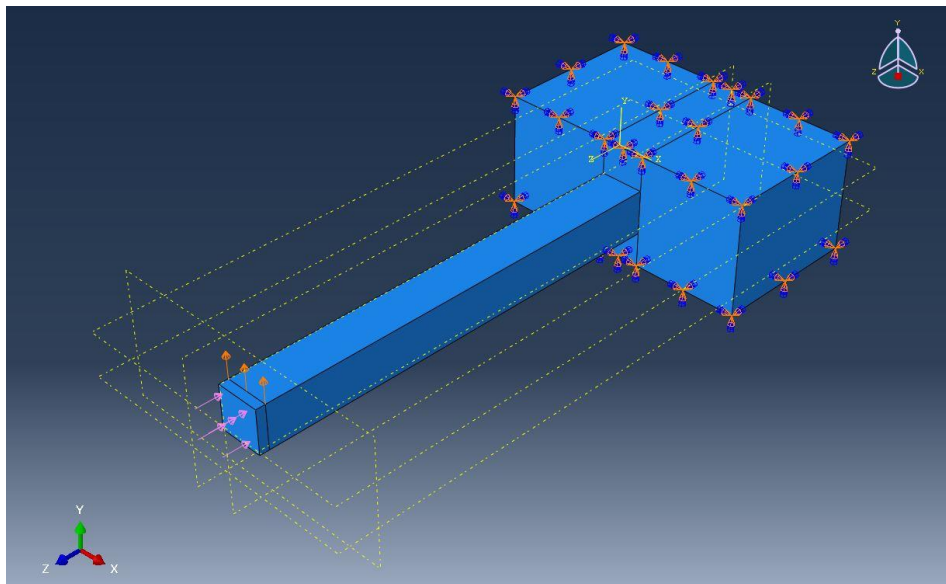


Figure 26: Model's assembly and boundary conditions.

A comparison of the FEM model and actual test results show reasonably good agreement. The load-displacement plot is shown in Figure 27. Moreover, tension plastic strain (PEEQT) and tension damaged elements (DAMAGET) in Figure 28 and Figure 29 show that there were elements that cracked closed to the pile-cap interface. The laboratory test also indicated two cracks appearing at 100mm from the pile-cap interface. These cracks occurred at imposed displacement of -14 mm (-0.55 in) and +10 mm (+0.39 in), while the FE model showed cracks at -13.7 mm (-0.54 in) and +9.6 mm (+0.38 in). The compression plastic strain (PEEQ) in Figure 30 showed that some elements reached the crushing strain at the higher imposed displacements ± 64 mm (± 2.5 in), and Figure 31 shows the Compression damage (DAMAGEC). The maximum von mises stress of 427 MPa shown on Figure 32, represent the stresses on the longitudinal steel reinforcement. The overall damage observed in the test and the predicted damage in the model are compared as shown in Figure 33 and Figure 34 and showed good agreement.

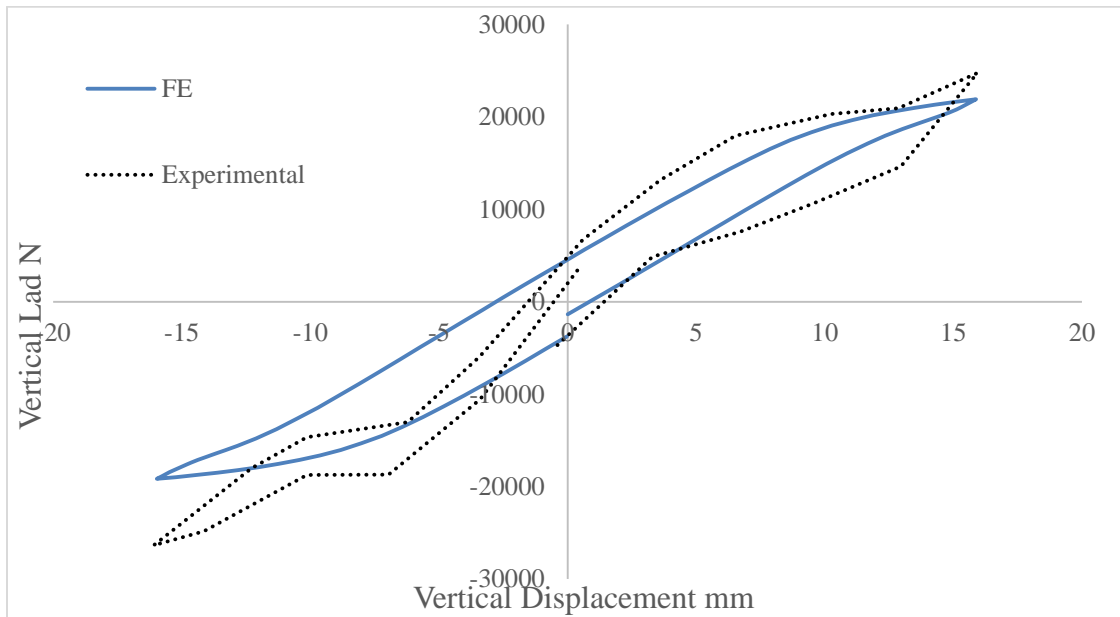


Figure 27: Vertical load vs. vertical displacement ± 16 mm (± 0.63 in).

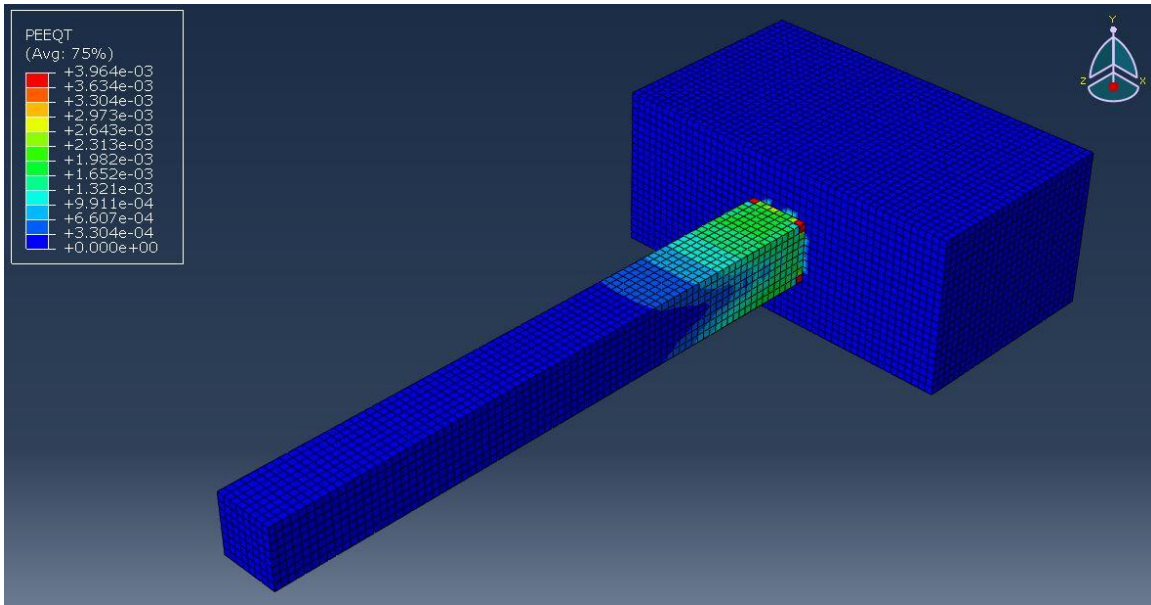


Figure 28: Tension plastic strain (PEEQT).

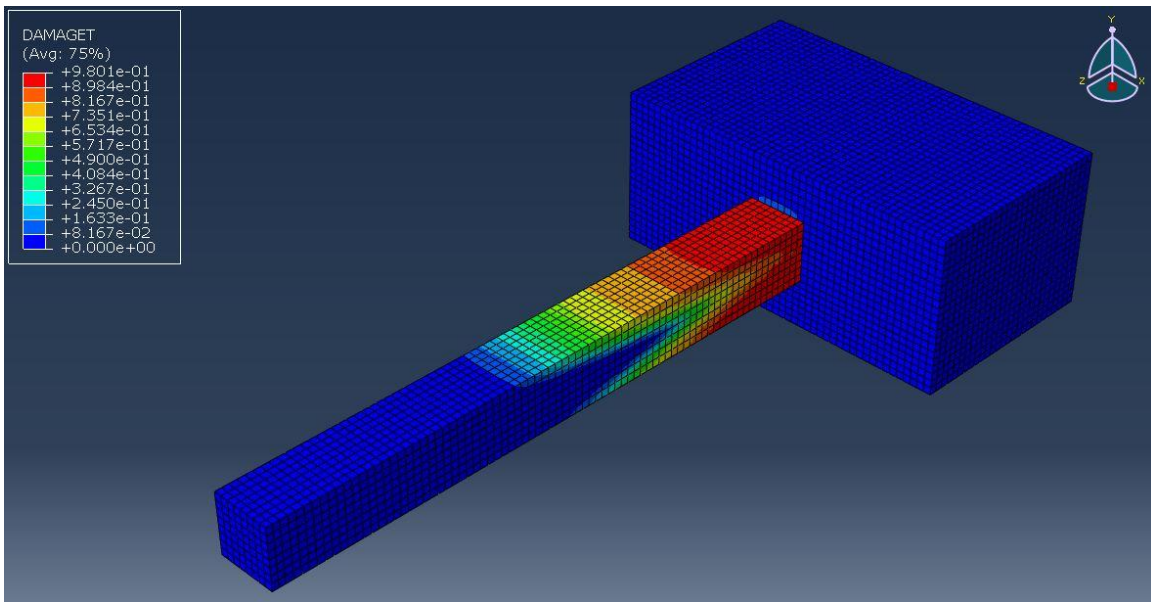


Figure 29: Tension damage.

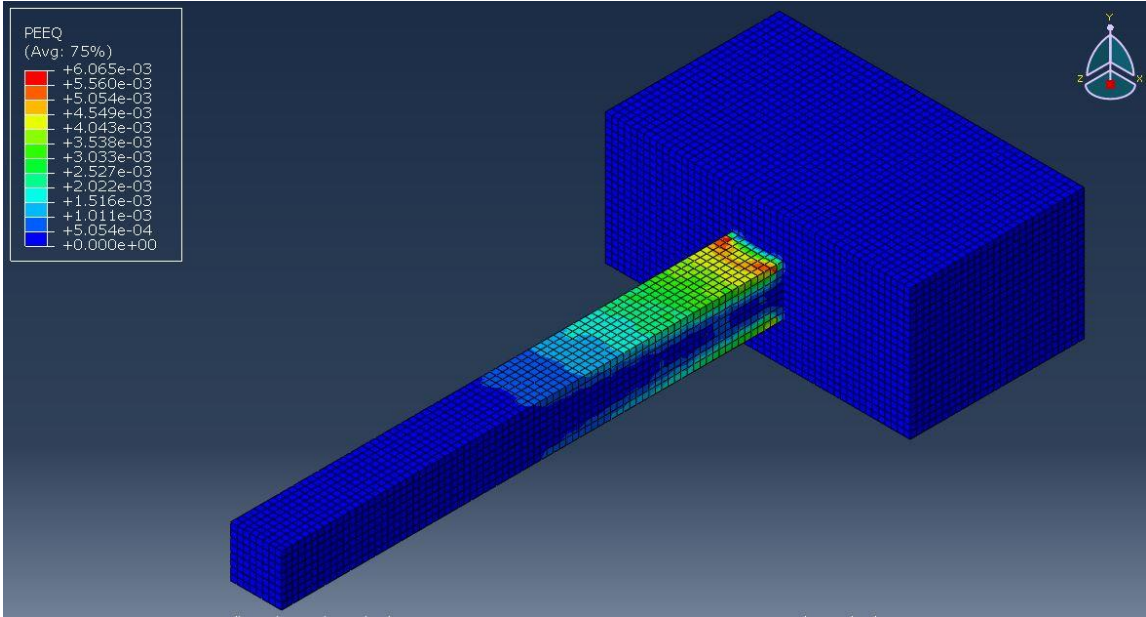


Figure 30: Compression plastic Strain (PEEQ)

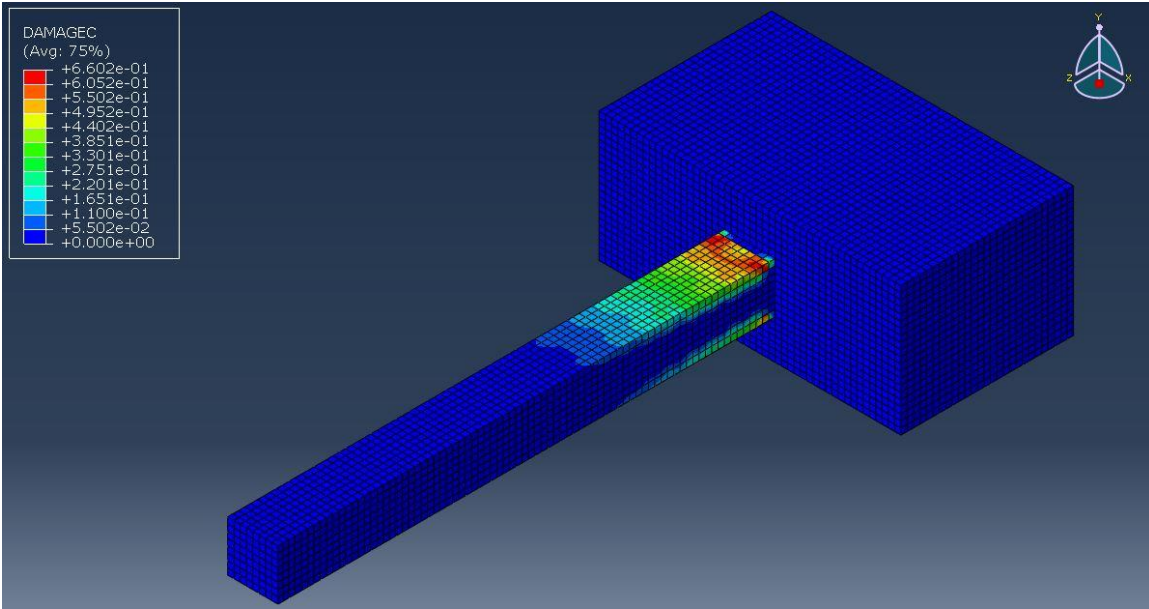


Figure 31: Compression damage.

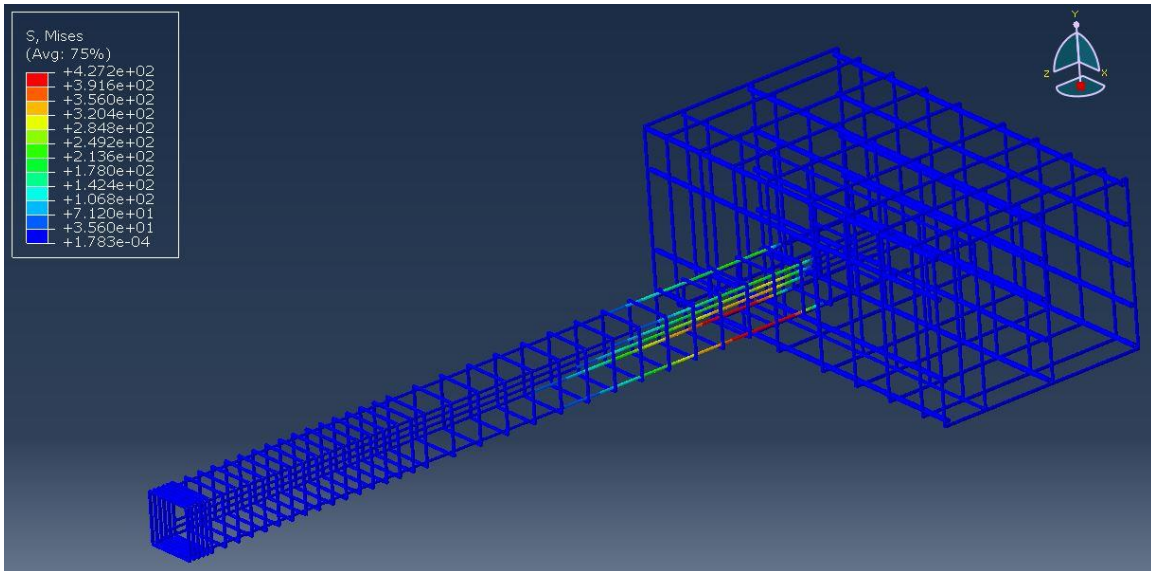


Figure 32: Stresses in reinforcing steel.

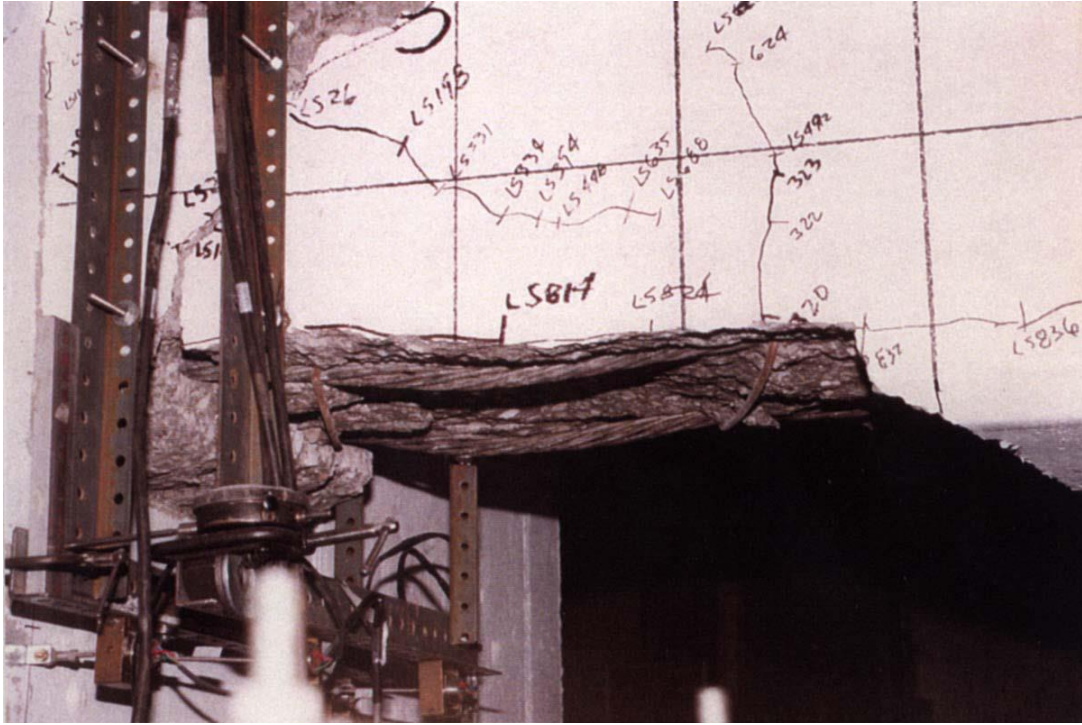


Figure 33: Concrete spalling damage during lab test (Tabatabai, Oesterle and Lawson 1999).

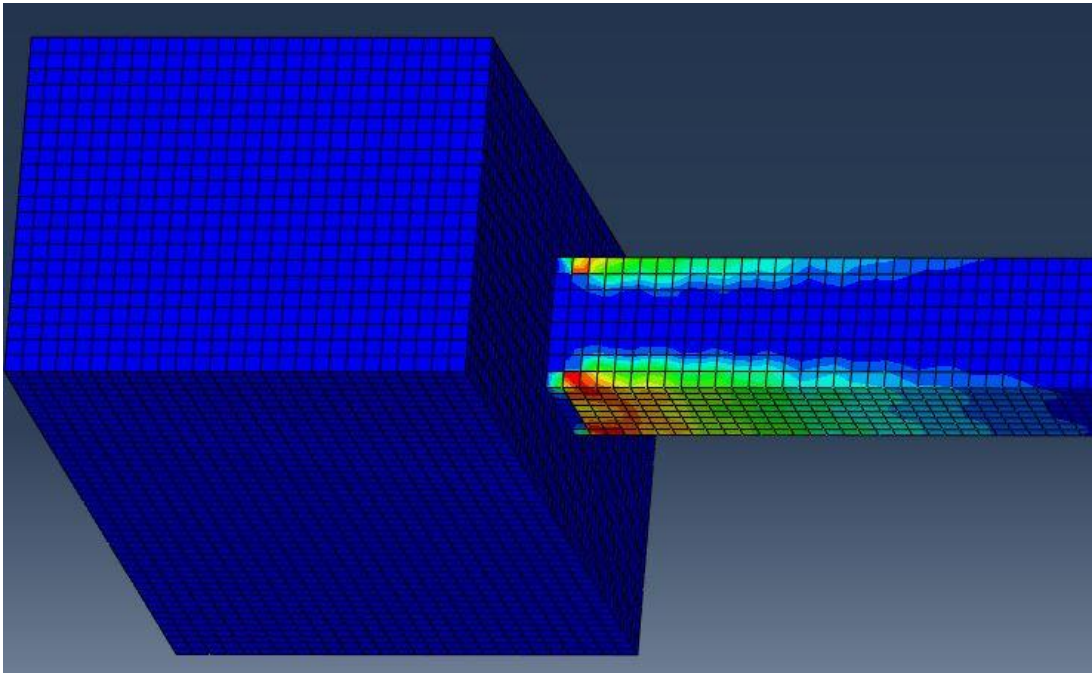


Figure 34: Predicted damage from FE model.

3.5.2 Verification model 2: Choi et al. (2015)

The experimental data used model was obtained during cyclic test on four columns. The first column was the control column without FRP. The second column was wrapped with one layer of carbon fiber reinforced polymer (CFRP). The third and fourth columns, involved a combination of CFRF and polyethylene terephthalate (PET). This verification model used the data from the results on the second column only. All columns had a circular cross section with a diameter of 400 mm (15.75 in). The test specimens were cast in two parts: column stub and column. The reinforcing steel bars were extended from the column stub into the columns without any splices. Shear reinforcement (ties) were used at 250 mm (9.8 in) o.c. The properties of steel reinforcement used are presented in Table 19. The concrete column dimensions and reinforcement details are shown in Figure 35 along with the test setup. The CFRP was wrapped around the column for the height of $2d$ ($d = 352$ mm (13.8 in), effective depth) above the column stub. The mechanical properties of CFRP are shown in Table 20. In this model, the CFRP was modeled as shell element and will be connected to the concrete solid element via surface-based contact elements.

Table 19: Mechanical properties of column reinforcement (Choi, et al. 2015).

Reinforcement	f_y (MPa)	f_{ult} (MPa)	E_s (GPa)
Main bar, 12 D16	347	522	178
Tie, D10 @ 250 o.c.	465	718	181
Column stub, D25	548	-	-

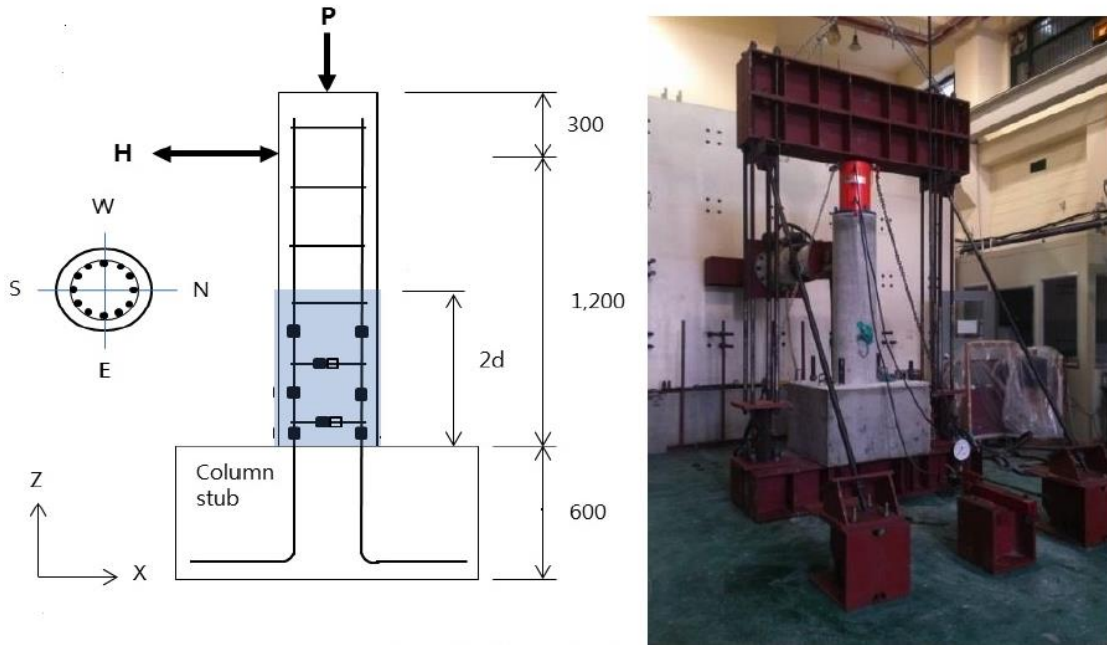


Figure 35: Test setup (Choi, et al. 2015).

Table 20: Mechanical properties of fibers (Choi, et al. 2015).

Fiber Type	Tensile Strength (MPa)	Maximum Strain in tension	Elastic modulus (GPa)	Cross-sectional area (mm ²)	Thickness (mm)	Density (g/mm ³)
CFRP	1970	0.0116	169	0.446	0.109	0.0018

An axial force of 350 kN was continuously applied during the test to simulate the applied dead load. The test procedure involved applying a displacement at multiple of ($\Delta_y \approx 8 \text{ mm}$ [0.32 in]) (1, 2, 3, 4, 5, 6, and $8\Delta_y$). The test was terminated when a maximum lateral load any cycle fallen below 80% of the maximum load recorded. Due to large number of element needed to model this test and the large number of cycles, the displacement cycles applied on the FE model was $\pm (2, 4, 6, 8\Delta_y)$ so we can capture the larger displacements.

The general concrete damage plasticity parameters used in this verification model are the same used in previous model and presented in Table 7 (section 3.2.1.2). The stress-strain curve data for the concrete was obtained from Tyau et al. (2009) and they presented in Tables 8 through 11 (section 3.2.1.2). In this case, the reinforcing bar is not subjected to pull out due to bond failure. Therefore, the actual stress-strain behavior of the mild steel bar was modeled (instead of the modified used to represent bond failure in the previous model). The mild reinforcing steel used in this test was 414 MPa (60 ksi) and the stress-strain data used to define steel model is shown in Table 21.

Table 21: Steel 414 MPa (60ksi) stress vs. plastic strains Data (Barker and Puckett 2006).

Stress MPa	Strain
414	0
460	0.0101
557	0.0221
660	0.0421
712	0.0621
720	0.0821
709	0.1021
705	0.1321

An ABAQUS model was generated and analyzed. Since this was a symmetrical three-dimensional geometry, only one-half of the full geometry was considered. The model assembly and boundary conditions are shown in Figure 36. The bottom surface of the column stub was fixed at all three directions. The tip of the column was subjected to

axial load of 350 kN (about 10% of the column axial capacity). A lateral displacement was applied at 1.2 m. A comparison of the FEM model and actual test results show good agreement regarding load-displacement behavior as shown in Figure 37 and Figure 38. The model aborted before finishing the last cyclic due to compression failure around -72 mm (-2.8 in). The maximum displacement reported in the FE model before failure was 77.9 mm (3.07 in) as compared to 78.4 mm (3.1 in) from actual test.

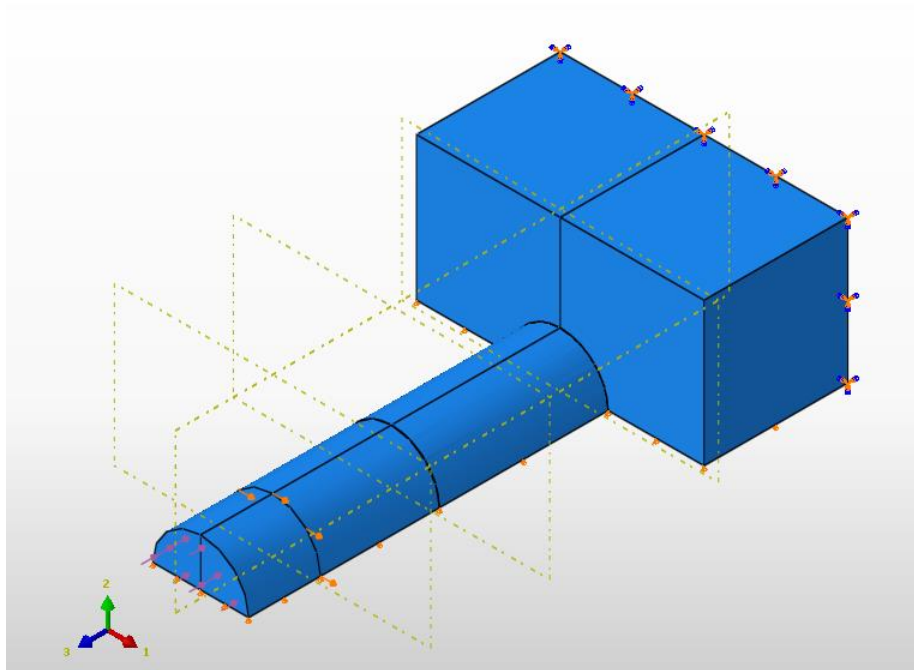


Figure 36: Model's assembly and boundary conditions.

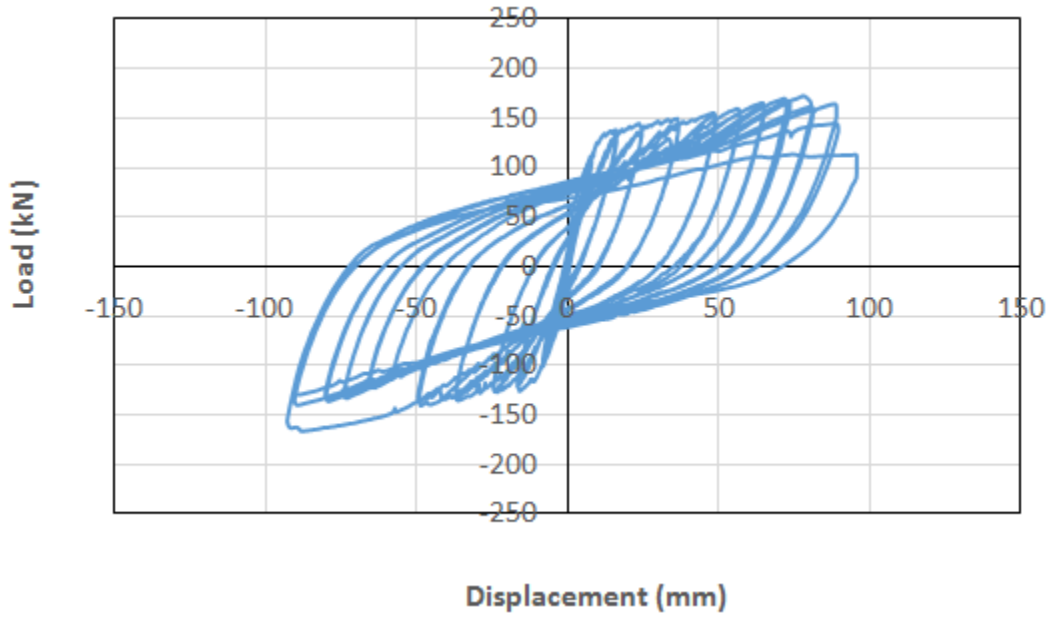


Figure 37: Experimental vertical load vs. vertical displacement (Choi, et al. 2015).

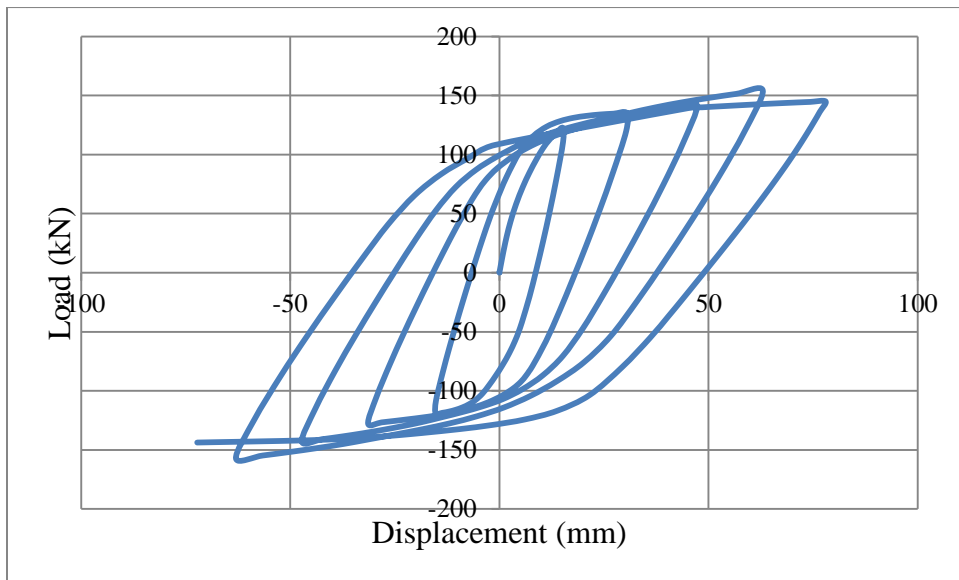


Figure 38: FE model vertical load vs. vertical displacement.

3.5.3 Verification model 3: Soil-Pile interaction test – Burdette et al. (2004)

A field test reported by Burdette et al. (2004) was used to verify the soil-pile interaction modeling approach. This field test was sponsored by the Tennessee Department of Transportation (TDOT) and to investigate the use of prestressed concrete piles to support integral abutment bridges. The pile used in the test was a 356mm (14in) square prestressed concrete pile. The cross sectional and material properties are presented in Table 16 section (3.5.1). The pile was driven 11m (36ft) into clay soil. Table 13 presents the soil properties used for MCP model in section (3.2.2). The pile was embedded a distance of 305mm (1ft) into the pile cap. The concrete pile cap dimensions and test setup are shown in Figure 39. An axial load of 400 kN (90 kips) was applied at the top surface of the abutment. The abutment in an actual bridge, the abutment slab was restrained against free rotation by using a hold down beam. One hundred displacement cycles of 25.4mm (1in) was applied laterally in one direction to follow TDOT's design criteria. The tests results showed that prestressed concrete piles were suitable for integral abutment bridges. Moreover, the results showed cracking in the concrete pile at the interface with the cap at displacement of 12.7 mm (0.5 in). The cracking in the abutment was considered to be minor.

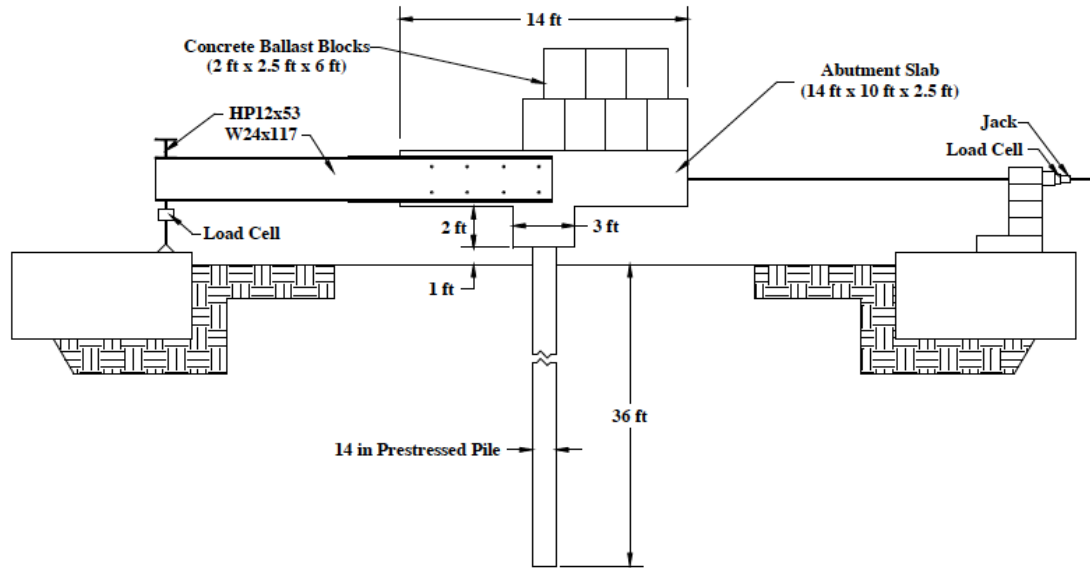


Figure 39: Test setup (Burdette, Howard and Tidwell, et al. 2004).

An ABAQUS model has been generated and analyzed. The general concrete damage plasticity parameters used in this verification model are the same as the previous two models. Three meters (10 ft) of soil around the pile was modeled, soil displacement due to pile displacement of 25.4 mm (1 in) is shown in Figure 40 and Figure 41. The Mohr-Coulomb plasticity model (MCP) was used in the verification model. MCP model require inclusion of the elastic properties of the soil (Modulus of Elasticity and poisson ratio), angle of dilation, and cohesive yield stress vs. plastic strain as shown in Table 13 (section 3.2.2).

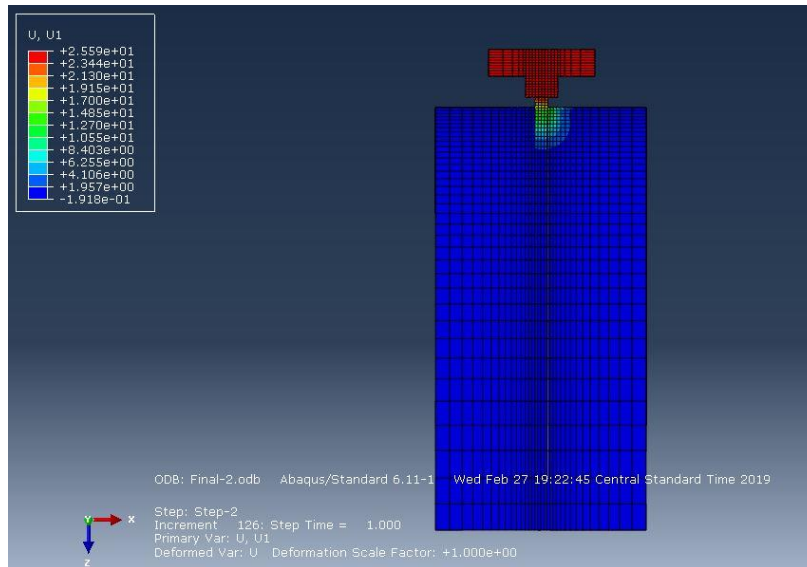


Figure 40: Front view shows the displacement at 25.4 mm (1 in).

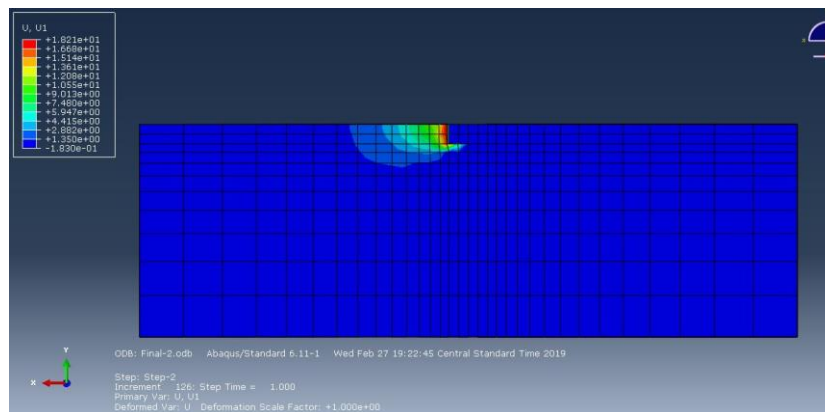


Figure 41: Top view shows the displacement at 25.4 mm (1 in).

A comparison of the FEM model and actual test results showed reasonably good agreement. The load-displacement plots from the experiment and the FEM are shown in Figure 42 and Figure 43. Cracking occurred at a displacement of 12.7 mm (0.5 in) during the experiment, while the FE model indicated cracking at 10.9 mm (0.43 in).

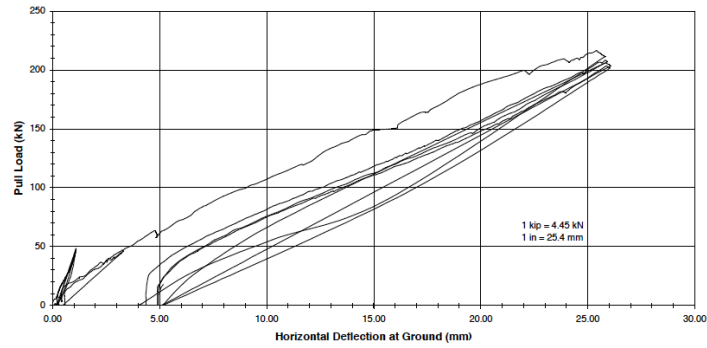


Figure 42: Load vs. displacement of view cycles of field test (Burdette, Howard and Tidwell, et al. 2004).

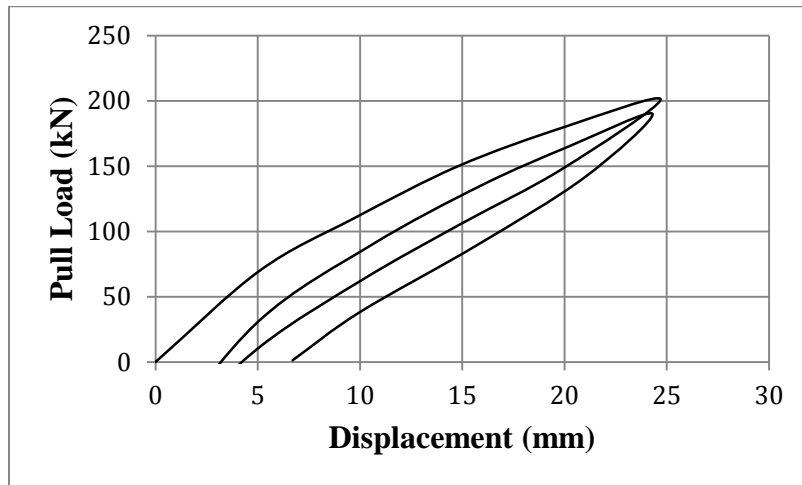


Figure 43: Load vs. displacement of first two cycles of FEM

3.6 Parametric Study

The purpose of this section is to investigate the importance of several parameters on the induced curvature at the pile/pile cap connection due to lateral movement. The parameters considered included pile shape, size, embankment soil type, pile external reinforcement near the abutment, abutment-superstructure connection (stiffness), pile axial load and imposed displacement. These parameters are summarized below:

- Pile Shape: square.
- Pile size: 457.2 mm (18 in).
- Embankment soil condition:
 - Sand (loose, medium and dense).
 - Clay (soft, medium and stiff).
- Pile-cap interface external confinement
 - None / control
 - CFRP (two layers)
- Embedment length = 609.6 mm (24 in) since most state DOTs prefer that embedment (Tabatabai et al. 2017).
- Abutment-superstructure connection (Rotational Stiffness)
 - Low-Short girder
 - Medium-Medium girder
 - High-Long girder
- Pile head lateral displacement
 - ± 12.7 mm (± 0.5 in): allow integral bridge length approximately – 122 m (400 ft).
 - ± 25.4 mm (± 1 in).
 - ± 50.8 mm (± 2 in).

4 NUMERICAL STUDY AND RESULTS

As discussed in Section 3.4, a general finite element model was generated that includes, pile, abutment, and girder. The main purpose of this model was to determine various abutment and pile response parameters including the maximum curvature at the pile/cap interface and the point of inflection (POI) on the pile in response to changes in the type of, rotational stiffness of the girder (span length), external confinement of the pile (with or without FRP) and range of imposed displacement. The general model is discussed in detail in the first part of this chapter. In the second part of this chapter, the localized model will be investigated and discussed in detail. The localized model includes the pile cap and a length of pile from the cap to the POI with or without the application of FRP confinement.

4.1 General Model

An example of the general model is shown in Figure 44. The pile was embedded in the soil for a height of 12.2 m (40 ft) in all such models. A prestressed concrete pile with a 457.2 mm (18 in) square cross section was used. The pile design standards were obtained from Florida DOT manual (Florida Department of Transportation 2013) as presented in Figure 45. Sixteen 12.7 mm (0.5 in) prestressing strands were included in the pile cross section. The soil behind the abutment was extended over a distance of 12.2 m (40 ft) to ensure that it can properly model the soil response to the imposed displacement from the abutment.

Six different types of soil condition were considered (three types of sand and clay each). Moreover, two different sets of models were generated based on confinement level (control and CFRP). The CFRP confinement consisted of two layers of carbon fiber

fabric wrapped around the perimeter of the pile with fibers oriented transverse to longitudinal direction of the pile. A 610 mm (24 in) embedment length of the pile was as assumed as this is considered to be preferred by states department of transportation (Tabatabai, Magbool, et al. 2017). Three different span lengths were assumed for the end span of the bridge to represent different rotational rigidities of the superstructure. The three span lengths were short (15.25 m or 50 ft), medium (30.5 m or 100 ft), and long (45.75 m or 150 ft) representing low, medium and high rotational rigidities, respectively. Finally, three ranges of cyclic displacement were applied to the model at the centroid of the composite bridge girder: ± 12.7 mm (± 0.5 in), ± 25.4 mm (± 1 in), and ± 50.8 mm (± 2 in).

The superstructure consisted of one girder representing a composite girder-slab beam with a girder spacing of 2438 mm (8 ft). A 2438 mm (8 ft) length of the abutment with one pile directly under the girder support was also considered. Due to symmetry, one-half of the girder, pile and abutment were modelled.

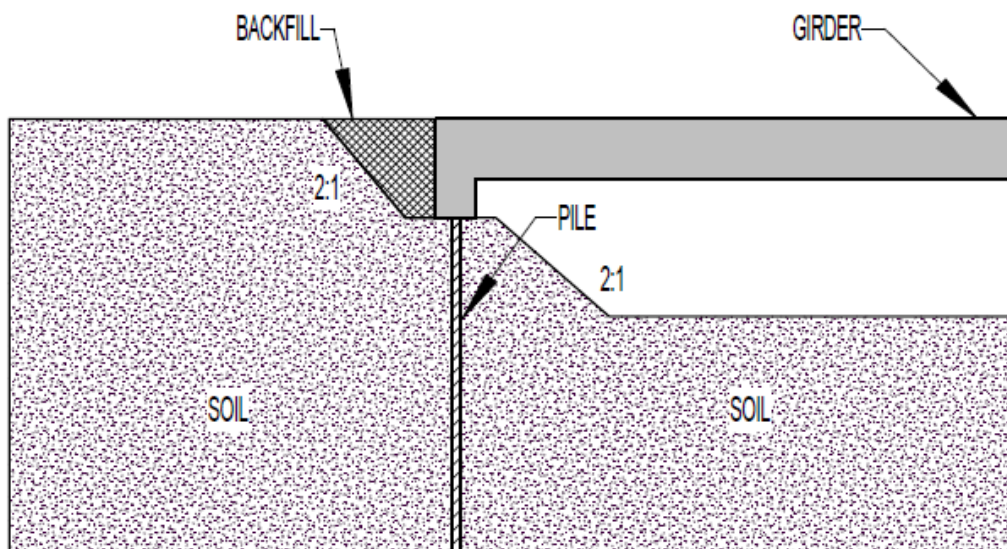


Figure 44: General model.

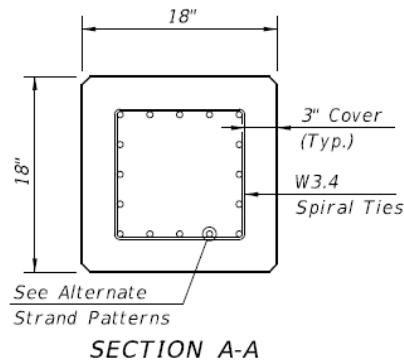


Figure 45: Pile details.

The sizes of the prestressed bridge girders were selected based on the three span lengths used. According to the Wisconsin DOT bridge manual (Wisconsin Department of Transportation 2014), the preferred girder for 15.25 m (50 ft) long concrete bridge girder with 2.438 m (8 ft) spacing is a 914.4 mm (36 in) Wisconsin standard prestressed I-girder. Similarly, Wisconsin standard 45W and 82W girders were selected for 30.5 m (100 ft) and 45.75 m (150ft) spans, respectively. However, to reduce the complexity of the model, each girder (with its composite slab) was modeled as a rectangular beam with cross-sectional properties (moment of inertia and position of neutral axis) that were equivalent to the composite bridge section as shown in Table 22 (See appendix A for calculations). As a result of the modeled section, the concrete self-weight will behave as axial load instead of applying it to the model. These axial loads for the different girders are presented in Table 22.

Table 22: Equivalent girder dimensions, moment of inertia, and pile loads for various span lengths.

Span Length	Girder Type	Composite moment of inertia I_{bc}		h		b		Pile Axial Loads	
		in ⁴	mm ⁴	in	mm	in	mm	kips	kN
15.25 m (50 ft)	36"	2.02E+05	8.35E+10	64.3	1634	9.1	230	55	243.5
30.5 m (100 ft)	45W"	4.72E+05	1.97E+11	71.2	1809	15.7	400	100	443.9
45.75 m (150 ft)	82W"	1.83E+06	7.63E+11	120.1	3050	12.7	323	178	791.7

* Half of the width was modeled due to symmetry.

4.1.1 Geometry

Taking advantage of symmetry, only half of the structure was modeled to reduce the number of elements. Four different components were modelled: concrete (abutment integrated with the pile and the girder), pile reinforcing steel cage, and CFRP as shown in Figures 46 through 49. Table 23 shows the dimensions of the models based on span lengths (H_T is the total height of the abutment including the height of the girder).

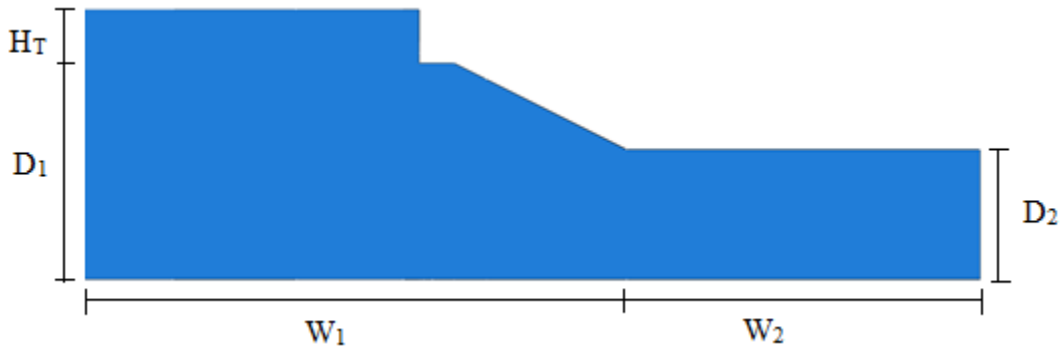


Figure 46: Soil part.

Table 23: Models dimensions based on span lengths.

Span Length	H _T		D ₁		D ₂		W ₁		W ₂	
	in	mm	in	mm	in	mm	in	mm	in	mm
15.25 m (50 ft)	112.3	2852.4	480	12192	288	7315	1206	30631.2	196.9	5000
30.5 m (100 ft)	119.2	3027.5	480	12192	288	7315	1206	30631.2	787.4	20000
45.75 m (150 ft)	168	4267	480	12192	288	7315	1206	30631.2	1378.0	35000

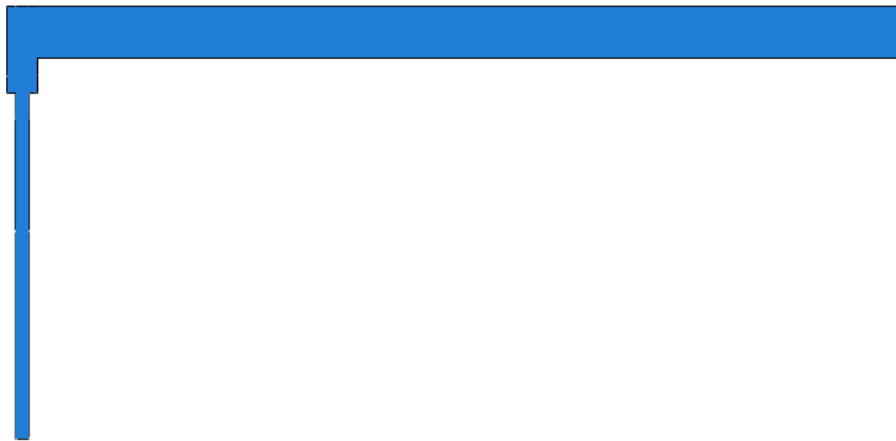


Figure 47: Abutment, pile and girder as one part.

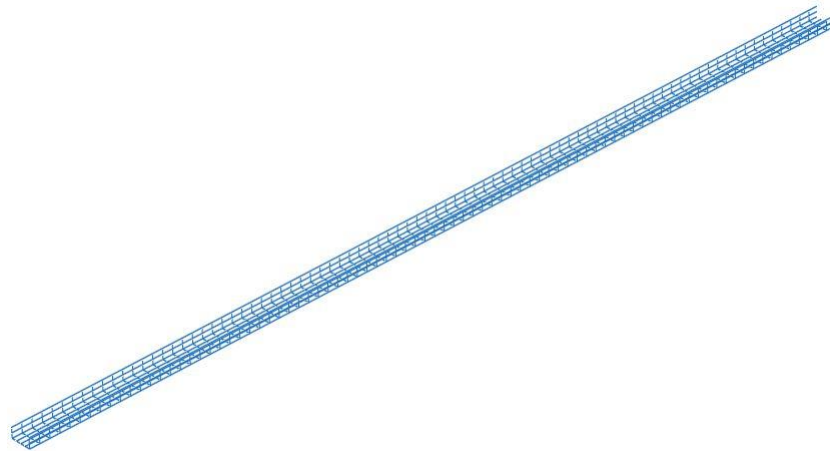


Figure 48: Steel reinforcing cage for the pile (half model).

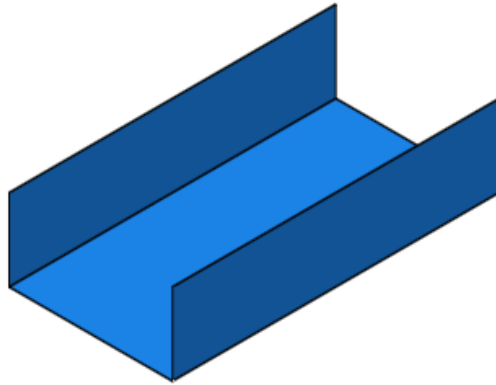


Figure 49: CFRP wrap (half model).

4.1.2 Boundary Conditions and Application of Displacements

To maintain accuracy, it is important to pay particular attention to the boundary conditions in any FEM model. Because of the consideration of symmetry, the model is restrained from displacement in the Y-direction (out of plane direction as shown in Figure 50). Moreover, all vertical ends of the soil model are restricted from moving in the X-direction. Also, the nodes at the bottom of the soil are pinned. The far end of girder is modelled as a roller with movement in the Z direction restricted.

The lateral (X direction) displacements were imposed at the centroid of the girder at the far support. The three different displacement cycles were applied by first pulling away from the backfill and then pushing against the backfill.

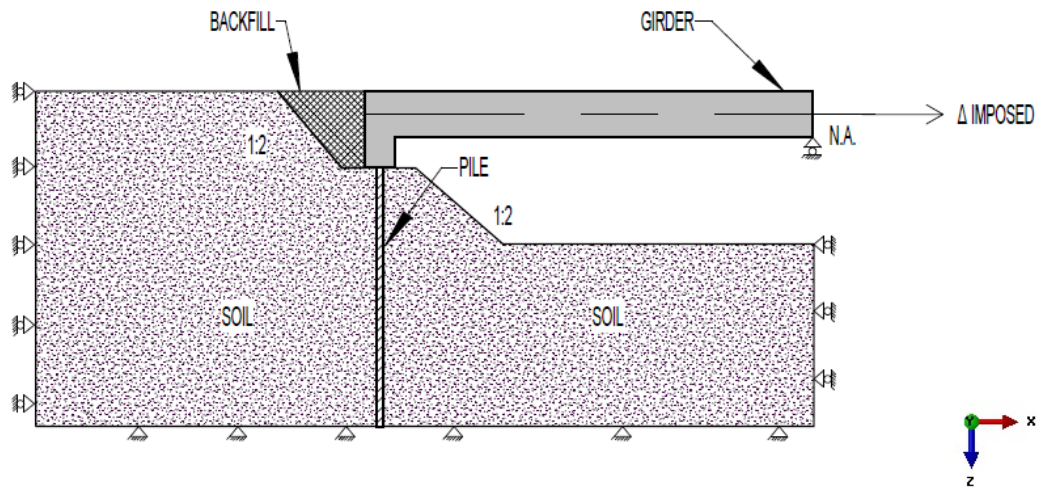


Figure 50: Boundary Conditions.

4.1.3 Meshing

The focus for the model was the area around the top of the pile. As shown in Figure 51, finer element sizes were used closer to the pile-abutment interface (80 mm [3.15 in] at plastic hinge zone). However, for elements away from the pile-abutment interface, the mesh size increases to 800 mm (31.5 in). Table 24 shows the number of elements used in the various models based on the span length.

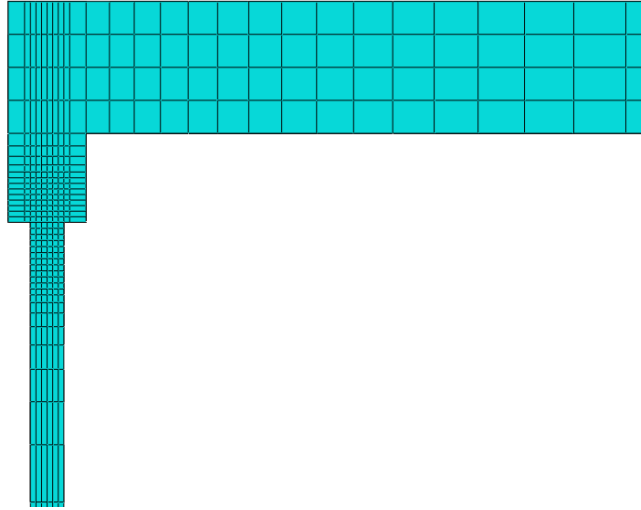


Figure 51: The mesh at the location of interest.

Table 24: Number of elements used in different models.

Span length/Rotational stiffness	Number of Elements
Low-12.2 m (50 ft)	15,980
Medium-30.5 m (100 ft)	20,236
High-45.8 m (150 ft)	22,042

4.1.4 Analysis Procedures

Two different steps were included in the analysis. In the first step, a geostatic load was applied to the soil part based on the type of soil used to ensure a stable model. Then, the concrete part, which includes the abutment, pile, and girder, was added. In the second step, three different ranges of cyclic lateral displacement were applied at the girder natural axis. The displacement cycle started by contracting the superstructure (pulling away from backfill) and then expanding (pushing against backfill) as shown in Figure 52 and Figure 53. A total of 108 runs were performed on the general model based on the study parameters in section 3.6.

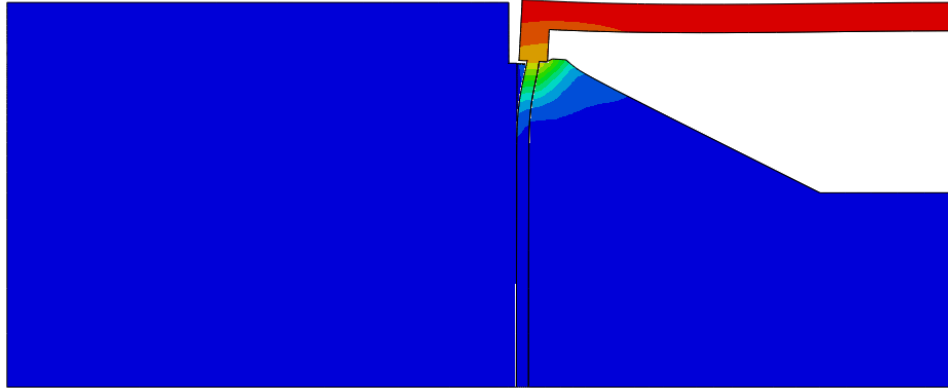


Figure 52: The maximum pull in the pull cycle with +50.8 mm (+2 in).

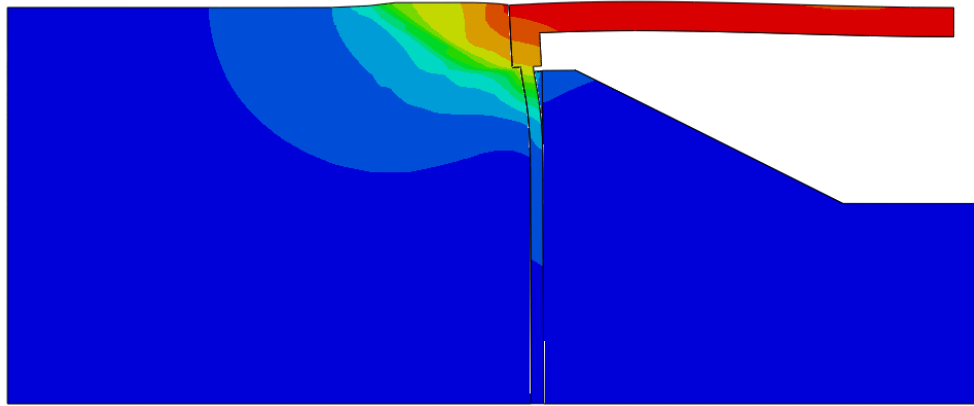


Figure 53: The maximum push in the push cycle -50.8 mm (-2 in).

4.1.5 Results

In the following sections, the results of the 108 runs of the general model are presented. Results are given for various girder (superstructure) movements imposed at the centroid of the girder section (Δ_g). Results that are reported include the rotation, lateral pile head movement (Δ_p), curvature along the pile and point of inflection (zero curvature) in the pile based upon the behavior of the pile as shown in Figure 54.

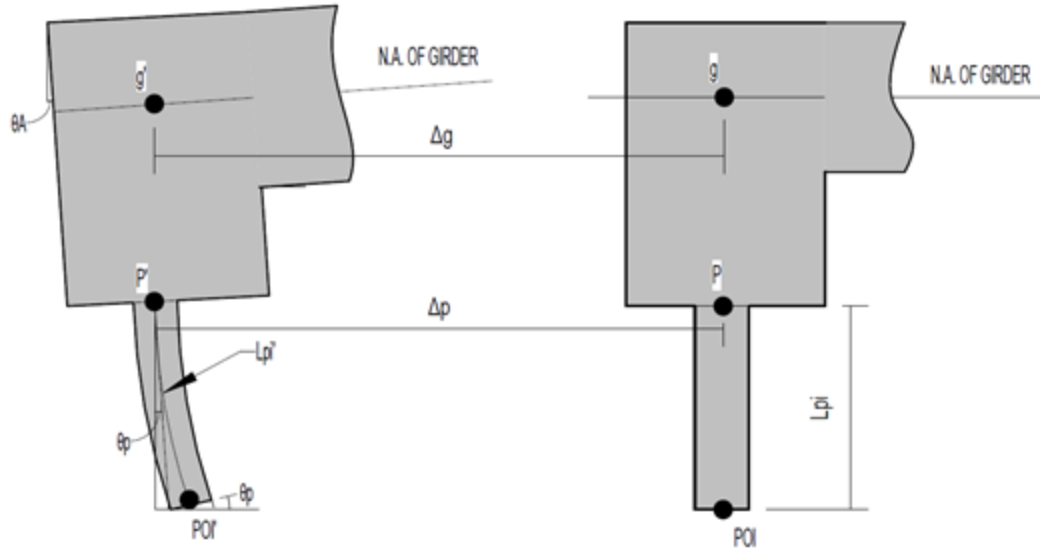


Figure 54: A schematic showing the results reported in this study.

4.1.5.1 Rotations

One of the parameters studied in the general model was the rotation of the abutment (θ_A) along with the rotations at the pile-abutment interface (θ_p) and at the POI (θ_{pi}). In this study, the effects of the three different girder rotational stiffnesses (based on girder length) were evaluated. As shown in Figures 55 through 57, the abutment rotation (θ_A) increases as the girder rotational stiffness decreases. In addition, the relative rotations between the pile and the POI ($\theta_{pi}-\theta_p$) decrease. As a result, the curvature demand and pile displacement decrease. In the medium and high rotational stiffness models, the relative rotation ($\theta_{pi}-\theta_p$) increases as result of a lower abutment rotation (θ_A). The absolute rotations (θ_A , θ_p and θ_{pi}) of all cases studied are presented in Tables 25 through 28 and Figures 58 through 63.

The results further show that the piles embedded in clay require more rotation at pile-abutment interface, due to larger lateral resistance provided by the soil. However, the

use of CFRP reduces the relative rotation at the pile. Moreover, CFRP tends to increase θ_p linearly with the increase of Δ_g as shown in Figures 64 to 69.

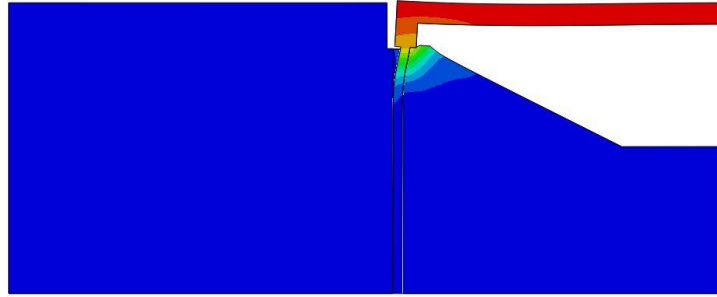


Figure 55: The deflected shape of the low rotational stiffness model, $\Delta_g = +50.8$ mm (+2 in), exaggerated.

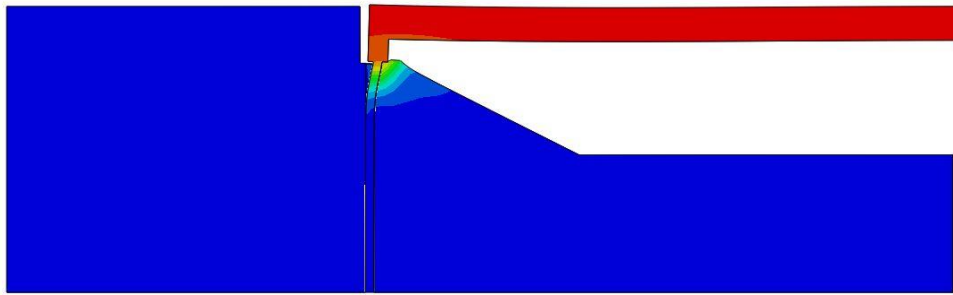


Figure 56: The deflected shape of the medium rotational stiffness model, $\Delta_g = +50.8$ mm (+2 in), exaggerated.

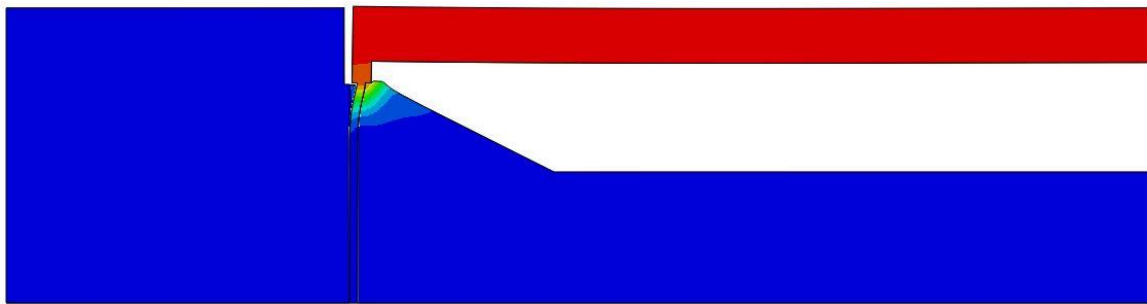


Figure 57: The deflected shape of the high rotational stiffness model, $\Delta_g = +50.8$ mm (+2 in), exaggerated.

Table 25: The recorded rotations in all control cases-pulling away from the backfill.

Type of Soil	Δ_g Pulling away from Backfill		Span Length								
			15.25 m (50 ft)			30.5 m (100 ft)			45.75 m (150 ft)		
Control	mm	in	rad			rad			rad		
			θ_A	θ_p	θ_{pi}	θ_A	θ_p	θ_{pi}	θ_A	θ_p	θ_{pi}
Sand Dense	12.7	0.5	0.0023	0.0029	0.0038	0.0014	0.0023	0.0040	0.0007	0.0018	0.0042
	25.4	1	0.0038	0.0051	0.0082	0.0022	0.0038	0.0089	0.0011	0.0030	0.0091
	50.8	2	0.0055	0.0077	0.0203	0.0029	0.0054	0.0214	0.0014	0.0042	0.0223
Sand Medium	12.7	0.5	0.0022	0.0028	0.0038	0.0013	0.0022	0.0039	0.0007	0.0018	0.0043
	25.4	1	0.0037	0.0050	0.0085	0.0021	0.0037	0.0089	0.0010	0.0029	0.0096
	50.8	2	0.0051	0.0073	0.0207	0.0027	0.0051	0.0217	0.0013	0.0040	0.0226
Sand Loose	12.7	0.5	0.0022	0.0028	0.0038	0.0013	0.0021	0.0039	0.0007	0.0018	0.0043
	25.4	1	0.0036	0.0048	0.0085	0.0020	0.0036	0.0088	0.0010	0.0029	0.0095
	50.8	2	0.0049	0.0071	0.0205	0.0026	0.0050	0.0215	0.0013	0.0039	0.0224
Clay Stiff	12.7	0.5	0.0026	0.0032	0.0039	0.0017	0.0026	0.0039	0.0009	0.0022	0.0042
	25.4	1	0.0050	0.0063	0.0086	0.0030	0.0049	0.0088	0.0016	0.0040	0.0096
	50.8	2	0.0085	0.0112	0.0216	0.0048	0.0082	0.0233	0.0024	0.0064	0.0251
Clay Medium	12.7	0.5	0.0026	0.0032	0.0039	0.0016	0.0025	0.0039	0.0009	0.0022	0.0042
	25.4	1	0.0049	0.0062	0.0086	0.0029	0.0048	0.0090	0.0015	0.0039	0.0096
	50.8	2	0.0081	0.0108	0.0220	0.0045	0.0078	0.0234	0.0023	0.0061	0.0255
Clay Soft	12.7	0.5	0.0025	0.0031	0.0038	0.0015	0.0024	0.0039	0.0008	0.0020	0.0042
	25.4	1	0.0045	0.0059	0.0086	0.0026	0.0044	0.0089	0.0014	0.0036	0.0096
	50.8	2	0.0071	0.0098	0.0223	0.0039	0.0069	0.0237	0.0019	0.0054	0.0252

Table 26: The recorded rotations in all control cases-pushing against backfill.

Type of Soil	Δ_g Pushing against Backfill		Span Length								
			15.25 m (50 ft)			30.5 m (100 ft)			45.75 m (150 ft)		
			mm	in	rad			rad			rad
θ_A	θ_p	θ_{pi}			θ_A	θ_p	θ_{pi}	θ_A	θ_p	θ_{pi}	
Sand Dense	12.7	0.5	-0.0019	-0.0021	-0.0026	-0.0012	-0.0016	-0.0025	-0.0007	-0.0012	-0.0025
	25.4	1	-0.0036	-0.0043	-0.0062	-0.0022	-0.0032	-0.0062	-0.0011	-0.0023	-0.0060
	50.8	2	-0.0058	-0.0077	-0.0168	-0.0031	-0.0054	-0.0181	-0.0013	-0.0039	-0.0180
Sand Medium	12.7	0.5	-0.0019	-0.0022	-0.0027	-0.0012	-0.0016	-0.0026	-0.0007	-0.0013	-0.0026
	25.4	1	-0.0035	-0.0043	-0.0064	-0.0021	-0.0031	-0.0062	-0.0011	-0.0024	-0.0065
	50.8	2	-0.0051	-0.0070	-0.0176	-0.0027	-0.0048	-0.0182	-0.0011	-0.0035	-0.0184
Sand Loose	12.7	0.5	-0.0018	-0.0021	-0.0026	-0.0011	-0.0016	-0.0025	-0.0006	-0.0012	-0.0025
	25.4	1	-0.0034	-0.0041	-0.0063	-0.0020	-0.0030	-0.0063	-0.0010	-0.0022	-0.0062
	50.8	2	-0.0048	-0.0067	-0.0175	-0.0024	-0.0045	-0.0182	-0.0010	-0.0033	-0.0184
Clay Stiff	12.7	0.5	-0.0022	-0.0025	-0.0026	-0.0014	-0.0019	-0.0024	-0.0008	-0.0014	-0.0023
	25.4	1	-0.0047	-0.0054	-0.0062	-0.0029	-0.0039	-0.0058	-0.0015	-0.0029	-0.0055
	50.8	2	-0.0086	-0.0107	-0.0162	-0.0047	-0.0075	-0.0177	-0.0022	-0.0056	-0.0185
Clay Medium	12.7	0.5	-0.0022	-0.0024	-0.0027	-0.0013	-0.0018	-0.0025	-0.0007	-0.0014	-0.0024
	25.4	1	-0.0046	-0.0054	-0.0063	-0.0027	-0.0038	-0.0059	-0.0014	-0.0028	-0.0057
	50.8	2	-0.0082	-0.0103	-0.0168	-0.0044	-0.0071	-0.0183	-0.0020	-0.0053	-0.0191
Clay Soft	12.7	0.5	-0.0021	-0.0024	-0.0027	-0.0012	-0.0017	-0.0024	-0.0007	-0.0013	-0.0024
	25.4	1	-0.0043	-0.0050	-0.0061	-0.0025	-0.0036	-0.0059	-0.0013	-0.0026	-0.0058
	50.8	2	-0.0072	-0.0103	-0.0169	-0.0038	-0.0063	-0.0182	-0.0017	-0.0046	-0.0190

Table 27: The recorded rotations in all CFRP cases-pulling away from backfill.

Type of Soil	Δ_g Pulling away from Backfill		Span Length								
			15.25 m (50 ft)			30.5 m (100 ft)			45.75 m (150 ft)		
CFRP	mm	in	rad			rad			rad		
			θ_A	θ_p	θ_{pi}	θ_A	θ_p	θ_{pi}	θ_A	θ_p	θ_{pi}
Sand Dense	12.7	0.5	0.0023	0.0029	0.0037	0.0014	0.0023	0.0038	0.0007	0.0019	0.0041
	25.4	1	0.0038	0.0051	0.0076	0.0022	0.0041	0.0083	0.0011	0.0034	0.0089
	50.8	2	0.0059	0.0091	0.0185	0.0032	0.0071	0.0193	0.0016	0.0060	0.0199
Sand Medium	12.7	0.5	0.0022	0.0029	0.0038	0.0014	0.0023	0.0040	0.0007	0.0019	0.0042
	25.4	1	0.0038	0.0052	0.0083	0.0021	0.0041	0.0087	0.0011	0.0033	0.0092
	50.8	2	0.0055	0.0088	0.0189	0.0029	0.0069	0.0197	0.0015	0.0059	0.0204
Sand Loose	12.7	0.5	0.0022	0.0028	0.0037	0.0013	0.0022	0.0038	0.0007	0.0019	0.0042
	25.4	1	0.0036	0.0051	0.0082	0.0021	0.0039	0.0085	0.0010	0.0033	0.0091
	50.8	2	0.0054	0.0086	0.0188	0.0029	0.0067	0.0195	0.0014	0.0057	0.0202
Clay Stiff	12.7	0.5	0.0026	0.0033	0.0038	0.0017	0.0026	0.0039	0.0009	0.0023	0.0041
	25.4	1	0.0050	0.0065	0.0083	0.0031	0.0049	0.0089	0.0017	0.0045	0.0091
	50.8	2	0.0090	0.0128	0.0193	0.0048	0.0100	0.0203	0.0027	0.0090	0.0217
Clay Medium	12.7	0.5	0.0026	0.0032	0.0038	0.0016	0.0026	0.0038	0.0009	0.0022	0.0041
	25.4	1	0.0049	0.0064	0.0084	0.0030	0.0051	0.0085	0.0016	0.0043	0.0092
	50.8	2	0.0086	0.0124	0.0197	0.0049	0.0100	0.0206	0.0025	0.0087	0.0219
Clay Soft	12.7	0.5	0.0025	0.0031	0.0038	0.0015	0.0024	0.0037	0.0008	0.0020	0.0039
	25.4	1	0.0046	0.0061	0.0084	0.0027	0.0048	0.0085	0.0014	0.0040	0.0091
	50.8	2	0.0077	0.0115	0.0199	0.0043	0.0091	0.0209	0.0022	0.0079	0.0221

Table 28: The recorded rotations in all CFRP cases-pushing against backfill.

Type of Soil	Δ_g Pushing against Backfill		Span Length								
			15.25 m (50 ft)			30.5 m (100 ft)			45.75 m (150 ft)		
CFRP	mm	in	rad			rad			rad		
			θ_A	θ_p	θ_{pi}	θ_A	θ_p	θ_{pi}	θ_A	θ_p	θ_{pi}
Sand Dense	12.7	0.5	-0.0019	-0.0022	-0.0026	-0.0012	-0.0016	-0.0025	-0.0007	-0.0013	-0.0024
	25.4	1	-0.0037	-0.0045	-0.0060	-0.0022	-0.0033	-0.0060	-0.0011	-0.0025	-0.0057
	50.8	2	-0.0064	-0.0088	-0.0156	-0.0034	-0.0066	-0.0162	-0.0015	-0.0052	-0.0163
Sand Medium	12.7	0.5	-0.0018	-0.0022	-0.0026	-0.0012	-0.0016	-0.0025	-0.0007	-0.0013	-0.0025
	25.4	1	-0.0036	-0.0044	-0.0063	-0.0021	-0.0032	-0.0060	-0.0011	-0.0025	-0.0060
	50.8	2	-0.0055	-0.0081	-0.0163	-0.0030	-0.0061	-0.0166	-0.0013	-0.0048	-0.0167
Sand Loose	12.7	0.5	-0.0018	-0.0021	-0.0026	-0.0012	-0.0016	-0.0026	-0.0006	-0.0013	-0.0025
	25.4	1	-0.0035	-0.0043	-0.0062	-0.0021	-0.0032	-0.0062	-0.0011	-0.0024	-0.0061
	50.8	2	-0.0055	-0.0081	-0.0163	-0.0028	-0.0058	-0.0168	-0.0012	-0.0046	-0.0168
Clay Stiff	12.7	0.5	-0.0022	-0.0025	-0.0026	-0.0014	-0.0019	-0.0024	-0.0008	-0.0015	-0.0023
	25.4	1	-0.0047	-0.0055	-0.0060	-0.0028	-0.0040	-0.0056	-0.0015	-0.0030	-0.0053
	50.8	2	-0.0089	-0.0113	-0.0150	-0.0089	-0.0113	-0.0150	-0.0024	-0.0070	-0.0164
Clay Medium	12.7	0.5	-0.0021	-0.0024	-0.0026	-0.0013	-0.0018	-0.0024	-0.0007	-0.0015	-0.0024
	25.4	1	-0.0047	-0.0054	-0.0061	-0.0027	-0.0039	-0.0057	-0.0014	-0.0030	-0.0056
	50.8	2	-0.0084	-0.0110	-0.0156	-0.0047	-0.0083	-0.0164	-0.0022	-0.0068	-0.0171
Clay Soft	12.7	0.5	-0.0020	-0.0024	-0.0026	-0.0013	-0.0018	-0.0024	-0.0007	-0.0014	-0.0024
	25.4	1	-0.0043	-0.0051	-0.0060	-0.0025	-0.0037	-0.0057	-0.0013	-0.0028	-0.0056
	50.8	2	-0.0075	-0.0101	-0.0158	-0.0041	-0.0076	-0.0165	-0.0019	-0.0061	-0.0170

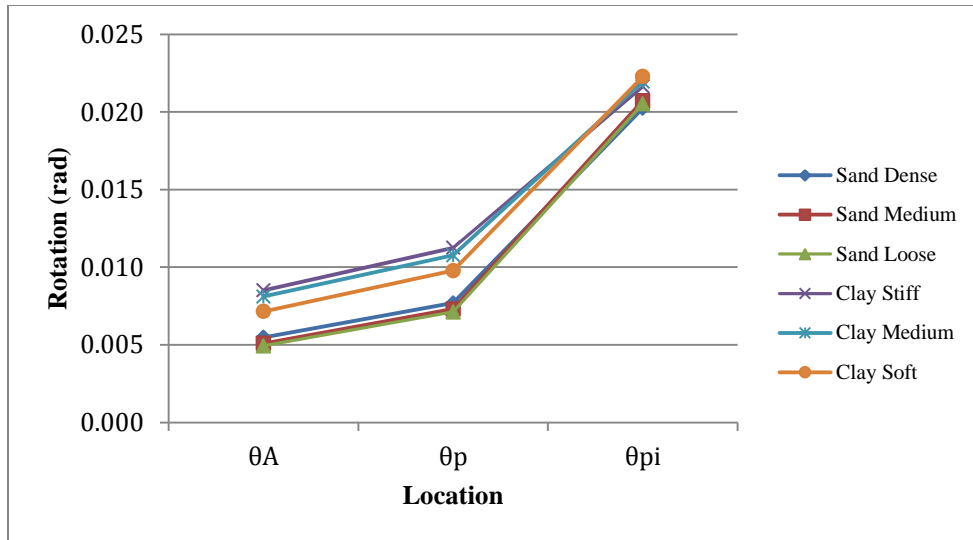


Figure 58: The rotations at the abutment (θ_A), pile (θ_p), and POI (θ_{pi}) for: control, short span, pulling away from backfill, +50.8 mm (+2 in) cases.

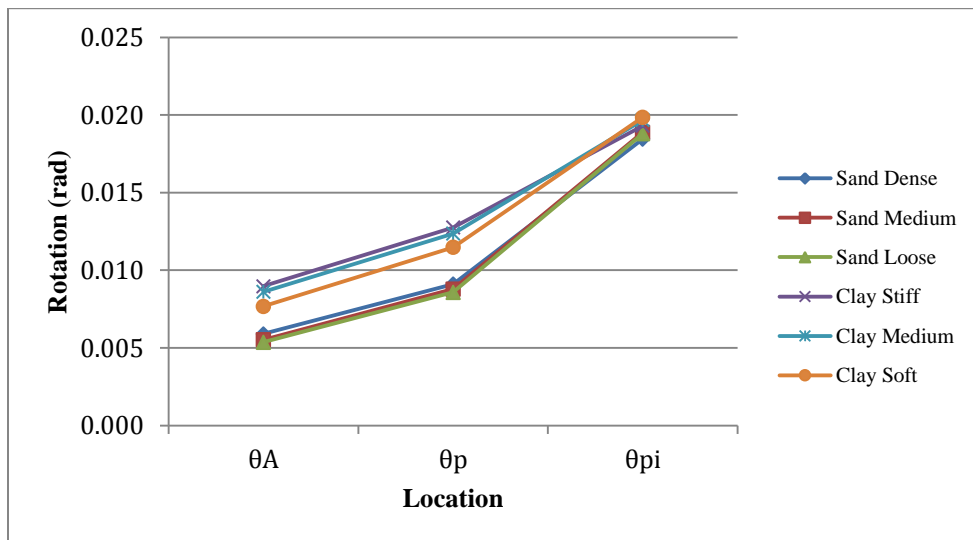


Figure 59: The rotations at the abutment (θ_A), pile (θ_p), and POI (θ_{pi}) for: CFRP, short span, pulling away from backfill, +50.8 mm (+2 in) cases.

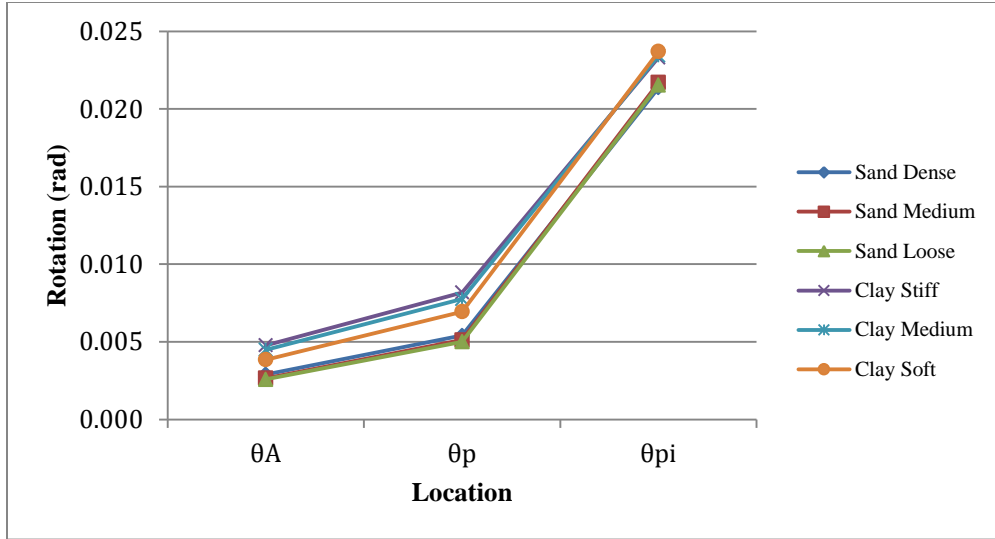


Figure 60: The rotations at the abutment (θ_A), pile (θ_p), and POI (θ_{pi}) for: control, medium span, pulling away from backfill, +50.8 mm (+2 in) cases.

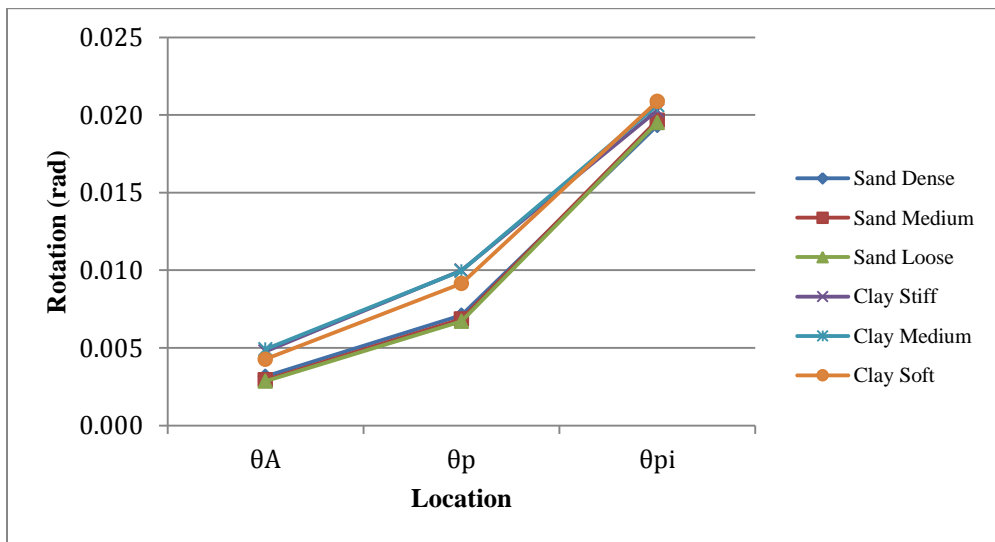


Figure 61: The rotations at the abutment (θ_A), pile (θ_p), and POI (θ_{pi}) for: CFRP, medium span, pulling away from backfill, +50.8 mm (+2 in) cases.

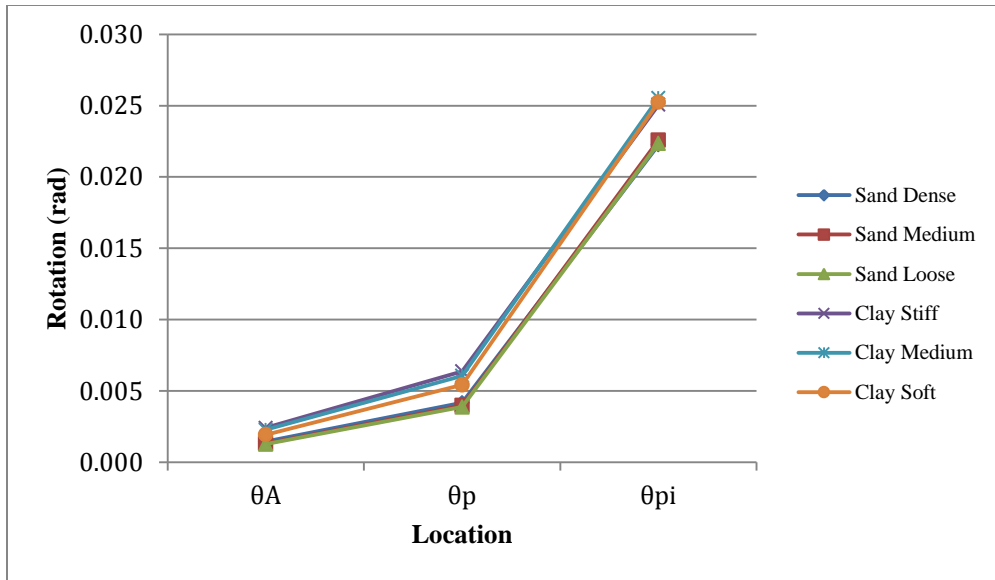


Figure 62: The rotations at the abutment (θ_A), pile (θ_p), and POI (θ_{pi}) for: control, long span, pulling away from backfill, +50.8 mm (+2 in) cases.

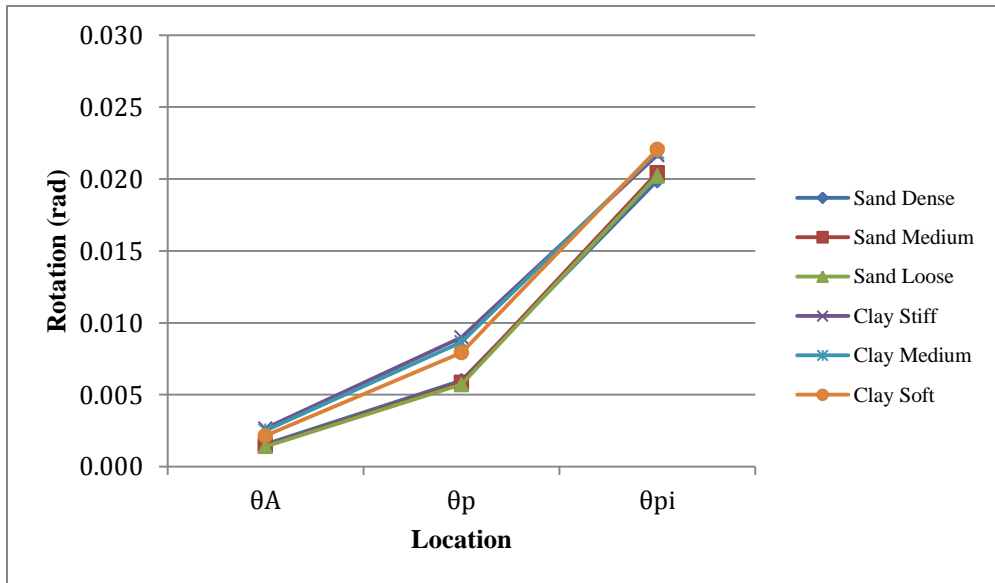


Figure 63: The rotations at the abutment (θ_A), pile (θ_p), and POI (θ_{pi}) for: CFRP, long span, pulling away from backfill, +50.8 mm (+2 in) cases.

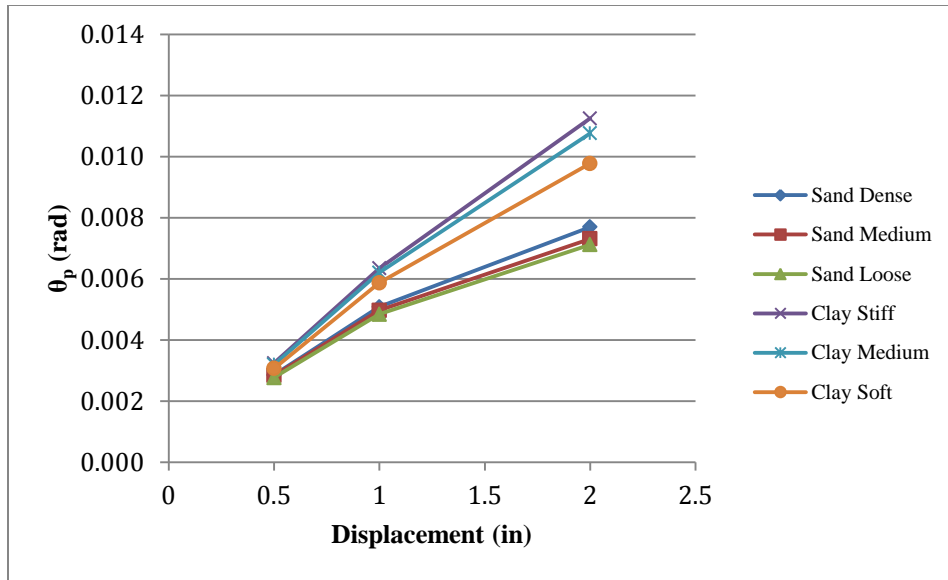


Figure 64: θ_p vs. Δ_g for: control, pulling away from backfill, short span.

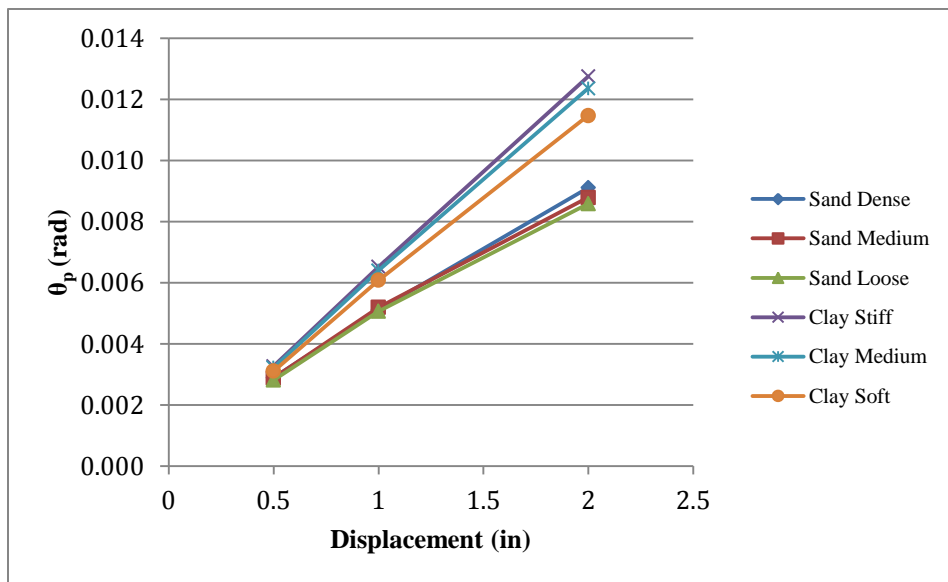


Figure 65: θ_p vs. Δ_g for: CFRP, pulling away from backfill, short span.

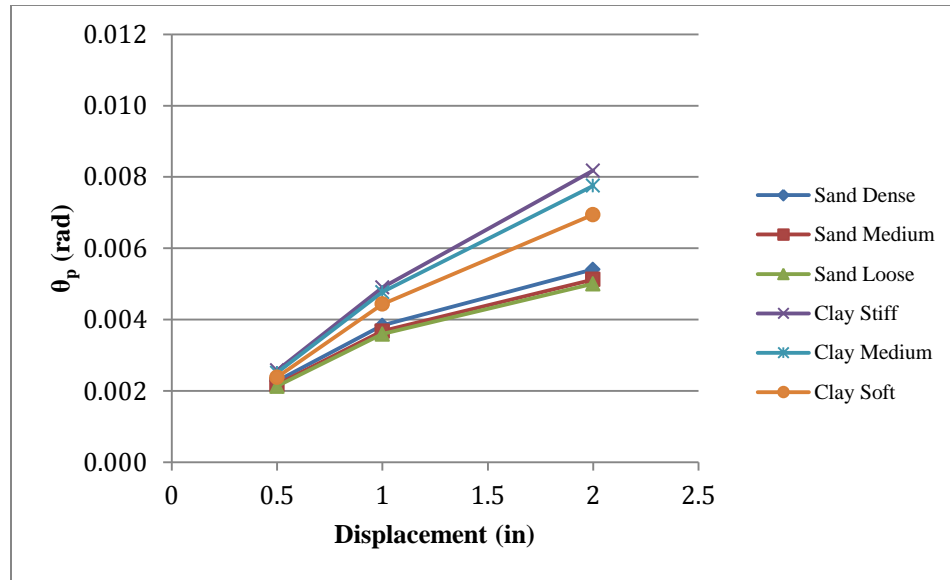


Figure 66: θ_p vs. Δ_g for: control, pulling away from backfill, medium span.

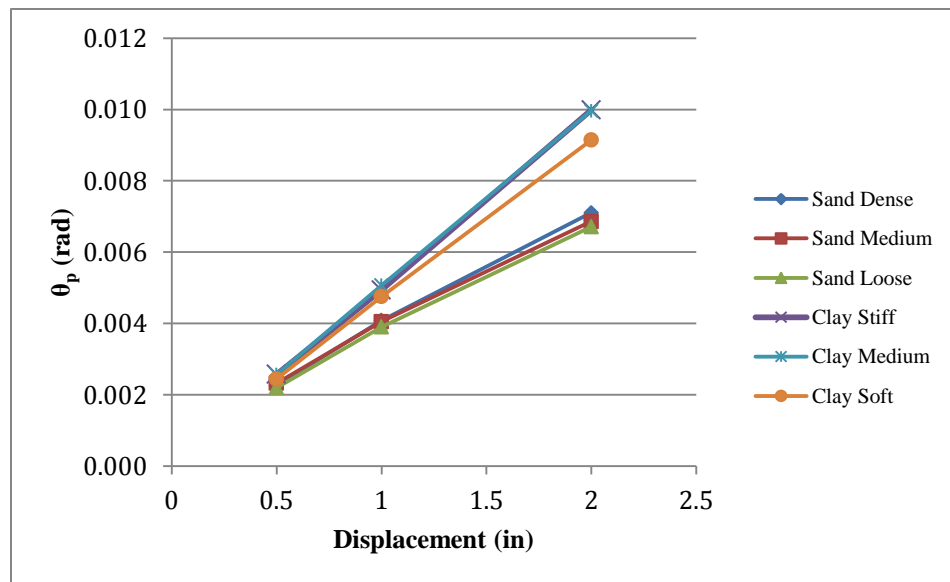


Figure 67: θ_p vs. Δ_g for: CFRP, pulling away from backfill, medium span.

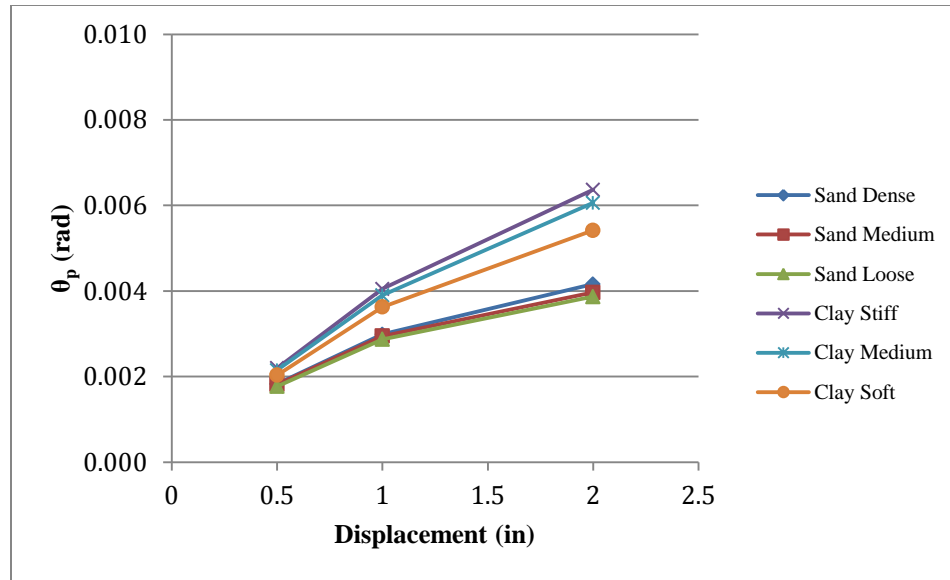


Figure 68: θ_p vs. Δ_g for: control, pulling away from backfill, long span.

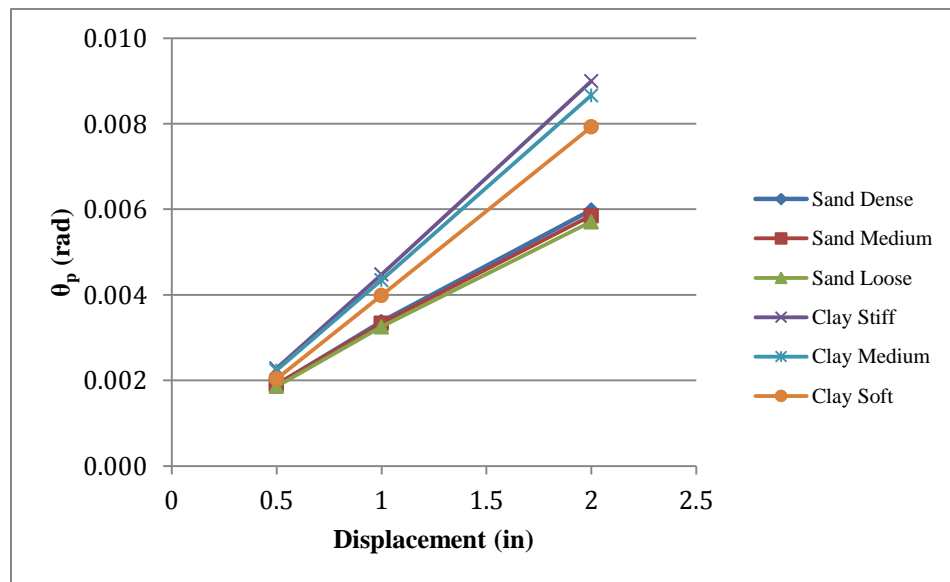


Figure 69: θ_p vs. Δ_g for: CFRP, pulling away from backfill, long span.

4.1.5.2 Displacements

The pile displacement results clearly indicate that the displacement at the pile-abutment interface (Δ_p) is lower than the imposed displacement at the natural axis of the girder (Δ_g) due mainly to the abutment rotation (θ_A). Therefore, the abutment in higher rotational stiffness models allows the pile to displace more. For example, in medium sand, the pile displacement was 39.6 mm (1.56 in) for a short span model compared to a pile displacement of 42.66 mm (1.68 in) for a long span model. The pile displacements of all cases that were studied are presented in Tables 29 through 32. Figure 70 shows the deflection along the depth for one of the study cases. Also, appendix B includes the displacement results for all cases studied along with the other results studied.

Moreover, it was evident that the pile displacements were lower when the pile was embedded in clays compared to when they were embedded in any of the sands. In the control model with $\Delta_g = 50.8$ mm (2 in), the highest Δ_p reported was 42.71 mm (1.68 in) in loose sand, while the lowest Δ_p was noted for a pile in stiff clay (36.79 mm or 1.45 in). That is roughly a 16% difference between the two types of soil. On the other hand, CFRP piles had slightly lower displacements compared to unconfined piles as a result of differences in rotation at the pile-abutment interface.

Table 29: Δ_p of all cases (control, pulling away from backfill).

Type Of Soil	Δ_g Pulling away from Backfill		Girder Length					
			m	ft	m	ft	m	ft
Control			15.25	50	30.5	100	45.75	150
	mm	in	mm	in	mm	in	mm	in
Sand Dense	12.7	0.5	7.62	0.30	7.99	0.31	8.46	0.33
	25.4	1	16.98	0.67	17.86	0.70	18.85	0.74
	50.8	2	39.34	1.55	40.90	1.61	42.13	1.66
Sand Medium	12.7	0.5	7.61	0.30	8.09	0.32	8.56	0.34
	25.4	1	17.09	0.67	18.22	0.72	19.09	0.75
	50.8	2	39.60	1.56	41.56	1.64	42.66	1.68
Sand Loose	12.7	0.5	7.70	0.30	8.16	0.32	8.60	0.34
	25.4	1	17.27	0.68	18.34	0.72	19.23	0.76
	50.8	2	39.84	1.57	41.69	1.64	42.71	1.68
Clay Stiff	12.7	0.5	6.83	0.27	7.02	0.28	7.41	0.29
	25.4	1	14.52	0.57	15.12	0.60	16.06	0.63
	50.8	2	32.85	1.29	34.84	1.37	36.79	1.45
Clay Medium	12.7	0.5	6.79	0.27	7.10	0.28	7.47	0.29
	25.4	1	14.47	0.57	15.36	0.60	16.33	0.64
	50.8	2	32.96	1.30	35.47	1.40	37.15	1.46
Clay Soft	12.7	0.5	7.03	0.28	7.35	0.29	7.72	0.30
	25.4	1	15.13	0.60	16.04	0.63	16.91	0.67
	50.8	2	34.99	1.38	37.34	1.47	38.85	1.53

Table 30: Δ_p of all cases (control, pushing against backfill).

Type Of Soil	Δ_g Pushing against Backfill		Girder Length					
			m	ft	m	ft	m	ft
Control			15.25	50	30.5	100	45.75	150
	mm	in	mm	in	mm	in	mm	in
Sand Dense	12.7	0.5	-8.14	-0.32	-8.16	-0.32	-8.16	-0.32
	25.4	1	-16.88	-0.66	-17.26	-0.68	-17.71	-0.70
	50.8	2	-36.85	-1.45	-39.02	-1.54	-40.40	-1.59
Sand Medium	12.7	0.5	-8.13	-0.32	-8.35	-0.33	-8.39	-0.33
	25.4	1	-16.83	-0.66	-17.41	-0.69	-18.31	-0.72
	50.8	2	-38.53	-1.52	-40.30	-1.59	-41.40	-1.63
Sand Loose	12.7	0.5	-8.19	-0.32	-8.35	-0.33	-8.51	-0.34
	25.4	1	-17.15	-0.68	-17.77	-0.70	-18.06	-0.71
	50.8	2	-39.20	-1.54	-41.30	-1.63	-41.97	-1.65
Clay Stiff	12.7	0.5	-7.43	-0.29	-7.67	-0.30	-7.75	-0.31
	25.4	1	-14.64	-0.58	-15.45	-0.61	-15.72	-0.62
	50.8	2	-31.06	-1.22	-34.44	-1.36	-36.47	-1.44
Clay Medium	12.7	0.5	-7.51	-0.30	-7.83	-0.31	-7.87	-0.31
	25.4	1	-14.82	-0.58	-15.67	-0.62	-15.96	-0.63
	50.8	2	-32.04	-1.26	-35.48	-1.40	-37.26	-1.47
Clay Soft	12.7	0.5	-7.93	-0.31	-8.16	-0.32	-8.20	-0.32
	25.4	1	-15.27	-0.60	-16.68	-0.66	-16.76	-0.66
	50.8	2	-34.00	-1.34	-37.25	-1.47	-38.86	-1.53

Table 31: Δ_p of all cases (CFRP, pulling away from backfill).

Type Of Soil	Δ_g Pulling away from Backfill		Girder Length					
			m	ft	m	ft	m	ft
CFRP			15.25	50	30.50	100	45.75	150
	mm	in	mm	in	mm	in	mm	in
Sand Dense	12.7	0.5	7.64	0.30	7.26	0.29	8.44	0.33
	25.4	1	16.92	0.67	17.74	0.70	18.62	0.73
	50.8	2	38.61	1.52	40.15	1.58	41.48	1.63
Sand Medium	12.7	0.5	7.59	0.30	8.06	0.32	8.52	0.34
	25.4	1	16.97	0.67	18.07	0.71	18.93	0.75
	50.8	2	38.81	1.53	40.86	1.61	42.09	1.66
Sand Loose	12.7	0.5	7.68	0.30	8.13	0.32	8.57	0.34
	25.4	1	17.15	0.68	18.19	0.72	19.00	0.75
	50.8	2	39.07	1.54	41.00	1.61	42.14	1.66
Clay Stiff	12.7	0.5	6.68	0.26	6.99	0.28	7.38	0.29
	25.4	1	14.13	0.56	14.98	0.59	15.88	0.63
	50.8	2	31.32	1.23	33.75	1.33	35.72	1.41
Clay Medium	12.7	0.5	6.77	0.27	7.08	0.28	7.45	0.29
	25.4	1	14.38	0.57	15.21	0.60	16.06	0.63
	50.8	2	32.05	1.26	34.37	1.35	36.19	1.42
Clay Soft	12.7	0.5	7.01	0.28	7.32	0.29	7.68	0.30
	25.4	1	15.03	0.59	15.88	0.63	16.71	0.66
	50.8	2	34.02	1.34	36.28	1.43	37.91	1.49

Table 32: Δ_p of all cases (CFRP, pushing against backfill).

Type Of Soil	Δ_g Pushing against Backfill		Girder Length					
			m	ft	m	ft	m	ft
CFRP			15.25	50	30.50	100	45.75	150
	mm	in	mm	in	mm	in	mm	in
Sand Dense	12.7	0.5	-8.07	-0.32	-8.08	-0.32	-8.05	-0.32
	25.4	1	-16.47	-0.65	-17.24	-0.68	-17.24	-0.68
	50.8	2	-35.81	-1.41	-38.27	-1.51	-39.50	-1.56
Sand Medium	12.7	0.5	-8.00	-0.32	-8.17	-0.32	-8.23	-0.32
	25.4	1	-16.88	-0.66	-17.34	-0.68	-17.79	-0.70
	50.8	2	-37.76	-1.49	-39.50	-1.55	-40.62	-1.60
Sand Loose	12.7	0.5	-8.22	-0.32	-8.42	-0.33	-8.42	-0.33
	25.4	1	-17.02	-0.67	-17.69	-0.70	-17.69	-0.70
	50.8	2	-37.76	-1.49	-40.31	-1.59	-41.17	-1.62
Clay Stiff	12.7	0.5	-7.43	-0.29	-7.70	-0.30	-7.74	-0.30
	25.4	1	-14.59	-0.57	-15.38	-0.61	-15.63	-0.62
	50.8	2	-30.57	-1.20	-33.79	-1.33	-35.63	-1.40
Clay Medium	12.7	0.5	-7.48	-0.29	-7.70	-0.30	-7.86	-0.31
	25.4	1	-14.75	-0.58	-15.59	-0.61	-16.00	-0.63
	50.8	2	-31.43	-1.24	-34.66	-1.36	-36.39	-1.43
Clay Soft	12.7	0.5	-7.79	-0.31	-8.15	-0.32	-8.18	-0.32
	25.4	1	-15.31	-0.60	-16.54	-0.65	-16.67	-0.66
	50.8	2	-33.39	-1.31	-36.48	-1.44	-37.98	-1.50

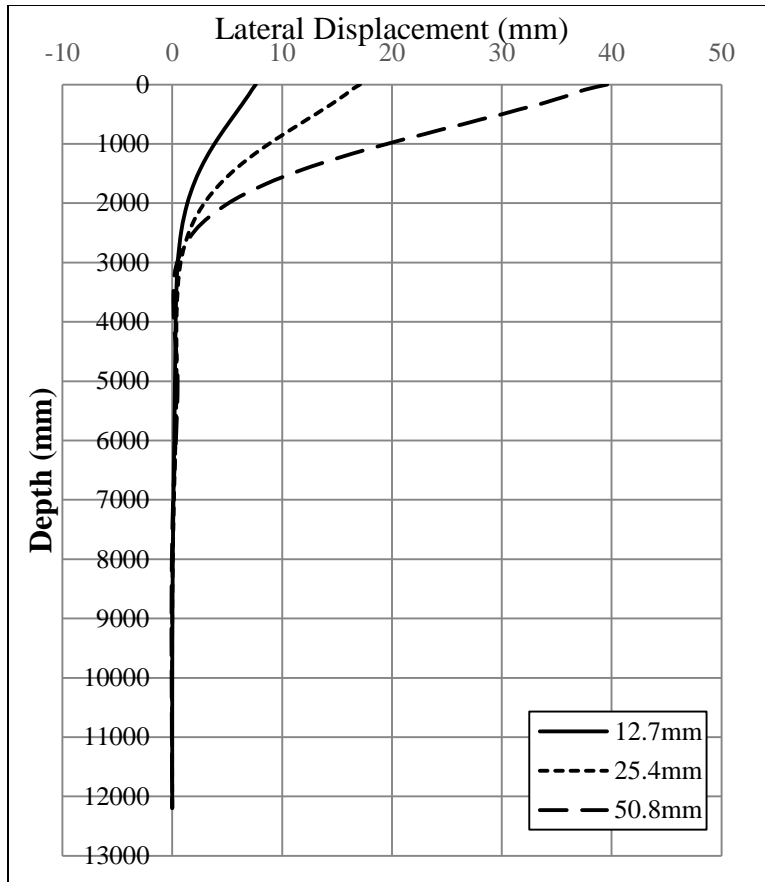


Figure 70: Deflection along the pile in control, medium sand, short span.

4.1.5.3 Curvature

Based on the results of the general model, the curvature along the length of the pile for all cases was evaluated. Knowing the measured strains for any two nodes on the pile at same depth along the Z-direction (Figure 71), the curvature could be calculated at that specific depth based on the assumption of linearity of strain (plane sections remain plane). Figure 72 shows the measured curvature along the pile for one model (medium sand, short span, pulling away from the backfill, without CFRP) for all three ranges of displacement. It is clear that the curvature demand increases as the displacement increases. The highest curvature demand corresponded to a 50.8 mm (2 in) and a 45.75 m (150 ft) long span (i.e. high rotational stiffness). However, the application of CFRP

reduced the curvature demand by almost 40% in all cases as shown in Figure 73.

Appendix B shows all curvature for all studied cases.

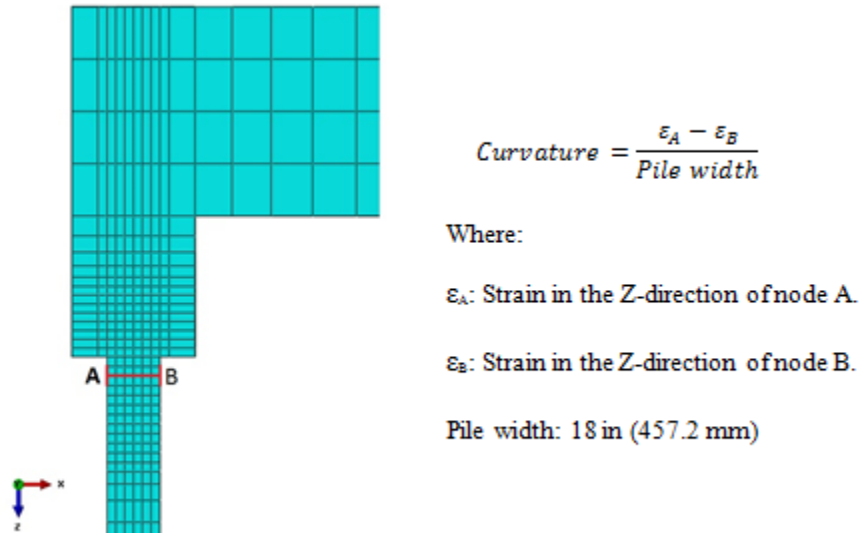


Figure 71: Calculation of curvature along the pile.

As shown in Figure 74 and Figure 75, the curvature demand in piles embedded in clay are higher than those embedded in sand. The highest curvature demand for a 50.8 mm (2 in) girder displacement was -5.8×10^{-5} /mm (0.00147/in) for both stiff and medium clays for a long span model without CFRP while pulling away from the backfill (Figure 76). The lowest curvature, for the same displacement range, was approximately 1.45×10^{-5} /mm (0.00037/in) in dense sand for a short span with CFRP confinement when pushing into the backfill (Figure 77). These curvatures are within the target curvature range of 0.0002 to 0.00152/in (7.87×10^{-6} to 5.98×10^{-5} /mm) for piles from literature review section (2.2.8) (Fanous, et al. 2010).

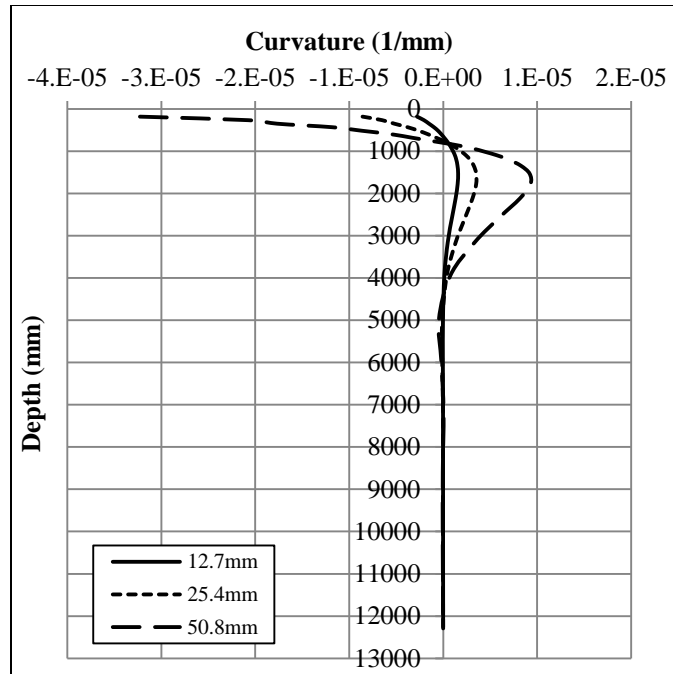


Figure 72: Curvature demand along the pile for: control, medium sand, short span, pulling away from backfill.

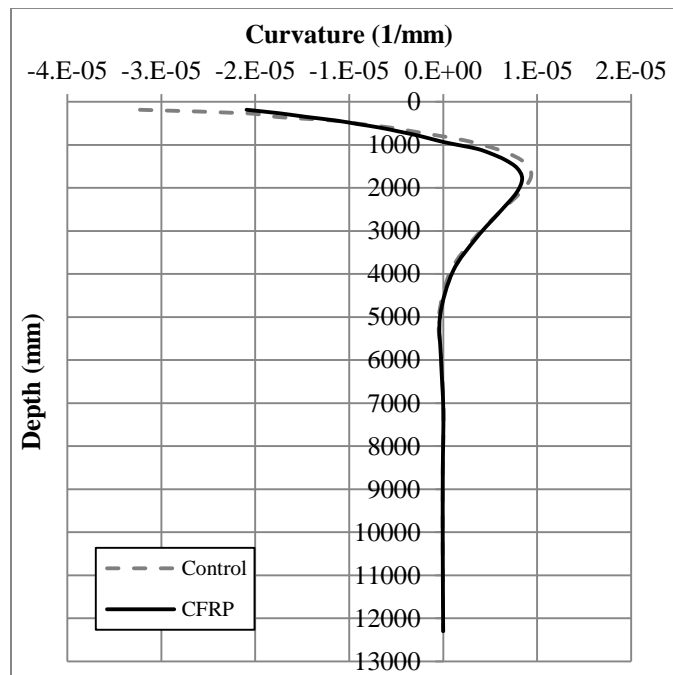


Figure 73: Curvature demand along the pile for: control vs. CFRP, medium sand, short span, pulling away from backfill.

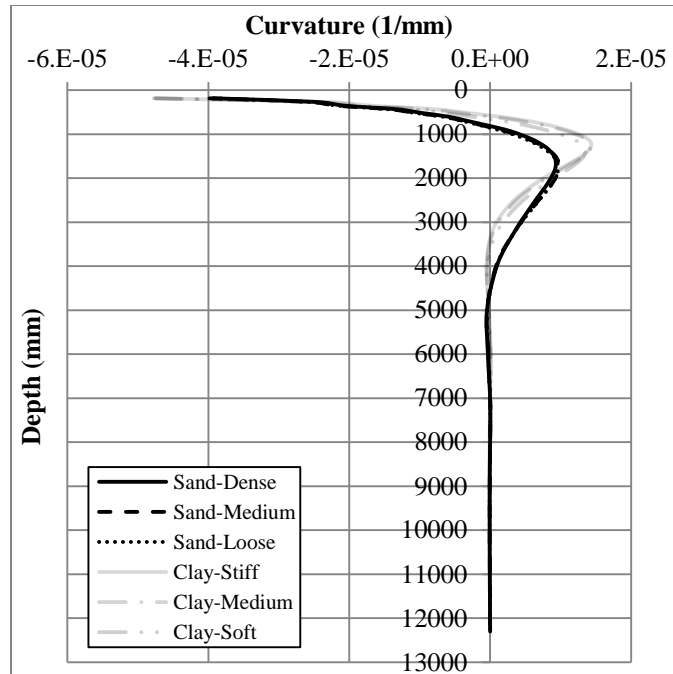


Figure 74: Curvature demand along the pile for all types of, medium span, pulling away from backfill, $\Delta_g = +50.8 \text{ mm (+ 2in)}$.

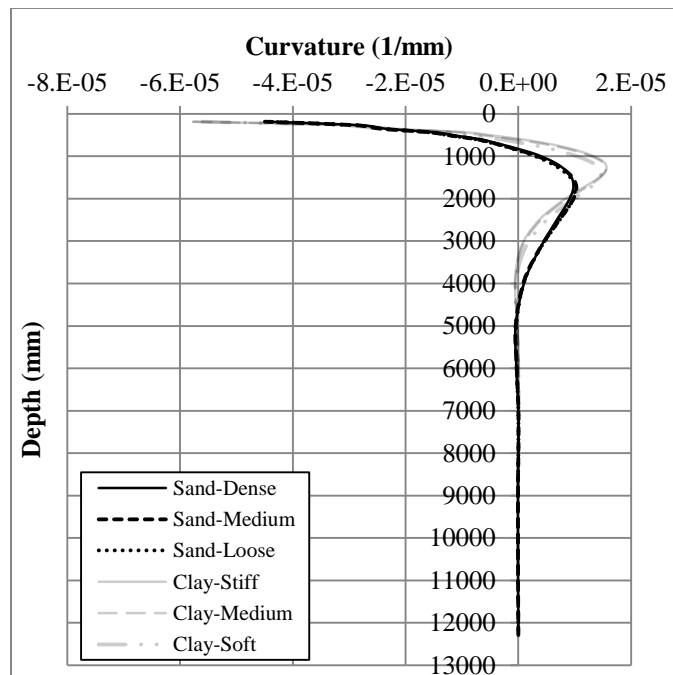


Figure 75: Curvature demand along the pile for all types of, long span, pulling away from backfill, $\Delta_g = +50.8 \text{ mm (+2 in)}$.

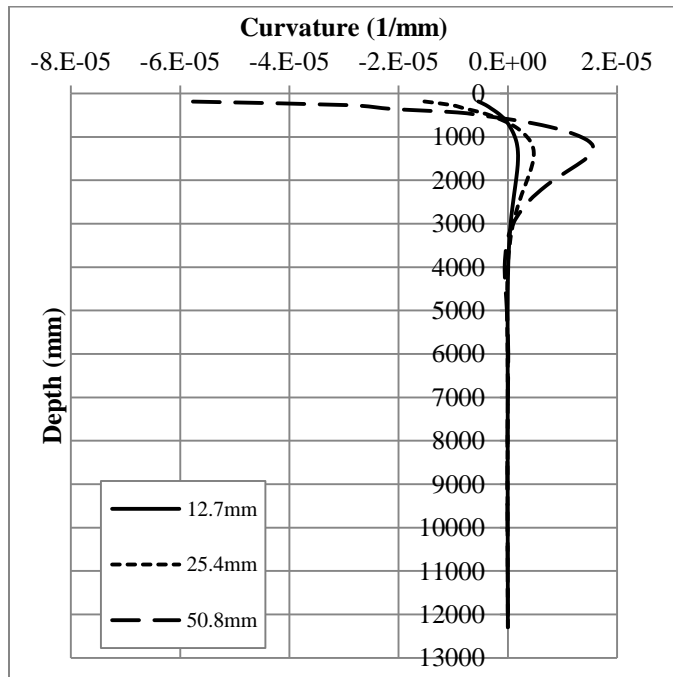


Figure 76: Curvature demand for: control (no CFRP), stiff clay, long span, pulling away from backfill.

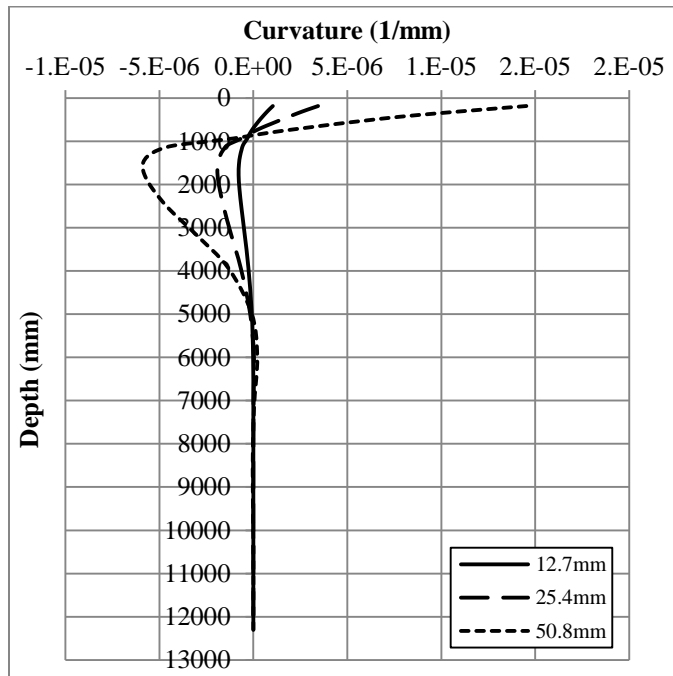


Figure 77: Curvature demand for: CFRP, sand dense, short span, pulling away from backfill.

4.1.5.4 Point of Inflection POI

An important objective of the general model was to locate the depth to POI (L_{pi}) for subsequent use in the localized model. POI is located at the point of zero curvature. The results show different L_{pi} values in different cases, all of which are listed in Tables 33 to 36. In some higher displacement cases, L_{pi} decreased slightly due to the increased rotation at the pile-abutment interface θ_p . In other words, with the increase in rotation, the POI moves slightly higher (L_{pi} decreases) as shown in Figure 78 (for dense sand, long span, pulling away from backfill, without CFRP). However, L_{pi} increases with the use of CFRP as shown in Figure 79. The results show shorter L_{pi} in clay models due to higher pile-abutment interface rotation θ_p (discussed in the previous section). The curvature plots for all the cases studied are presented Appendix B. All L_{pi} values are used to generate the localized models. However, the two L_{pi} values in each cycle (positive and negative displacement) were slightly different from each other. Therefore, the two values were averaged for use in the localized model.

Table 33: L_{pi} for the control cases (pulling away from backfill)

Type Of Soil	Δ_g Pulling away from Backfill		Girder Length					
			m	ft	m	ft	m	ft
Control			15.25	50	30.5	100	45.75	150
	mm	in	mm	in	mm	in	mm	in
Sand-Dense	12.7	0.5	632.21	24.89	788.21	31.03	868.06	34.18
	25.4	1	721.87	28.42	830.95	32.71	879.76	34.64
	50.8	2	774.48	30.49	816.07	32.13	827.80	32.59
Sand-Medium	12.7	0.5	653.31	25.72	805.09	31.70	882.27	34.74
	25.4	1	754.51	29.71	860.02	33.86	904.49	35.61
	50.8	2	804.51	31.67	843.23	33.20	851.74	33.53
Sand-Loose	12.7	0.5	675.55	26.60	822.30	32.37	901.54	35.49
	25.4	1	776.31	30.56	877.05	34.53	922.40	36.32
	50.8	2	820.01	32.28	856.44	33.72	866.20	34.10
Clay-Stiff	12.7	0.5	467.98	18.42	606.97	23.90	688.87	27.12
	25.4	1	512.01	20.16	621.33	24.46	674.07	26.54
	50.8	2	533.87	21.02	577.58	22.74	589.64	23.21
Clay-Medium	12.7	0.5	488.42	19.23	633.26	24.93	708.24	27.88
	25.4	1	535.30	21.07	645.48	25.41	694.10	27.33
	50.8	2	556.79	21.92	601.53	23.68	614.00	24.17
Clay-Soft	12.7	0.5	531.07	20.91	679.50	26.75	754.37	29.70
	25.4	1	586.01	23.07	699.09	27.52	745.98	29.37
	50.8	2	614.66	24.20	661.60	26.05	672.31	26.47

Table 34: L_{pi} for the control cases (pushing against backfill)

Type Of Soil	Δ_g Pushing against Backfill		Girder Length					
			m	ft	m	ft	m	ft
Control			15.25	50	30.5	100	45.75	150
	mm	in	mm	in	mm	in	mm	in
Sand-Dense	12.7	0.5	702.77	27.67	868.20	34.18	985.65	38.81
	25.4	1	765.60	30.14	893.95	35.19	1013.30	39.89
	50.8	2	773.29	30.44	814.81	32.08	866.44	34.11
Sand-Medium	12.7	0.5	707.12	27.84	890.71	35.07	980.04	38.58
	25.4	1	776.38	30.57	922.52	36.32	1010.62	39.79
	50.8	2	830.62	32.70	882.21	34.73	917.42	36.12
Sand-Loose	12.7	0.5	740.47	29.15	909.68	35.81	1002.23	39.46
	25.4	1	811.64	31.95	945.54	37.23	1034.01	40.71
	50.8	2	857.57	33.76	915.51	36.04	939.26	36.98
Clay-Stiff	12.7	0.5	394.59	15.54	611.77	24.09	729.92	28.74
	25.4	1	427.79	16.84	610.86	24.05	712.25	28.04
	50.8	2	537.86	21.18	629.72	24.79	663.13	26.11
Clay-Medium	12.7	0.5	438.99	17.28	658.62	25.93	757.29	29.81
	25.4	1	469.92	18.50	655.31	25.80	739.45	29.11
	50.8	2	571.86	22.51	656.72	25.86	683.19	26.90
Clay-Soft	12.7	0.5	497.30	19.58	717.96	28.27	813.40	32.02
	25.4	1	531.42	20.92	718.58	28.29	796.38	31.35
	50.8	2	638.94	25.15	717.92	28.26	741.58	29.20

Table 35: L_{pi} for the CFRP cases (pulling away from backfill)

Type Of Soil	Δ_g Pulling away from Backfill		Girder Length					
			m	ft	m	ft	m	ft
CFRP			15.25	50.00	30.50	100.00	45.75	150.00
	mm	in	mm	in	mm	in	mm	in
Sand-Dense	12.7	0.5	641.35	25.25	807.33	31.78	909.67	35.81
	25.4	1	746.73	29.40	883.51	34.78	951.31	37.45
	50.8	2	896.65	35.30	966.84	38.06	1003.22	39.50
Sand-Medium	12.7	0.5	662.66	26.09	832.25	32.77	916.34	36.08
	25.4	1	791.10	31.15	917.88	36.14	971.60	38.25
	50.8	2	930.84	36.65	994.02	39.13	1026.67	40.42
Sand-Loose	12.7	0.5	685.84	27.00	844.73	33.26	936.00	36.85
	25.4	1	813.76	32.04	933.62	36.76	990.31	38.99
	50.8	2	944.59	37.19	1009.29	39.74	1042.47	41.04
Clay-Stiff	12.7	0.5	471.12	18.55	606.97	23.90	716.24	28.20
	25.4	1	525.85	20.70	621.33	24.46	725.22	28.55
	50.8	2	595.23	23.43	577.58	22.74	721.30	28.40
Clay-Medium	12.7	0.5	491.60	19.35	650.20	25.60	735.17	28.94
	25.4	1	551.55	21.71	680.63	26.80	745.95	29.37
	50.8	2	629.03	24.77	716.28	28.20	750.89	29.56
Clay-Soft	12.7	0.5	536.69	21.13	699.79	27.55	782.12	30.79
	25.4	1	607.22	23.91	740.75	29.16	802.13	31.58
	50.8	2	704.87	27.75	787.10	30.99	821.50	32.34

Table 36: L_{pi} for the CFRP cases (pushing against backfill)

Type Of Soil	Δ_g Pushing against Backfill		Girder Length					
			m	ft	m	ft	m	ft
CFRP			15.25	50.00	30.50	100.00	45.75	150.00
	mm	in	mm	in	mm	in	mm	in
Sand-Dense	12.7	0.5	694.06	27.33	903.20	35.56	1001.15	39.42
	25.4	1	778.35	30.64	956.84	37.67	1064.88	41.92
	50.8	2	857.71	33.77	952.43	37.50	1005.92	39.60
Sand-Medium	12.7	0.5	718.55	28.29	914.05	35.99	1006.40	39.62
	25.4	1	818.99	32.24	975.11	38.39	1072.46	42.22
	50.8	2	938.44	36.95	1018.61	40.10	1072.43	42.22
Sand-Loose	12.7	0.5	742.91	29.25	927.16	36.50	1020.44	40.17
	25.4	1	845.13	33.27	989.07	38.94	1084.93	42.71
	50.8	2	938.44	36.95	1044.89	41.14	1089.25	42.88
Clay-Stiff	12.7	0.5	391.50	15.41	627.75	24.71	754.58	29.71
	25.4	1	430.67	16.96	635.84	25.03	750.68	29.55
	50.8	2	577.19	22.72	706.61	27.82	763.01	30.04
Clay-Medium	12.7	0.5	439.03	17.28	675.77	26.61	785.55	30.93
	25.4	1	474.51	18.68	683.60	26.91	781.82	30.78
	50.8	2	622.20	24.50	745.40	29.35	792.43	31.20
Clay-Soft	12.7	0.5	499.69	19.67	739.29	29.11	842.17	33.16
	25.4	1	544.96	21.46	753.91	29.68	842.86	33.18
	50.8	2	706.72	27.82	820.38	32.30	863.58	34.00

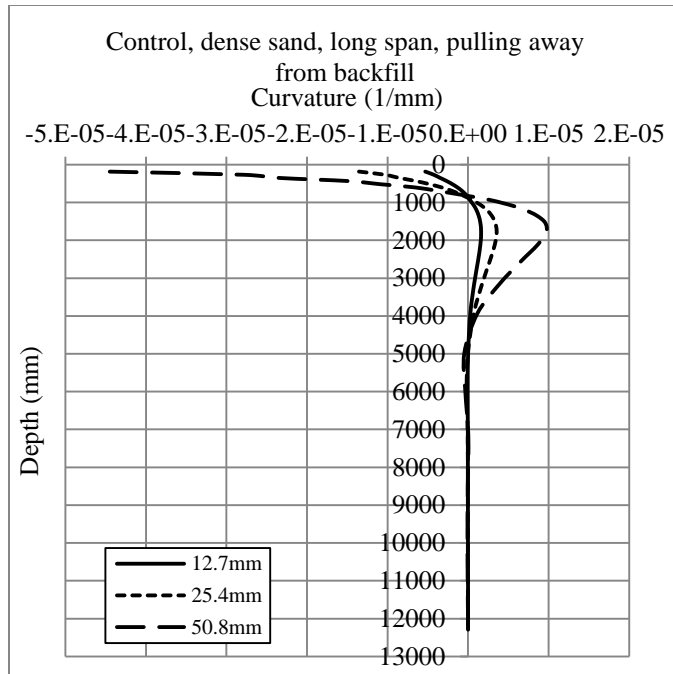


Figure 78: The curvature along the pile showing (L_{pi}) decreased at 50.8mm (2in) displacement in control model.

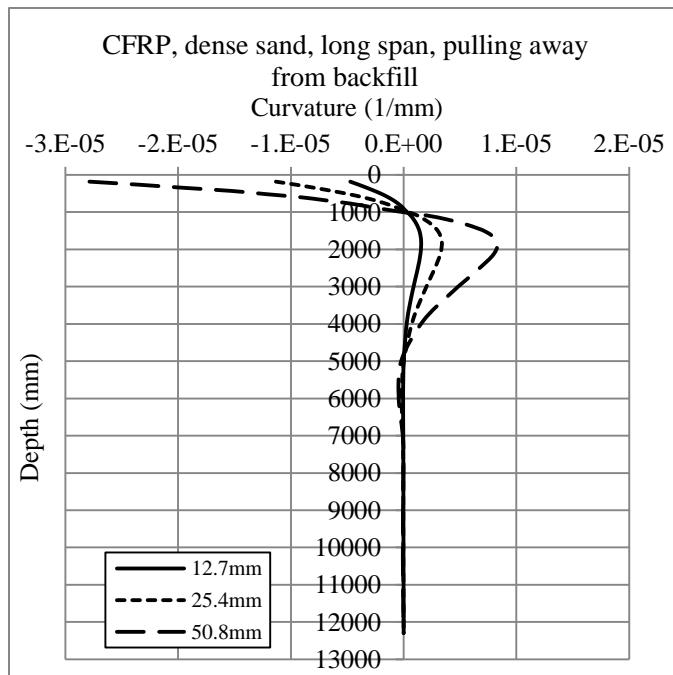


Figure 79: The curvature along the pile showing (L_{pi}) increased at 50.8mm (2in) displacement with the use of CFRP.

4.2 Localized Model

Following the completion of studies on the general model, a set of 3-dimensional localized models were created. These models incorporated a pile cap along with a length of pile that extended to the POI determined from the general models. The soil was not modelled. The curvature response between the POI and the pile cap was essentially linear based on the results from the general model. Therefore, a transverse force at the POI can represent the curvature response without the need for incorporating the soil in the localized model. As shown in Figure 80, the pile cap was fixed along its perimeter surfaces except the face that received the pile. The transverse displacement that was applied at POI was determined from the deformations obtained in the general models. The parameters needed from the general model were the depth to the point of inflection (L_{pi}) and the relative displacement between pile and POI ($\Delta_m = \Delta_p - \Delta_{pi}$). Tables 37 through 40 show the displacement at POI (Δ_{pi}) for all studied cases. The values of Δ_m are given in section 4.2.1.

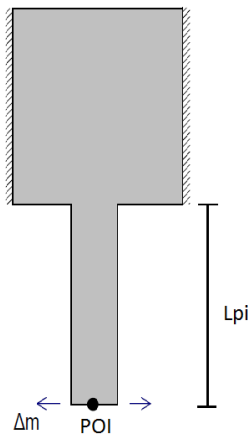


Figure 80: A schematic of the localized model showing the pile to the POI and the pile's cap.

Table 37: Δ_{pi} for the control cases (pulling away from backfill)

Type of Soil	Δ_g Pulling away from Backfill		Span Length					
			m	ft	m	ft	m	ft
Control			15.25	50	30.5	100	45.75	150
	mm	in	mm	in	mm	in	mm	in
Sand-Dense	12.7	0.5	5.72	0.23	5.59	0.22	5.78	0.23
	25.4	1	12.20	0.48	12.57	0.49	12.77	0.50
	50.8	2	26.09	1.03	27.51	1.08	28.48	1.12
Sand-Medium	12.7	0.5	5.72	0.23	5.69	0.22	5.85	0.23
	25.4	1	12.32	0.49	12.15	0.48	12.99	0.51
	50.8	2	26.44	1.04	28.28	1.11	27.21	1.07
Sand-Loose	12.7	0.5	5.84	0.23	5.79	0.23	5.93	0.23
	25.4	1	11.86	0.47	12.35	0.49	13.20	0.52
	50.8	2	26.87	1.06	26.76	1.05	27.53	1.08
Clay-Stiff	12.7	0.5	5.50	0.22	5.15	0.20	5.23	0.21
	25.4	1	11.48	0.45	10.73	0.42	11.57	0.46
	50.8	2	22.70	0.89	24.07	0.95	25.27	0.99
Clay-Medium	12.7	0.5	5.45	0.21	5.22	0.21	5.28	0.21
	25.4	1	10.65	0.42	10.94	0.43	10.97	0.43
	50.8	2	22.78	0.90	22.88	0.90	23.84	0.94
Clay-Soft	12.7	0.5	5.38	0.21	5.49	0.22	5.55	0.22
	25.4	1	11.39	0.45	10.92	0.43	11.68	0.46
	50.8	2	23.30	0.92	25.14	0.99	26.10	1.03

Table 38: Δ_{pi} for the control cases (pushing against backfill)

Type of Soil	Δ_g Pushing against Backfill		Span Length					
			m	ft	m	ft	m	ft
Control			15.25	50	30.5	100	45.75	150
	mm	in	mm	in	mm	in	mm	in
Sand-Dense	12.70	0.50	-6.65	-0.26	-6.37	-0.25	-6.15	-0.24
	25.40	1.00	-12.95	-0.51	-13.02	-0.51	-13.36	-0.53
	50.80	2.00	-26.36	-1.04	-27.94	-1.10	-28.12	-1.11
Sand-Medium	12.70	0.50	-6.61	-0.26	-6.55	-0.26	-6.47	-0.25
	25.40	1.00	-12.80	-0.50	-13.22	-0.52	-13.65	-0.54
	50.80	2.00	-27.86	-1.10	-28.12	-1.11	-29.27	-1.15
Sand-Loose	12.70	0.50	-6.72	-0.26	-6.60	-0.26	-6.64	-0.26
	25.40	1.00	-13.21	-0.52	-13.08	-0.51	-13.11	-0.52
	50.80	2.00	-27.24	-1.07	-29.27	-1.15	-28.46	-1.12
Clay-Stiff	12.70	0.50	-6.76	-0.27	-6.47	-0.25	-6.44	-0.25
	25.40	1.00	-13.05	-0.51	-12.57	-0.49	-12.62	-0.50
	50.80	2.00	-24.15	-0.95	-25.63	-1.01	-27.33	-1.08
Clay-Medium	12.70	0.50	-6.59	-0.26	-6.61	-0.26	-6.53	-0.26
	25.40	1.00	-12.68	-0.50	-12.81	-0.50	-12.79	-0.50
	50.80	2.00	-24.69	-0.97	-26.55	-1.05	-27.97	-1.10
Clay-Soft	12.70	0.50	-7.03	-0.28	-6.77	-0.27	-6.70	-0.26
	25.40	1.00	-12.71	-0.50	-13.36	-0.53	-13.18	-0.52
	50.80	2.00	-25.65	-1.01	-27.15	-1.07	-28.44	-1.12

Table 39: Δ_{pi} for the CFRP cases (pulling away from backfill)

Type of Soil	Δ_g Pulling away from Backfill		Span Length					
			m	ft	m	ft	m	ft
CFRP			15.25	50.00	30.50	100.00	45.75	150.00
	mm	in	mm	in	mm	in	mm	in
Sand-Dense	12.7	0.5	5.77	0.23	5.12	0.20	5.83	0.23
	25.4	1	12.30	0.48	11.99	0.47	12.23	0.48
	50.8	2	25.09	0.99	25.28	1.00	26.55	1.05
Sand-Medium	12.7	0.5	5.72	0.23	5.70	0.22	5.87	0.23
	25.4	1	11.65	0.46	12.24	0.48	12.44	0.49
	50.8	2	25.31	1.00	25.95	1.02	25.43	1.00
Sand-Loose	12.7	0.5	5.84	0.23	5.80	0.23	5.95	0.23
	25.4	1	11.89	0.47	12.44	0.49	12.60	0.50
	50.8	2	24.19	0.95	26.31	1.04	25.75	1.01
Clay-Stiff	12.7	0.5	5.35	0.21	5.14	0.20	5.24	0.21
	25.4	1	10.43	0.41	10.75	0.42	10.84	0.43
	50.8	2	22.23	0.88	24.36	0.96	22.26	0.88
Clay-Medium	12.7	0.5	5.44	0.21	5.21	0.21	5.29	0.21
	25.4	1	10.66	0.42	10.95	0.43	10.99	0.43
	50.8	2	21.32	0.84	21.52	0.85	22.78	0.90
Clay-Soft	12.7	0.5	5.38	0.21	5.16	0.20	5.24	0.21
	25.4	1	10.69	0.42	10.96	0.43	11.03	0.43
	50.8	2	21.71	0.85	22.05	0.87	23.22	0.91

Table 40: Δ_{pi} for the CFRP cases (pushing against backfill)

Type of Soil	Δ_g Pushing against Backfill		Span Length					
			m	ft	m	ft	m	ft
CFRP			15.25	50.00	30.50	100.00	45.75	150.00
	mm	in	mm	in	mm	in	mm	in
Sand-Dense	12.70	0.50	-6.56	-0.26	-6.34	-0.25	-6.23	-0.25
	25.40	1.00	-12.57	-0.49	-12.66	-0.50	-12.61	-0.50
	50.80	2.00	-24.67	-0.97	-25.82	-1.02	-27.28	-1.07
Sand-Medium	12.70	0.50	-6.51	-0.26	-6.42	-0.25	-6.37	-0.25
	25.40	1.00	-12.89	-0.51	-12.75	-0.50	-12.92	-0.51
	50.80	2.00	-25.15	-0.99	-25.88	-1.02	-27.25	-1.07
Sand-Loose	12.70	0.50	-6.72	-0.26	-6.63	-0.26	-6.35	-0.25
	25.40	1.00	-13.11	-0.52	-13.04	-0.51	-13.20	-0.52
	50.80	2.00	-25.15	-0.99	-26.71	-1.05	-27.83	-1.10
Clay-Stiff	12.70	0.50	-6.75	-0.27	-6.51	-0.26	-6.44	-0.25
	25.40	1.00	-13.02	-0.51	-12.61	-0.50	-12.63	-0.50
	50.80	2.00	-24.09	-0.95	-24.09	-0.95	-26.18	-1.03
Clay-Medium	12.70	0.50	-6.57	-0.26	-6.51	-0.26	-6.33	-0.25
	25.40	1.00	-12.64	-0.50	-12.30	-0.48	-12.41	-0.49
	50.80	2.00	-23.49	-0.92	-25.25	-0.99	-25.30	-1.00
Clay-Soft	12.70	0.50	-6.91	-0.27	-6.77	-0.27	-6.70	-0.26
	25.40	1.00	-12.78	-0.50	-13.33	-0.52	-13.21	-0.52
	50.80	2.00	-24.25	-0.95	-26.00	-1.02	-25.94	-1.02

4.2.1 Transverse displacement of POI (Δ_m)

The different studied cases resulted in generally similar but different L_{pi} values. Similarly, in each study case, slightly different L_{pi} values were obtained during contraction (Pulling away from backfill) and expansion (Pushing against backfill). Therefore, to apply the cyclic POI displacement Δ_m , the L_{pi} for each model was averaged as presented in Table 41 and Table 42.

Table 41: Average L_{pi} values for all control cases.

Type Of Soil	$\pm \Delta_g$		Span Length					
			m		ft		m	
Control			15.25	50	30.5	100	45.75	150
	mm	in	mm	in	mm	in	mm	in
Sand-Dense	12.7	0.5	667.49	26.28	828.21	32.61	926.86	36.49
	25.4	1	743.74	29.28	862.45	33.95	946.53	37.27
	50.8	2	773.88	30.47	815.44	32.10	847.12	33.35
Sand-Medium	12.7	0.5	680.22	26.78	847.90	33.38	931.16	36.66
	25.4	1	765.45	30.14	891.27	35.09	957.55	37.70
	50.8	2	817.56	32.19	862.72	33.97	884.58	34.83
Sand-Loose	12.7	0.5	708.01	27.87	865.99	34.09	951.88	37.48
	25.4	1	793.97	31.26	911.30	35.88	978.21	38.51
	50.8	2	838.79	33.02	885.98	34.88	902.73	35.54
Clay-Stiff	12.7	0.5	431.29	16.98	609.37	23.99	709.40	27.93
	25.4	1	469.90	18.50	616.10	24.26	693.16	27.29
	50.8	2	535.86	21.10	603.65	23.77	626.39	24.66
Clay-Medium	12.7	0.5	463.70	18.26	645.94	25.43	732.76	28.85
	25.4	1	502.61	19.79	650.39	25.61	716.78	28.22
	50.8	2	564.33	22.22	629.13	24.77	648.60	25.54
Clay-Soft	12.7	0.5	514.19	20.24	698.73	27.51	783.89	30.86
	25.4	1	558.71	22.00	708.83	27.91	771.18	30.36
	50.8	2	626.80	24.68	689.76	27.16	706.95	27.83

Table 42: Average L_{pi} for all CFRP cases.

Type Of Soil	$\pm \Delta_g$		Span Length					
			m	ft	m	ft	m	ft
CFRP			15.25	50.00	30.50	100.00	45.75	150.00
	mm	in	mm	in	mm	in	mm	in
Sand-Dense	12.7	0.5	667.70	26.29	855.27	33.67	955.41	37.61
	25.4	1	762.54	30.02	920.18	36.23	1008.09	39.69
	50.8	2	877.18	34.53	959.64	37.78	1004.57	39.55
Sand-Medium	12.7	0.5	690.61	27.19	873.15	34.38	961.37	37.85
	25.4	1	805.05	31.69	946.50	37.26	1022.03	40.24
	50.8	2	934.64	36.80	1006.31	39.62	1049.55	41.32
Sand-Loose	12.7	0.5	714.37	28.12	885.94	34.88	978.22	38.51
	25.4	1	829.45	32.66	961.35	37.85	1037.62	40.85
	50.8	2	941.51	37.07	1027.09	40.44	1065.86	41.96
Clay-Stiff	12.7	0.5	431.31	16.98	617.36	24.31	735.41	28.95
	25.4	1	478.26	18.83	628.59	24.75	737.95	29.05
	50.8	2	586.21	23.08	642.10	25.28	742.16	29.22
Clay-Medium	12.7	0.5	465.31	18.32	662.98	26.10	760.36	29.94
	25.4	1	513.03	20.20	682.11	26.85	763.89	30.07
	50.8	2	625.62	24.63	730.84	28.77	771.66	30.38
Clay-Soft	12.7	0.5	518.19	20.40	719.54	28.33	812.15	31.97
	25.4	1	576.09	22.68	747.33	29.42	822.50	32.38
	50.8	2	705.80	27.79	803.74	31.64	842.54	33.17

Since the pile cap was modeled with fixed rotational boundary condition in the localized model, the relative displacement ($\Delta_p - \Delta_{pi}$) was applied to POI as shown in Figure 81. Moreover, the displacement due to the rotation at the pile-abutment ($\theta_p L_{pi}$) was considered. The equation shown below is used to calculate (Δ_m) assuming the deflected

$$L_{pi}^* = L_{pi}$$

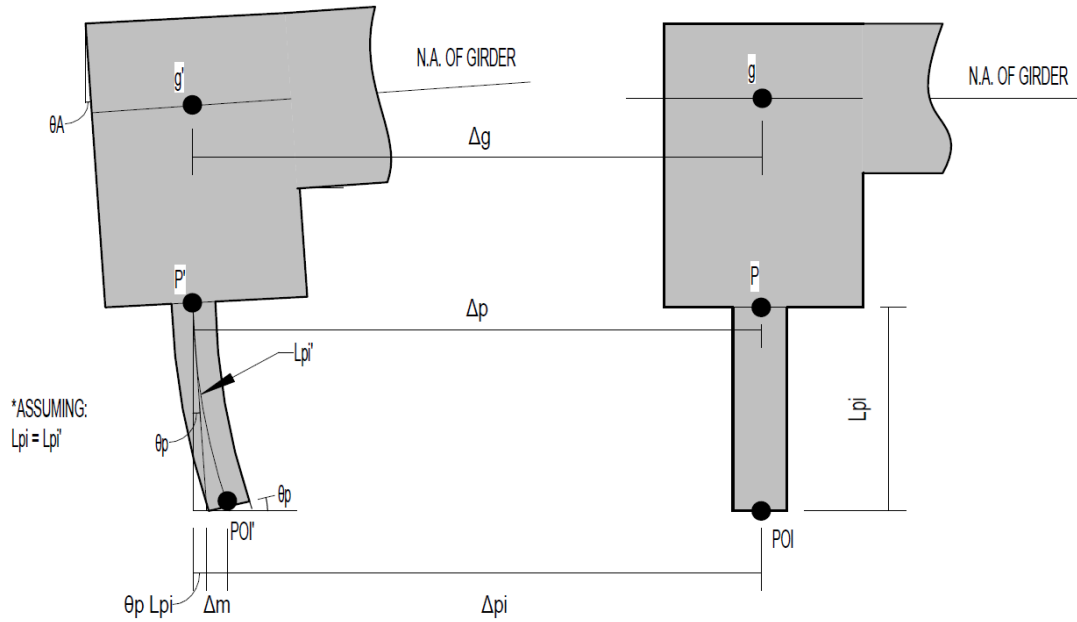


Figure 81: The localized model displacement (Δ_m).

$$\Delta_m = \Delta_p - \Delta_{pi} - \theta_p L_{pi}$$

Where:

Δ_m : the imposed displacement in the localized model

Δ_p : the pile displacement (Tables 29 to 32)

Δ_{pi} : the displacement at POI (Tables 37 to 40)

θ_p : the rotation at the pile/abutment interface (Tables 25 to 28)

L_{pi} : the depth to the point of inflection (Tables 33 to 36)

For example, the following calculations show the calculated Δ_m values for the control case (without CFRP) in medium sand with an end span length of 30.5 m (100 ft) and a Δ_g of 50.8 mm (2 in):

Pulling away from backfill= 41.56 mm - 28.28 mm - (0.0051 rad x 843.23 mm) = 8.97mm

Pushing against backfill= -40.30mm - (-28.12mm) - (-0.0048 rad x 882.21mm) = -7.94mm

Results for all cases are presented in Tables 43 to 46. However, in some of low rotational stiffness cases (50 ft-long girder) the POI was pushed to the opposite side of the displacement due to the high rotation at the abutment. At this phase of the study, only the higher displacement ranges of ± 50.8 mm (± 2 in) were analyzed for calculating Δ_m .

Table 43: Δ_m for the control cases (pulling away from backfill)

Type Of Soil	Δ_g Pulling away from Backfill		Girder Length							
			m		ft		m		ft	
Control			15.25	50	30.5	100	45.75	150		
	mm	in	mm	in	mm	in	mm	in		
Sand-Dense	12.7	0.5	0.09	0.00	0.60	0.02	1.10	0.04		
	25.4	1	1.11	0.04	2.11	0.08	3.45	0.14		
	50.8	2	7.29	0.29	8.98	0.35	10.20	0.40		
Sand-Medium	12.7	0.5	0.04	0.00	0.65	0.03	1.11	0.04		
	25.4	1	1.03	0.04	2.91	0.11	3.44	0.14		
	50.8	2	7.28	0.29	8.97	0.35	12.07	0.48		
Sand-Loose	12.7	0.5	0.00	0.00	0.62	0.02	1.08	0.04		
	25.4	1	1.66	0.07	2.84	0.11	3.39	0.13		
	50.8	2	7.13	0.28	10.65	0.42	11.82	0.47		
Clay-Stiff	12.7	0.5	-0.18	-0.01	0.31	0.01	0.67	0.03		
	25.4	1	-0.21	-0.01	1.35	0.05	1.75	0.07		
	50.8	2	4.14	0.16	6.04	0.24	7.76	0.31		
Clay-Medium	12.7	0.5	-0.22	-0.01	0.29	0.01	0.67	0.03		
	25.4	1	0.49	0.02	1.35	0.05	2.66	0.10		
	50.8	2	4.19	0.16	7.93	0.31	9.59	0.38		
Clay-Soft	12.7	0.5	0.02	0.00	0.24	0.01	0.63	0.02		
	25.4	1	0.30	0.01	2.02	0.08	2.52	0.10		
	50.8	2	5.69	0.22	7.61	0.30	9.11	0.36		

Table 44: Δ_m for the control cases (pushing against backfill)

Type Of Soil	Δ_g Pushing against Backfill		Girder Length					
			m	ft	m	ft	m	ft
Control			15.25	50	30.5	100	45.75	150
	mm	in	mm	in	mm	in	mm	in
Sand-Dense	12.70	0.50	0.01	0.00	-0.37	-0.01	-0.78	-0.03
	25.40	1.00	-0.63	-0.02	-1.38	-0.05	-2.03	-0.08
	50.80	2.00	-4.53	-0.18	-6.66	-0.26	-8.93	-0.35
Sand-Medium	12.70	0.50	0.00	0.00	-0.36	-0.01	-0.68	-0.03
	25.40	1.00	-0.69	-0.03	-1.35	-0.05	-2.29	-0.09
	50.80	2.00	-4.86	-0.19	-7.94	-0.31	-8.95	-0.35
Sand-Loose	12.70	0.50	0.05	0.00	-0.33	-0.01	-0.65	-0.03
	25.40	1.00	-0.60	-0.02	-1.86	-0.07	-2.66	-0.10
	50.80	2.00	-6.21	-0.24	-7.90	-0.31	-10.41	-0.41
Clay-Stiff	12.70	0.50	0.29	0.01	-0.07	0.00	-0.26	-0.01
	25.40	1.00	0.73	0.03	-0.48	-0.02	-1.04	-0.04
	50.80	2.00	-1.17	-0.05	-4.07	-0.16	-5.45	-0.21
Clay-Medium	12.70	0.50	0.16	0.01	-0.03	0.00	-0.26	-0.01
	25.40	1.00	0.37	0.01	-0.39	-0.02	-1.09	-0.04
	50.80	2.00	-1.49	-0.06	-4.27	-0.17	-5.70	-0.22
Clay-Soft	12.70	0.50	0.28	0.01	-0.15	-0.01	-0.41	-0.02
	25.40	1.00	0.09	0.00	-0.76	-0.03	-1.48	-0.06
	50.80	2.00	-1.80	-0.07	-5.58	-0.22	-6.99	-0.28

Table 45: Δ_m for the CFRP cases (pulling away from backfill)

Type Of Soil	Δ_g Pulling away from Backfill		Girder Length					
			m	ft	m	ft	m	ft
CFRP			15.25	50.00	30.50	100.00	45.75	150.00
	mm	in	mm	in	mm	in	mm	in
Sand-Dense	12.7	0.5	0.01	0.00	0.31	0.01	0.88	0.03
	25.4	1	0.79	0.03	2.13	0.08	3.17	0.12
	50.8	2	5.35	0.21	8.01	0.32	8.93	0.35
Sand-Medium	12.7	0.5	-0.04	0.00	0.43	0.02	0.90	0.04
	25.4	1	1.21	0.05	2.11	0.08	3.25	0.13
	50.8	2	5.32	0.21	8.09	0.32	10.66	0.42
Sand-Loose	12.7	0.5	-0.09	0.00	0.48	0.02	0.87	0.03
	25.4	1	1.13	0.04	2.10	0.08	3.18	0.13
	50.8	2	6.77	0.27	7.90	0.31	10.44	0.41
Clay-Stiff	12.7	0.5	-0.21	-0.01	0.29	0.01	0.51	0.02
	25.4	1	0.26	0.01	1.16	0.05	1.79	0.07
	50.8	2	1.50	0.06	3.62	0.14	6.97	0.27
Clay-Medium	12.7	0.5	-0.25	-0.01	0.19	0.01	0.51	0.02
	25.4	1	0.18	0.01	0.81	0.03	1.82	0.07
	50.8	2	2.95	0.12	5.72	0.23	6.90	0.27
Clay-Soft	12.7	0.5	-0.03	0.00	0.44	0.02	0.84	0.03
	25.4	1	0.64	0.03	1.40	0.06	2.48	0.10
	50.8	2	4.22	0.17	7.03	0.28	8.17	0.32

Table 46: Δ_m for the CFRP cases (pushing against backfill)

Type Of Soil	Δ_g Pushing against Backfill		Girder Length					
			m	ft	m	ft	m	ft
CFRP			15.25	50.00	30.50	100.00	45.75	150.00
	mm	in	mm	in	mm	in	mm	in
Sand-Dense	12.70	0.50	0.02	0.00	-0.26	-0.01	-0.54	-0.02
	25.40	1.00	-0.40	-0.02	-1.41	-0.06	-2.02	-0.08
	50.80	2.00	-3.57	-0.14	-6.14	-0.24	-6.95	-0.27
Sand-Medium	12.70	0.50	0.05	0.00	-0.27	-0.01	-0.57	-0.02
	25.40	1.00	-0.35	-0.01	-1.44	-0.06	-2.22	-0.09
	50.80	2.00	-5.03	-0.20	-7.42	-0.29	-8.24	-0.32
Sand-Loose	12.70	0.50	0.09	0.00	-0.26	-0.01	-0.77	-0.03
	25.40	1.00	-0.29	-0.01	-1.47	-0.06	-1.84	-0.07
	50.80	2.00	-5.03	-0.20	-7.52	-0.30	-8.30	-0.33
Clay-Stiff	12.70	0.50	0.28	0.01	-0.03	0.00	-0.18	-0.01
	25.40	1.00	0.78	0.03	-0.24	-0.01	-0.73	-0.03
	50.80	2.00	0.03	0.00	-1.72	-0.07	-4.11	-0.16
Clay-Medium	12.70	0.50	0.16	0.01	0.03	0.00	-0.38	-0.02
	25.40	1.00	0.45	0.02	-0.62	-0.02	-1.24	-0.05
	50.80	2.00	-1.11	-0.04	-3.19	-0.13	-5.72	-0.23
Clay-Soft	12.70	0.50	0.29	0.01	-0.08	0.00	-0.32	-0.01
	25.40	1.00	0.23	0.01	-0.44	-0.02	-1.11	-0.04
	50.80	2.00	-1.98	-0.08	-4.27	-0.17	-6.77	-0.27

4.2.2 Geometry and Model Assembly

The pile to pile-pile cap section was generated as one part (the pile extruded from the pile cap based on the specifics of each case) as shown in Figure 82. The abutment height and width were 1,220 mm (4 ft) and 1,067mm (3.5 ft), respectively. The abutment was 1.2 m (4 ft) long on either side of the pile center (to represent a 2.4 m or 8 ft pile spacing). The pile reinforcing steel cage was embedded for 610 mm (2 ft) inside the pile cap. Three different models were considered. The first model was the control (i.e. without any external CFRP confinement). The second model represented the application of CFRP as retrofit of an existing pile (i.e. the CFRP was stopped at the face of the cap and did not go inside the cap). The retrofit CFRP (consisting of two layers of CFRP wrap) had a length of twice the pile size or 914.4 mm (36 in). Finally, the extended CFRP (ECFRP)

application represented application during new construction where CFRP can extend into the cap before casting of the abutment. The three types of localized model are shown in Figure 83.

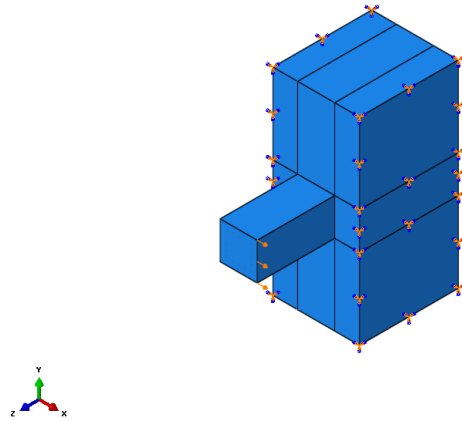


Figure 82: Pile-pile cap assembly and boundary condition.

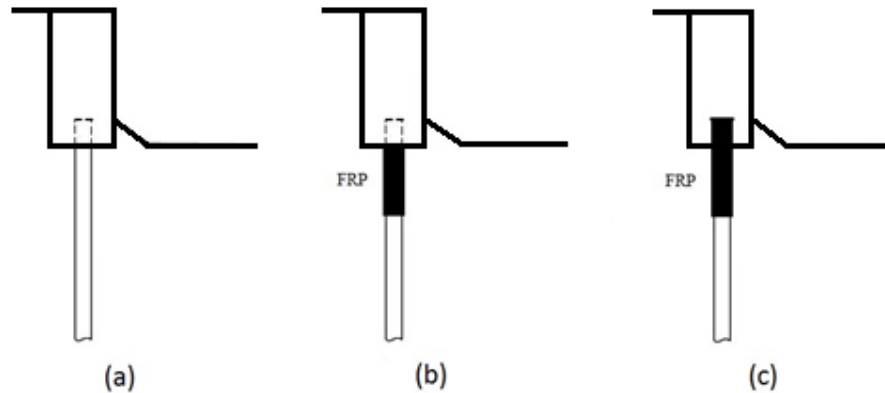


Figure 83: Three different models: (a) Control (b) Retrofit (c) ECFRP.

4.2.3 Mesh Sensitivity

The control model was used to determine the optimum size of elements to reduce the analysis time and maintain reasonable accuracy. Three different mesh sizes were considered (40mm, 60mm, and 80mm). The largest size (80mm) was the size of element used in the general model at the plastic hinge zone. Table 47 show a comparison between

the numbers of element and the time needed to complete the analysis. Despite the large difference in analysis time for the different models, the load-displacement results show little change as shown in Figure 84. However, the tensile plastic strain results, which are important to the study with respect to assessing damage, were somewhat different for different element sizes. For the 40 mm and 60 mm sizes, the peak plastic strains recorded were 0.077 and 0.075, respectively. However, in the 80 mm case, the peak tensile plastic strain was 0.065 as shown in Figure 85. Therefore, a 60 mm element size was used in the localized model.

Table 47: Control model (elements number vs. analysis time).

Mesh Size	Number of Elements		Time needed to run 5 cycles
	Concrete	Steel	
40mm	58,793	53,787	10 hrs
60mm	19,580	17,212	2 hrs 20 mins
80mm	8,778	7,444	40 mins

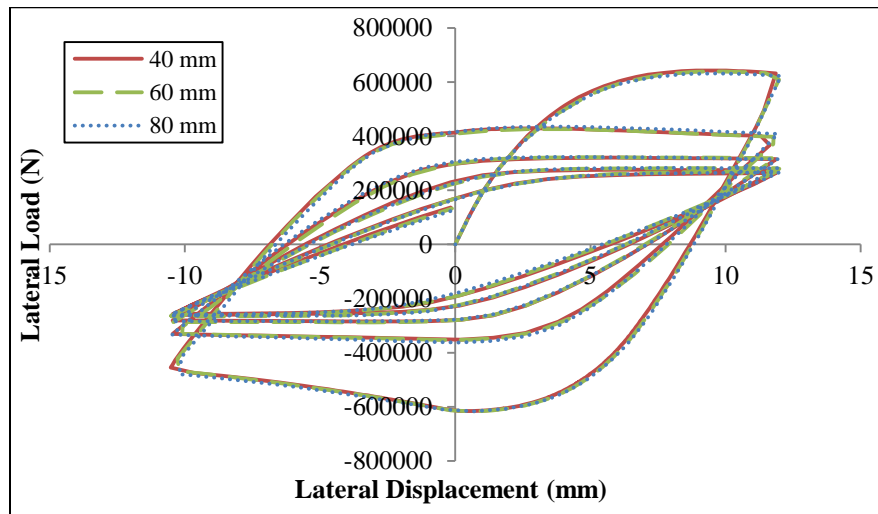
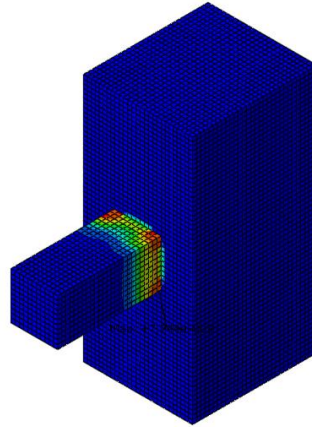
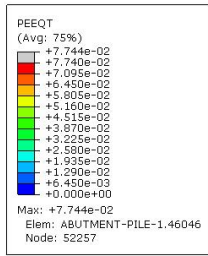
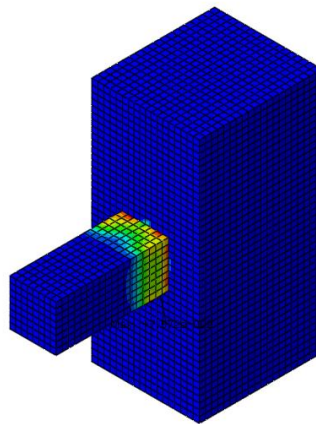
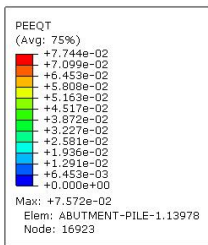


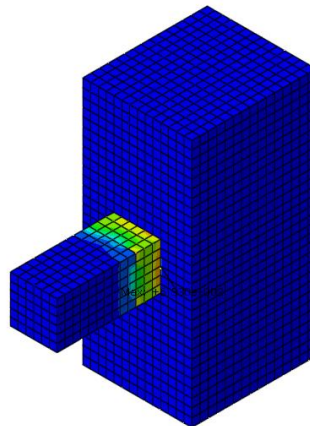
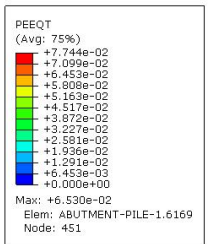
Figure 84: Load-displacement results from the localized models with three different mesh sizes.



(a)



(b)



(c)

Figure 85: The tensile plastic strains for the different mesh sizes (a) 40mm
(b) 60mm (c) 80mm.

4.2.4 Analysis Procedures

Although soil types were not specifically modelled in the localized model. However, the results of the general models indicated that there were changes in the distance to POI for various soil types. Therefore, the different soil types (L_{pi} values) needed to be modelled with three different span lengths and two types of confinement. The Table 48 indicates that the difference in the L_{pi} for the three types of sand for each span length was within 76.2 mm (3 in), while the corresponding difference for the different clay soils was less than 88.9 mm (3.5 in). Since these differences were relatively small, the averages of the L_{pi} values sand and clay (for each span length and confinement level) were used to reduce the number of models shown in Table 50 and

Table 51 . Using this approach, the number of models was reduced to twelve from thirty-six.

A verification analysis was conducted to test this approach using the L_{pi} values for selected individual dense sand and soft clay soils compared with the average L_{pi} for sand and clay. Each model was run for several displacement cycles. The load-displacement results showed minor difference for both types of soil as shown in Figure 86 and Figure 87. Thus, the average L_{pi} values for sand and clay were used in all subsequent models. Five displacement cycles ($\pm\Delta_m$) were applied.

Table 48: L_{pi-avg} for all control cases.

Type Of Soil	Δ_g		Span Length					
			m	ft	m	ft	m	ft
Control			15.25	50	30.5	100	45.75	150
	mm	in	mm	in	mm	in	mm	in
Sand-Dense	50.8	2	773.88	30.47	815.44	32.10	847.12	33.35
Sand-Medium			817.56	32.19	862.72	33.97	884.58	34.83
Sand-Loose			838.79	33.02	885.98	34.88	902.73	35.54
Clay-Stiff			535.86	21.10	603.65	23.77	626.39	24.66
Clay-Medium			564.33	22.22	629.13	24.77	648.60	25.54
Clay-Soft			626.80	24.68	689.76	27.16	706.95	27.83

Table 49: L_{pi-avg} for all CFRP cases.

Type Of Soil	Δ_g		Span Length					
			m	ft	m	ft	m	ft
CFRP			15.25	50.00	30.50	100.00	45.75	150.00
	mm	in	mm	in	mm	in	mm	in
Sand-Dense	50.8	2	877.18	34.53	959.64	37.78	1004.57	39.55
Sand-Medium			934.64	36.80	1006.31	39.62	1049.55	41.32
Sand-Loose			941.51	37.07	1027.09	40.44	1065.86	41.96
Clay-Stiff			586.21	23.08	642.10	25.28	742.16	29.22
Clay-Medium			625.62	24.63	730.84	28.77	771.66	30.38
Clay-Soft			705.80	27.79	803.74	31.64	842.54	33.17

Table 50: Average L_{pi-avg} for all control cases.

Type Of Soil	Δ_g		Span Length					
			m	ft	m	ft	m	ft
Control			15.25	50	30.5	100	45.75	150
	mm	in	mm	in	mm	in	mm	in
Sand-Dense	50.8	2	810.08	31.89	854.71	33.65	878.14	34.57
Sand-Medium								
Sand-Loose								
Clay-Stiff			575.66	22.66	640.85	25.23	660.64	26.01
Clay-Medium								
Clay-Soft								

Table 51: Average L_{pi-avg} for all CFRP cases.

Type Of Soil	Δ_g		Span Length					
			m	ft	m	ft	m	ft
CFRP			15.25	50.00	30.50	100.00	45.75	150.00
	mm	in	mm	in	mm	in	mm	in
Sand-Dense	50.8	2	917.78	36.13	997.68	39.28	1039.99	40.94
Sand-Medium								
Sand-Loose								
Clay-Stiff			639.21	25.17	725.56	28.57	785.45	30.92
Clay-Medium								
Clay-Soft								

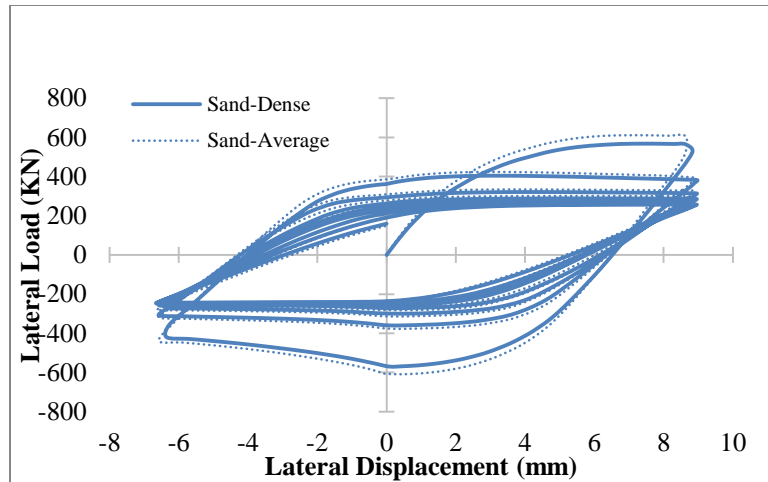


Figure 86: Load-displacement curves using L_{pi} for dense sand vs. L_{pi-avg} .

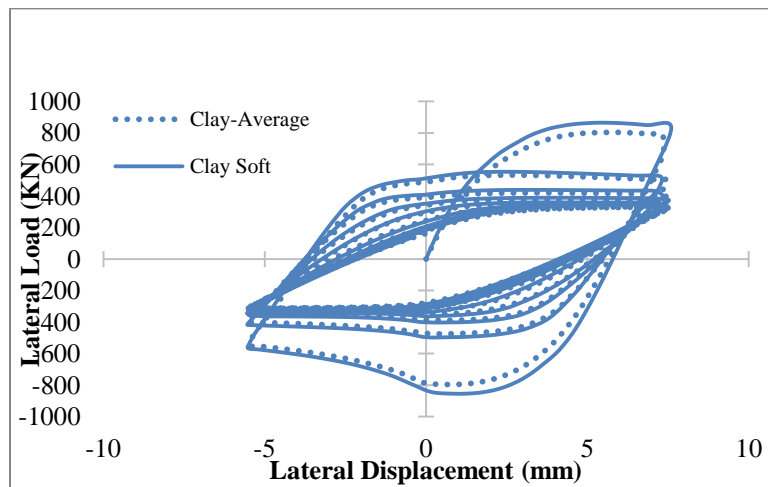


Figure 87: Load-displacement curves using L_{pi} for soft clay vs. L_{pi-avg} .

4.2.5 Results

A total of 54 models were analyzed (18 control, 318 retrofit (CFRP) and 18 new construction (ECFRP)). The cyclic lateral load response and the extent of damage near the pile-cap interface were examined. The assessment of the extent of damage was based on the damage parameters for the CDP model in ABAQUS including tensile plastic strain (PEEQT), tensile damage (DAMAGET) and section stiffness degradation (SDEG). The effect of FRP external confinement on the extent of damage was evaluated. To shed light

on the behavior of different soil types, the results from models with the corresponding average L_{pi} values are discussed in the following section. The results for sand and clay soils are presented here. Also, medium span length is shown here. Results for other span lengths are given in appendix C.

4.2.5.1 Lateral (shear) load on the Piles

The lateral (shear) load required to displace the pile by $\pm\Delta_m$ was evaluated. Five cycles were applied to capture any reduction in the applied load due to the pile damage. The results show that a lateral load of 564 kN (127 kips) was generated at the peak of the first cycle in the medium sand case as shown in Figure 88. While about 799 kN (180 kips) is the peak load of the first cycle for the medium clay soil as shown in Figure 91, Tables 52 to 54 present the piles lateral capacity. Also, Tables 55 to 57 show the calculated moment based on L_{pi} of each model at the pile-pile cap interface. All control cases experience large reduction after the first cycle. This indicates that most of damage occurred in the first cycle. Moreover, after the fifth cycle both models reach almost the same lateral load, mainly due to bond-slip in strands. However, with the use of CFRP the lateral load capacity increased in both cases as shown in Figures 88 through 93. It is evident that the use of CFRP has improved the overall performance of the piles for certain type of soil. Models CFRP and ECFRP have exhibited highly steady force vs displacement hysteresis. Furthermore, the use of ECFRP has exhibited significant ductile behavior in comparison to Control model.

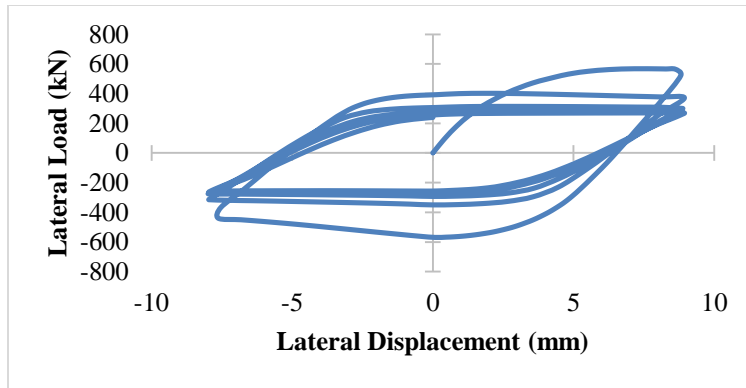


Figure 88: Lateral load vs. displacement for medium sand, control, medium span case.

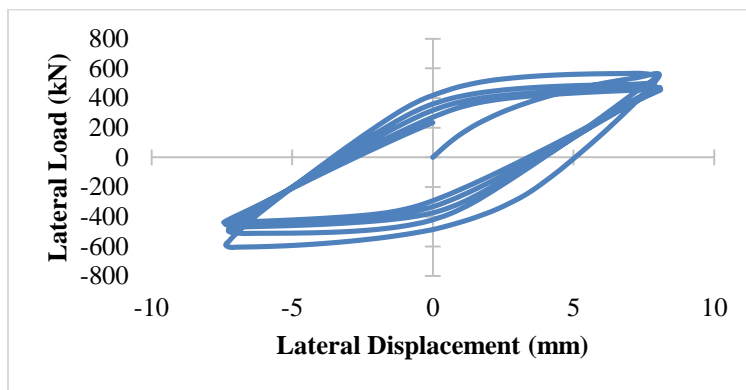


Figure 89: Lateral load vs. displacement for medium sand, CFRP, medium span case.

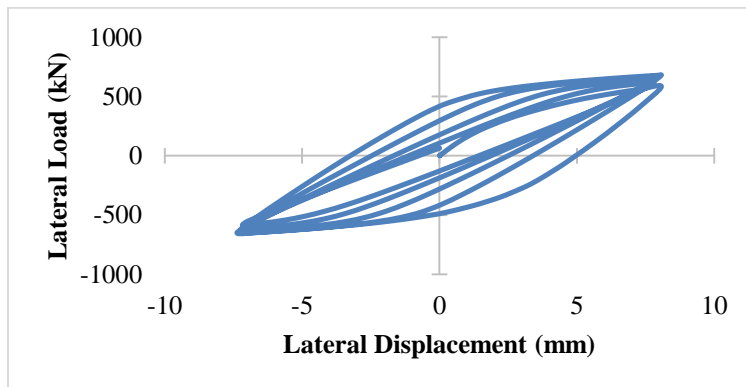


Figure 90: Lateral load vs. displacement for medium sand, ECFRP, medium span case.

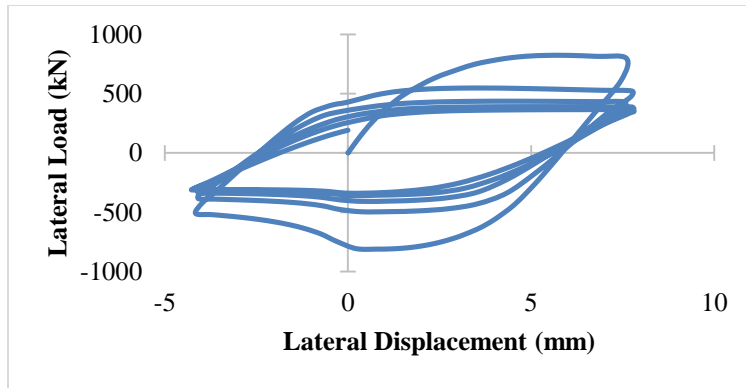


Figure 91: Lateral load vs. displacement for medium clay, control, medium span case.

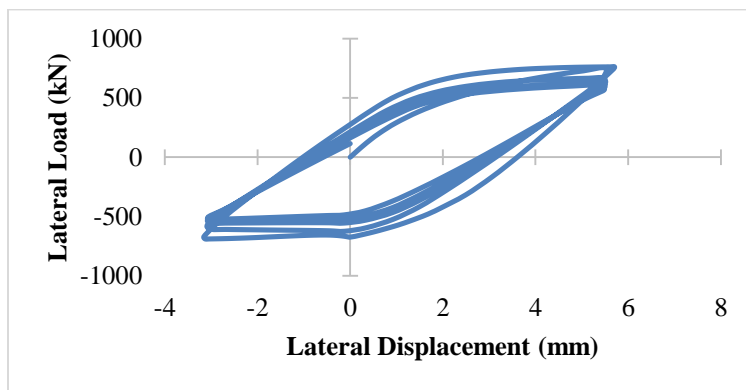


Figure 92: Lateral load vs. displacement for medium clay, CFRP, medium span case.

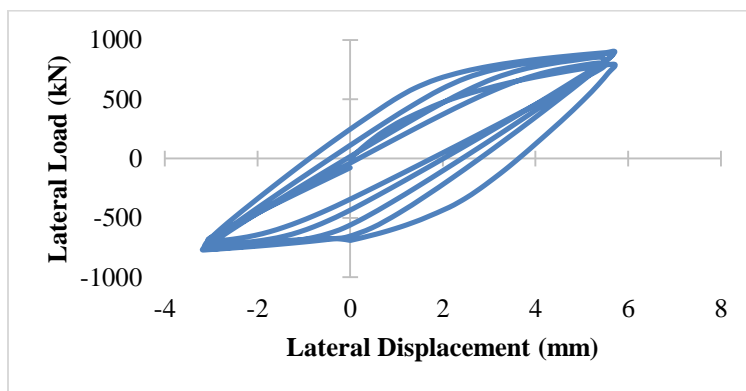


Figure 93: Lateral load vs. displacement for medium clay, ECFRP, medium span case.

Table 52: Maximum lateral force at the fifth cycle - control.

Type of Soil	Span Length					
	Short		Medium		Long	
Control	kN	Kips	kN	Kips	kN	Kips
Sand-Dense	286	64	273	61	244	55
Sand-Medium	290	65	270	61	241	54
Sand-Loose	273	61	273	61	232	52
Clay-Stiff	430	97	361	81	313	70
Clay-Medium	445	100	365	82	316	71
Clay-Soft	405	91	339	76	305	69

Table 53: Maximum lateral force at the fifth cycle - CFRP

Type of Soil	Span Length					
	Short		Medium		Long	
CFRP	kN	Kips	kN	Kips	kN	Kips
Sand-Dense	457	103	450	101	417	94
Sand-Medium	455	102	459	103	413	93
Sand-Loose	477	107	453	102	404	91
Clay-Stiff	328	74	559	126	564	127
Clay-Medium	591	133	608	137	557	125
Clay-Soft	644	145	627	141	560	126

Table 54: Maximum lateral force at the fifth cycle - ECFRP.

Type of Soil	Span Length					
	Short		Medium		Long	
ECFRP	kN	Kips	kN	Kips	kN	Kips
Sand-Dense	614	138	628	141	568	128
Sand-Medium	626	141	617	139	544	122
Sand-Loose	615	138	609	137	538	121
Clay-Stiff	364	82	708	159	753	169
Clay-Medium	725	163	805	181	729	164
Clay-Soft	840	189	767	173	679	153

Table 55: Control piles calculated moment.

Type of Soil	Span Length					
Control	Short		Medium		Long	
	kN-m	Kips-ft	kN-m	Kips-ft	kN-m	Kips-ft
Sand-Dense	232	171	233	172	214	158
Sand-Medium	235	173	231	170	212	156
Sand-Loose	221	163	233	172	204	150
Clay-Stiff	248	183	231	171	207	153
Clay-Medium	256	189	234	173	209	154
Clay-Soft	233	172	217	160	201	149

Table 56: CFRP piles calculated moment.

Type of Soil	Span Length					
CFRP	Short		Medium		Long	
	kN-m	Kips-ft	kN-m	Kips-ft	kN-m	Kips-ft
Sand-Dense	419	310	449	331	434	320
Sand-Medium	418	308	458	338	430	317
Sand-Loose	438	323	452	334	420	310
Clay-Stiff	210	155	406	299	443	327
Clay-Medium	378	279	441	326	437	323
Clay-Soft	412	304	455	336	440	325

Table 57: ECFRP piles calculated moment.

Type of Soil	Span Length					
ECFRP	Short		Medium		Long	
	kN-m	Kips-ft	kN-m	Kips-ft	kN-m	Kips-ft
Sand-Dense	564	416	627	463	591	436
Sand-Medium	575	424	616	454	566	418
Sand-Loose	564	417	608	449	560	413
Clay-Stiff	233	172	514	379	591	437
Clay-Medium	463	342	584	431	573	423
Clay-Soft	537	396	557	411	533	394

The load-displacement results for the fifth displacement cycle shows that models confined with CFRP (retrofit) developed an average of approximately 70% more lateral load compared with the control for the medium sand model. The corresponding increase for the ECFRP case was 128% in as shown in Figure 94. Figure 95 shows 78% and 133% increase in lateral force (compared to control) with the use of CFRP and ECFRP, respectively. Figures 96 to 98 show the load-displacement curves for the fifth displacement cycle in each model, where this comparison could be clearly seen.

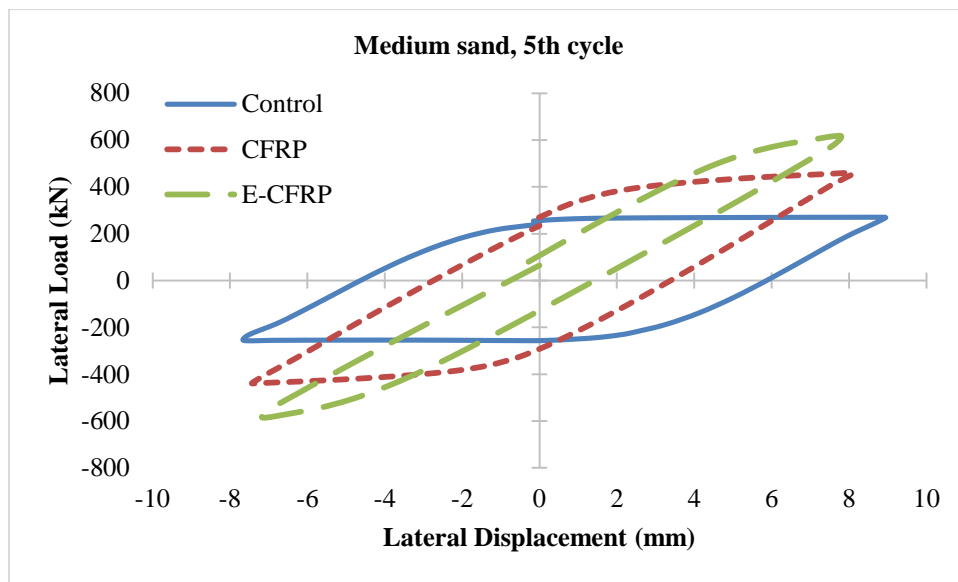


Figure 94: Lateral load vs. Displacement for: medium sand, all types of confinement, medium span cases.

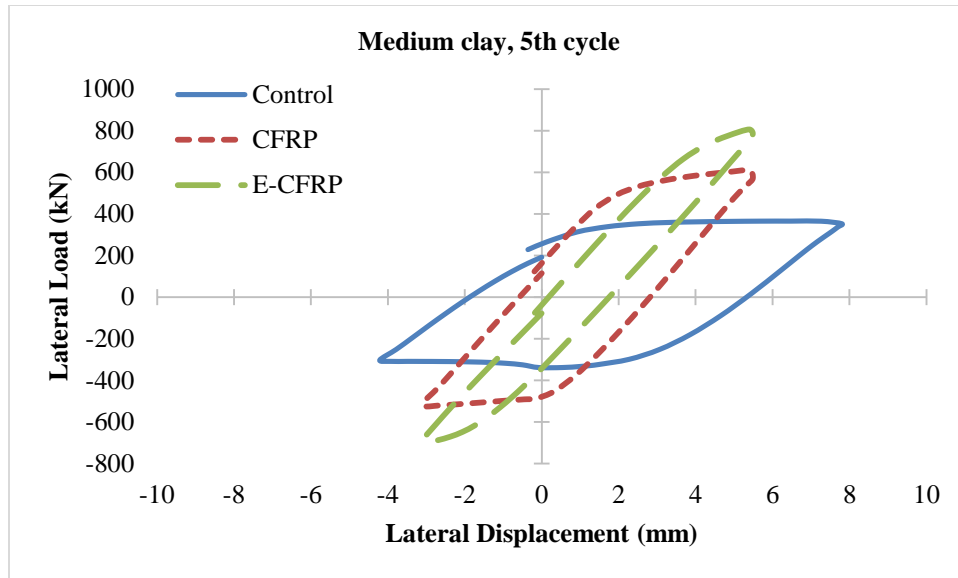


Figure 95: Lateral load vs. Displacement for: medium clay, all types of confinement, medium span cases.

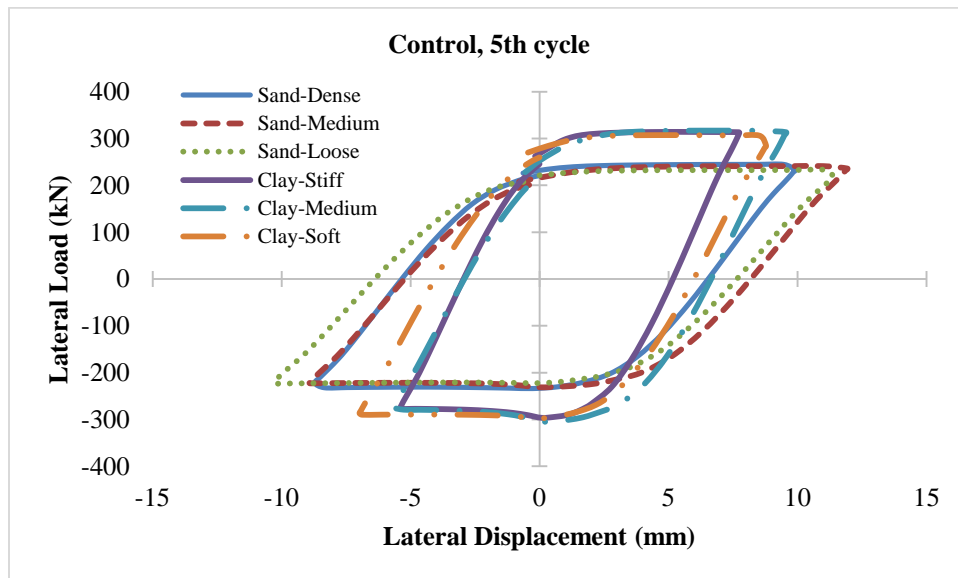


Figure 96: Lateral load vs. Displacement of all types for: control, all types of, medium span cases.

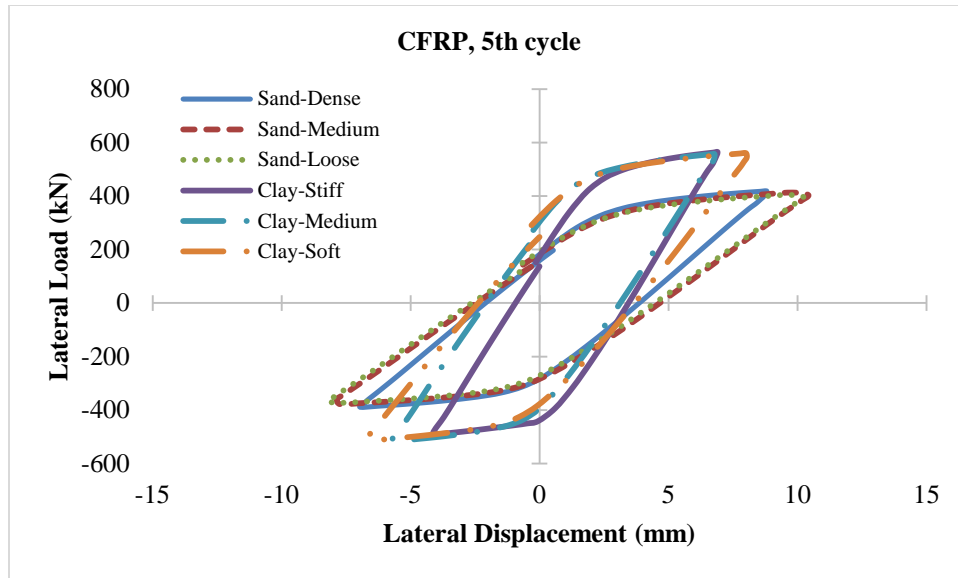


Figure 97: Lateral load vs. Displacement of all types for: CFRP, all types of, medium span cases.

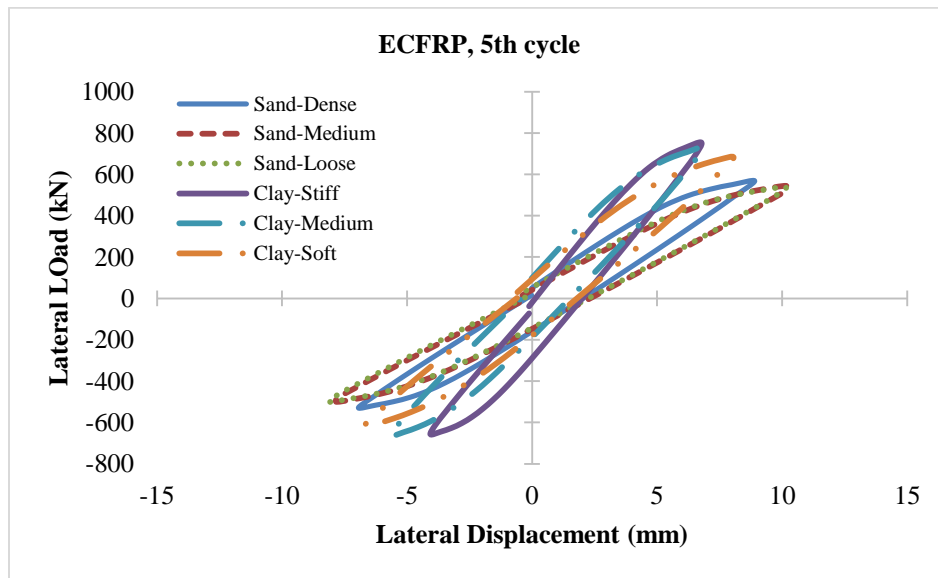


Figure 98: Lateral load vs. Displacement of all types for: ECFRP, all types of, medium span cases.

Figures 99 to 104 show the load-displacement behavior of the localized model for Δ_m values associated with different span lengths and $\Delta_g = \pm 50.8 \text{ mm}$ ($\pm 2 \text{ in}$). It can be observed that the shorter spans provide stiffer load-displacement response. Also, the addition of CFRP increases the linearity of pile response.

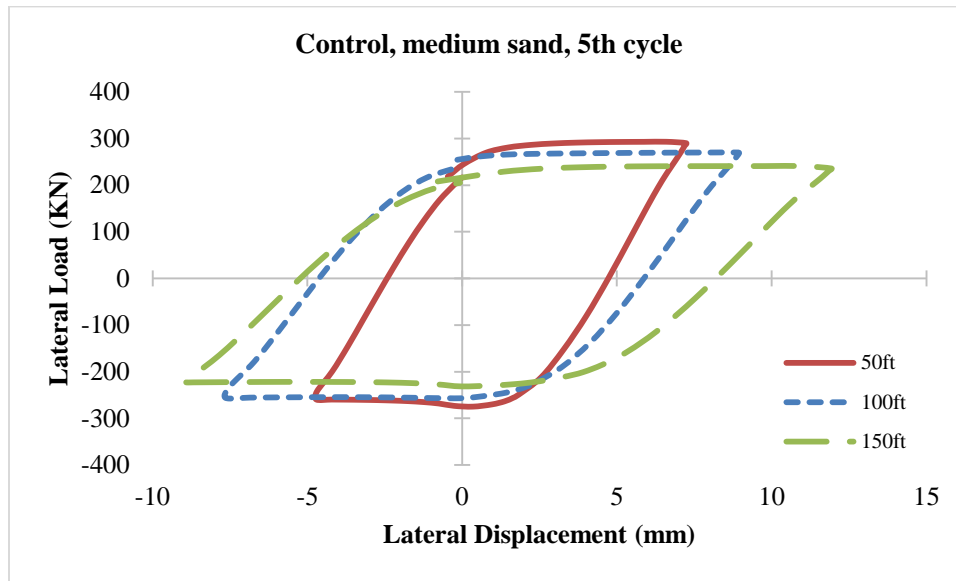


Figure 99: Lateral load vs. Displacement for: control, medium sand, all different span lengths.

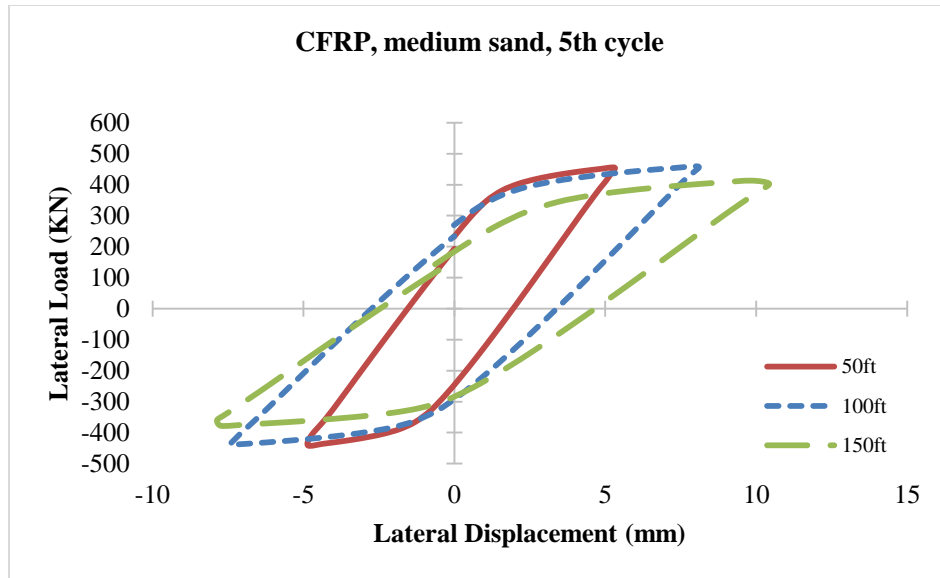


Figure 100: Lateral load vs. Displacement for: CFRP, medium sand, all different span lengths.

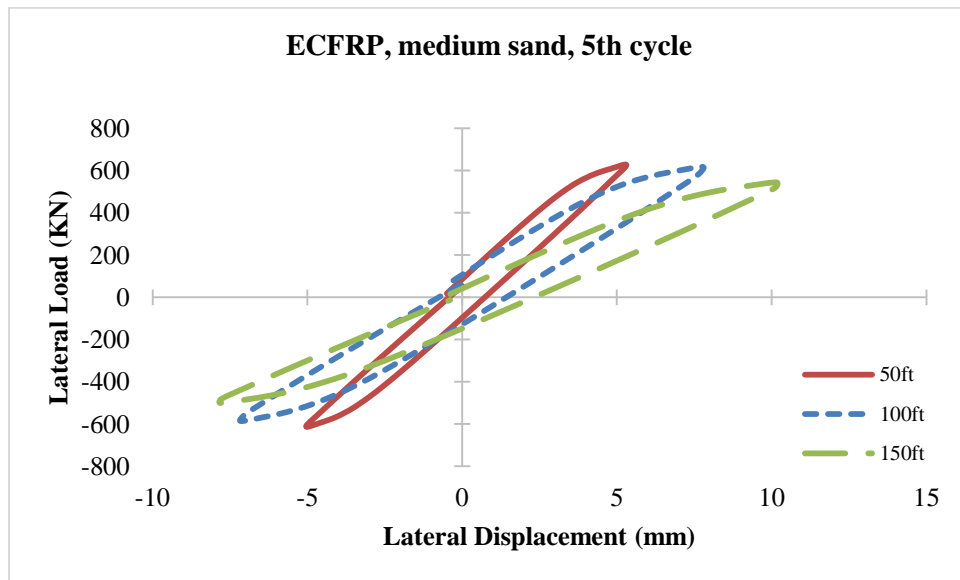


Figure 101: Lateral load vs. Displacement for: ECFRP, medium sand, all different span lengths.

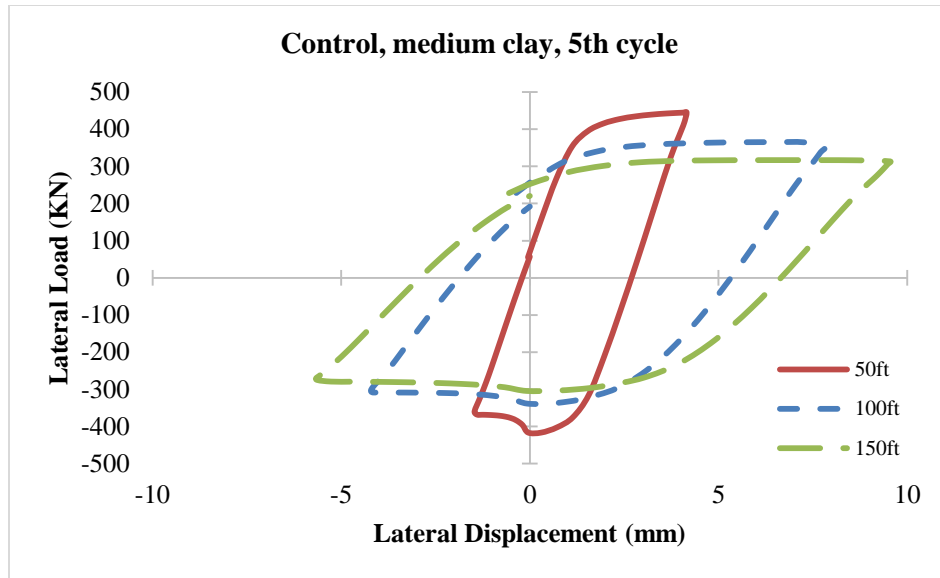


Figure 102: Lateral load vs. Displacement for: control, medium clay, all different span lengths.

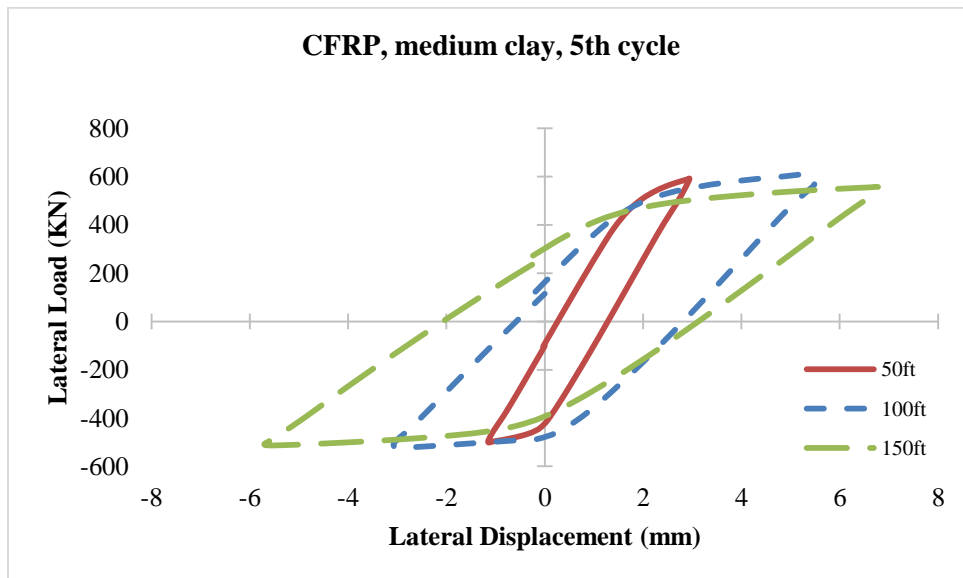


Figure 103: Lateral load vs. Displacement for: CFRP, medium clay, all different span lengths.

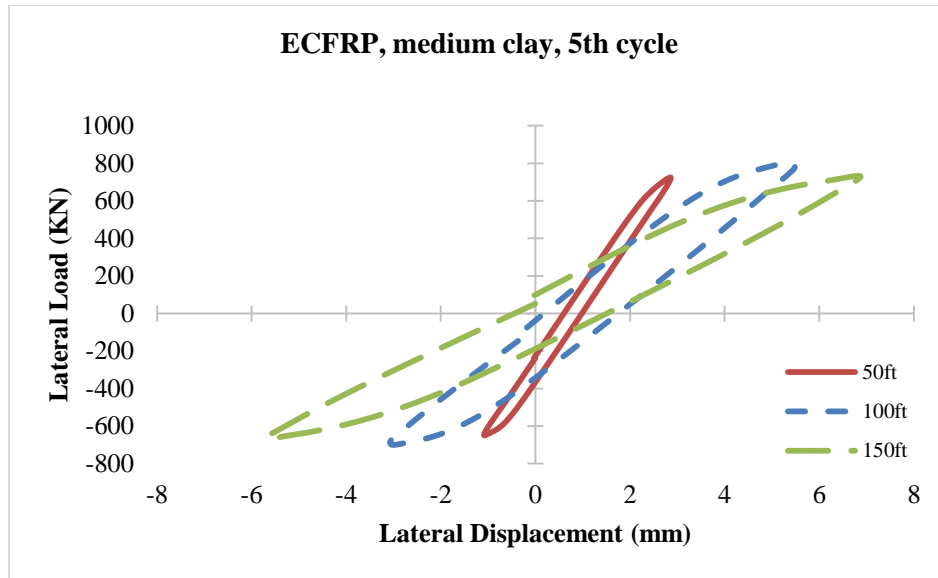


Figure 104: Lateral load vs. Displacement for: ECFRP, medium clay, all different span lengths.

4.2.5.2 The effect of CFRP on Control of Damage

The effect of CFRP on controlling damage at the pile-cap interface was evaluated. As mentioned in the previous section, five displacement cycles ($\pm\Delta_m$) were applied to capture the reduction in strength due to the pile damage. The results show about 29% reduction in the shear force between the first and fifth cycles for the medium sand soil condition. However, in CFRP and ECFRP confinement cases, the corresponding reduction in shear force was less pronounced at about 14% and 5%, respectively. Results from the ABAQUS models show that more elements in the control model exhibited tensile plastic strains (PEEQT) when compared to the CFRP and ECFRP models as shown in Figures 105 to 107. Moreover, extending the CFRP inside the pile cap can reduce the plastic tensile strains significantly. On the other hand, there is evidence of damage in the form of tensile plastic strain along a line at the pile-cap interface in the CFRP model as shown in Figure 106. Figures 108 through 110 show the tensile damage

distribution along the pile. It is observed that the use of CFRP and ECFRP showed lower intensity of damage over larger area. The results further indicate the same type of damage in the clay and sand models without confinement (control) as shown in Figure 111 and Figure 112. On the other hand, models associated with longer span lengths shows more elements reaching plastic tensile strain when compared with the shorter span models as shown in Figures 113 to 115. A longer plastic hinge zone appeared in the long span model as seen in Figures 116 to 118. Thus, it is evident that damage increased as the span length increased.

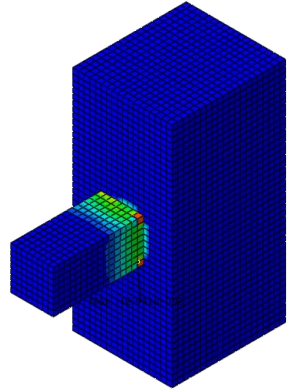
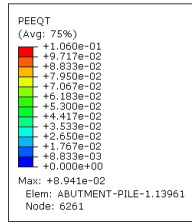


Figure 105: Tensile plastic strain: control, sand medium, medium span.

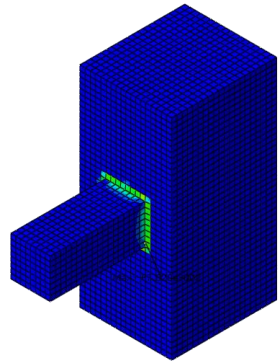
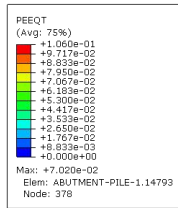


Figure 106: Tensile plastic strain: CFRP, sand medium, medium span.

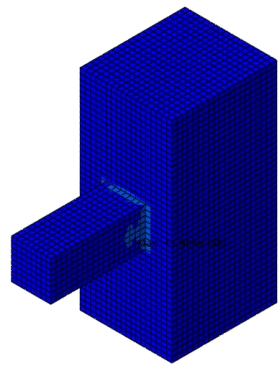
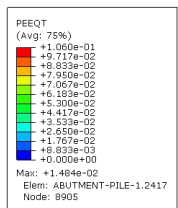


Figure 107: Tensile plastic strain: ECFRP, sand medium, medium span.

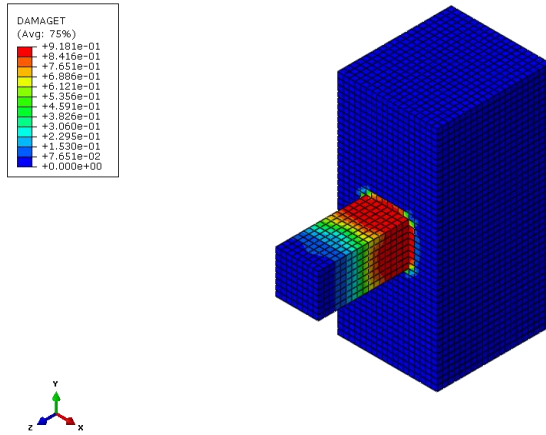


Figure 108: Tensile damage: control, medium sand, medium span.

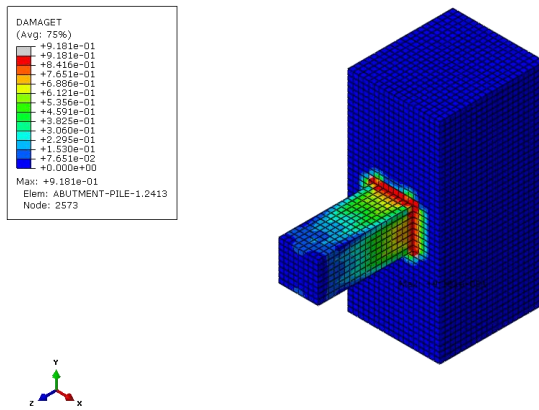


Figure 109: Tensile damage: CFRP, medium sand, medium span.

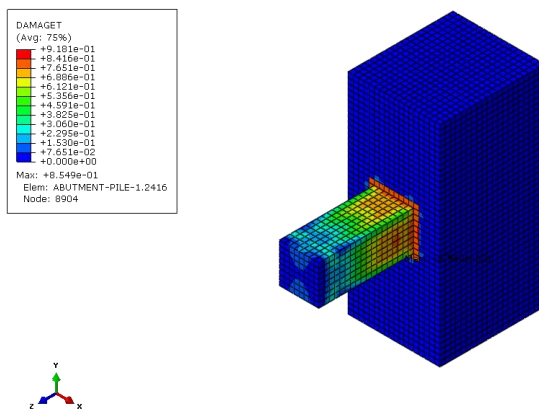


Figure 110: Tensile damage: ECFRP, medium sand, medium span.

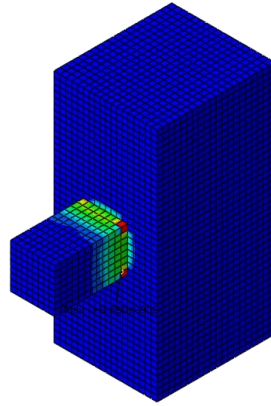
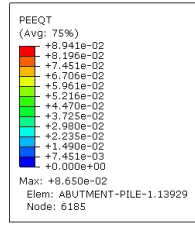


Figure 111: Tensile plastic strain: control, medium clay, medium span.

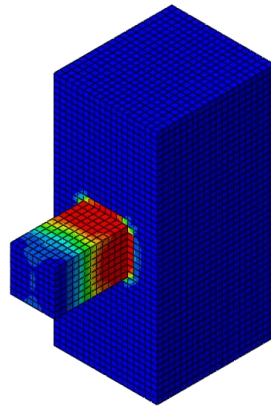
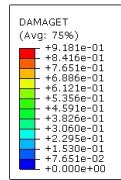


Figure 112: Tensile damage: control, medium clay, medium span.

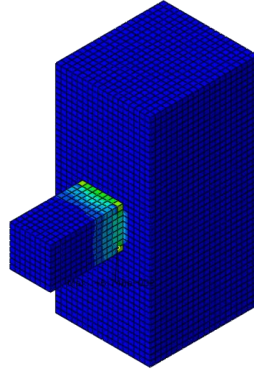
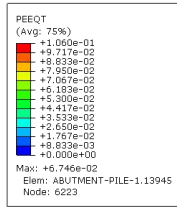


Figure 113: Tensile plastic strain: control, sand medium, short span.

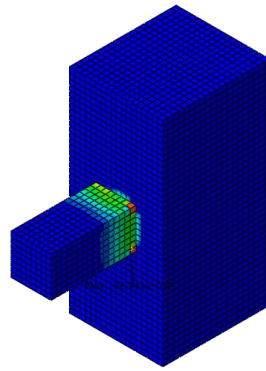
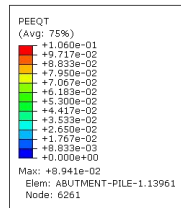


Figure 114: Tensile plastic strain: control, sand medium, medium span.

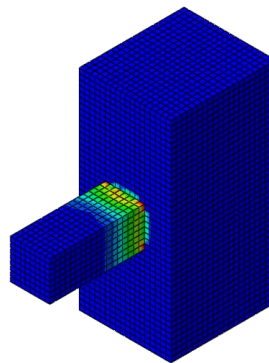
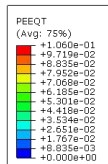


Figure 115: Tensile plastic strain: control, sand medium, long span.

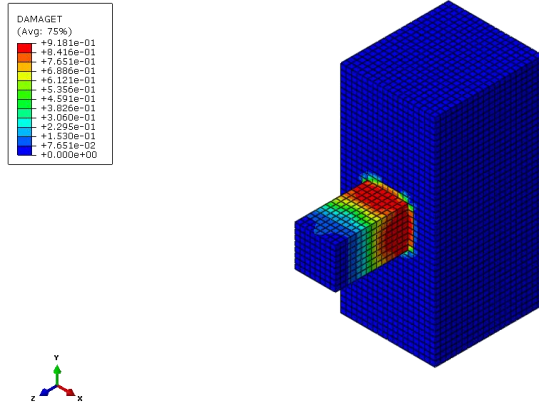


Figure 116: Tensile damage: control, medium sand, short span.

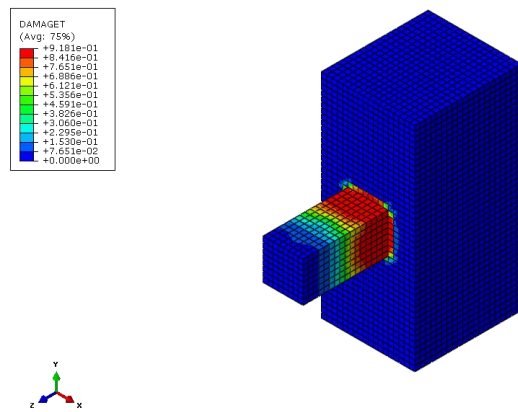


Figure 117: Tensile damage: control, medium sand, medium span.

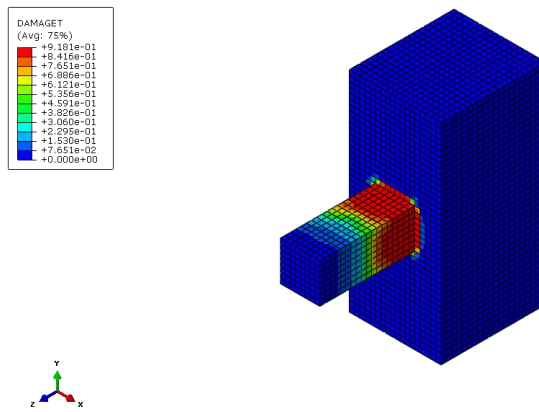


Figure 118: Tensile damage: control, medium sand, long span.

Table 58 shows the maximum strain in the longitudinal steel reinforcement in the piles for all models at the pile-abutment interface. The control model shows substantially higher steel strains. It should be noted that the modified stress-strain behavior was assumed to model the strand-slip due to bond failure. Higher strains in the control models indicate substantial strand slippage. Lower strains (slippage) are noted for the CFRP and ECFRP cases.

Table 58: The maximum strains in steel at the pile-abutment interface.

Type Of Soil	Control			CFRP			ECFRP		
Girder Length	Short	Medium	Long	Short	Medium	Long	Short	Medium	Long
Sand-Dense	0.045	0.058	0.064	0.019	0.031	0.031	0.009	0.013	0.013
Sand-Medium	0.054	0.063	0.067	0.024	0.035	0.035	0.010	0.013	0.014
Sand-Loose	0.052	0.069	0.070	0.028	0.034	0.034	0.012	0.013	0.014
Clay-Stiff	0.026	0.047	0.056	0.001	0.012	0.030	0.001	0.006	0.011
Clay-Medium	0.000	0.055	0.065	0.009	0.028	0.035	0.005	0.011	0.012
Clay-Soft	0.028	0.058	0.068	0.020	0.037	0.042	0.009	0.012	0.013

4.3 Development of Empirical Equations

The results of the general model indicated that the displacement at the pile-abutment interface (Δ_p) was less than the imposed displacement at the girder centroid (Δ_g). Moreover, the rotation of the abutment (θ_A) has an important influence on Δ_p . A correlation study was conducted to find relationships between Δ_g and Δ_p . Furthermore, an empirical equation was developed based on the results of the general model. The parameters considered in these relationships were the span length (L), the partial abutment height from the pile-cap interface up to the centroid of the composite section (H_A) and the abutment rotation (θ_A).

To find a relationship between the Δ_g and Δ_p , a correlation study was conducted using the least square method. The dimensionless value (Δ_p/Δ_g) was plotted as a function of $(\theta_A H_A/\Delta_g)$ for the different girder lengths as shown in Figures 119 to 121.

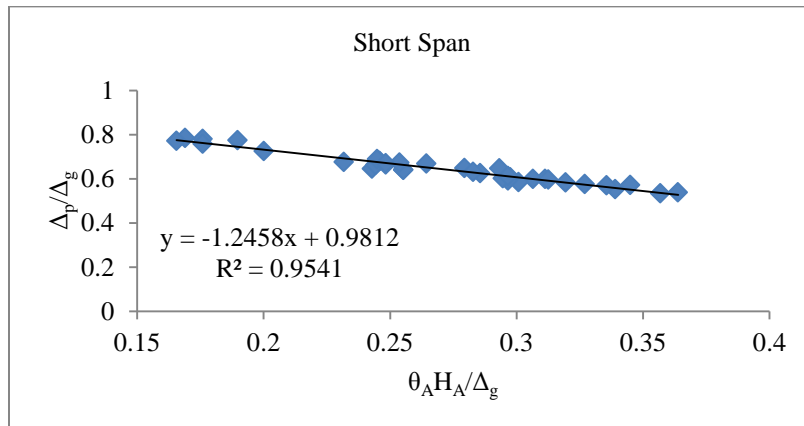


Figure 119: $(\theta_A H_A/\Delta_g)$ vs. (Δ_p/Δ_g) for short span, all Δ_g .

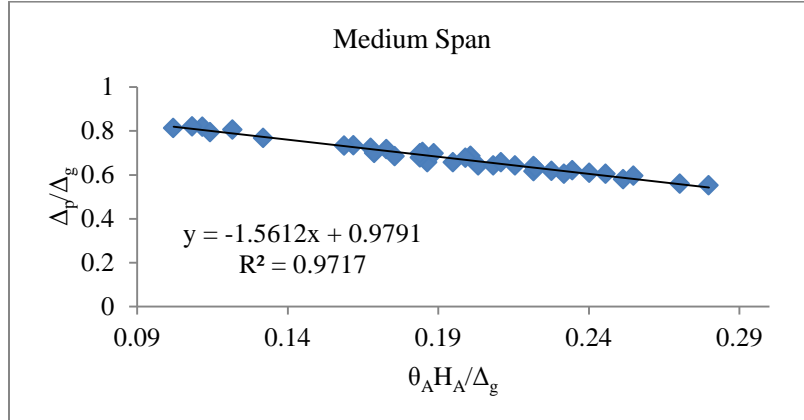


Figure 120: $(\theta_A H_A/\Delta_g)$ vs. (Δ_p/Δ_g) for medium span, all Δ_g .

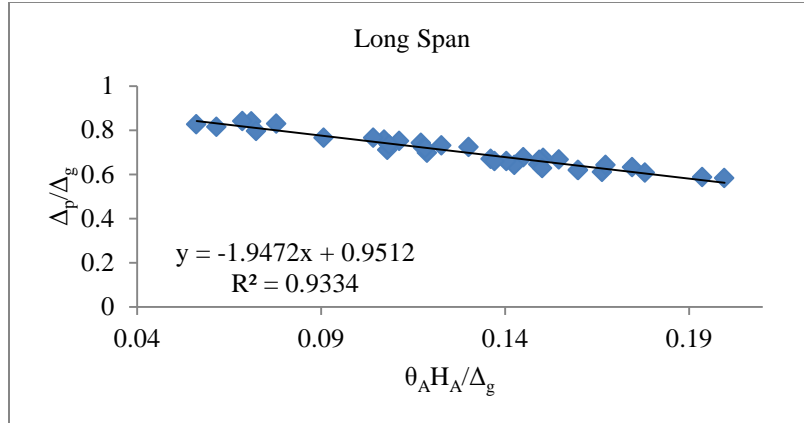


Figure 121: $(\theta_A H_A/\Delta_g)$ vs. (Δ_p/Δ_g) for long span, all Δ_g .

Then, the slopes and intercepts for all three span lengths were plotted to find the equation for the estimated $(\Delta_p/\Delta_g)_e$ as a function of L as shown Figure 122 and Figure 123. This indicates that Δ_p can be estimated reasonably well using L , H_A and θ_A In Equation (1). In Equation (1), L must be entered in ft, θ_A in radians, and H_A and Δ_g in consistent units (such as in). The resulting equation (1) for (Δ_p/Δ_g) resulted in a coefficient of determination $R^2=0.94$ when compared with the FE results as shown in Figure 124.

$$\left(\frac{\Delta_p}{\Delta_g}\right)_e = (-0.007L - 0.8833) \frac{\theta_A H_A}{\Delta_g} + (-0.0003L + 0.998) \quad (1)$$

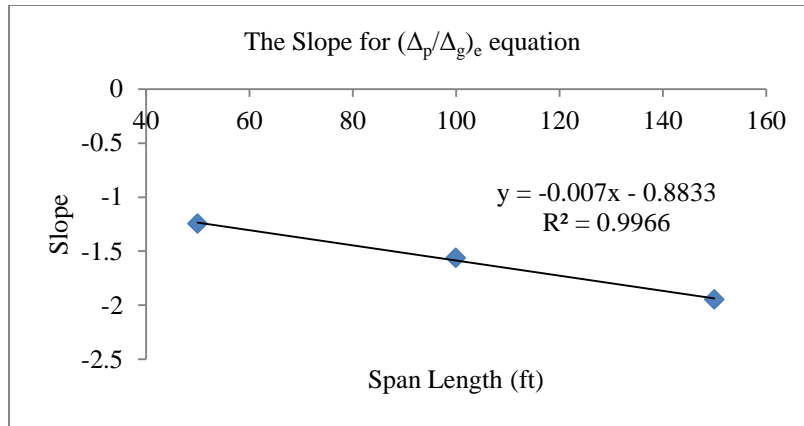


Figure 122: The slope for $(\Delta_p/\Delta_g)_e$ equation

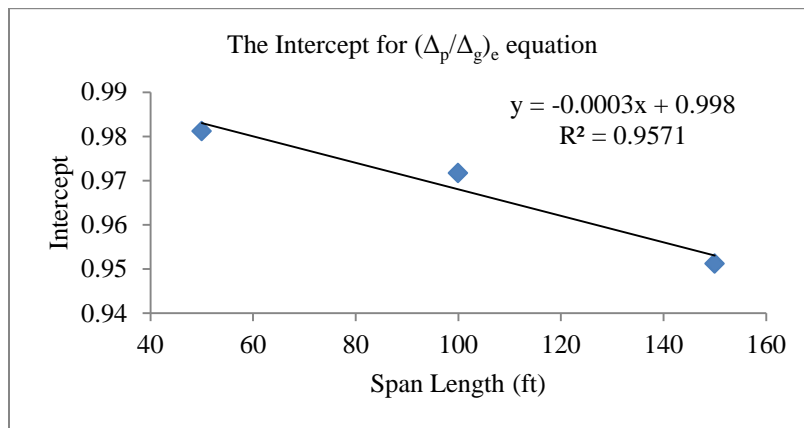


Figure 123: The intercept for $(\Delta_p/\Delta_g)_e$ equation

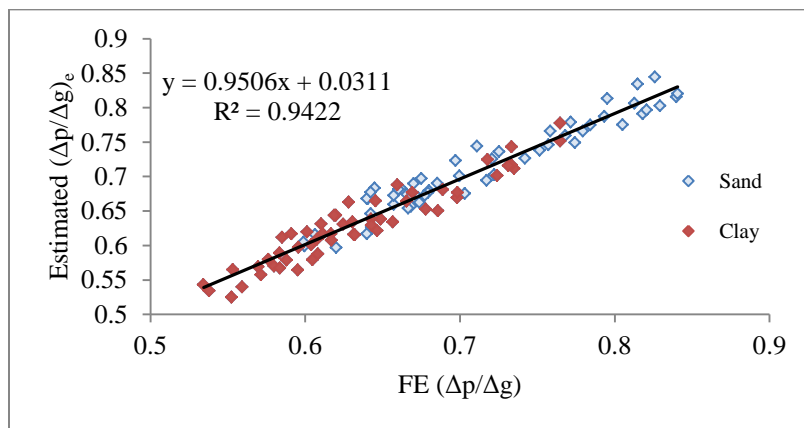


Figure 124: FE (Δ_p/Δ_g) vs. estimated $(\Delta_p/\Delta_g)_e$

Additionally, a study was conducted to develop an empirical equation to estimate θ_A . The FE results show that θ_A had a strong connection with Δ_g and the span length, but not with the type of soil. These correlations are illustrated in Figures 125 to 127. It was further determined that the relationship with Δ_g can best be represented with a second order polynomial equation. Also, it was determined that θ_A was inversely proportional to L. Therefore, equation (2) was proposed to relate θ_A with Δ_g and L. However, the parameters of the equation would be different for sand clay soils.

$$\theta_A = x_1 \frac{\Delta_g^2}{L} + x_2 \frac{\Delta_g}{L} + x_3/L + x_4 \quad (2)$$

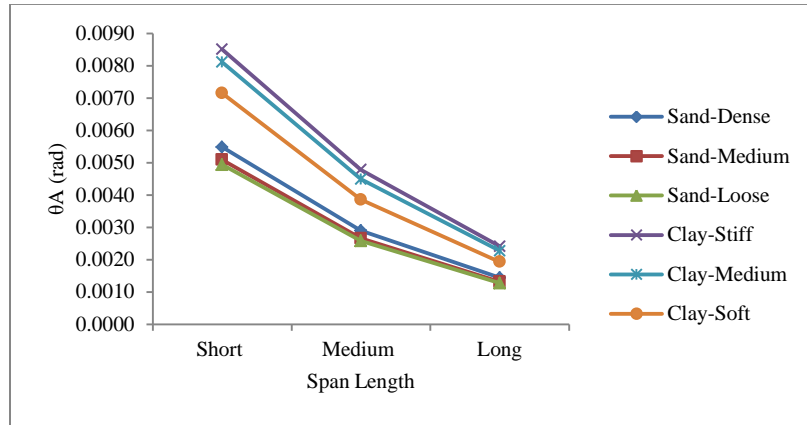


Figure 125: The rotation at the abutment (θ_A) for different girder, $\Delta_g = +50.8\text{mm}$ (+2 in).

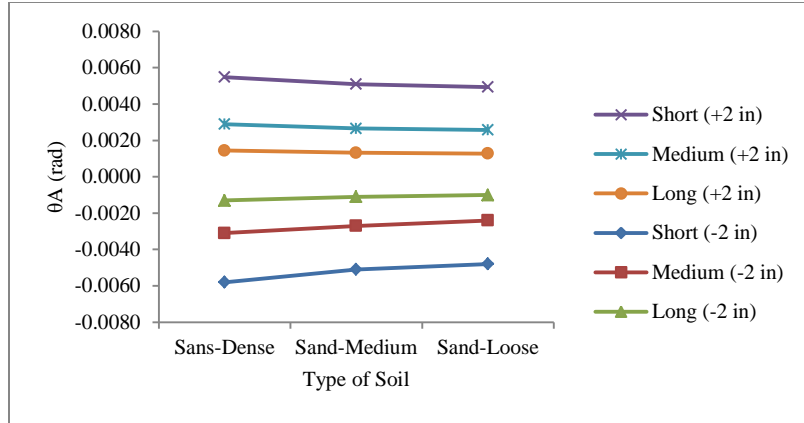


Figure 126: The rotation at the abutment (θ_A) for sands.

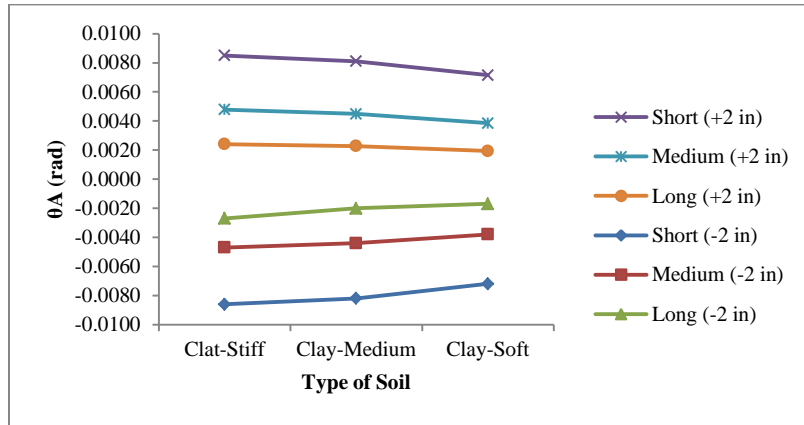


Figure 127: The rotation at the abutment (θ_A) for clays.

A nonlinear regression analysis was performed using the least square method to find the best fit parameters for the θ_A equation. Table 59 and

Table 60 show the regression parameters for both sand and clay. Therefore, the final equations (3) and (4) to estimate θ_A for both sand and clay soils can be written as follow:

$$(\theta_{A-sand})_e = -2.22E \times 10^{-3} \frac{\Delta g^2}{L} + 1.43 \times 10^{-1} \frac{\Delta g}{L} + 8.59 \times 10^{-3} / L - 1.21 \times 10^{-5} \quad (3)$$

$$(\theta_{A-clay})_e = -2.60E \times 10^{-3} \frac{\Delta g^2}{L} + 2.36 \times 10^{-1} \frac{\Delta g}{L} - 1.56 \times 10^{-3} / L + 2.64 \times 10^{-4} \quad (4)$$

Table 59: The regression parameters for sand.

Parameter	Value
x_1	-2.22E-03
x_2	1.43E-01
x_3	8.59E-03
x_4	-1.21E-05

Table 60: The regression parameters for clay.

Parameter	Value
x_1	-2.60E-03
x_2	2.36E-01
x_3	-1.56E-03
x_4	2.64E-04

The proposed empirical equation was evaluated after adding the regression parameters for both sand and clay. Then, the accuracy of both equations were evaluated by plotting the estimated results against the corresponding abutment rotations determined from FE results. The results show good agreement with the FE results. As shown in Figure 128 and Figure 129, both equations show coefficients of determination of 0.96 and 0.91 for sand and clay, respectively.

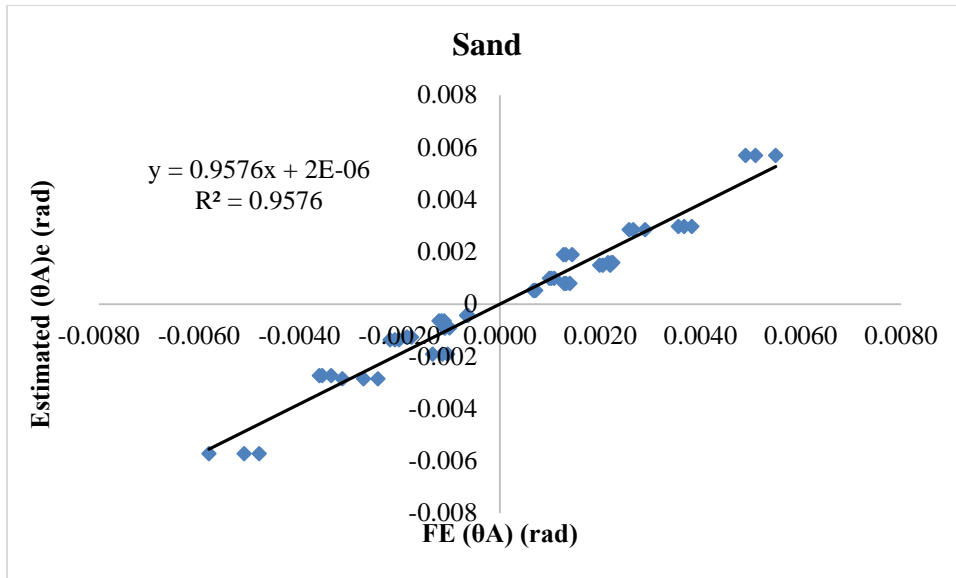


Figure 128: FE (θ_A) vs. estimated (θ_A) for sand.

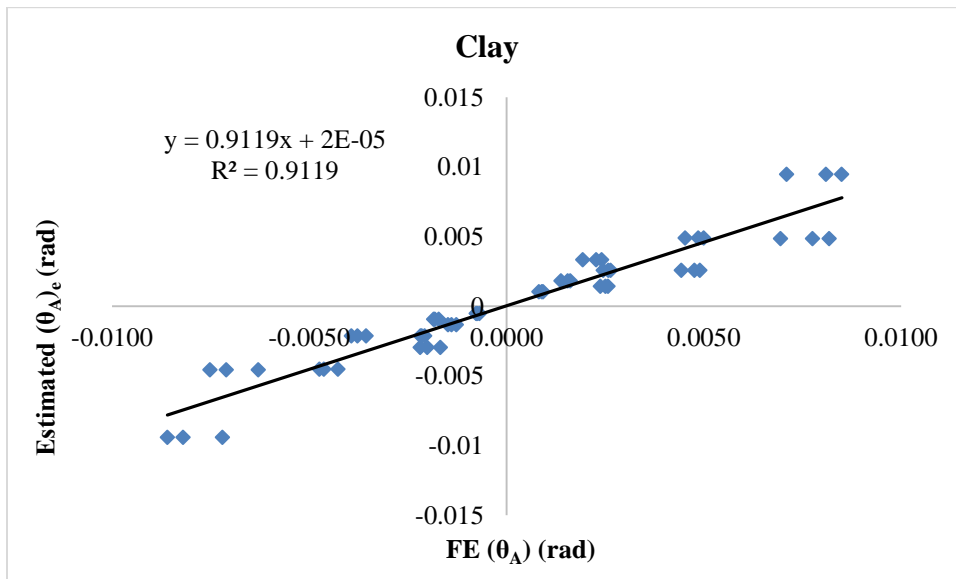


Figure 129: FE (θ_A) vs. estimated (θ_A) for clay.

5 SUMMARY AND CONCLUSIONS

This research evaluates the behavior of integral abutment bridges that utilize concrete piles and studies the effect of FRP composites on the behavior of concrete piles at the interface with the pile cap. These types of bridges rely on the interaction of the structure and surrounding soil to accommodate bridge movements without use of any expansion joints on the bridge superstructure. These joints and bearings are the source of several long-term maintenance problems in conventional bridges that utilize expansion joints.

Steel piles are commonly used in integral abutment bridges in lieu of concrete piles. The steel piles undergo cyclic lateral movement, which can result in localized yielding and buckling. Some regions in the United State and other countries prefer using concrete piles due to soil conditions and other economic factors. However, concrete piles under cyclic movements would be expected to crack and spall at the interface with the pile cap due to the large and reversible moment. These cracks and spall affect the long-term durability and strength of the pile. The integral abutment piles have significant ductility demands at the interface with the pile cap under lateral movement, which should be considered in design. The primary objectives of this research are highlighted and listed below:

1. Determine the performance parameters in integral abutment bridges supported by concrete piles.
2. Understand the behavior of concrete pile at the interface with the pile cap in integral abutment bridges with or without external FRP reinforcement.

3. Evaluate the effect of soil and soil-structure interaction on the behavior of concrete pile in integral abutment bridges.
4. Evaluate the effectiveness of localized FRP external reinforcement in enhancing the strength and ductility of reinforced concrete piles in integral abutment bridges.
5. Evaluate the deformation and strength and strength of concrete piles in integral abutment bridges.

To achieve these objectives, a comprehensive review of literature was first conducted. Two sets of analytical models were prepared using the ABAQUS finite element program to analyze reinforced concrete piles under bridge integral abutments with or without localized FRP reinforcement at the interface between the pile and the pile cap. The effectiveness and accuracy of FE method was verified using three sets of available experimental data.

A general model was created that included piles, abutment,, and girder. The main purpose of this model was to determine pile deformation and the point of inflection (POI) based on various parameters including six types of, external confinement (no confinement-control and CFRP wrap), rotational stiffness of the superstructure (three girder span lengths representing short, Medium, Long span), and three ranges of girder displacement (± 12.7 mm [± 0.5 in], ± 25.4 mm [± 1 in] and ± 50.8 mm [± 2 in]). A second localized model focused on the pile behavior near the cap was created. This model included the pile cap and the pile up to the POI (L_{pi}). The pile deformation determined in the general model was imposed on the pile.

The results from general model are highlighted below:

- The horizontal deformation of the pile at the interface with the cap (Δ_p) is a function of the rotation of the abutment (θ_A), height of the abutment (H_A), span length (L) and the horizontal deformation of the girder (Δ_g).
- The rotation of the abutment is a function of the soil type, (Δ_g) and (L). for different type of sand (dense, medium, and loose), the rotation of the abutment is essentially unchanged. The rotation of the abutment in clay soils is higher than the sand, and is approximately equal in stiff and medium clays. The rotation of soft clay soil is somewhat lower.
- The displacement at the pile-abutment interface (Δ_p) is clearly lower than the imposed displacement at the natural axis of the girder (Δ_g) mainly due to the abutment rotation (θ_A). A set of empirical equations were developed to estimate Δ_p and θ_A based on the span length L , the height of the abutment H_A and the girder displacement (Δ_g) as shown below:

- For both sand and clay:

$$\left(\frac{\Delta_p}{\Delta_g}\right)_e = (-0.007L - 0.8833) \frac{\theta_A H_A}{\Delta_g} + (-0.0003L + 0.998) \quad (L \text{ in ft})$$

- For sand:

$$(\theta_{A-Sand})_e = -2.22E \times 10^{-3} \frac{\Delta_g^2}{L} + 1.43 \times 10^{-1} \frac{\Delta_g}{L} + \frac{8.59 \times 10^{-3}}{L} - 1.21 \times 10^{-5} \quad (L \text{ in ft})$$

- For clay:

$$(\theta_{A-clay})_e = -2.60E \times 10^{-3} \frac{\Delta_g^2}{L} + 2.36 \times 10^{-1} \frac{\Delta_g}{L} - \frac{1.56 \times 10^{-3}}{L} + 2.64 \times 10^{-4} \quad (L \text{ in ft})$$

- The curvature demand in piles embedded in clay (at the interface with the cap) is higher than those embedded in sand.

- The application of CFRP reduces the curvature demand by almost 40% in all cases.

Based on a parametric study on the general model, the depth to point of inflection was located and the localized model was generated. Since the pile cap was modeled with fixed rotational boundary condition in the localized model, the relative displacement ($\Delta_m = \Delta_p - \Delta_{pi} - \theta_p L_{pi}$) was applied to POI as shown in Figure 130. Two cases of CFRP reinforcement was considered in addition to the control (No FRP). In the first case CFRP was applied over a length of twice the pile size just below the cap. This case represented retrofit of an existing bridge. The second case involved application of CFRP over an extended length (ECFRP) into the cap.

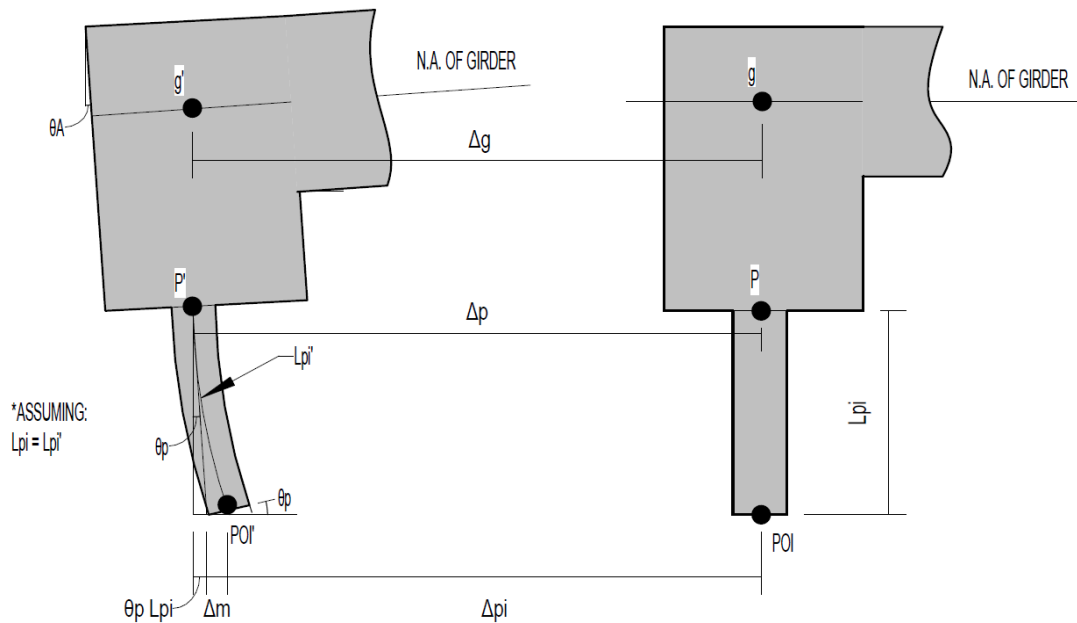


Figure 130: Displacements of pile and girder..

$$\Delta_m = \Delta_p - \Delta_{pi} - \theta_p L_{pi}$$

- The results from localized model show that after the first cycle a large reduction in pile strength occurred in all types of soil. This indicates that most of the

damage occurred in during first cycle. After the first cycle, the type of soil did not affect the maximum lateral (shear) force and the moment generated at the pile-abutment interface. A comparison of the lateral force generated and the corresponding moment at the pile-abutment interface indicates that the maximum shear and moment in the pile were relatively unchanged for various soils. The results of the load and moments show close behavior due to strand slippage.

- The use of CFRP resulted in an increase in shear and moment in the pile. Both CFRP and ECFRP exhibited highly steady force vs displacement hysteresis curves. Furthermore, the use of ECFRP exhibited significant ductile behavior in comparison to control model (without CFRP). Also, a plot of tensile plastic strains shows more elements in control model than CFRP and ECFRP. This indicates substantial reduction in damage due to application of CFRP and ECFRP.
- The use of CFRP increased the shear and moment forced in the pile. This would in turn transfer large forces into the structure that must be considered in design.
- The results support the use CFRP and ECFRP to improve the performance and capacity of concrete piles in integral abutment bridges. Additionally, it is evident and based on the results of this study that the use of CFRP and ECFRP enhanced the ductile behavior of the concrete piles. Thus, the use of CFRP is recommended in retrofit and new construction of integral abutment bridges that incorporate concrete piles.

5.1 Design Recommendations

Based on the findings, the use of CFRP is recommended to improve concrete pile performance in integral abutment bridges. In existing bridges, CFRP can be applied as

retrofit from the pile-abutment interface to the depth of $2d$ (size of the concrete pile).

However, in new bridges, the CFRP can be extended in to the cap (ECFRP)

Alternatively, more conventional (internal) confinement (steel reinforcement) can be used in the end regions of the pile to improve performance in lieu of CFRP use, in a manner similar to reinforced concrete members that are subjected to seismic loads.

The equation equations developed in this study can be used to estimate pile displacement and abutment rotation based on various parameters. Estimates of shears and moments developed in the piles under various conditions can be obtained from the reported results.

5.2 Recommendations for Future Study

This study was conducted using a square prestressed concrete pile that is commonly used in the United States. This work can be extended to different shapes and sizes of precast piles or cast-in-place piles.

REFERENCES

- ABAQUS, Analysis User's Guide. *Abaqus 2016 Online Documentation*. Dassault Systemes, 2015, 2015.
- Abdel-Mohti, Ahmed , and Yasser Khodair. "Analytical investigation of pile–soil interaction in sand under axial and lateral loads." *The International Journal of Advanced Structural Engineering*, 2014: 1-16.
- Abendroth , Robert E., Lowell F. Greimann , and Michael D. LaViolette . *An Integral Abutment Bridge with Precast Concrete Piles* . Iowa State University , Ames, IA : Center for Transportation Research and Education , 2007, 72.
- Abendroth, Robert E., and Lowell F. Greimann. *Field Testing of Integral Abutments*. Iowa State University, Ames, IA: Center for Transportation Research and Education, 2005.
- Allen, David L, and Bobby W Meade. *Soil-Bridge Abutment Interaction*. Kentucky Transportation Research Program, College of Engineering, University of Kentucky, 1988.
- American Concrete Institute. *Guide for the Design and Construction of Externally Bonded FRP Systems for Structure Concrete Structure*. aci, 2008.
- Arsoy, Sami, J. M. Duncan, and R. M. Barker. *Performance of Piles Supporting Integral Bridges*. Transportation Research Board, 2002, 162-167.
- Arsoy, Sami, Richard M. Barker, and J. Michael Duncan. *The Behavior of Integral Abutment Bridges*. Charlottesville, VA: Virginia Transportation Research Council, 1999, 33.

- Barker, Richard M., and Jay A. Puckett. *Design of Highway Bridges An LRFD Approach*. John Wiley & Sons, Inc., 2006.
- Braga, Franco, Rosario Gigliotti, Michelangelo Laterza, D'Amato Michele, and Sashi Kunnath. "Modified Steel Bar Model Incorporating Bond-Slip for Seismic Assessment of Concrete Structure." *Journal of Structural Engineering*, 2012.
- Burdette, Edwin G., et al. "Lateral Load Tests on Prestressed Concrete Piles Supporting Integral Abutments." *PCI*, 2004: 70-77.
- Burdette, Edwin G., Samuel C. Howard, Earl E. Ingram, David W. Goodpasture, and J. Harold Deatherage. "BEHAVIOR OF PRESTRESSED CONCRETE PILES SUPPORTING INTEGRAL ABUTMENTS." *ASCE*, 2004.
- Burdette, Edwin G., Samuel C. Howard, Earl E. Ingram, Harold J. Deatherage, and David W. Goodpasture. "Behavior of Pile Supported Integral Abutments." *Integral Abutment and Jointless Bridges (IAJB 2005)*. Baltimore, Maryland: FHWA, 2005. 222-253.
- Burke, Martin P. *Integral and Semi-Integral Bridges*. Wiley-Blackwell, 2009.
- Burke, Martin P. *Integral Bridges: Attributes and Limitations*. National Research Council, D.C.: Transportation Research Board, 1993, 1-8.
- Charan, Biswanath, and Pijush Topdar. "On Finite Element Analysis of Steel and RC Beams : Performance of Different Elements." *IOSR Journal of Mechanical and Civil Engineering*, 2013: 13-18.
- Cheng, Hsiao-Lin, Elisa D. Sotelino, and Wai-Fah Chen. "Sensitivity Study and Design Procedure for FRP Wrapped Reinforced Concrete Circular Columns." *International Journal of Applied Science and Engineering*, 2004: 148-162.

- Choi, Donguk, S. Vachirapanyakun, S. Kim, and S. Ha. "Ductile fiber wrapping for seismic retrofit of reinforced concrete columns." *Journal of Asian Concrete Federation*, 2015: 37-46.
- Clatrans. *CALTRANS Seismic Design Criteria* . California Departement of Transportation , 2006.
- Conte, E., A. Troncone, and M. Vena. "Nonlinear three-dimensional analysis of reinforced concrete piles subjected to horizontal loading." *Computers and Geotechnics*, 2013: 123-133.
- D'Amato, Michele, Franco Braga, Rosario Gigliotti, Sashi Kunnath, and Michelangr Laterza. "Validation of Modified Steel Bar Model Incorporating Bond-Slip for Seismic Assessment of Concrete Structures." *Journal of Structure Engineering*, 2012.
- Das, Sankar C, Reda Bakeer, Jianqiang Zhong, and Mark Schutt. *Assessment of mitigating embakment settlement with pile supported approach slabs*. Tulane University, Civil and Environmental Engineering Department, 1999.
- Duncan, J. M., and Sami Arsoy. *TRB Annual Meeting*. Transportation Research Board, 2003. 23.
- Fanous, Ann-Marie, Sri Sritharan, Muhannad Suleiman, Jinwei Huang, and Arul K. Arulmoli. "Minimum Spiral Reinforcement Requirements and Lateral Displacement Limits for Prestressed Concrete Piles in High Seismic Regions." Final Report, Department of Civil, Construction and Environmental Engineering, Iowa State University, Ames, IA, 2010, 164.

Fekadu, Petros. "Simulating the dynamic response of a soil-pile system using ABAQUS."

CHALMERS UNIVERSITY OF TECHNOLOGY, 2010.

Florida Department of Transportation. "FODT Design Standards." 2013.

Greimann, Lowell, and Amde M. Wolde-Tinsae. "DESIGN MODEL FOR PILES IN JOINTLESS BRIDGES." *ASCE*, 1988: 1354-1371.

Greimann, L. F., M. A. Wolde-Tinsae, and S. P. Yang. *Skewed Bridges With Integral Abutments*. Washington, DC: TRB, 1983, 64-72.

Greimann, L. F., P. S. Yang, S. K. Edmunds, and A. M. Wolde-Tinsae. *Design of Piles for Integral Abutment Bridges*. Final, Department of Civil Engineering, Engineering Research Institute, Iowa State University, Ames: Iowa Department of Transportation, 1984, 260.

Greimann, L. F., R. E. Abendroth, D. E. Johnson, and P. B. Ebner. *Pile Design and Tests for Integral Abutment Bridges*. Final, Department of Civil Engineering, Engineering Research Institute, Iowa State University, Ames: Iowa DOT, 1987, 302.

Jankowiak, Tomasz, and Tomasz Lodygowski. "Identification of parameters of concrete damage plasticity constitutive model." Poznan University of Technology, 2005.

Joel, Pam H, and R Park. "Simulated Seismic Load Test on Prestressed Concrete Piles and Pile-Pile Cap Connections." (*PCI Journal*) 35 , no. 6 (1990).

Jorgenson, J.L. *Behavior of Abutment Piles in an Integral Abutment Bridge*. Engineering Experiment Station, North Dakota State University, Fargo, ND: FHWA-ND-1-75-B, 1981.

- Kamel, Mounir R., Joseph V. Benak, Maher K. Tadros, and Mostafa Jamshidi.
"Prestressed Concrete Piles in Jointless Bridges." *PCI Journal* 41, no. 2 (1996):
56-67.
- Lacobucci, R. D., S. A. Sheikh, and O. Bayrak. "Retrofit of Square Concrete Columns
with Carbon Fiber-Reinforced Polymer for Seismic resistance." *ACI Struct.*, 2003:
785-794.
- Maruri, Rodolfo F., and Samer H. Petro. "Integral Abutments and Jointless Bridges
(IAJB) 2004 Survey Summary." *THE 2005 – FHWA CONFERENCE*. Baltimore,
Maryland: FHWA, 2004. 12-29.
- Mistry, Vasant C. "Integral Abutment and Jointless Bridges." *Integral Abutment and
Jointless Bridges (IAJB 2005)*. Baltimore, Maryland: Federal Highway
Administration, 2005. 3-11.
- Monley, Gregory L, and Jonathan Wu. "Tensile Reinforcement Effects on Bridge-
Approach Settlement." (Journal of Geotechnical Engineering) 1993.
- Moulton, L. K., H. V.S. GangaRao, and G. T. Halvorsen. *Tolerable Movement Criteria
for Highway Bridges*. McLean, VA: FHWA Research Development Technology,
1985, 1-109.
- Nabizadeh, Azam, Habib Tabatabai, and Mohammad A Tabatabai. "Survival Analysis of
Bridge Superstructure in Wisconsin." *Applied Sciences* (MDPI, 8, 2079), 2018.
- Oesterle, R. G., H. Tabatabai, T. J. Lawson, T. M. Refai, J. S. Volz, and A. Scanlon.
Jointless Bridges - Volume III - Summary Report. Report Submitted to the Federal
Highway Administration, 1999.

- Parvin, Azadeh , and David Brighton. "FRP Composites Strengthening of Concrete Columns under Various Loading Conditions." *Polymers* 6 (2014): 1040-1056.
- Rajan, Sen, and Gray Mullins. "Application of FRP composites for underwater piles repair." *Composites: Part B* (ScienceDirect), 2007: 751-758.
- Ramachandran, Jayram. "Analysis of Pile Foundations under Seismic Loading." CBE Institute, 2005.
- Reese, Lymon C., and William Van Impe. *Single Piles and Pile Groups Under Lateral Loading*. 2nd. London: Taylor & Francis Group, 2011.
- Shah, Bhavic. *3d Finite Element Analysis Of Integral Abutment Bridges Subjected To Thermal Loading*. Manhattan, Kansas : Kansas Sstate University, 2007.
- Song, S. T., Y. H. Chai, and Tome H. Hale. "LIMIT STATE ANALYSIS OF FIXED-HEAD CONCRETE PILES UNDER LATERAL LOADS." *13th World Conference on Earthquake Engineering*. Vancouver, B.C., Canada, 2004.
- Suh, Kwangsuk. *Underwater FRP Repair of Corrosion Damaged Prestressed Piles*. Doctoral Dissertation, Department of Civil and Environmental Engineering - College of Engineering, University of South Florida, Graduate School at Scholar Commons, 2006.
- Sushma, P., and R. Pradeep Kumar. "Numerical Modeling of Interface Between Soil and Pile to Account for Loss of Contact during Seismic Excitation." *15th World Conference on Earthquake Engineering*. Lisboa: WCEE, 2012.
- Tabatabai, Habib , and Ralph G. Oesterle . *Jointless Bridges - Volume I - Experimental Research and Field Studies*. Report Submitted to the Federal Highway Administration, 1999, 71-101.

- Tabatabai, Habib , Hassan Magbool, Ahmed Bahumdain, and Cui Fu. "Criteria and Practices of Various States for the Design of Jointless and Integral Abutment Bridges." (Research Gate) 2017.
- Tabatabai, Habib, and Azam Nabizadeh. "Evaluation of Thin Polymer Overlays for Bridge Decks." *Proceeding of Structural Faults and Repair Conference*. Edinburgh, UK, 2018.
- Tabatabai, Habib, Azam Nabizadeh, and Mohammad A Tabatabai. "Overview of Survival Analysis Techniques for Probabilistic Assessment of Bridge Service Life." *Proceeding of Structural Faults and Repair Conference*. Edinburgh, UK, 2018.
- Taheri, Omid, Reza Ziaie Moayed, and Mohammadamin Nozari. "Lateral Soil-Pile Stiffness Subjected to Vertical and Lateral Loading." *Journal of Geotechnical and Transportation Engineering* 1 (2015): 30-37.
- Tyau, Joshua S. "Finite Element Modeling of Reinforced Concrete Using 3D Solid Elements with Discrete Rebar." Brigham Young University, 2009.
- Wasserman, Edward P., and John Houston Walker. *Integral Abutments for Steel Bridges*. Vol. 2, in *Highway Structures Design Handbook*, by NSBA, 44. American Iron and Steel Institute, 1996.
- Wisconsin Department of Transportation. "WisDOT Bridge Manual." 2014.
- Wu, Hwai Chung. *Strengthening of concrete structures using fiber reinforced polymers (FRP) : design, construction and practical applications*. 2017.

Yusuf, Sümer , and Muharrem Aktaş . "Defining parameters for concrete damage
plasticity model." *CHALLENGE JOURNAL OF STRUCTURAL MECHANICS*,
2015: 149–155.

Appendix A: Girders Details for the General Model

Table A - 1: General model girder details.

Span Length	Girder Type	Girder details		*Y _{bc} (in)	*I _{bc} (in ⁴)	*h (in)	*b (in)
Short (50 ft)	36"	Y _b (in)	15.83	32.16	200681.39	64.31	9.05
		Y _t (in)	20.17				
		A (in ²)	369.00				
		I (in ⁴)	50979.00				
Medium (100 ft)	45W"	Y _b (in)	20.74	35.61	473776.20	71.21	15.74
		Y _t (in)	24.26				
		A (in ²)	692				
		I (in ⁴)	178971				
Long (150 ft)	82W"	Y _b (in)	39.68	60.03	1833359.66	120.06	12.71
		Y _t (in)	42.32				
		A (in ²)	980				
		I (in ⁴)	905453				

*Y_{bc} and *I_{bc} (composite girder with 8 in thick slab and 8 ft girder spacing).

(1 in = 25.4 mm)

$$*h = 2xY_{bc}$$

$$*b = \frac{12I}{h^3}$$

Appendix B: General Model Results for All Cases Studied.

Table B - 1: General model results: control, short span, $\Delta_g = \pm 12.7$ mm (± 0.5 in)

Δ_g		Type of Soil	θ_A	θ_p	θ_{pi}	Δ_p		Δ_{pi}		L_{ip}		Curvature	
in	mm		rad	rad	rad	in	mm	in	mm	in	mm	1/in	1/mm
0.5	12.7	Sand-Dense	0.0023	0.0029	0.0038	0.30	7.62	0.23	5.72	24.89	632.21	-6.73E-05	-2.65E-06
		Sand-Medium	0.0022	0.0028	0.0038	0.30	7.61	0.23	5.72	25.72	653.29	-7.07E-05	-2.78E-06
		Sand-Loose	0.0022	0.0028	0.0038	0.30	7.70	0.23	5.84	26.60	675.64	-7.17E-05	-2.82E-06
		Clay-Stiff	0.0026	0.0032	0.0039	0.27	6.83	0.22	5.50	18.42	467.87	-5.72E-05	-2.25E-06
		Clay-Medium	0.0026	0.0032	0.0039	0.27	6.79	0.21	5.45	19.23	488.44	-6.05E-05	-2.38E-06
		Clay-Soft	0.0025	0.0031	0.0038	0.28	7.03	0.21	5.38	20.91	531.11	-6.43E-05	-2.53E-06
-0.5	-12.7	Sand-Dense	-0.0019	-0.0021	-0.0026	-0.32	-8.14	-0.26	-6.65	27.67	702.82	2.99E-05	1.18E-06
		Sand-Medium	-0.0019	-0.0022	-0.0027	-0.32	-8.13	-0.26	-6.61	27.84	707.14	3.22E-05	1.27E-06
		Sand-Loose	-0.0018	-0.0021	-0.0026	-0.32	-8.19	-0.26	-6.72	29.15	740.41	3.25E-05	1.28E-06
		Clay-Stiff	-0.0022	-0.0025	-0.0026	-0.29	-7.43	-0.27	-6.76	15.54	394.72	1.80E-05	7.10E-07
		Clay-Medium	-0.0022	-0.0024	-0.0027	-0.30	-7.51	-0.26	-6.59	17.28	438.91	2.23E-05	8.77E-07
		Clay-Soft	-0.0021	-0.0024	-0.0027	-0.31	-7.93	-0.28	-7.03	19.58	497.33	2.55E-05	1.01E-06

Table B - 2: General model results: control, short span, $\Delta_g = \pm 25.4$ mm (± 1 in)

Δ_g		Type of Soil	θ_A	θ_p	θ_{pi}	Δ_p		Δ_{pi}		L_{ip}		Curvature	
in	mm		rad	rad	rad	in	mm	in	mm	in	mm	1/in	1/mm
1	25.4	Sand-Dense	0.0038	0.0051	0.0082	0.67	16.98	0.48	12.20	28.42	721.87	-2.05E-04	-8.06E-06
		Sand-Medium	0.0037	0.0050	0.0085	0.67	17.09	0.49	12.32	29.71	754.63	-2.18E-04	-8.58E-06
		Sand-Loose	0.0036	0.0048	0.0085	0.68	17.27	0.47	11.86	30.56	776.22	-2.18E-04	-8.60E-06
		Clay-Stiff	0.0050	0.0063	0.0086	0.57	14.52	0.45	11.48	20.16	512.06	-1.87E-04	-7.37E-06
		Clay-Medium	0.0049	0.0062	0.0086	0.57	14.47	0.42	10.65	21.07	535.18	-1.98E-04	-7.78E-06
		Clay-Soft	0.0045	0.0059	0.0086	0.60	15.13	0.45	11.39	23.07	585.98	-2.07E-04	-8.16E-06
-1	-25.4	Sand-Dense	-0.0036	-0.0043	-0.0062	-0.66	-16.88	-0.51	-12.95	30.14	765.56	1.05E-04	4.12E-06
		Sand-Medium	-0.0035	-0.0043	-0.0064	-0.66	-16.83	-0.50	-12.80	30.57	776.48	1.15E-04	4.52E-06
		Sand-Loose	-0.0034	-0.0041	-0.0063	-0.68	-17.15	-0.52	-13.21	31.95	811.53	1.17E-04	4.61E-06
		Clay-Stiff	-0.0047	-0.0054	-0.0062	-0.58	-14.64	-0.51	-13.05	16.84	427.74	6.98E-05	2.75E-06
		Clay-Medium	-0.0046	-0.0054	-0.0063	-0.58	-14.82	-0.50	-12.68	18.50	469.90	8.01E-05	3.15E-06
		Clay-Soft	-0.0043	-0.0050	-0.0061	-0.60	-15.27	-0.50	-12.71	20.92	531.37	8.52E-05	3.35E-06

Table B - 3: General model results: control, short span, $\Delta_g = \pm 50.8$ mm (± 2 in)

Δ_g		Type of Soil	θ_A	θ_p	θ_{pi}	Δ_p		Δ_{pi}		L_{ip}		Curvature	
in	mm		rad	rad	rad	in	mm	in	mm	in	mm	1/in	1/mm
2	50.8	Sand-Dense	0.0055	0.0077	0.0203	1.55	39.34	1.03	26.09	30.49	774.45	-7.89E-04	-3.11E-05
		Sand-Medium	0.0051	0.0073	0.0207	1.56	39.60	1.04	26.44	31.67	804.42	-8.20E-04	-3.23E-05
		Sand-Loose	0.0049	0.0071	0.0205	1.57	39.84	1.06	26.87	32.28	819.91	-8.11E-04	-3.19E-05
		Clay-Stiff	0.0085	0.0112	0.0216	1.29	32.85	0.89	22.70	21.02	533.91	-8.54E-04	-3.36E-05
		Clay-Medium	0.0081	0.0108	0.0220	1.30	32.96	0.90	22.78	21.92	556.77	-8.85E-04	-3.48E-05
		Clay-Soft	0.0071	0.0098	0.0223	1.38	34.99	0.92	23.30	24.20	614.68	-9.18E-04	-3.62E-05
-2	-50.8	Sand-Dense	-0.0058	-0.0077	-0.0168	-1.45	-36.85	-1.04	-26.36	30.44	773.18	5.40E-04	2.13E-05
		Sand-Medium	-0.0051	-0.0070	-0.0176	-1.52	-38.53	-1.10	-27.86	32.70	830.58	6.08E-04	2.39E-05
		Sand-Loose	-0.0048	-0.0067	-0.0175	-1.54	-39.20	-1.07	-27.24	33.76	857.50	6.06E-04	2.38E-05
		Clay-Stiff	-0.0086	-0.0107	-0.0162	-1.22	-31.06	-0.95	-24.15	21.18	537.97	4.26E-04	1.68E-05
		Clay-Medium	-0.0082	-0.0103	-0.0168	-1.26	-32.04	-0.97	-24.69	22.51	571.75	4.84E-04	1.91E-05
		Clay-Soft	-0.0072	-0.0103	-0.0169	-1.34	-34.00	-1.01	-25.65	25.15	638.81	5.36E-04	2.11E-05

Table B - 4: General model results: CFRP, short span, $\Delta_g = \pm 12.7$ mm (± 0.5 in)

Δ_g		Type of Soil	θ_A	θ_p	θ_{pi}	Δ_p		Δ_{pi}		L_{ip}		Curvature	
in	mm		rad	rad	rad	in	mm	in	mm	in	mm	1/in	1/mm
0.5	12.7	Sand-Dense	0.0023	0.0029	0.0037	0.30	7.64	0.23	5.77	25.25	641.35	-6.01E-05	-2.37E-06
		Sand-Medium	0.0022	0.0029	0.0038	0.30	7.59	0.23	5.72	26.09	662.69	-6.31E-05	-2.49E-06
		Sand-Loose	0.0022	0.0028	0.0037	0.30	7.68	0.23	5.84	27	685.80	-6.41E-05	-2.52E-06
		Clay-Stiff	0.0026	0.0033	0.0038	0.26	6.68	0.21	5.35	18.55	471.17	-5.04E-05	-1.98E-06
		Clay-Medium	0.0026	0.0032	0.0038	0.27	6.77	0.21	5.44	19.35	491.49	-5.33E-05	-2.10E-06
		Clay-Soft	0.0025	0.0031	0.0038	0.28	7.01	0.21	5.38	21.13	536.70	-5.69E-05	-2.24E-06
-0.5	-12.7	Sand-Dense	-0.0019	-0.0022	-0.0026	-0.32	-8.07	-0.26	-6.56	27	685.80	2.63E-05	1.04E-06
		Sand-Medium	-0.0018	-0.0022	-0.0026	-0.32	-8.00	-0.26	-6.51	28.29	718.57	2.82E-05	1.11E-06
		Sand-Loose	-0.0018	-0.0021	-0.0026	-0.32	-8.22	-0.26	-6.72	29.25	742.95	2.98E-05	1.17E-06
		Clay-Stiff	-0.0022	-0.0025	-0.0026	-0.29	-7.43	-0.27	-6.75	15.41	391.41	1.55E-05	6.12E-07
		Clay-Medium	-0.0021	-0.0024	-0.0026	-0.29	-7.48	-0.26	-6.57	17.28	438.91	1.93E-05	7.58E-07
		Clay-Soft	-0.0020	-0.0024	-0.0026	-0.31	-7.79	-0.27	-6.91	19.67	499.62	2.19E-05	8.64E-07

Table B - 5: General model results: CFRP, short span, $\Delta_g = \pm 25.4$ mm (± 1 in)

Δ_g		Type of Soil	θ_A	θ_p	θ_{pi}	Δ_p		Δ_{pi}		L_{ip}		Curvature	
in	mm		rad	rad	rad	in	mm	in	mm	in	mm	1/in	1/mm
1	25.4	Sand-Dense	0.0038	0.0051	0.0076	0.67	16.92	0.48	12.30	29.40	746.76	-1.61E-04	-6.33E-06
		Sand-Medium	0.0038	0.0052	0.0083	0.67	16.97	0.46	11.65	31.15	791.21	-1.82E-04	-7.18E-06
		Sand-Loose	0.0036	0.0051	0.0082	0.68	17.15	0.47	11.89	32.04	813.82	-1.83E-04	-7.20E-06
		Clay-Stiff	0.0050	0.0065	0.0083	0.56	14.13	0.41	10.43	20.70	525.78	-1.54E-04	-6.07E-06
		Clay-Medium	0.0049	0.0064	0.0084	0.57	14.38	0.42	10.66	21.71	551.43	-1.62E-04	-6.39E-06
		Clay-Soft	0.0046	0.0061	0.0084	0.59	15.03	0.42	10.69	23.91	607.31	-1.71E-04	-6.74E-06
-1	-25.4	Sand-Dense	-0.0037	-0.0045	-0.0060	-0.65	-16.47	-0.49	-12.57	30.64	778.26	8.75E-05	3.44E-06
		Sand-Medium	-0.0036	-0.0044	-0.0063	-0.66	-16.88	-0.51	-12.89	32.24	818.90	9.91E-05	3.90E-06
		Sand-Loose	-0.0035	-0.0043	-0.0062	-0.67	-17.02	-0.52	-13.11	33.27	845.06	1.02E-04	4.00E-06
		Clay-Stiff	-0.0047	-0.0055	-0.0060	-0.57	-14.59	-0.51	-13.02	16.96	430.78	5.69E-05	2.24E-06
		Clay-Medium	-0.0047	-0.0054	-0.0061	-0.58	-14.75	-0.50	-12.64	18.68	474.47	6.54E-05	2.57E-06
		Clay-Soft	-0.0043	-0.0051	-0.0060	-0.60	-15.31	-0.50	-12.78	21.46	545.08	7.23E-05	2.85E-06

Table B - 6: General model results: CFRP, short span, $\Delta_g = \pm 50.8$ mm (± 2 in)

Δ_g		Type of Soil	θ_A	θ_p	θ_{pi}	Δ_p		Δ_{pi}		L_{ip}		Curvature	
in	mm		rad	rad	rad	in	mm	in	mm	in	mm	1/in	1/mm
2	50.8	Sand-Dense	0.005897	0.009107	0.0185	1.52	38.61	0.99	25.09	35.30	896.62	-5.11E-04	-2.01E-05
		Sand-Medium	0.005525	0.008791	0.0189	1.53	38.81	1.00	25.31	36.65	930.91	-5.31E-04	-2.09E-05
		Sand-Loose	0.005364	0.008585	0.0188	1.54	39.07	0.95	24.19	37.19	944.63	-5.27E-04	-2.07E-05
		Clay-Stiff	0.008977	0.012752	0.0193	1.23	31.32	0.88	22.23	23.43	595.12	-5.26E-04	-2.07E-05
		Clay-Medium	0.008609	0.012362	0.0197	1.26	32.05	0.84	21.32	24.77	629.16	-5.43E-04	-2.14E-05
		Clay-Soft	0.007678	0.011472	0.01986	1.34	34.02	0.85	21.71	27.75	704.85	-5.67E-04	-2.23E-05
-2	-50.8	Sand-Dense	-0.00635	-0.00883	-0.0156	-1.41	-35.81	-0.97	-24.67	33.77	857.76	3.69E-04	1.45E-05
		Sand-Medium	-0.00547	-0.0081	-0.0163	-1.49	-37.76	-0.99	-25.15	36.95	938.53	4.15E-04	1.63E-05
		Sand-Loose	-0.00547	-0.00807	-0.0163	-1.49	-37.76	-0.99	-25.15	36.95	938.53	4.15E-04	1.63E-05
		Clay-Stiff	-0.00886	-0.01129	-0.0150	-1.20	-30.57	-0.95	-24.09	22.72	577.09	2.91E-04	1.14E-05
		Clay-Medium	-0.00844	-0.01098	-0.0156	-1.24	-31.43	-0.92	-23.49	24.50	622.30	3.27E-04	1.29E-05
		Clay-Soft	-0.0075	-0.01013	-0.0158	-1.31	-33.39	-0.95	-24.25	27.82	706.63	3.64E-04	1.43E-05

Table B - 7: General model results: control, medium span, $\Delta_g = \pm 12.7$ mm (± 0.5 in)

Δ_g		Type of Soil	θ_A	θ_p	θ_{pi}	Δ_p		Δ_{pi}		L_{ip}		Curvature	
in	mm		rad	rad	rad	in	mm	in	mm	in	mm	1/in	1/mm
0.5	12.7	Sand-Dense	0.0014	0.0023	0.0040	0.31	7.87	0.22	5.59	31.03	788.16	-1.07E-04	-4.23E-06
		Sand-Medium	0.0013	0.0022	0.0039	0.32	8.13	0.22	5.69	31.70	805.18	-1.05E-04	-4.15E-06
		Sand-Loose	0.0013	0.0021	0.0039	0.32	8.16	0.23	5.79	32.37	822.20	-1.05E-04	-4.15E-06
		Clay-Stiff	0.0017	0.0026	0.0039	0.28	7.02	0.20	5.15	23.90	607.06	-9.65E-05	-3.80E-06
		Clay-Medium	0.0016	0.0025	0.0039	0.28	7.10	0.21	5.22	24.93	633.22	-9.95E-05	-3.92E-06
		Clay-Soft	0.0015	0.0024	0.0039	0.29	7.37	0.22	5.49	26.75	679.45	-1.02E-04	-4.00E-06
-0.5	-12.7	Sand-Dense	-0.0012	-0.0016	-0.0025	-0.32	-8.16	-0.25	-6.37	34.18	868.17	4.77E-05	1.88E-06
		Sand-Medium	-0.0012	-0.0016	-0.0026	-0.33	-8.35	-0.26	-6.55	35.07	890.78	5.06E-05	1.99E-06
		Sand-Loose	-0.0011	-0.0016	-0.0025	-0.33	-8.35	-0.26	-6.60	35.81	909.57	4.97E-05	1.95E-06
		Clay-Stiff	-0.0014	-0.0019	-0.0024	-0.30	-7.67	-0.25	-6.47	24.09	611.89	4.12E-05	1.62E-06
		Clay-Medium	-0.0013	-0.0018	-0.0025	-0.31	-7.83	-0.26	-6.61	25.93	658.62	4.57E-05	1.80E-06
		Clay-Soft	-0.0012	-0.0017	-0.0024	-0.32	-8.16	-0.27	-6.77	28.27	718.06	4.68E-05	1.84E-06

Table B - 8: General model results: control, medium span, $\Delta_g = \pm 25.4$ mm (± 1 in)

Δ_g		Type of Soil	θ_A	θ_p	θ_{pi}	Δ_p		Δ_{pi}		L_{ip}		Curvature	
in	mm		rad	rad	rad	in	mm	in	mm	in	mm	1/in	1/mm
1	25.4	Sand-Dense	0.0022	0.0038	0.0089	0.70	17.86	0.49	12.57	32.71	830.83	-2.94E-04	-1.16E-05
		Sand-Medium	0.0021	0.0037	0.0089	0.72	18.22	0.48	12.15	33.86	860.04	-2.96E-04	-1.16E-05
		Sand-Loose	0.0020	0.0036	0.0088	0.72	18.34	0.49	12.35	34.53	877.06	-2.94E-04	-1.16E-05
		Clay-Stiff	0.0030	0.0049	0.0088	0.60	15.12	0.42	10.73	24.46	621.28	-2.84E-04	-1.12E-05
		Clay-Medium	0.0029	0.0048	0.0090	0.60	15.36	0.43	10.94	25.41	645.41	-2.98E-04	-1.17E-05
		Clay-Soft	0.0026	0.0044	0.0089	0.63	16.04	0.43	10.92	27.52	699.01	-3.01E-04	-1.18E-05
-1	-25.4	Sand-Dense	-0.0022	-0.0032	-0.0062	-0.68	-17.26	-0.51	-13.02	35.19	893.83	1.53E-04	6.03E-06
		Sand-Medium	-0.0021	-0.0031	-0.0062	-0.69	-17.41	-0.52	-13.22	36.32	922.53	1.56E-04	6.14E-06
		Sand-Loose	-0.0020	-0.0030	-0.0063	-0.70	-17.77	-0.51	-13.08	37.23	945.64	1.58E-04	6.23E-06
		Clay-Stiff	-0.0029	-0.0039	-0.0058	-0.61	-15.45	-0.49	-12.57	24.05	610.87	1.29E-04	5.09E-06
		Clay-Medium	-0.0027	-0.0038	-0.0059	-0.62	-15.67	-0.50	-12.81	25.80	655.32	1.38E-04	5.43E-06
		Clay-Soft	-0.0025	-0.0036	-0.0059	-0.66	-16.68	-0.53	-13.36	28.29	718.57	1.46E-04	5.73E-06

Table B - 9: General model results: control, medium span, $\Delta_g = \pm 50.8$ mm (± 2 in)

Δ_g		Type of Soil	θ_A	θ_p	θ_{pi}	Δ_p		Δ_{pi}		L_{ip}		Curvature	
in	mm		rad	rad	rad	in	mm	in	mm	in	mm	1/in	1/mm
2	50.8	Sand-Dense	0.0029	0.0054	0.0214	1.61	40.90	1.08	27.51	32.13	816.10	-9.96E-04	-3.92E-05
		Sand-Medium	0.0027	0.0051	0.0217	1.64	41.56	1.11	28.28	33.20	843.28	-1.01E-03	-3.98E-05
		Sand-Loose	0.0026	0.0050	0.0215	1.64	41.69	1.05	26.76	33.72	856.49	-9.98E-04	-3.93E-05
		Clay-Stiff	0.0048	0.0082	0.0233	1.37	34.84	0.95	24.07	22.74	577.60	-1.20E-03	-4.74E-05
		Clay-Medium	0.0045	0.0078	0.0234	1.40	35.47	0.90	22.88	23.68	601.47	-1.21E-03	-4.77E-05
		Clay-Soft	0.0039	0.0069	0.0237	1.47	37.34	0.99	25.14	26.05	661.67	-1.21E-03	-4.75E-05
-2	-50.8	Sand-Dense	-0.0031	-0.0054	-0.0181	-1.54	-39.02	-1.10	-27.94	32.08	814.83	7.62E-04	3.00E-05
		Sand-Medium	-0.0027	-0.0048	-0.0182	-1.59	-40.30	-1.11	-28.12	34.73	882.14	7.61E-04	3.00E-05
		Sand-Loose	-0.0024	-0.0045	-0.0182	-1.63	-41.30	-1.15	-29.27	36.04	915.42	7.60E-04	2.99E-05
		Clay-Stiff	-0.0047	-0.0075	-0.0177	-1.36	-34.44	-1.01	-25.63	24.79	629.67	7.18E-04	2.83E-05
		Clay-Medium	-0.0044	-0.0071	-0.0183	-1.40	-35.48	-1.05	-26.55	25.86	656.84	7.73E-04	3.04E-05
		Clay-Soft	-0.0038	-0.0063	-0.0182	-1.47	-37.25	-1.07	-27.15	28.26	717.80	7.90E-04	3.11E-05

Table B - 10: General model results: CFRP, medium span, $\Delta_g = \pm 12.7$ mm (± 0.5 in)

Δ_g		Type of Soil	θ_A	θ_p	θ_{pi}	Δ_p		Δ_{pi}		L_{ip}		Curvature	
in	mm		rad	rad	rad	in	mm	in	mm	in	mm	1/in	1/mm
0.5	12.7	Sand-Dense	0.0014	0.0023	0.0038	0.29	7.26	0.20	5.12	31.78	807.21	-9.13E-05	-3.59E-06
		Sand-Medium	0.0014	0.0023	0.0040	0.32	8.06	0.22	5.70	32.77	832.36	-9.95E-05	-3.92E-06
		Sand-Loose	0.0013	0.0022	0.0038	0.32	8.13	0.23	5.80	33.26	844.80	-9.45E-05	-3.72E-06
		Clay-Stiff	0.0017	0.0026	0.0039	0.28	6.99	0.20	5.14	23.9	607.06	-9.65E-05	-3.80E-06
		Clay-Medium	0.0016	0.0026	0.0038	0.28	7.08	0.21	5.21	25.6	650.24	-8.86E-05	-3.49E-06
		Clay-Soft	0.0015	0.0024	0.0037	0.29	7.32	0.20	5.16	27.55	699.77	-9.06E-05	-3.57E-06
-0.5	-12.7	Sand-Dense	-0.0012	-0.0016	-0.0025	-0.32	-8.08	-0.25	-6.34	35.56	903.22	4.24E-05	1.67E-06
		Sand-Medium	-0.0012	-0.0016	-0.0025	-0.32	-8.17	-0.25	-6.42	35.99	914.15	4.47E-05	1.76E-06
		Sand-Loose	-0.0012	-0.0016	-0.0026	-0.33	-8.42	-0.26	-6.63	36.5	927.10	4.65E-05	1.83E-06
		Clay-Stiff	-0.0014	-0.0019	-0.0024	-0.30	-7.70	-0.26	-6.51	24.71	627.63	3.71E-05	1.46E-06
		Clay-Medium	-0.0013	-0.0018	-0.0024	-0.30	-7.70	-0.26	-6.51	26.61	675.89	4.02E-05	1.58E-06
		Clay-Soft	-0.0013	-0.0018	-0.0024	-0.32	-8.15	-0.27	-6.77	29.11	739.39	4.23E-05	1.66E-06

Table B - 11: General model results: CFRP, medium span, $\Delta_g = \pm 25.4$ mm (± 1 in)

Δ_g		Type of Soil	θ_A	θ_p	θ_{pi}	Δ_p		Δ_{pi}		L_{ip}		Curvature	
in	mm		rad	rad	rad	in	mm	in	mm	in	mm	1/in	1/mm
1	25.4	Sand-Dense	0.0022	0.0041	0.0083	0.70	17.74	0.47	11.99	34.78	883.41	-2.35E-04	-9.27E-06
		Sand-Medium	0.0021	0.0041	0.0087	0.71	18.07	0.48	12.24	36.14	917.96	-2.51E-04	-9.90E-06
		Sand-Loose	0.0021	0.0039	0.0085	0.72	18.19	0.49	12.44	36.76	933.70	-2.43E-04	-9.58E-06
		Clay-Stiff	0.0031	0.0049	0.0089	0.59	14.98	0.42	10.75	24.46	621.28	-2.89E-04	-1.14E-05
		Clay-Medium	0.0030	0.0051	0.0085	0.60	15.21	0.43	10.95	26.80	680.72	-2.42E-04	-9.55E-06
		Clay-Soft	0.0027	0.0048	0.0085	0.63	15.88	0.43	10.96	29.16	740.66	-2.47E-04	-9.71E-06
-1	-25.4	Sand-Dense	-0.0022	-0.0033	-0.0060	-0.68	-17.24	-0.50	-12.66	37.67	956.82	1.29E-04	5.08E-06
		Sand-Medium	-0.0021	-0.0032	-0.0060	-0.68	-17.34	-0.50	-12.75	38.39	975.11	1.34E-04	5.26E-06
		Sand-Loose	-0.0021	-0.0032	-0.0062	-0.70	-17.69	-0.51	-13.04	38.94	989.08	1.39E-04	5.45E-06
		Clay-Stiff	-0.0028	-0.0040	-0.0056	-0.61	-15.38	-0.50	-12.61	25.03	635.76	1.08E-04	4.26E-06
		Clay-Medium	-0.0027	-0.0039	-0.0057	-0.61	-15.59	-0.48	-12.30	26.91	683.51	1.17E-04	4.61E-06
		Clay-Soft	-0.0025	-0.0037	-0.0057	-0.65	-16.54	-0.52	-13.33	29.68	753.87	1.23E-04	4.84E-06

Table B - 12: General model results: CFRP, medium span, $\Delta_g = \pm 50.8$ mm (± 2 in)

Δ_g		Type of Soil	θ_A	θ_p	θ_{pi}	Δ_p		Δ_{pi}		L_{ip}		Curvature	
in	mm		rad	rad	rad	in	mm	in	mm	in	mm	1/in	1/mm
2	50.8	Sand-Dense	0.0032	0.0071	0.0193	1.58	40.15	1.00	25.28	38.06	966.72	-6.35E-04	-2.50E-05
		Sand-Medium	0.0029	0.0069	0.0197	1.61	40.86	1.02	25.95	39.13	993.90	-6.44E-04	-2.54E-05
		Sand-Loose	0.0029	0.0067	0.0195	1.61	41.00	1.04	26.31	39.74	1009.40	-6.37E-04	-2.51E-05
		Clay-Stiff	0.0048	0.0010	0.0203	1.33	33.75	0.96	24.36	22.74	577.60	-1.20E-03	-4.74E-05
		Clay-Medium	0.0049	0.0010	0.0206	1.35	34.37	0.85	21.52	28.20	716.28	-7.34E-04	-2.89E-05
		Clay-Soft	0.0043	0.0091	0.0209	1.43	36.28	0.87	22.05	30.99	787.15	-7.38E-04	-2.91E-05
-2	-50.8	Sand-Dense	-0.0034	-0.0066	-0.0162	-1.51	-38.27	-1.02	-25.82	37.50	952.50	4.90E-04	1.93E-05
		Sand-Medium	-0.0030	-0.0061	-0.0166	-1.55	-39.50	-1.02	-25.88	40.10	1018.54	4.96E-04	1.95E-05
		Sand-Loose	-0.0028	-0.0058	-0.0168	-1.59	-40.31	-1.05	-26.71	41.14	1044.96	5.05E-04	1.99E-05
		Clay-Stiff	-0.0089	-0.0113	-0.0150	-1.33	-33.79	-0.95	-24.09	27.82	706.63	2.91E-04	1.14E-05
		Clay-Medium	-0.0047	-0.0083	-0.0164	-1.36	-34.66	-0.99	-25.25	29.35	745.49	5.06E-04	1.99E-05
		Clay-Soft	-0.0041	-0.0076	-0.0165	-1.44	-36.48	-1.02	-26.00	32.30	820.42	5.15E-04	2.03E-05

Table B - 13: General model results: control, long span, $\Delta_g = \pm 12.7$ mm (± 0.5 in)

Δ_g		Type of Soil	θ_A	θ_p	θ_{pi}	Δ_p		Δ_{pi}		L_{ip}		Curvature	
in	mm		rad	rad	rad	in	mm	in	mm	in	mm	1/in	1/mm
0.5	12.7	Sand-Dense	0.0007	0.0018	0.0042	0.33	8.46	0.23	5.78	34.18	868.17	-1.35E-04	-5.32E-06
		Sand-Medium	0.0007	0.0018	0.0043	0.34	8.56	0.23	5.85	34.74	882.40	-1.39E-04	-5.49E-06
		Sand-Loose	0.0007	0.0018	0.0043	0.34	8.60	0.23	5.93	35.49	901.45	-1.38E-04	-5.44E-06
		Clay-Stiff	0.0009	0.0022	0.0042	0.29	7.41	0.21	5.23	27.12	688.85	-1.37E-04	-5.40E-06
		Clay-Medium	0.0009	0.0022	0.0042	0.29	7.47	0.21	5.28	27.88	708.15	-1.40E-04	-5.51E-06
		Clay-Soft	0.0008	0.0020	0.0042	0.30	7.72	0.22	5.55	29.70	754.38	-1.40E-04	-5.50E-06
-0.5	-12.7	Sand-Dense	-0.0007	-0.0012	-0.0025	-0.32	-8.16	-0.24	-6.15	38.81	985.77	5.96E-05	2.35E-06
		Sand-Medium	-0.0007	-0.0013	-0.0026	-0.33	-8.39	-0.25	-6.47	38.58	979.93	6.28E-05	2.47E-06
		Sand-Loose	-0.0006	-0.0012	-0.0025	-0.34	-8.51	-0.26	-6.64	39.46	1002.28	6.21E-05	2.44E-06
		Clay-Stiff	-0.0008	-0.0014	-0.0023	-0.31	-7.75	-0.25	-6.44	28.74	730.00	5.68E-05	2.24E-06
		Clay-Medium	-0.0007	-0.0014	-0.0024	-0.31	-7.87	-0.26	-6.53	29.81	757.17	6.11E-05	2.41E-06
		Clay-Soft	-0.0007	-0.0013	-0.0024	-0.32	-8.20	-0.26	-6.70	32.02	813.31	6.12E-05	2.41E-06

Table B - 14: General model results: control, long span, $\Delta_g = \pm 25.4$ mm (± 1 in)

Δ_g		Type of Soil	θ_A	θ_p	θ_{pi}	Δ_p		Δ_{pi}		L_{ip}		Curvature	
in	mm		rad	rad	rad	in	mm	in	mm	in	mm	1/in	1/mm
1	25.4	Sand-Dense	0.0011	0.0030	0.0091	0.74	18.85	0.50	12.77	34.64	879.86	-3.44E-04	-1.36E-05
		Sand-Medium	0.0010	0.0029	0.0096	0.75	19.09	0.51	12.99	35.61	904.49	-3.66E-04	-1.44E-05
		Sand-Loose	0.0010	0.0029	0.0095	0.76	19.23	0.52	13.20	36.32	922.53	-3.60E-04	-1.42E-05
		Clay-Stiff	0.0016	0.0040	0.0096	0.63	16.06	0.46	11.57	26.54	674.12	-3.88E-04	-1.53E-05
		Clay-Medium	0.0015	0.0039	0.0096	0.64	16.33	0.43	10.97	27.33	694.18	-3.94E-04	-1.55E-05
		Clay-Soft	0.0014	0.0036	0.0096	0.67	16.91	0.46	11.68	29.37	746.00	-3.92E-04	-1.54E-05
-1	-25.4	Sand-Dense	-0.0011	-0.0023	-0.0060	-0.70	-17.71	-0.53	-13.36	39.89	1013.21	1.75E-04	6.88E-06
		Sand-Medium	-0.0011	-0.0024	-0.0065	-0.72	-18.31	-0.54	-13.65	39.79	1010.67	1.94E-04	7.63E-06
		Sand-Loose	-0.0010	-0.0022	-0.0062	-0.71	-18.06	-0.52	-13.11	40.71	1034.03	1.84E-04	7.22E-06
		Clay-Stiff	-0.0015	-0.0029	-0.0055	-0.62	-15.72	-0.50	-12.62	28.04	712.22	1.66E-04	6.54E-06
		Clay-Medium	-0.0014	-0.0028	-0.0057	-0.63	-15.96	-0.50	-12.79	29.11	739.39	1.79E-04	7.04E-06
		Clay-Soft	-0.0013	-0.0026	-0.0058	-0.66	-16.76	-0.52	-13.18	31.35	796.29	1.81E-04	7.11E-06

Table B - 15: General model results: control, long span, $\Delta_g = \pm 50.8$ mm (± 2 in)

Δ_g		Type of Soil	θ_A	θ_p	θ_{pi}	Δ_p		Δ_{pi}		L_{ip}		Curvature	
in	mm		rad	rad	rad	in	mm	in	mm	in	mm	1/in	1/mm
2	50.8	Sand-Dense	0.0014	0.0042	0.0223	1.66	42.13	1.12	28.48	32.59	827.79	-1.13E-03	-4.45E-05
		Sand-Medium	0.0013	0.0040	0.0226	1.68	42.66	1.07	27.21	33.53	851.66	-1.14E-03	-4.50E-05
		Sand-Loose	0.0013	0.0039	0.0224	1.68	42.71	1.08	27.53	34.10	866.14	-1.12E-03	-4.41E-05
		Clay-Stiff	0.0024	0.0064	0.0251	1.45	36.79	0.99	25.27	23.21	589.53	-1.46E-03	-5.77E-05
		Clay-Medium	0.0023	0.0061	0.0255	1.46	37.15	0.94	23.84	24.17	613.92	-1.46E-03	-5.76E-05
		Clay-Soft	0.0019	0.0054	0.0252	1.53	38.85	1.03	26.10	26.47	672.34	-1.42E-03	-5.60E-05
-2	-50.8	Sand-Dense	-0.0013	-0.0039	-0.0180	-1.59	-40.40	-1.11	-28.12	34.11	866.39	8.38E-04	3.30E-05
		Sand-Medium	-0.0011	-0.0035	-0.0184	-1.63	-41.40	-1.15	-29.27	36.12	917.45	8.47E-04	3.33E-05
		Sand-Loose	-0.0010	-0.0033	-0.0184	-1.65	-41.97	-1.12	-28.46	36.98	939.29	8.33E-04	3.28E-05
		Clay-Stiff	-0.0022	-0.0056	-0.0185	-1.44	-36.47	-1.08	-27.33	26.11	663.19	9.09E-04	3.58E-05
		Clay-Medium	-0.0020	-0.0053	-0.0191	-1.47	-37.26	-1.10	-27.97	26.90	683.26	9.65E-04	3.80E-05
		Clay-Soft	-0.0017	-0.0046	-0.0190	-1.53	-38.86	-1.12	-28.44	29.20	741.68	9.63E-04	3.79E-05

Table B - 16: General model results: CFRP, long span, $\Delta_g = \pm 12.7$ mm (± 0.5 in)

Δ_g		Type of Soil	θ_A	θ_p	θ_{pi}	Δ_p		Δ_{pi}		L_{ip}		Curvature	
in	mm		rad	rad	rad	in	mm	in	mm	in	mm	1/in	1/mm
0.5	12.7	Sand-Dense	0.0007	0.0019	0.0041	0.33	8.44	0.23	5.83	35.81	909.57	-1.20E-04	-4.74E-06
		Sand-Medium	0.0007	0.0019	0.0042	0.34	8.52	0.23	5.87	36.08	916.43	-1.25E-04	-4.91E-06
		Sand-Loose	0.0007	0.0019	0.0042	0.34	8.57	0.23	5.95	36.85	935.99	-1.24E-04	-4.86E-06
		Clay-Stiff	0.0009	0.0023	0.0041	0.29	7.38	0.21	5.24	28.2	716.28	-1.22E-04	-4.82E-06
		Clay-Medium	0.0009	0.0022	0.0041	0.29	7.45	0.21	5.29	28.94	735.08	-1.25E-04	-4.90E-06
		Clay-Soft	0.0008	0.0020	0.0039	0.30	7.68	0.21	5.24	30.79	782.07	-1.18E-04	-4.66E-06
-0.5	-12.7	Sand-Dense	-0.0007	-0.0013	-0.0024	-0.32	-8.05	-0.25	-6.23	39.42	1001.27	5.34E-05	2.10E-06
		Sand-Medium	-0.0007	-0.0013	-0.0025	-0.32	-8.23	-0.25	-6.37	39.62	1006.35	5.60E-05	2.21E-06
		Sand-Loose	-0.0006	-0.0013	-0.0025	-0.33	-8.42	-0.25	-6.35	40.17	1020.32	5.68E-05	2.23E-06
		Clay-Stiff	-0.0008	-0.0015	-0.0023	-0.30	-7.74	-0.25	-6.44	29.71	754.63	5.15E-05	2.03E-06
		Clay-Medium	-0.0007	-0.0015	-0.0024	-0.31	-7.86	-0.25	-6.33	30.93	785.62	5.53E-05	2.18E-06
		Clay-Soft	-0.0007	-0.0014	-0.0024	-0.32	-8.18	-0.26	-6.70	33.16	842.26	5.55E-05	2.19E-06

Table B - 17: General model results: CFRP, long span, $\Delta_g = \pm 25.4$ mm (± 1 in)

Δ_g		Type of Soil	θ_A	θ_p	θ_{pi}	Δ_p		Δ_{pi}		L_{ip}		Curvature	
in	mm		rad	rad	rad	in	mm	in	mm	in	mm	1/in	1/mm
1	25.4	Sand-Dense	0.0011	0.0034	0.0089	0.73	18.62	0.48	12.23	37.45	951.23	-2.88E-04	-1.13E-05
		Sand-Medium	0.0011	0.0033	0.0092	0.75	18.93	0.49	12.44	38.25	971.55	-2.98E-04	-1.17E-05
		Sand-Loose	0.0010	0.0033	0.0091	0.75	19.00	0.50	12.60	38.99	990.35	-2.94E-04	-1.16E-05
		Clay-Stiff	0.0017	0.0045	0.0091	0.63	15.88	0.43	10.84	28.55	725.17	-3.13E-04	-1.23E-05
		Clay-Medium	0.0016	0.0043	0.0092	0.63	16.06	0.43	10.99	29.37	746.00	-3.19E-04	-1.26E-05
		Clay-Soft	0.0014	0.0040	0.0091	0.66	16.71	0.43	11.03	31.58	802.13	-3.09E-04	-1.22E-05
-1	-25.4	Sand-Dense	-0.0011	-0.0025	-0.0057	-0.68	-17.24	-0.50	-12.61	41.92	1064.77	1.47E-04	5.78E-06
		Sand-Medium	-0.0011	-0.0025	-0.0060	-0.70	-17.79	-0.51	-12.92	42.22	1072.39	1.59E-04	6.27E-06
		Sand-Loose	-0.0011	-0.0024	-0.0061	-0.70	-17.69	-0.52	-13.20	42.71	1084.83	1.61E-04	6.34E-06
		Clay-Stiff	-0.0015	-0.0030	-0.0053	-0.62	-15.63	-0.50	-12.63	29.55	750.57	1.42E-04	5.59E-06
		Clay-Medium	-0.0014	-0.0030	-0.0056	-0.63	-16.00	-0.49	-12.41	30.78	781.81	1.54E-04	6.08E-06
		Clay-Soft	-0.0013	-0.0028	-0.0056	-0.66	-16.67	-0.52	-13.21	33.18	842.77	1.54E-04	6.08E-06

Table B - 18: General model results: CFRP, long span, $\Delta_g = \pm 50.8$ mm (± 2 in)

Δ_g		Type of Soil	θ_A	θ_p	θ_{pi}	Δ_p		Δ_{pi}		L_{ip}		Curvature	
in	mm		rad	rad	rad	in	mm	in	mm	in	mm	1/in	1/mm
2	50.8	Sand-Dense	0.0016	0.0060	0.0199	1.63	41.48	1.05	26.55	39.50	1003.30	-7.08E-04	-2.79E-05
		Sand-Medium	0.0015	0.0059	0.0204	1.66	42.09	1.00	25.43	40.42	1026.67	-7.18E-04	-2.83E-05
		Sand-Loose	0.0014	0.0057	0.0202	1.66	42.14	1.01	25.75	41.04	1042.42	-7.05E-04	-2.78E-05
		Clay-Stiff	0.0027	0.0090	0.0217	1.41	35.72	0.88	22.26	28.40	721.36	-8.88E-04	-3.49E-05
		Clay-Medium	0.0025	0.0087	0.0219	1.42	36.19	0.90	22.78	29.56	750.82	-8.86E-04	-3.49E-05
		Clay-Soft	0.0022	0.0079	0.0221	1.49	37.91	0.91	23.22	32.34	821.44	-8.69E-04	-3.42E-05
-2	-50.8	Sand-Dense	-0.0015	-0.0052	-0.0163	-1.56	-39.50	-1.07	-27.28	39.60	1005.84	5.52E-04	2.18E-05
		Sand-Medium	-0.0013	-0.0048	-0.0167	-1.60	-40.62	-1.07	-27.25	42.22	1072.39	5.48E-04	2.16E-05
		Sand-Loose	-0.0012	-0.0046	-0.0168	-1.62	-41.17	-1.10	-27.83	42.88	1089.15	5.54E-04	2.18E-05
		Clay-Stiff	-0.0024	-0.0070	-0.0164	-1.40	-35.63	-1.03	-26.18	30.04	763.02	5.98E-04	2.35E-05
		Clay-Medium	-0.0022	-0.0068	-0.0171	-1.43	-36.39	-1.00	-25.30	31.20	792.48	6.25E-04	2.46E-05
		Clay-Soft	-0.0019	-0.0061	-0.0170	-1.50	-37.98	-1.02	-25.94	34.00	863.60	6.15E-04	2.42E-05

Appendix C: Localized Model Results: Lateral (Shear) Load vs. Displacement Δ_m

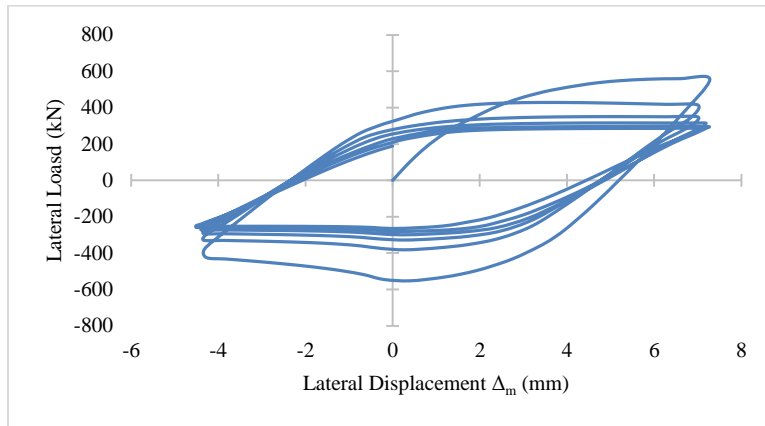


Figure C - 1: Lateral load vs. displacement Δ_m : control, dense sand, short span.

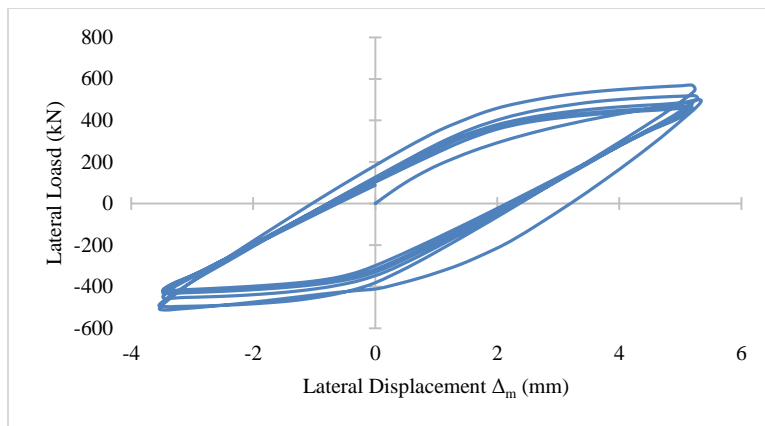


Figure C - 2: Lateral load vs. displacement Δ_m : CFRP, dense sand, short span.

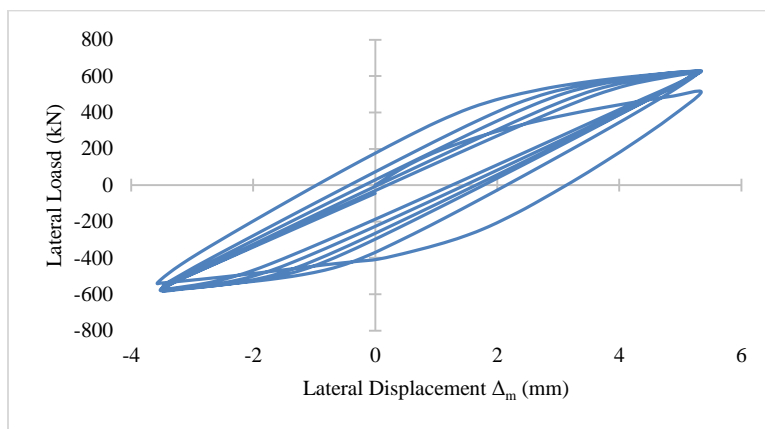


Figure C - 3: Lateral load vs. displacement Δ_m : ECFRP, dense sand, short span.

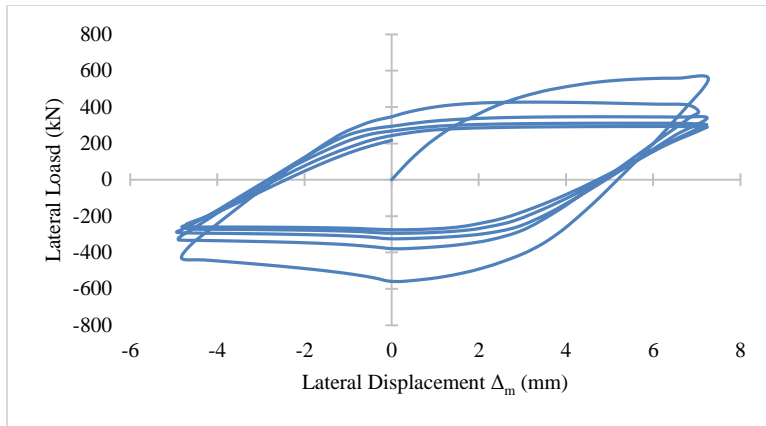


Figure C - 4: Lateral load vs. displacement Δ_m : control, medium sand, short span.

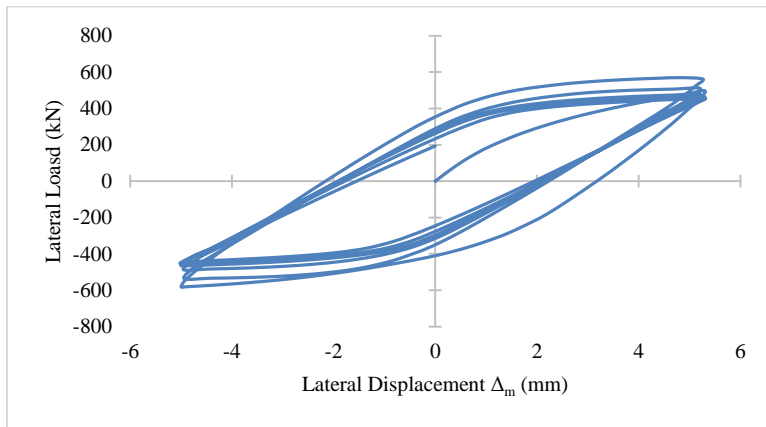


Figure C - 5: Lateral load vs. displacement Δ_m : CFRP, medium sand, short span.

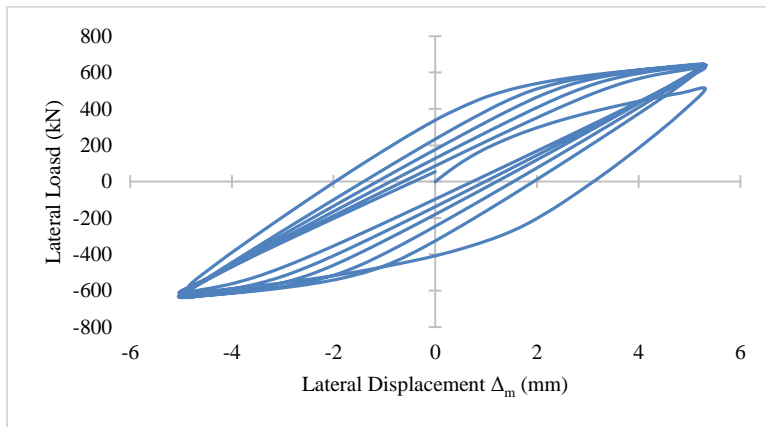


Figure C - 6: Lateral load vs. displacement Δ_m : ECFRP, medium sand, short span.

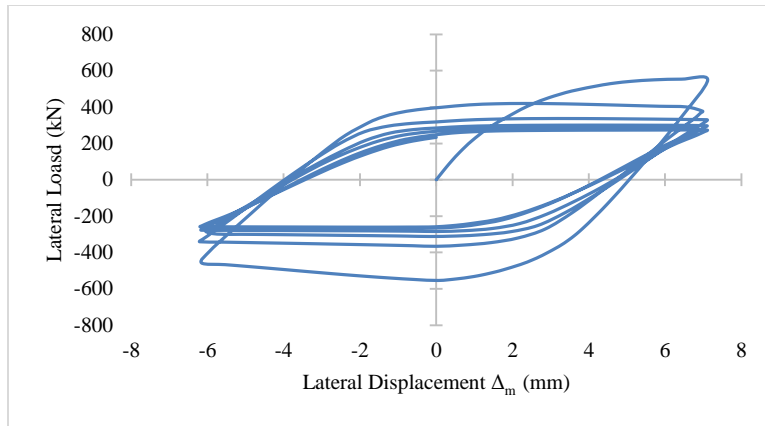


Figure C - 7: Lateral load vs. displacement Δ_m : control, loose sand, short span.

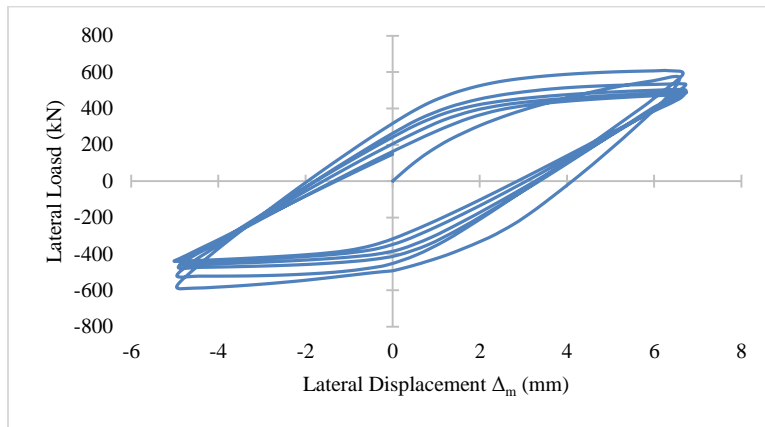


Figure C - 8: Lateral load vs. displacement Δ_m : CFRP, loose sand, short span.

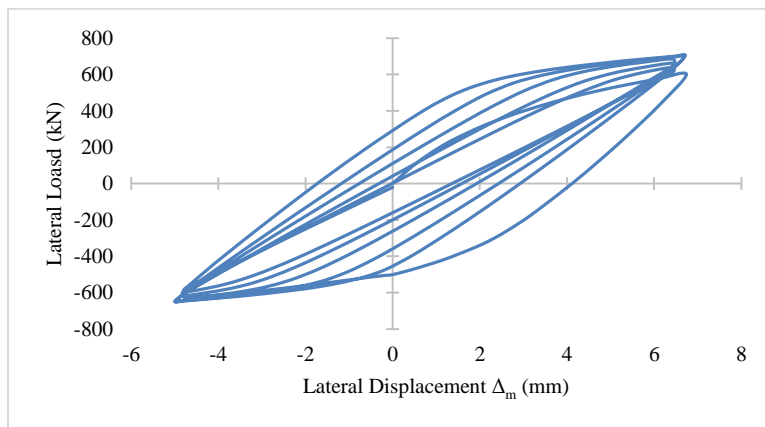


Figure C - 9: Lateral load vs. displacement Δ_m : ECFRP, loose sand, short span.

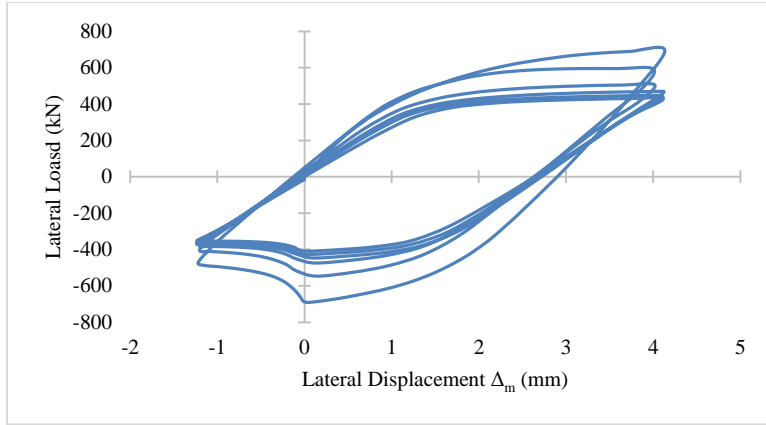


Figure C - 10: Lateral load vs. displacement Δ_m : control, stiff clay, short span.

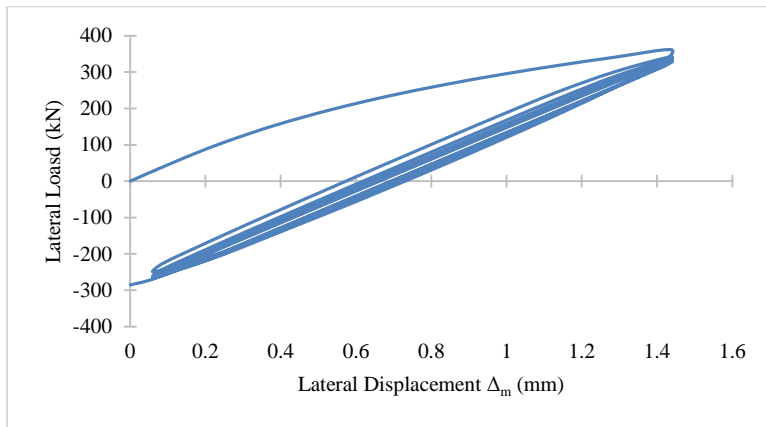


Figure C - 11: Lateral load vs. displacement Δ_m : CFRP, stiff clay, short span.

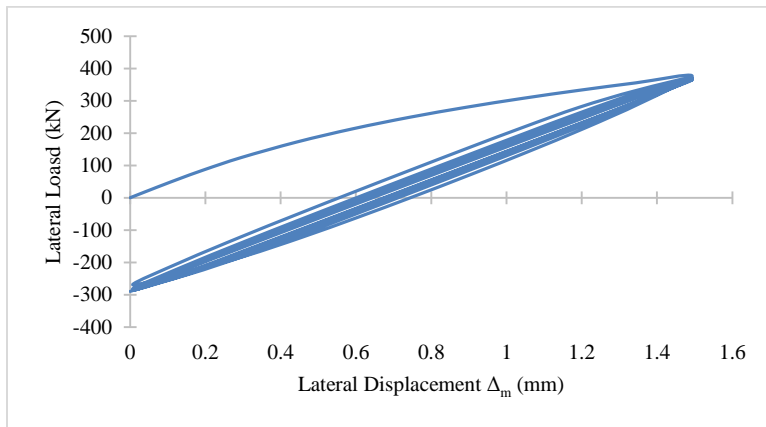


Figure C - 12: Lateral load vs. displacement Δ_m : ECFRP, stiff clay, short span.

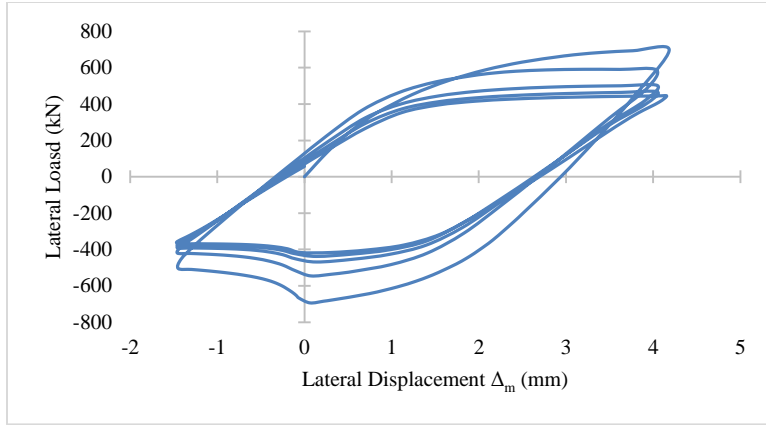


Figure C - 13: Lateral load vs. displacement Δ_m : control, medium clay, short span.

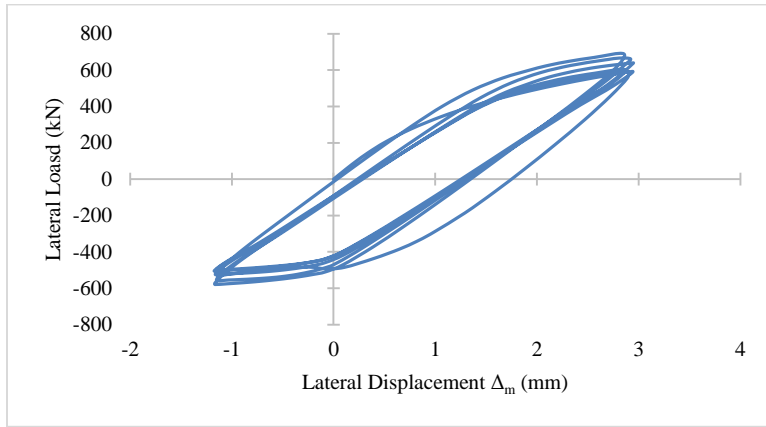


Figure C - 14: Lateral load vs. displacement Δ_m : CFRP, medium clay, short span.

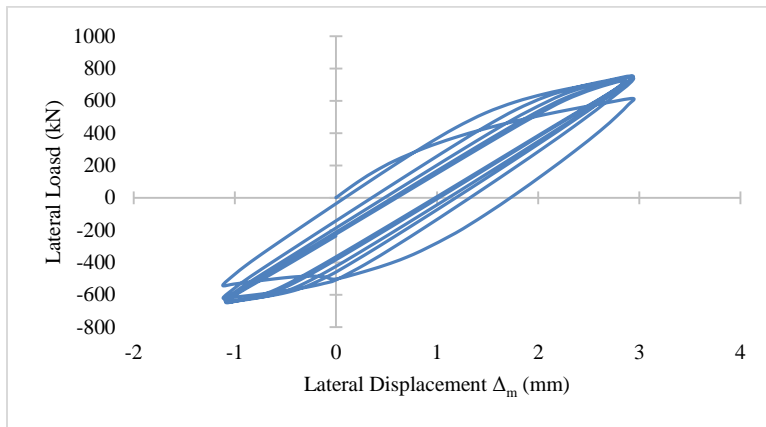


Figure C - 15: Lateral load vs. displacement Δ_m : ECFRP, medium clay, short span.

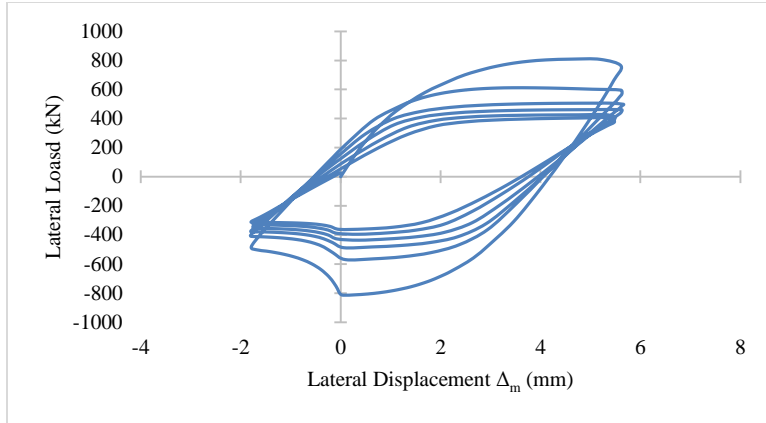


Figure C - 16: Lateral load vs. displacement Δ_m : control, soft clay, short span.

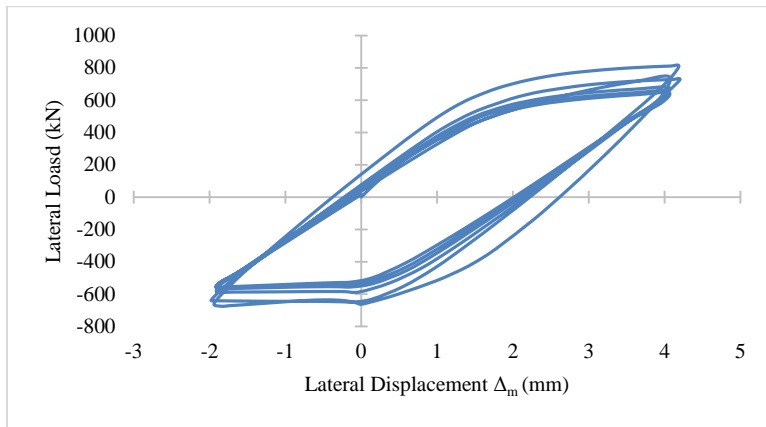


Figure C - 17: Lateral load vs. displacement Δ_m : CFRP, soft clay, short span.

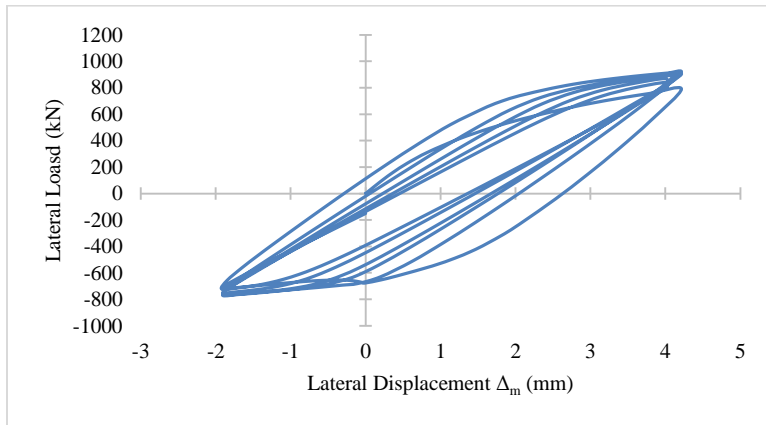


Figure C - 18: Lateral load vs. displacement Δ_m : ECFRP, soft clay, short span.

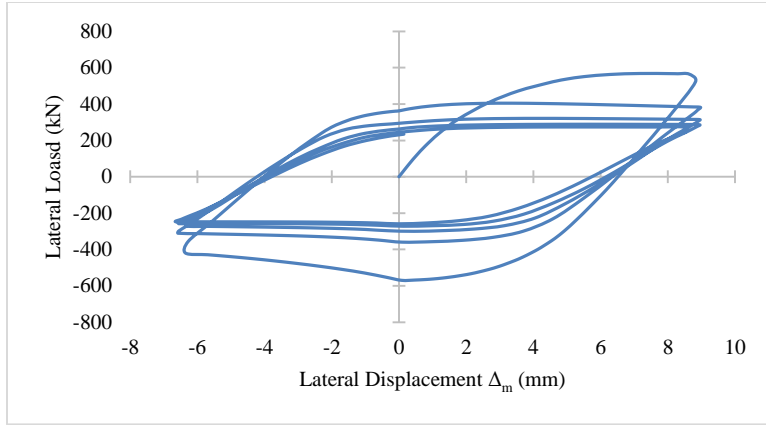


Figure C - 19: Lateral load vs. displacement Δ_m : control, dense sand, medium span.

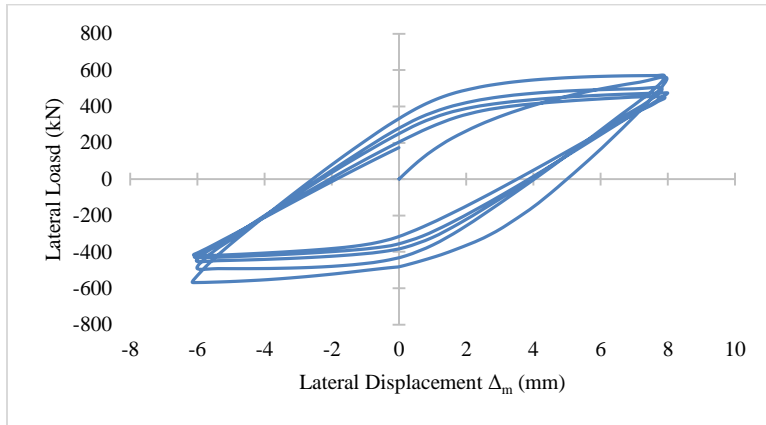


Figure C - 20: Lateral load vs. displacement Δ_m : CFRP, dense sand, medium span.

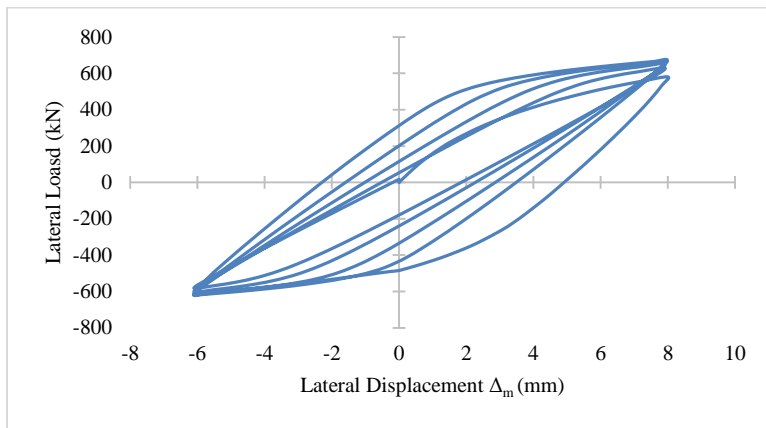


Figure C - 21: Lateral load vs. displacement Δ_m : ECFRP, dense sand, medium span.

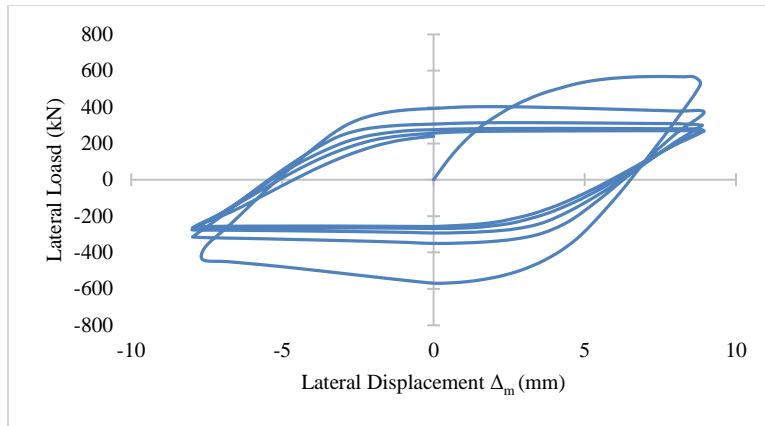


Figure C - 22: Lateral load vs. displacement Δ_m : control, medium sand, medium span.

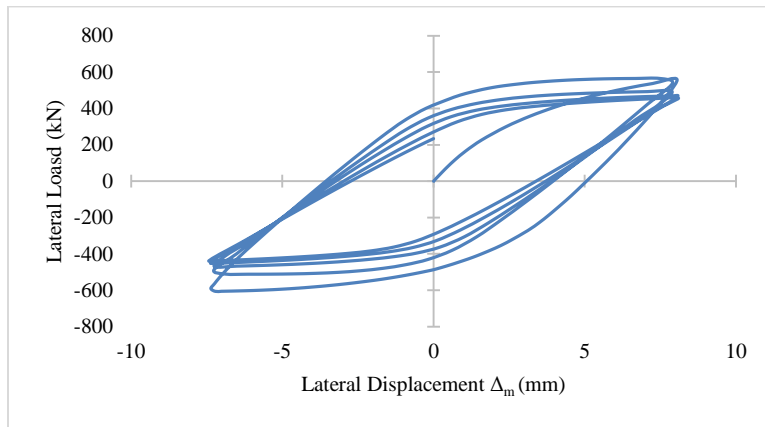


Figure C - 23: Lateral load vs. displacement Δ_m : CFRP, medium sand, medium span.

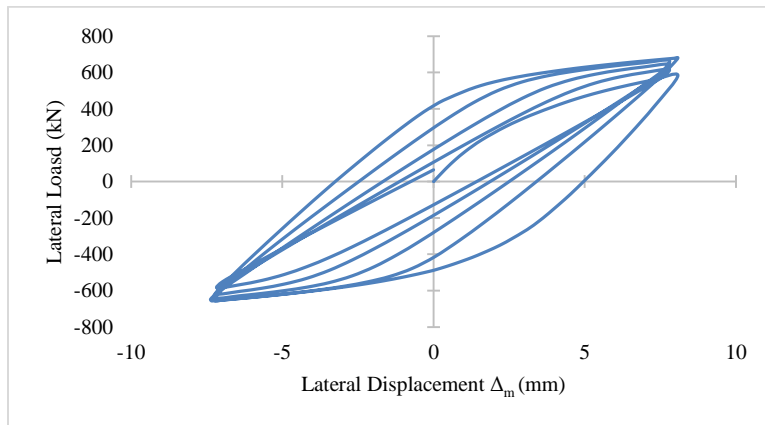


Figure C - 24: Lateral load vs. displacement Δ_m : ECFRP, medium sand, medium span.

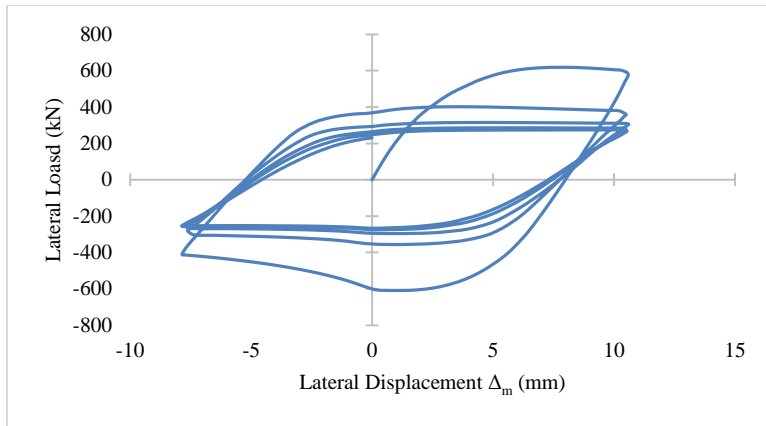


Figure C - 25: Lateral load vs. displacement Δ_m : control, loose sand, medium span.

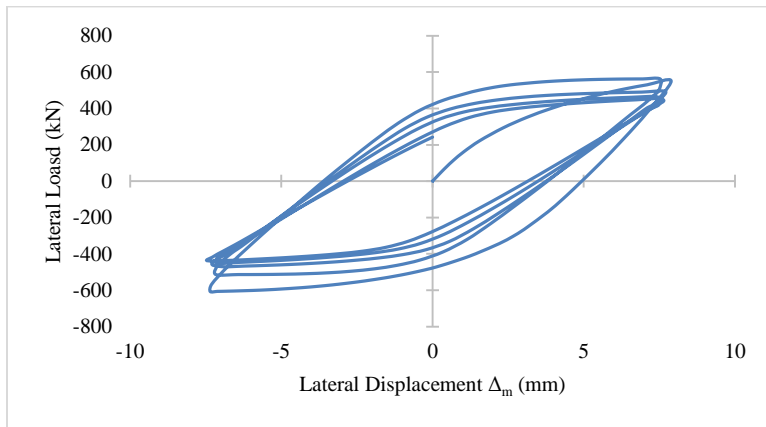


Figure C - 26: Lateral load vs. displacement Δ_m : CFRP, loose sand, medium span.

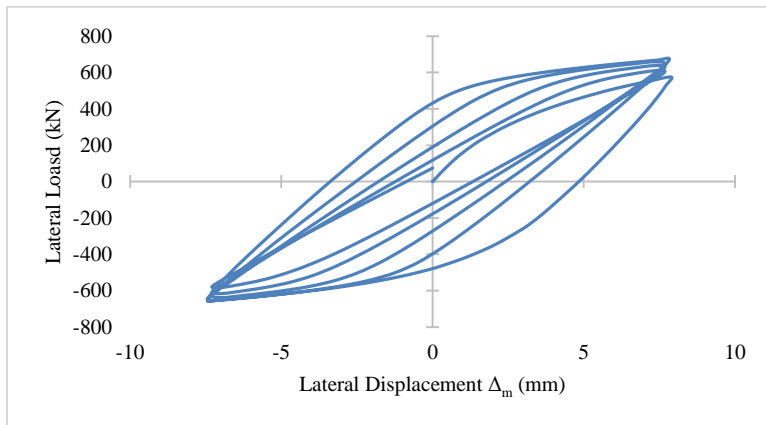


Figure C - 27: Lateral load vs. displacement Δ_m : ECFRP, loose sand, medium span.

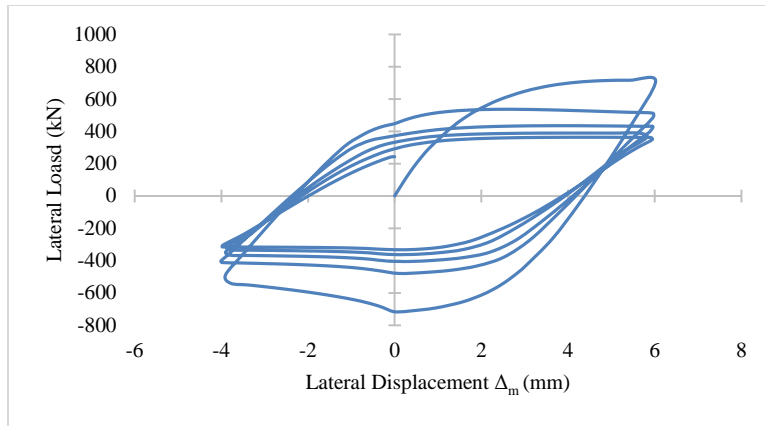


Figure C - 28: Lateral load vs. displacement Δ_m : control, stiff clay, medium span.

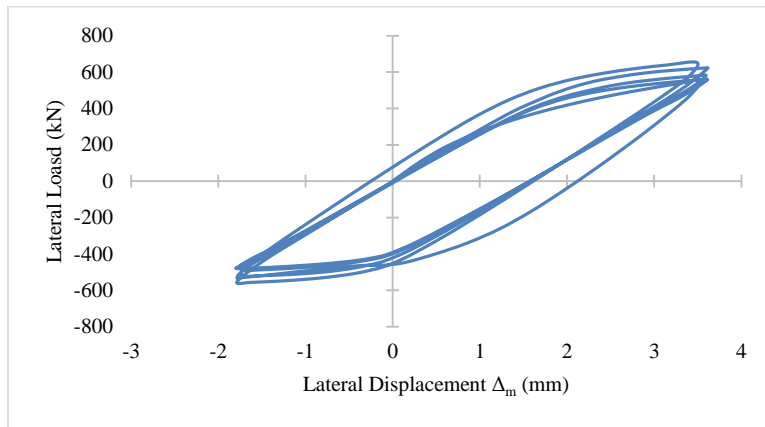


Figure C - 29: Lateral load vs. displacement Δ_m : CFRP, stiff clay, medium span.

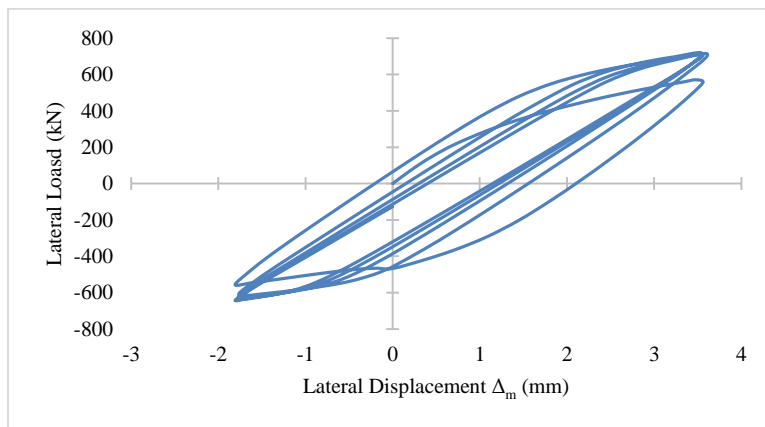


Figure C - 30: Lateral load vs. displacement Δ_m : ECFRP, stiff clay, medium span.

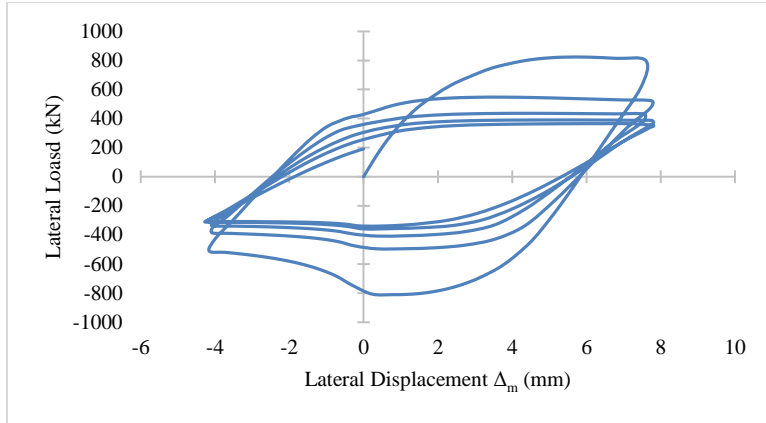


Figure C - 31: Lateral load vs. displacement Δ_m : control, medium clay, medium span.

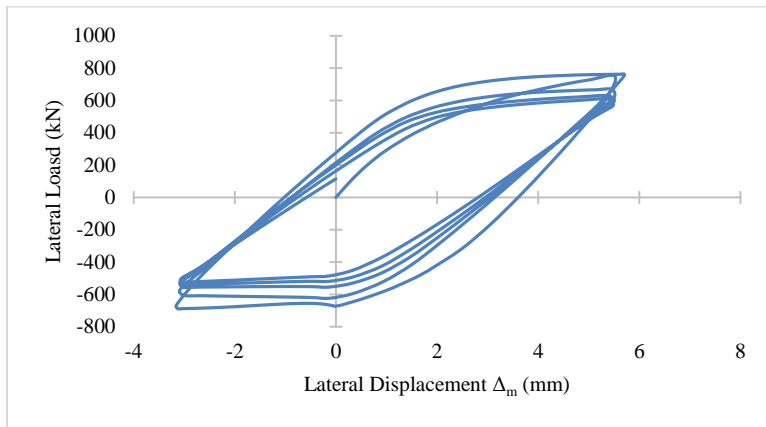


Figure C - 32: Lateral load vs. displacement Δ_m : CFRP, medium clay, medium span.

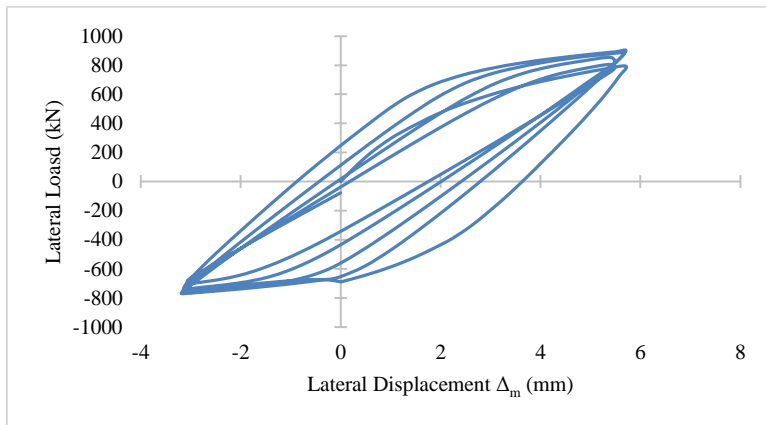


Figure C - 33: Lateral load vs. displacement Δ_m : ECFRP, medium clay, medium span.

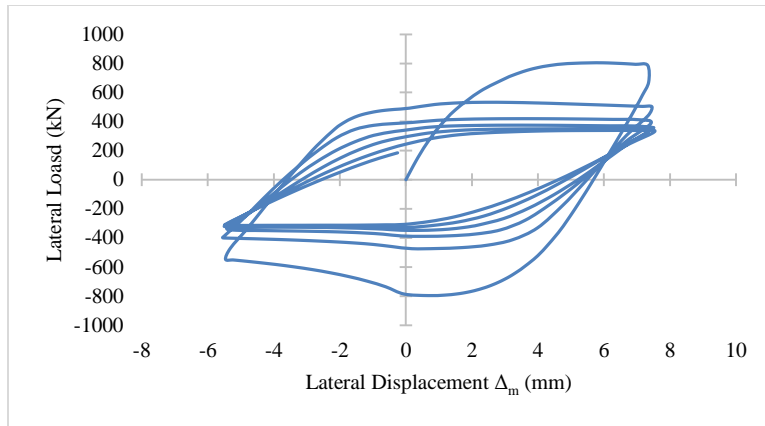


Figure C - 34: Lateral load vs. displacement Δ_m : control, soft clay, medium span.

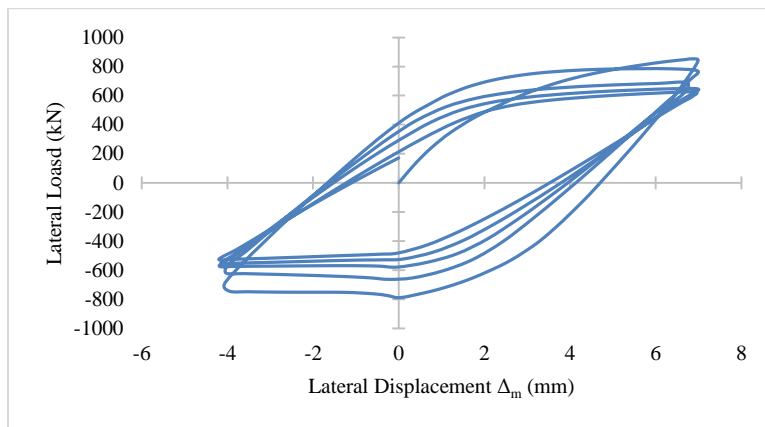


Figure C - 35: Lateral load vs. displacement Δ_m : CFRP, soft clay, medium span.

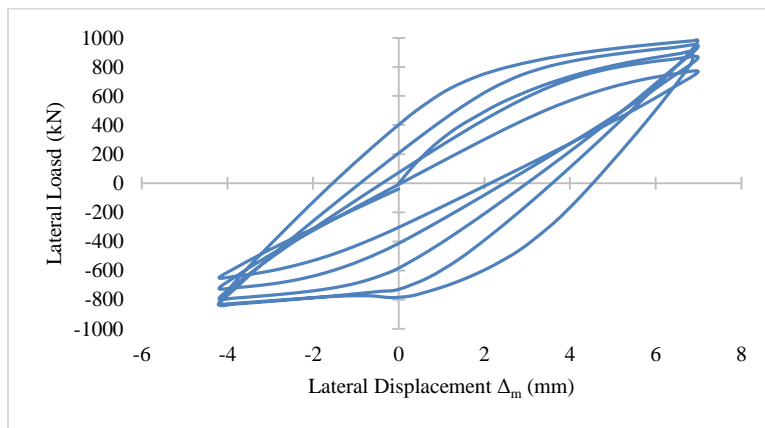


Figure C - 36: Lateral load vs. displacement Δ_m : ECFRP, soft clay, medium span.

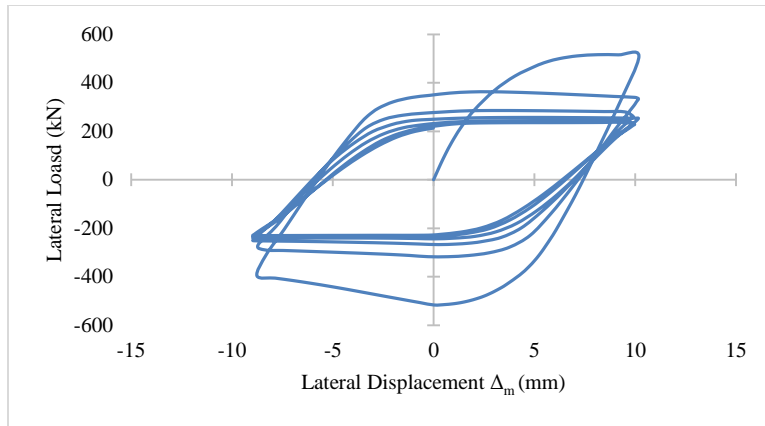


Figure C - 37: Lateral load vs. displacement Δ_m : control, dense sand, long span.

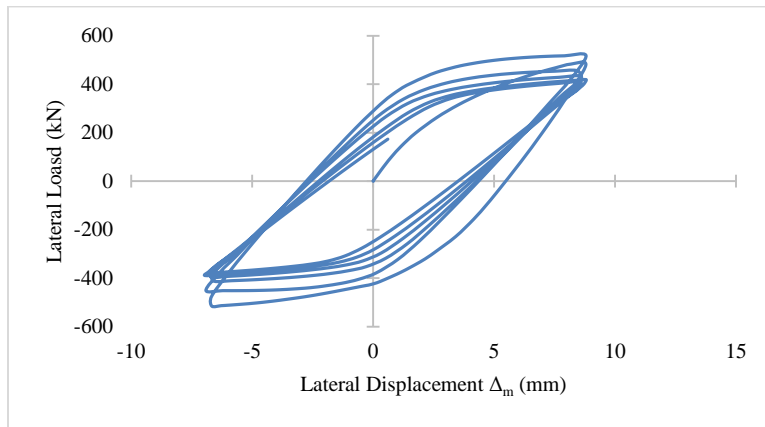


Figure C - 38: Lateral load vs. displacement Δ_m : CFRP, dense sand, long span.

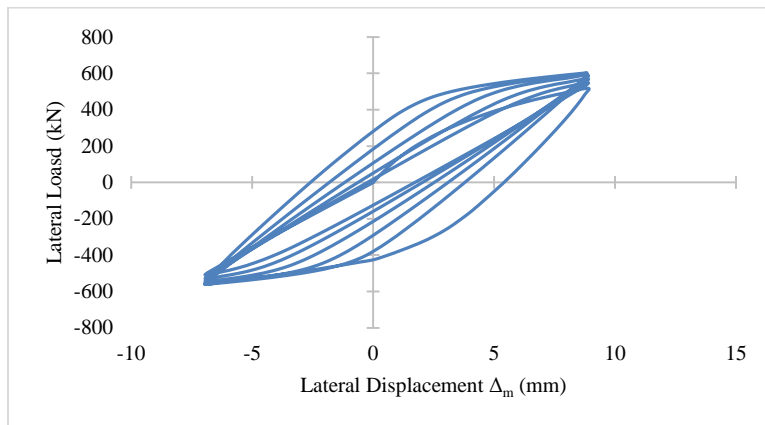


Figure C - 39: Lateral load vs. displacement Δ_m : ECFRP, dense sand, long span.

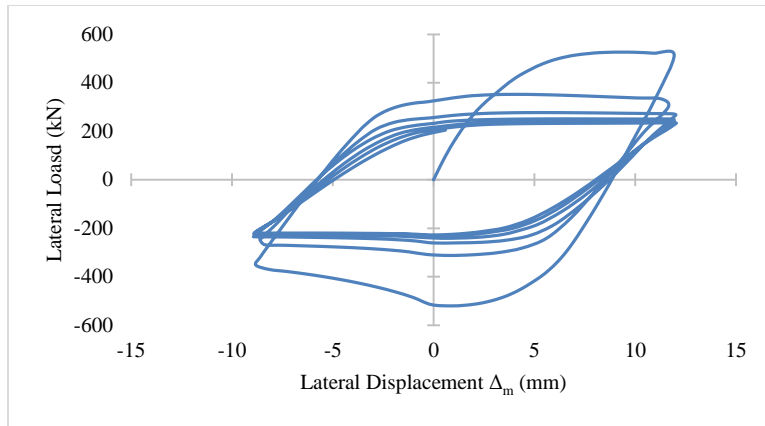


Figure C - 40: Lateral load vs. displacement Δ_m : control, medium sand, long span.

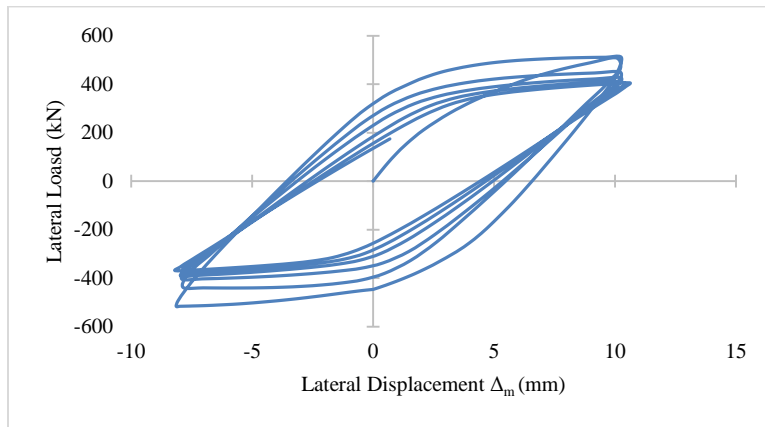


Figure C - 41: Lateral load vs. displacement Δ_m : CFRP, medium sand, long span.

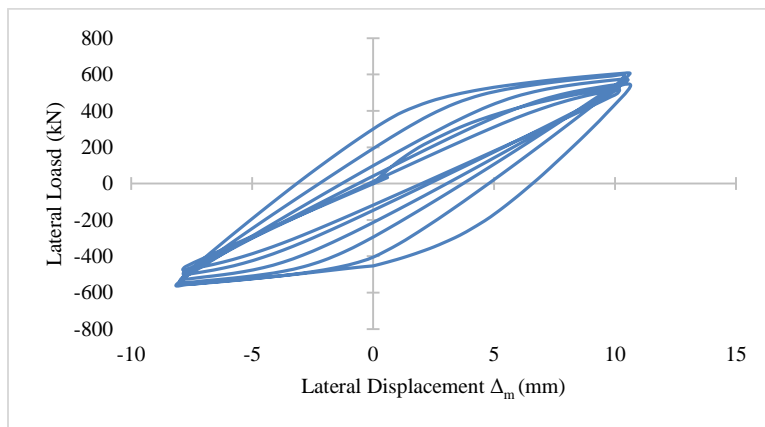


Figure C - 42: Lateral load vs. displacement Δ_m : ECFRP, medium sand, long span.

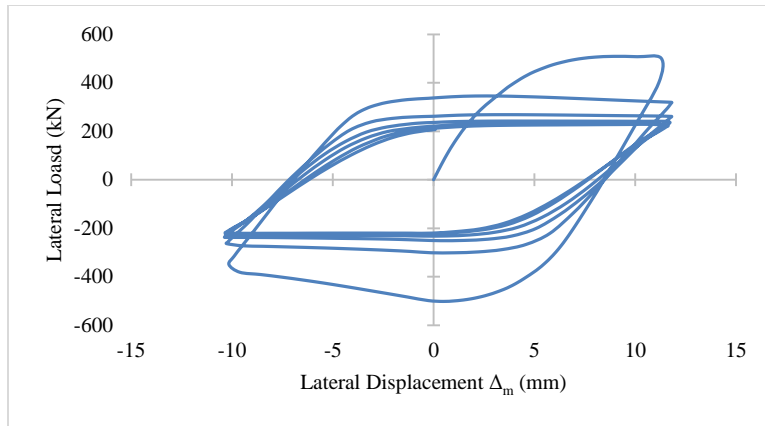


Figure C - 43: Lateral load vs. displacement Δ_m : control, loose sand, long span.

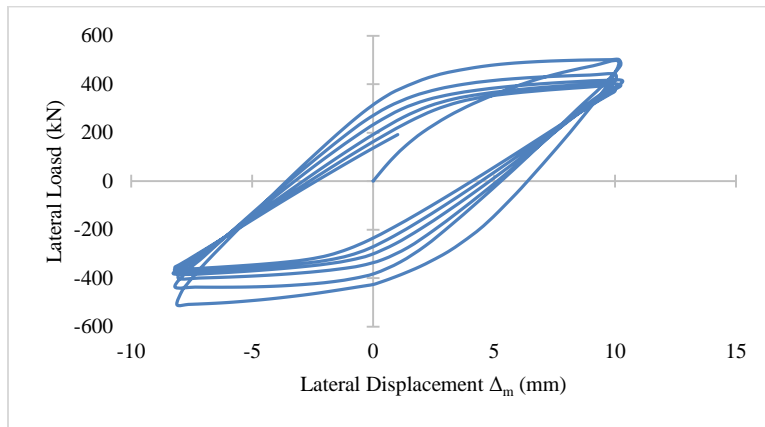


Figure C - 44: Lateral load vs. displacement Δ_m : CFRP, loose sand, long span.

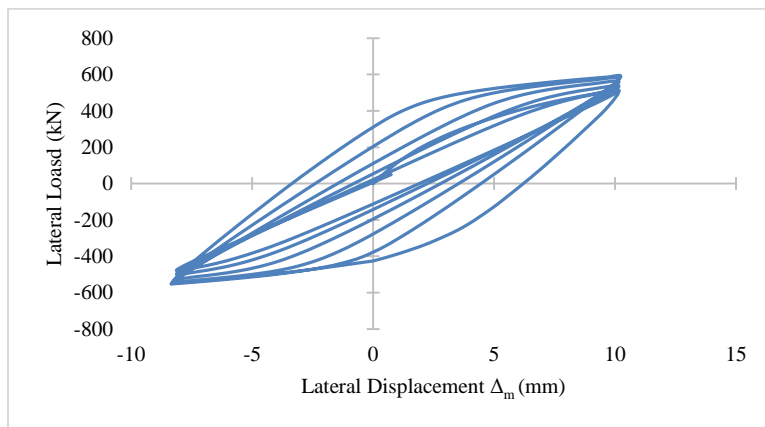


Figure C - 45: Lateral load vs. displacement Δ_m : ECFRP, loose sand, long span.

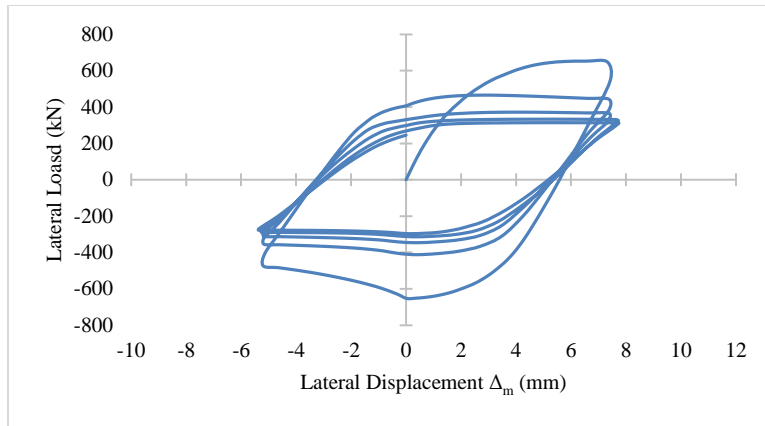


Figure C - 46: Lateral load vs. displacement Δ_m : control, stiff clay, long span.

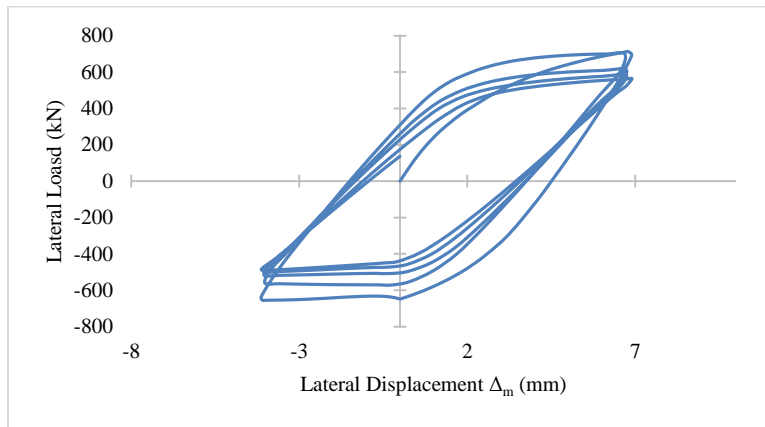


Figure C - 47: Lateral load vs. displacement Δ_m : CFRP, stiff clay, long span.

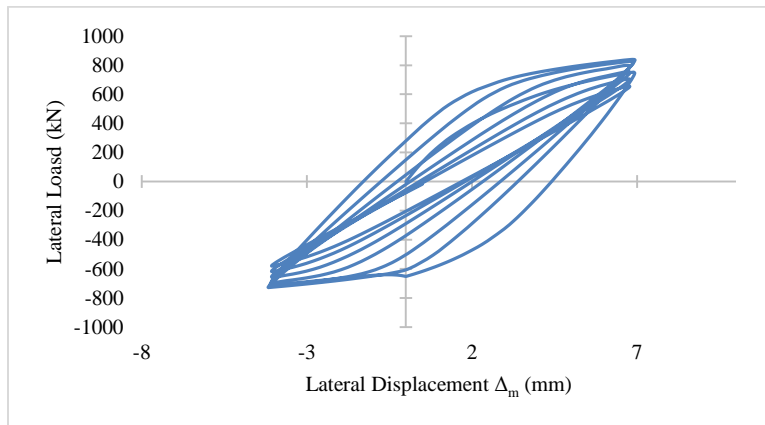


Figure C - 48: Lateral load vs. displacement Δ_m : ECFRP, stiff clay, long span.

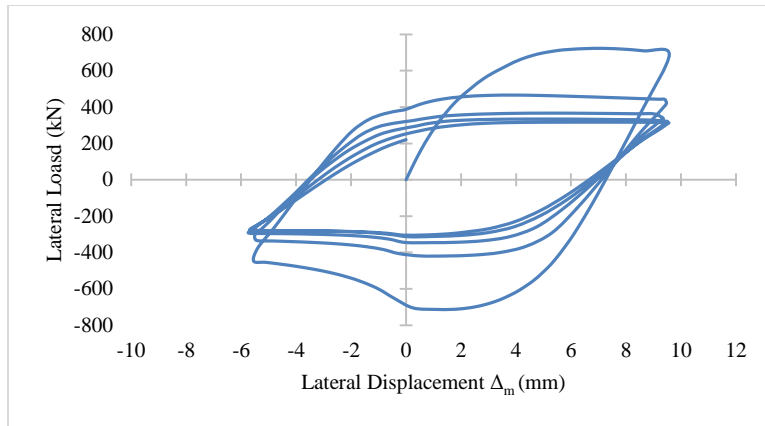


Figure C - 49: Lateral load vs. displacement Δ_m : control, medium clay, long span.

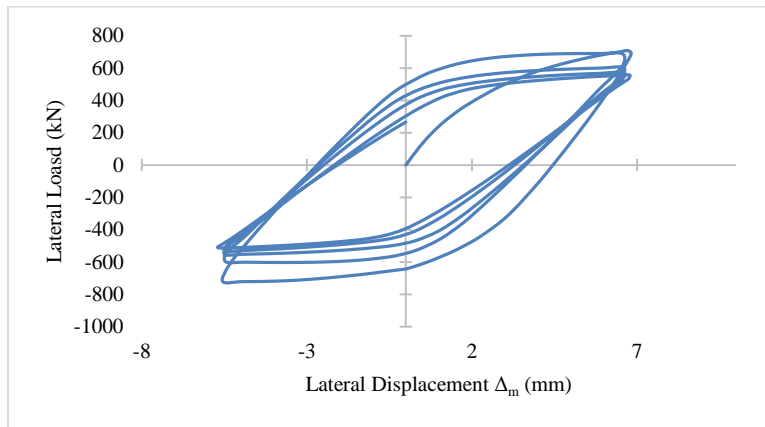


Figure C - 50: Lateral load vs. displacement Δ_m : CFRP, medium clay, long span.

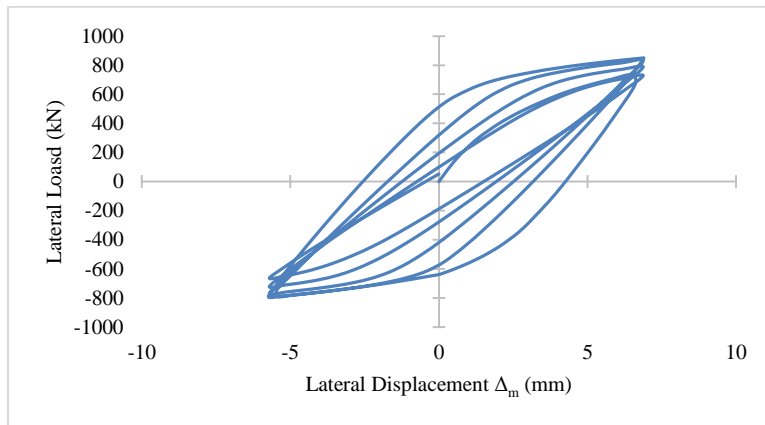


Figure C - 51: Lateral load vs. displacement Δ_m : ECFRP, medium clay, long span.

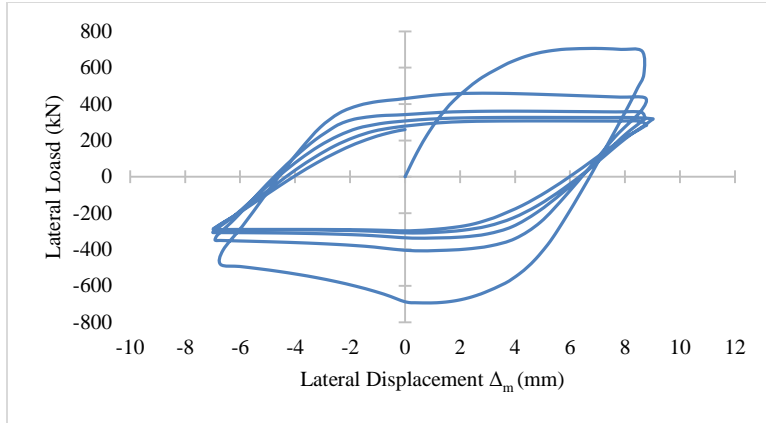


Figure C - 52: Lateral load vs. displacement Δ_m : control, soft clay, long span.

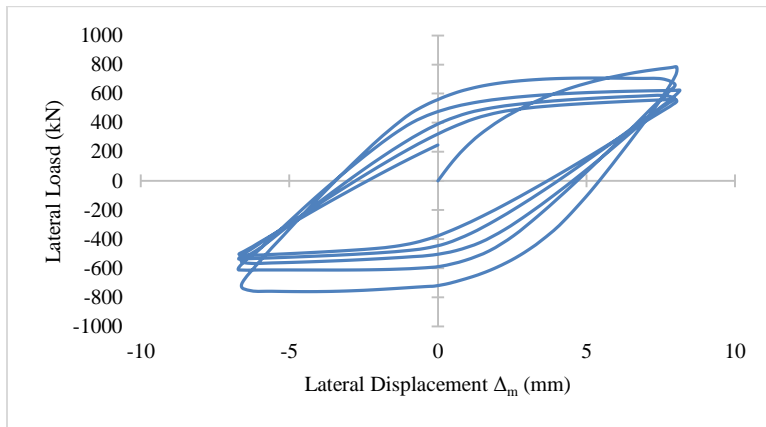


Figure C - 53: Lateral load vs. displacement Δ_m : CFRP, soft clay, long span.

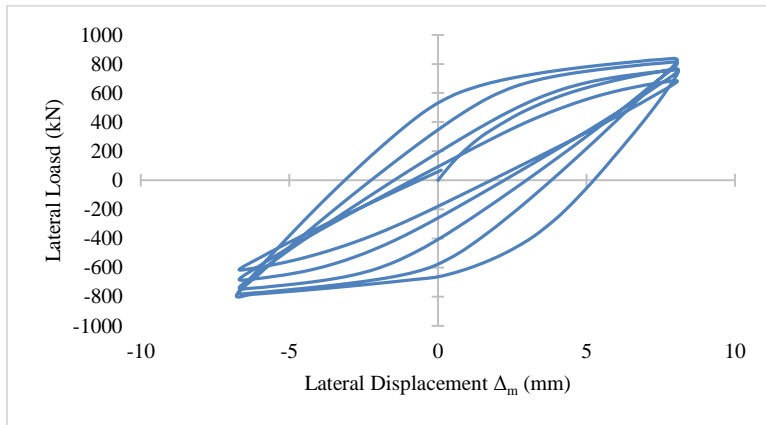


Figure C - 54: Lateral load vs. displacement Δ_m : ECFRP, soft clay, long span.

Appendix D: Localized Model Results: Damage Indicators for $\Delta_g = \pm 50.8$ mm (± 2 in)

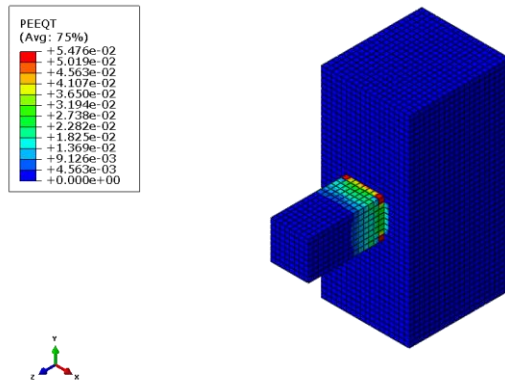


Figure D - 1: Tensile plastic strain: control, dense sand, short span.

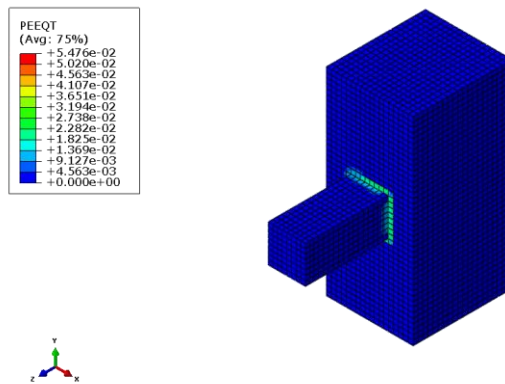


Figure D - 2: Tensile plastic strain: CFRP, dense sand, short span.

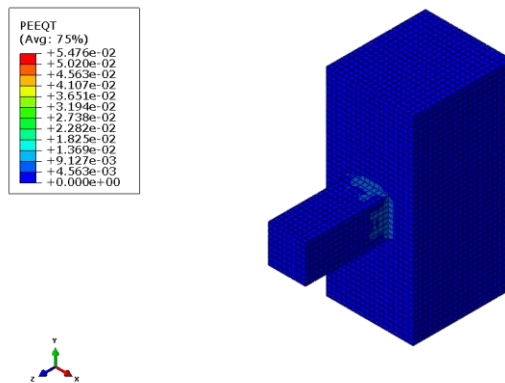


Figure D - 3: Tensile plastic strain: ECFRP, dense sand, short span.

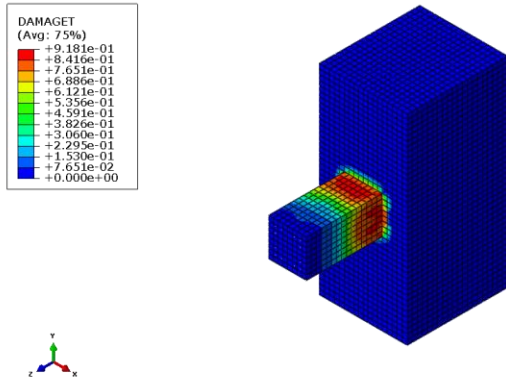


Figure D - 4: Tensile damage: control, dense sand, short span.

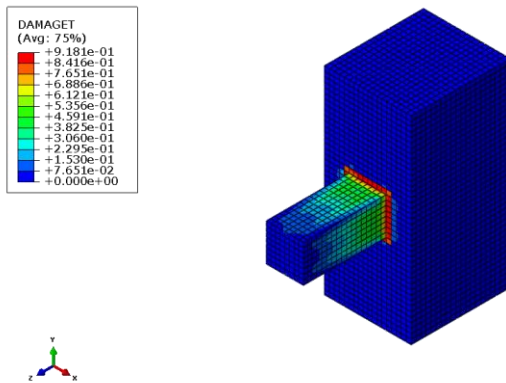


Figure D - 5: Tensile damage: CFRP, dense sand, short span.

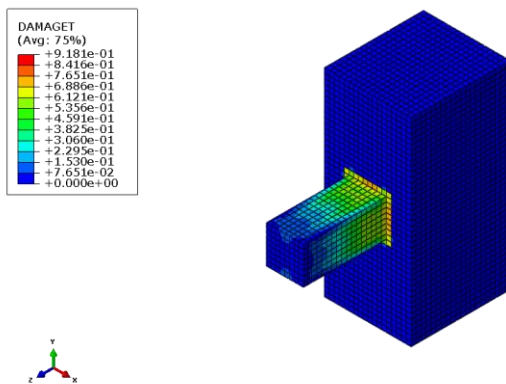


Figure D - 6: Tensile damage: ECFRP, dense sand, short span.

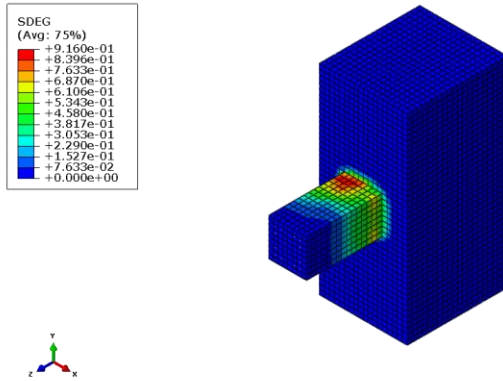


Figure D - 7: Stiffness degradation: control, dense sand, short span.

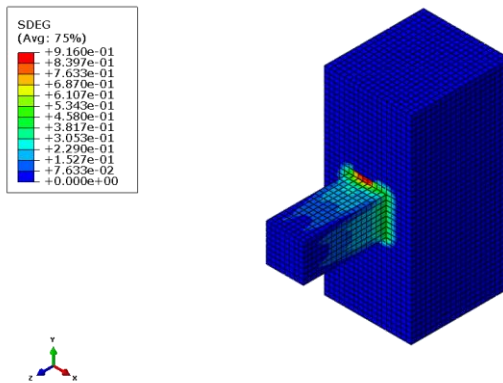


Figure D - 8: Stiffness degradation: CFRP, dense sand, short span.

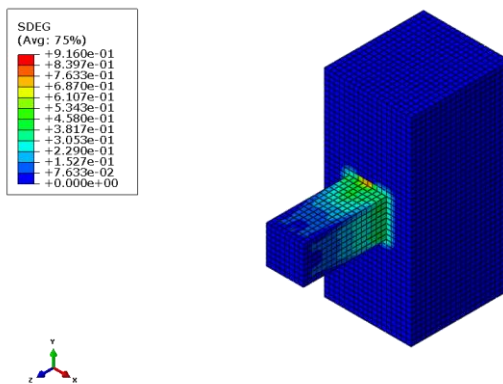


Figure D - 9: Stiffness degradation: ECFRP, dense sand, short span.

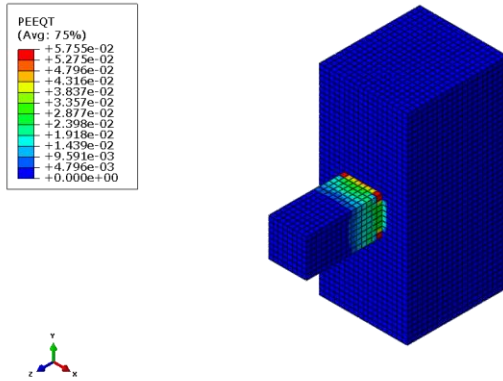


Figure D - 10: Tensile plastic strain: control, medium sand, short span.

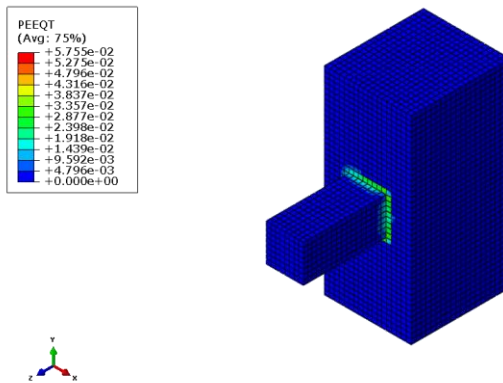


Figure D - 11: Tensile plastic strain: CFRP, medium sand, short span.

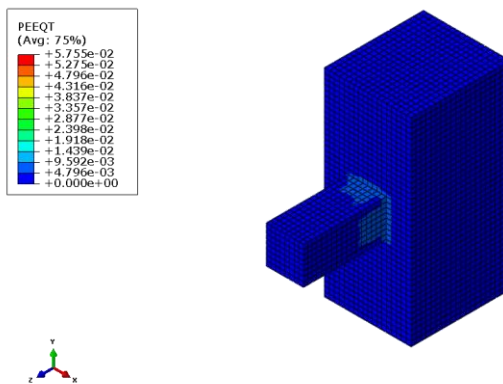


Figure D - 12: Tensile plastic strain: ECFRP, medium sand, short span.

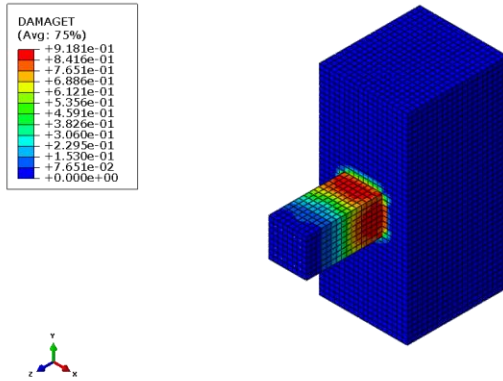


Figure D - 13: Tensile damage: control, medium sand, short span.

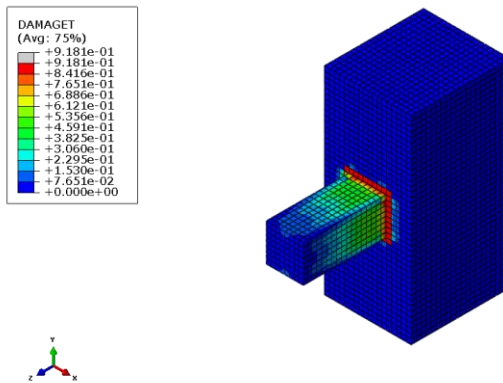


Figure D - 14: Tensile damage: CFRP, medium sand, short span.

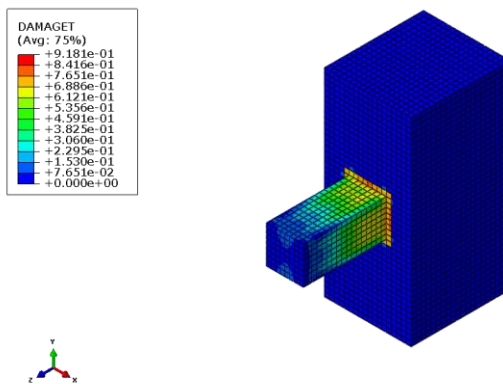


Figure D - 15: Tensile damage: ECFRP, medium sand, short span.

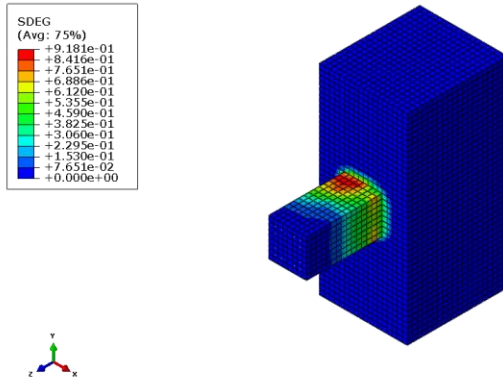


Figure D - 16: Stiffness degradation: control, medium sand, short span.

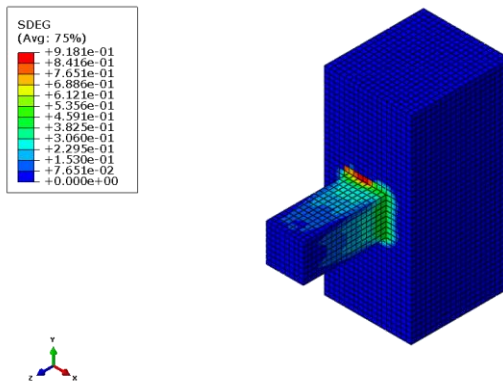


Figure D - 17: Stiffness degradation: CFRP, medium sand, short span.

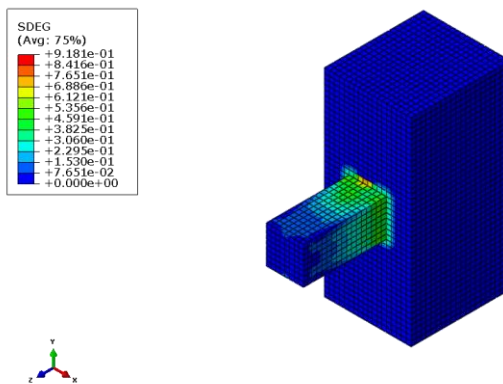


Figure D - 18: Stiffness degradation: ECFRP, medium sand, short span.

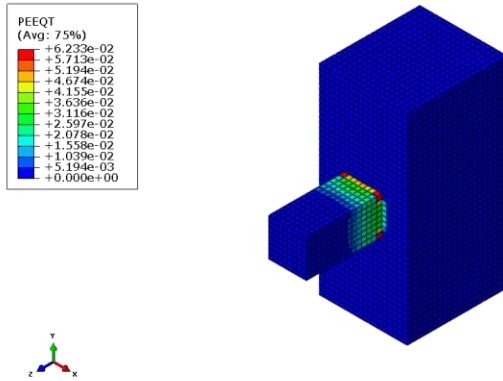


Figure D - 19: Tensile plastic strain: control, loose sand, short span.

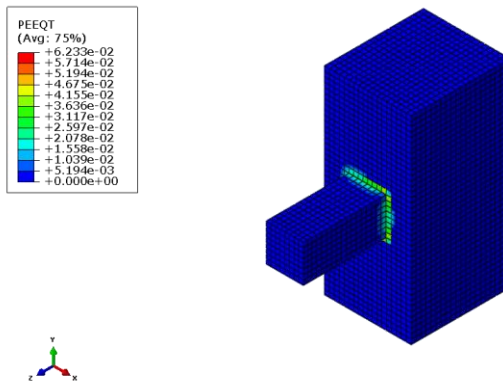


Figure D - 20: Tensile plastic strain: CFRP, loose sand, short span.

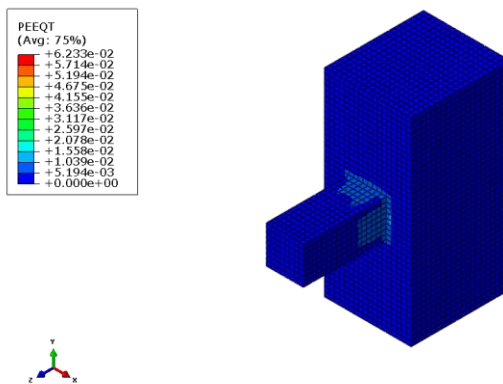


Figure D - 21: Tensile plastic strain: ECFRP, loose sand, short span.

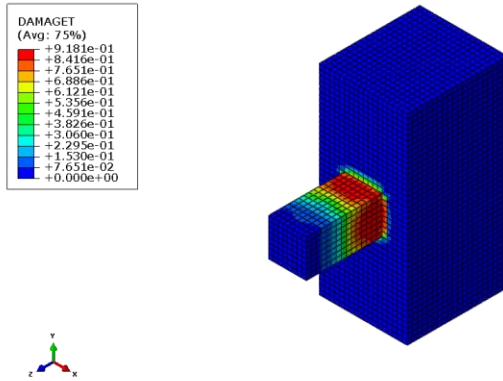


Figure D - 22: Tensile damage: control, loose sand, short span.

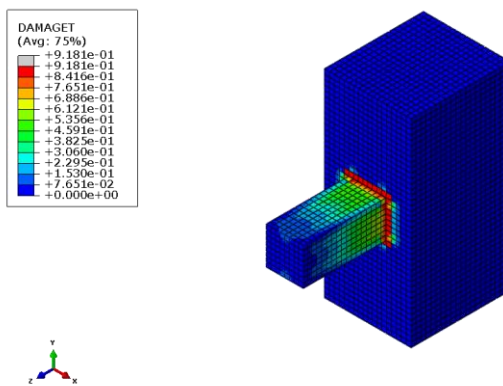


Figure D - 23: Tensile damage: CFRP, loose sand, short span.

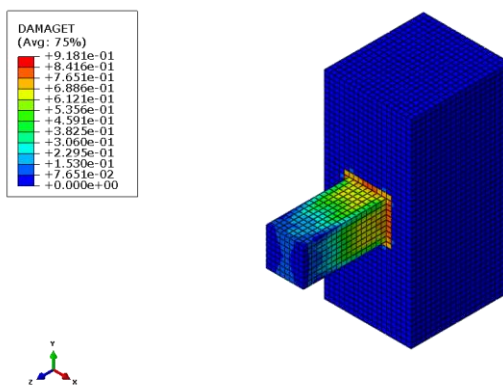


Figure D - 24: Tensile damage: ECFRP, loose sand, short span.

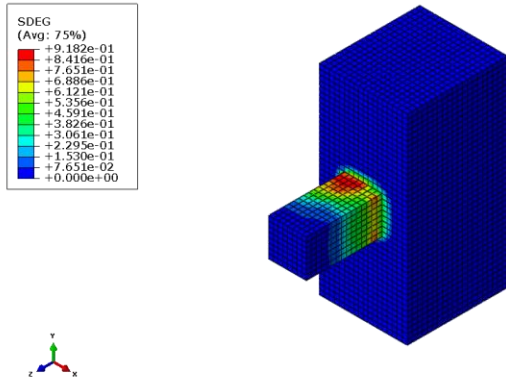


Figure D - 25: Stiffness degradation: control, loose sand, short span.

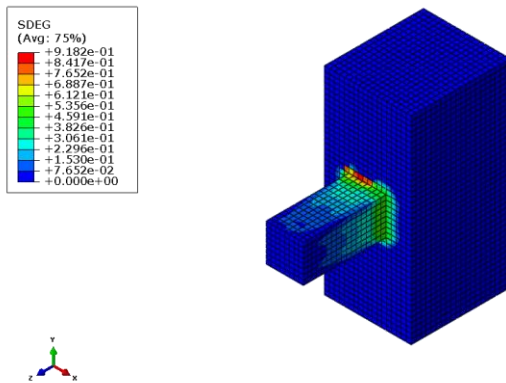


Figure D - 26: Stiffness degradation: CFRP, loose sand, short span.

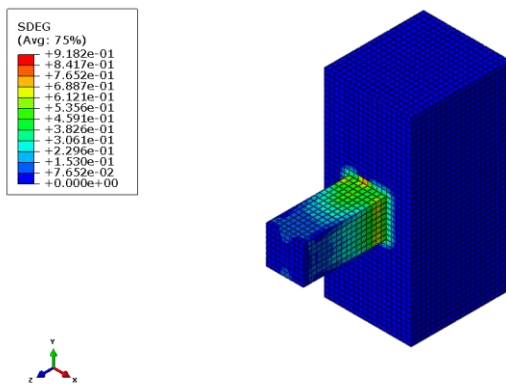


Figure D - 27: Stiffness degradation: ECFRP, loose sand, short span.

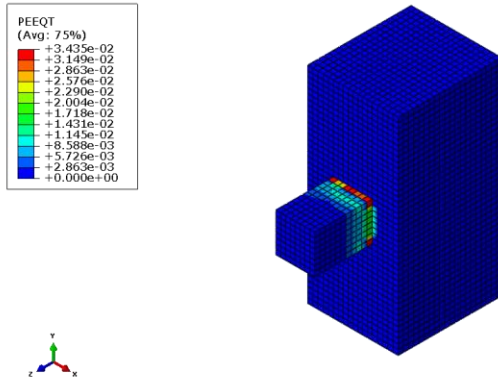


Figure D - 28: Tensile plastic strain: control, stiff clay, short span.

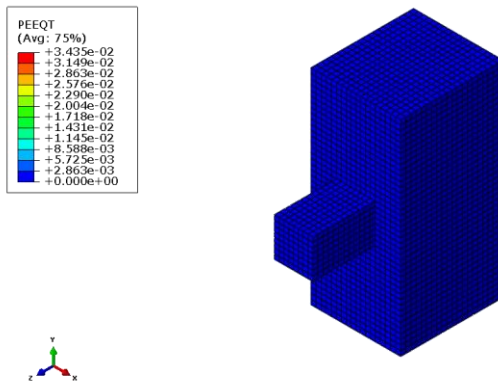


Figure D - 29: Tensile plastic strain: CFRP, stiff clay, short span.

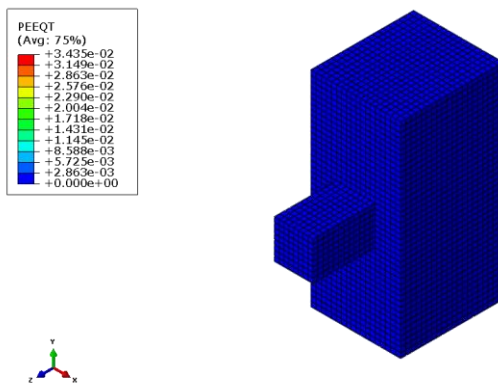


Figure D - 30: Tensile plastic strain: ECFRP, stiff clay, short span.

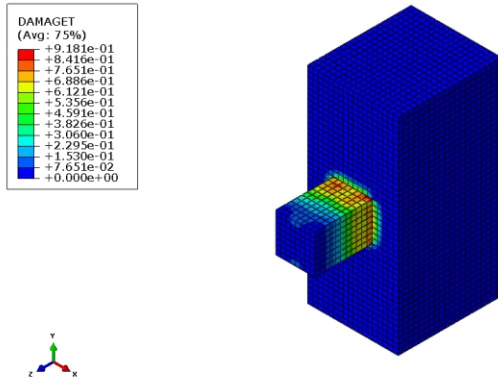


Figure D - 31: Tensile damage: control, stiff clay, short span.

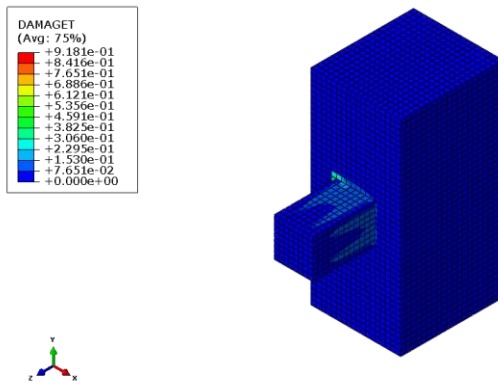


Figure D - 32: Tensile damage: CFRP, stiff clay, short span.

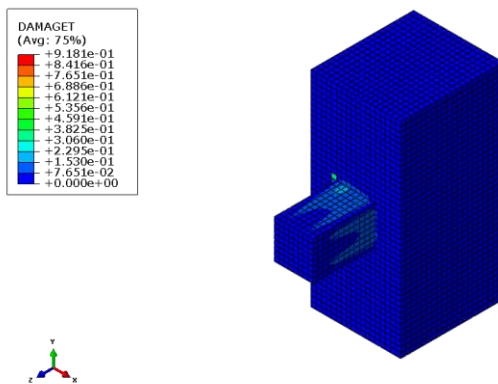


Figure D - 33: Tensile damage: ECFRP, stiff clay, short span.

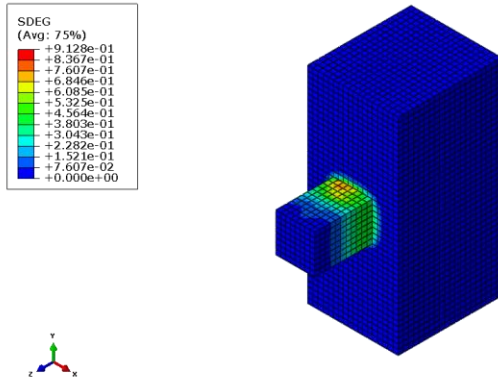


Figure D - 34: Stiffness degradation: control, stiff clay, short span.

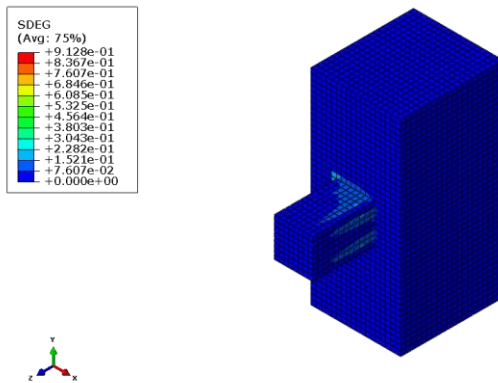


Figure D - 35: Stiffness degradation: CFRP, stiff clay, short span.

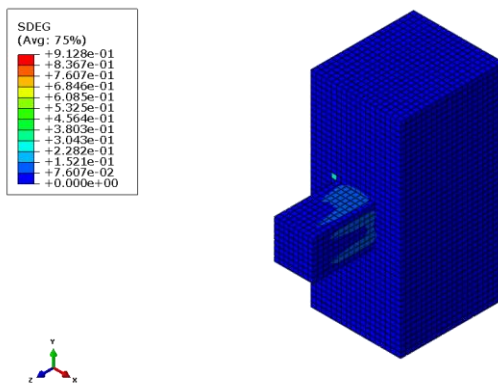


Figure D - 36: Stiffness degradation: ECFRP, stiff clay, short span.

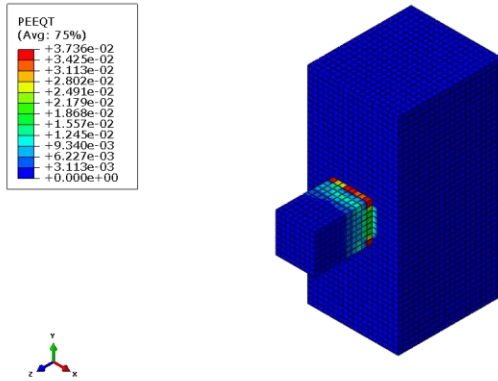


Figure D - 37: Tensile plastic strain: control, medium clay, short span.

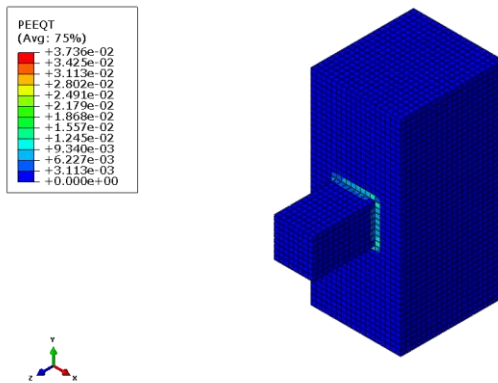


Figure D - 38: Tensile plastic strain: CFRP, medium clay, short span.

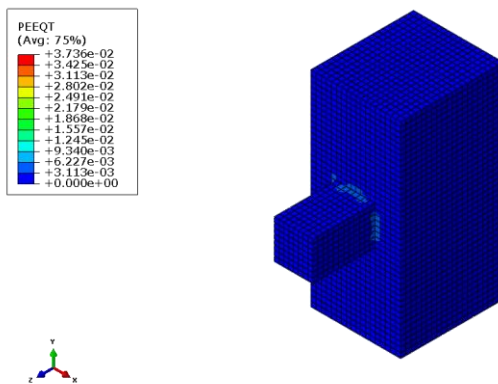


Figure D - 39: Tensile plastic strain: ECFRP, medium clay, short span.

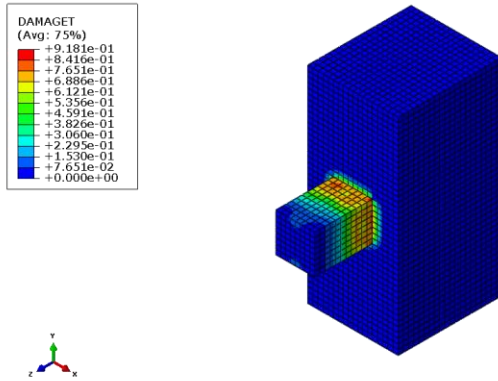


Figure D - 40: Tensile damage: control, medium clay, short span.

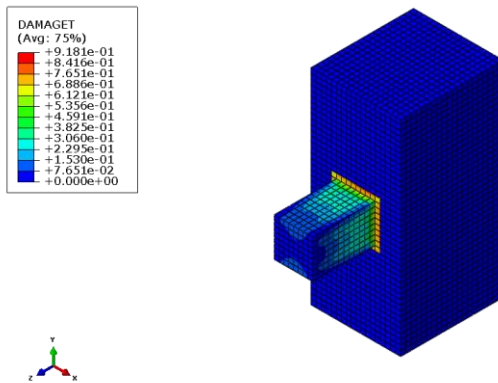


Figure D - 41: Tensile damage: CFRP, medium clay, short span.

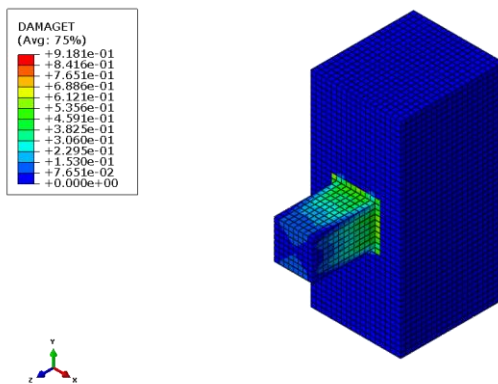


Figure D - 42: Tensile damage: ECFRP, medium clay, short span.

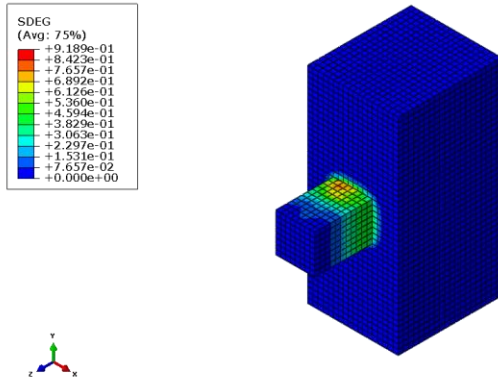


Figure D - 43: Stiffness degradation: control, medium clay, short span.

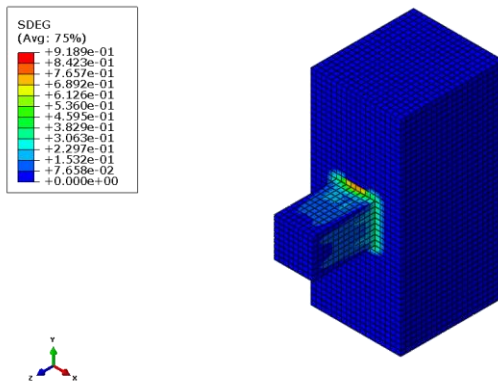


Figure D - 44: Stiffness degradation: CFRP, medium clay, short span.

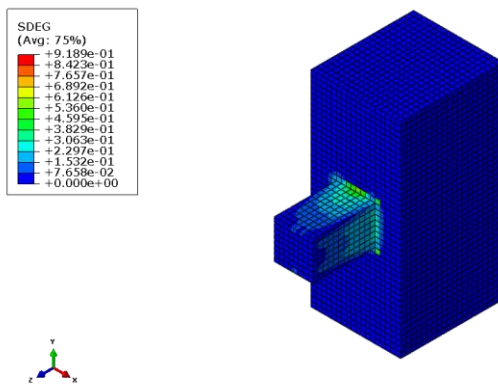


Figure D - 45: Stiffness degradation: ECFRP, medium clay, short span.

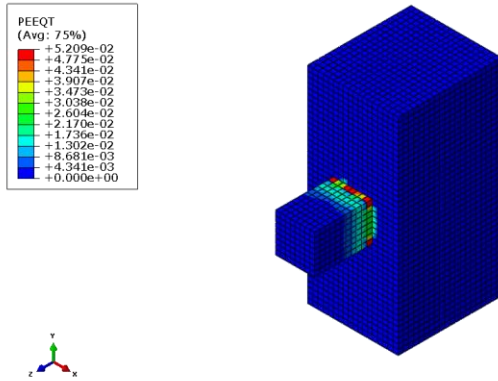


Figure D - 46: Tensile plastic strain: control, soft clay, short span.

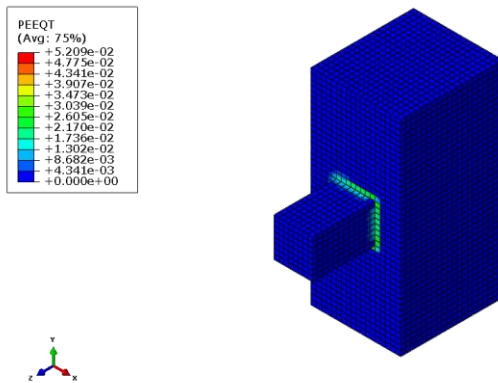


Figure D - 47: Tensile plastic strain: CFRP, soft clay, short span.

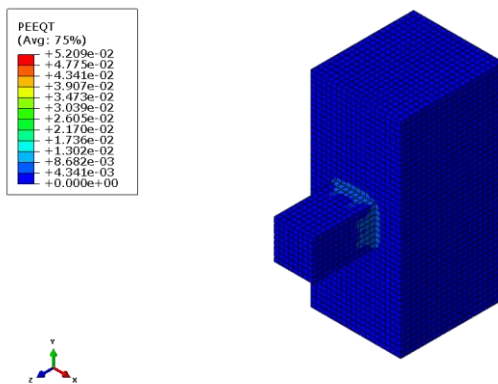


Figure D - 48: Tensile plastic strain: ECFRP, soft clay, short span.

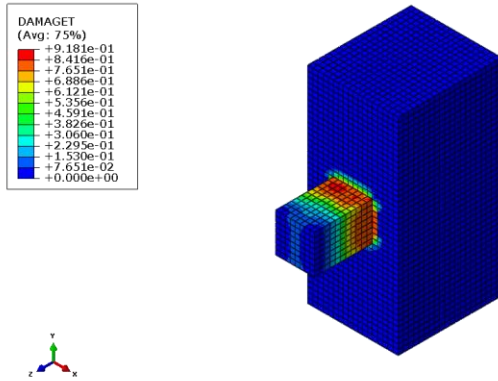


Figure D - 49: Tensile damage: control, soft clay, short span.

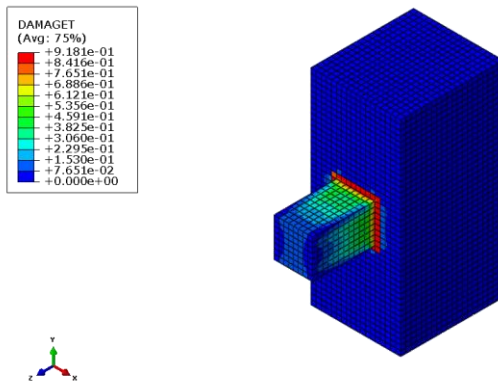


Figure D - 50: Tensile damage: CFRP, soft clay, short span.

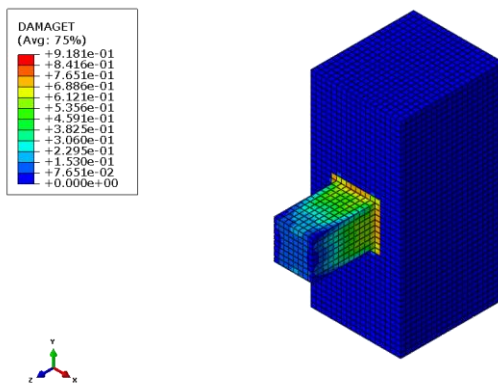


Figure D - 51: Tensile damage: ECFRP, soft clay, short span.

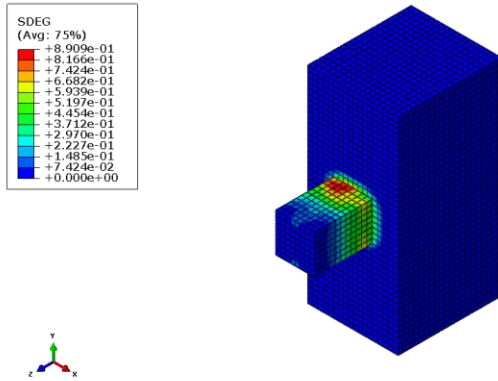


Figure D - 52: Stiffness degradation: control, soft clay, short span.

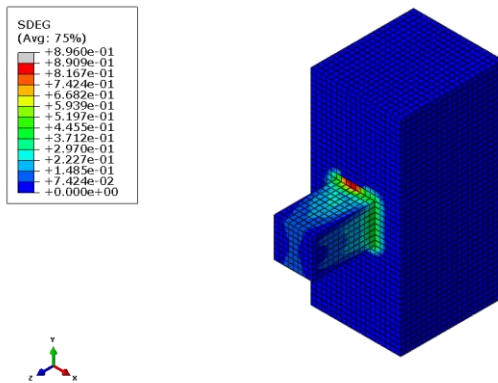


Figure D - 53: Stiffness degradation: CFRP, soft clay, short span.

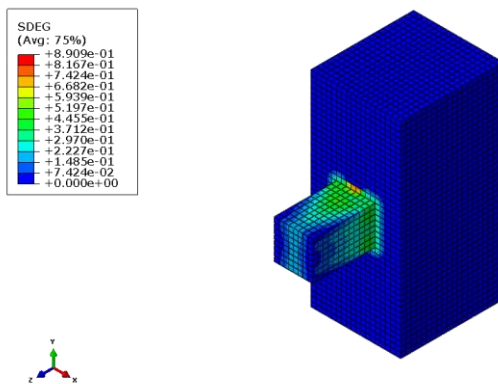


Figure D - 54: Stiffness degradation: ECFRP, soft clay, short span.

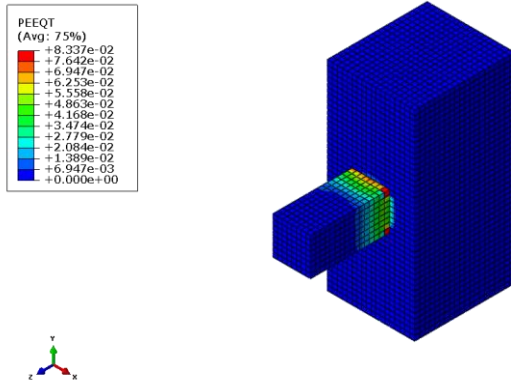


Figure D - 55: Tensile plastic strain: control, dense sand, medium span.

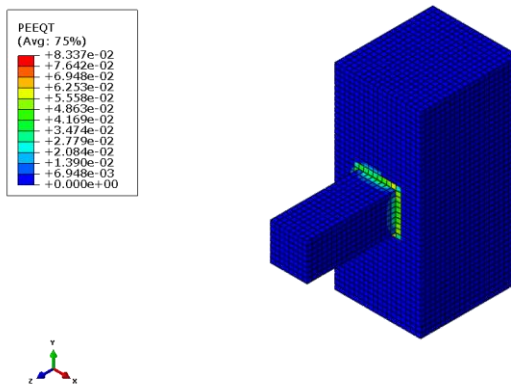


Figure D - 56: Tensile plastic strain: CFRP, dense sand, medium span.

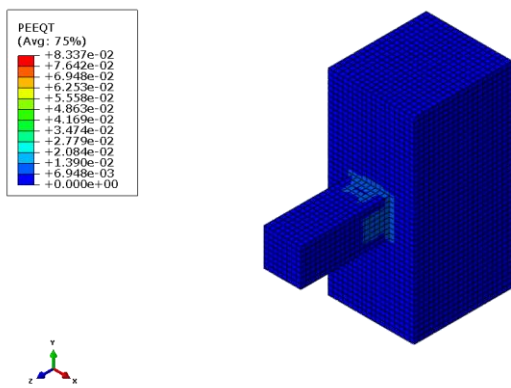


Figure D - 57: Tensile plastic strain: ECFRP, dense sand, medium span.

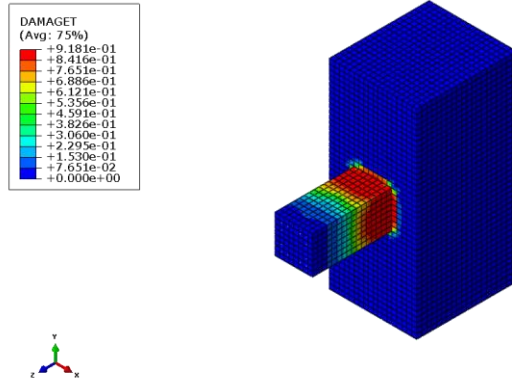


Figure D - 58: Tensile damage: control, dense sand, medium span.

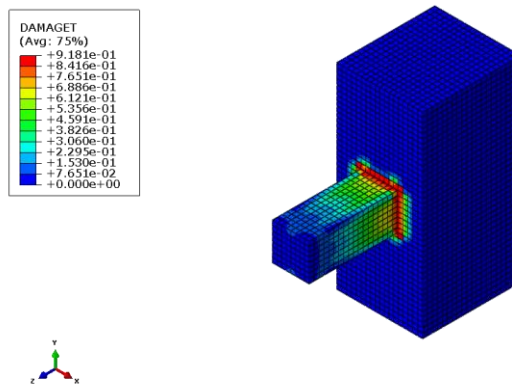


Figure D - 59: Tensile damage: CFRP, dense sand, medium span.

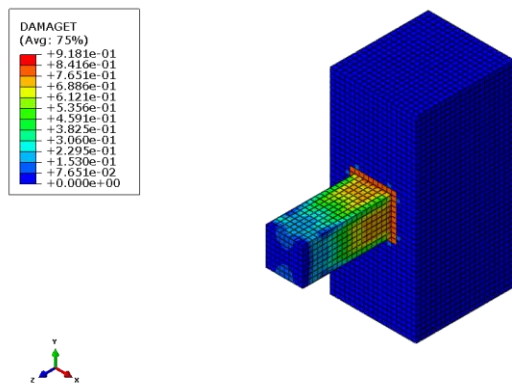


Figure D - 60: Tensile damage: ECFRP, dense sand, medium span.

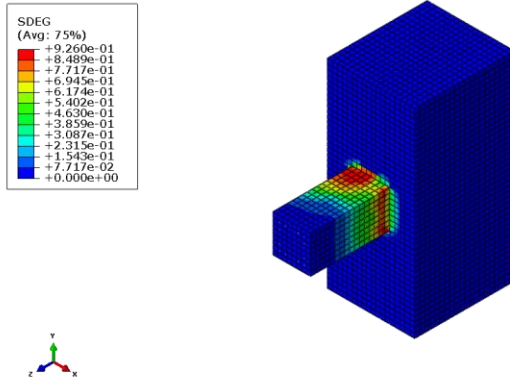


Figure D - 61: Stiffness degradation: control, dense sand, medium span.

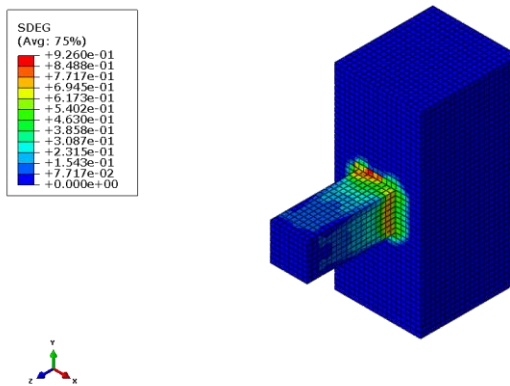


Figure D - 62: Stiffness degradation: CFRP, dense sand, medium span.

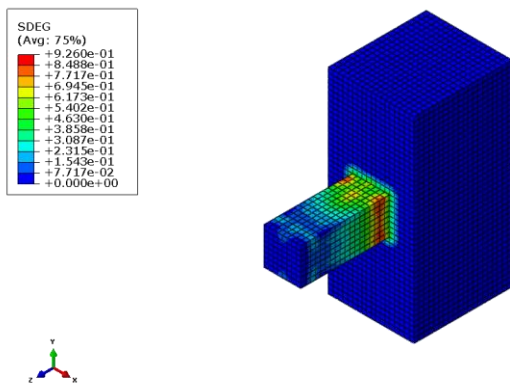


Figure D - 63: Stiffness degradation: ECFRP, dense sand, medium span.

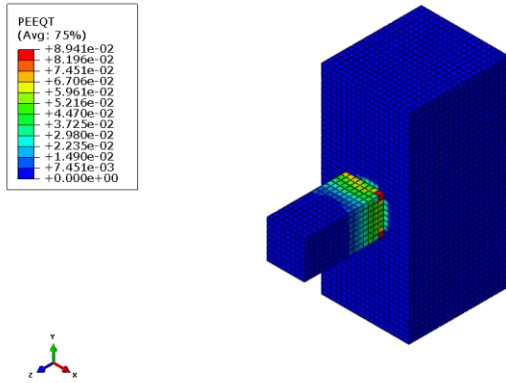


Figure D - 64: Tensile plastic strain: control, medium sand, medium span.

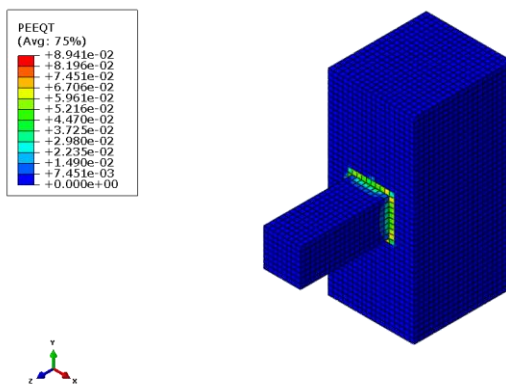


Figure D - 65: Tensile plastic strain: CFRP, medium sand, medium span.

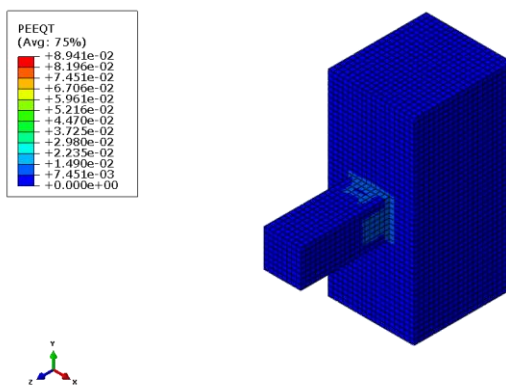


Figure D - 66: Tensile plastic strain: ECFRP, medium sand, medium span.

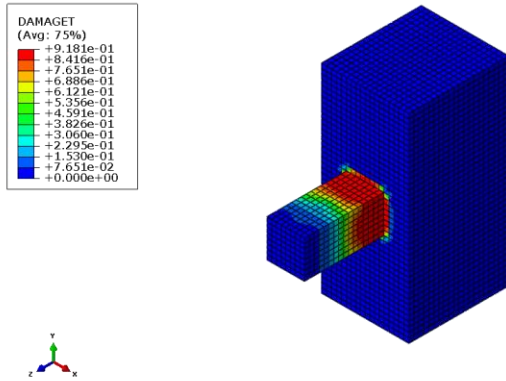


Figure D - 67: Tensile damage: control, medium sand, medium span.

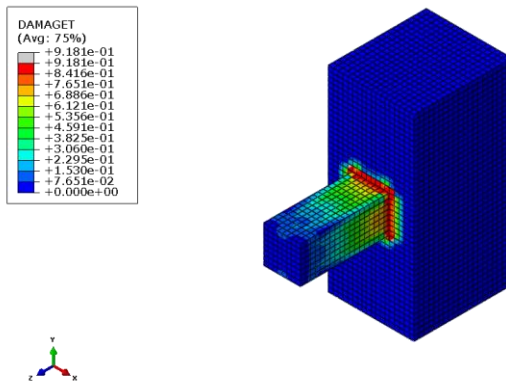


Figure D - 68: Tensile damage: CFRP, medium sand, medium span.

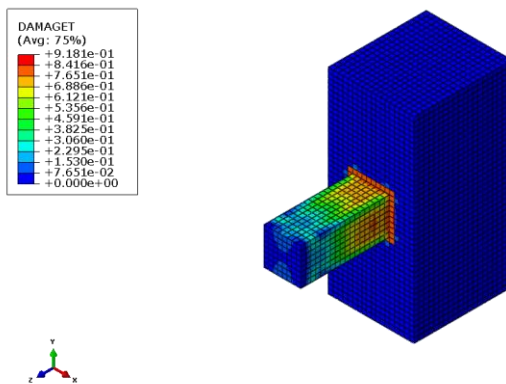


Figure D - 69: Tensile damage: ECFRP, medium sand, medium span.

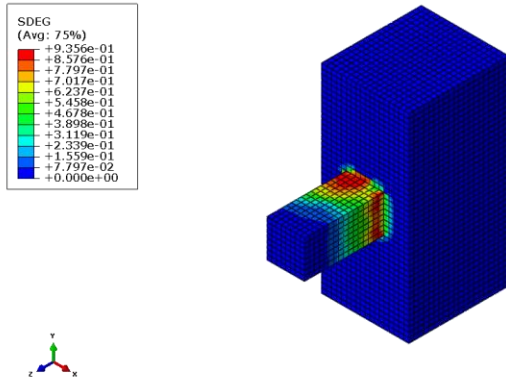


Figure D - 70: Stiffness degradation: control, medium sand, medium span.

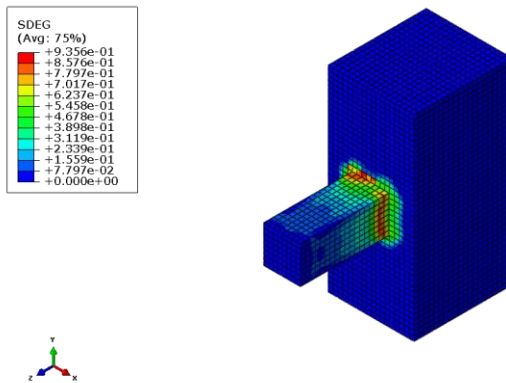


Figure D - 71: Stiffness degradation: CFRP, medium sand, medium span.

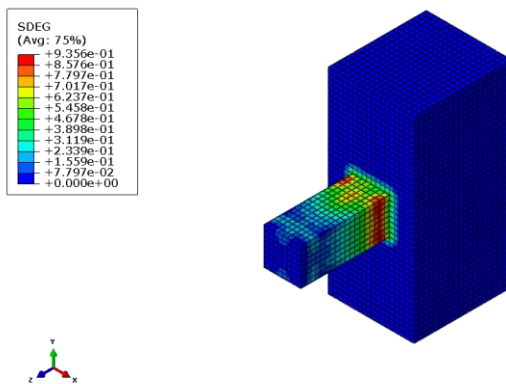


Figure D - 72: Stiffness degradation: ECFRP, medium sand, medium span.

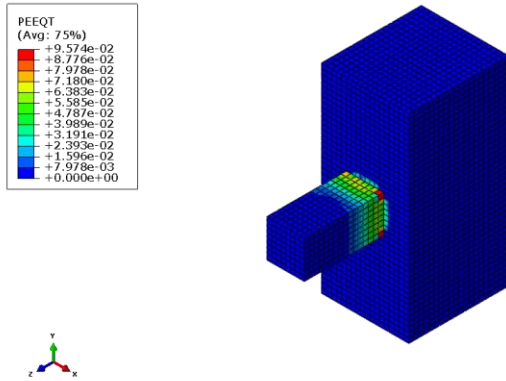


Figure D - 73: Tensile plastic strain: control, loose sand, medium span.

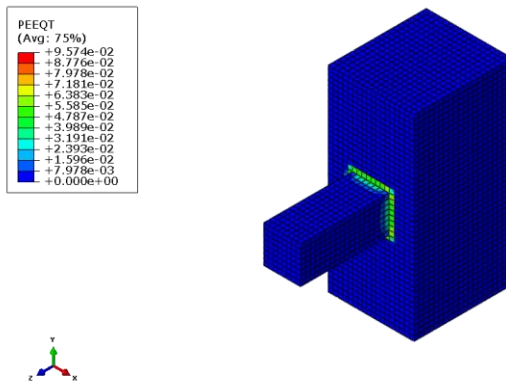


Figure D - 74: Tensile plastic strain: CFRP, loose sand, medium span.

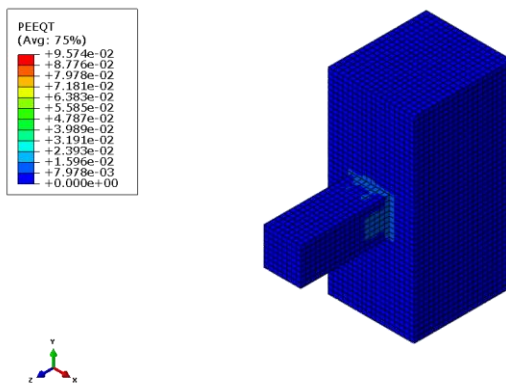


Figure D - 75: Tensile plastic strain: ECFRP, loose sand, medium span.

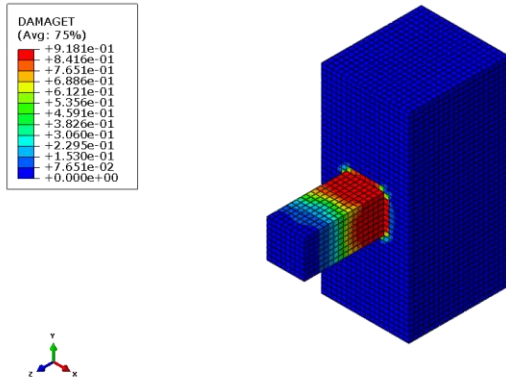


Figure D - 76: Tensile damage: control, loose sand, medium span.

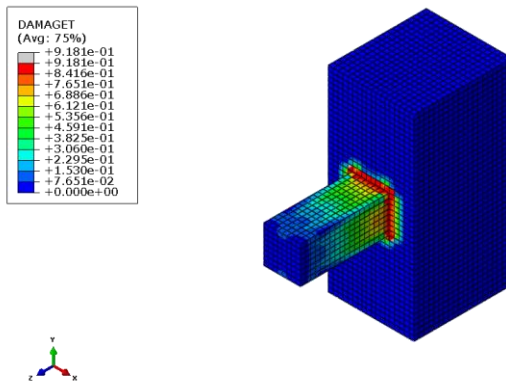


Figure D - 77: Tensile damage: CFRP, loose sand, medium span.

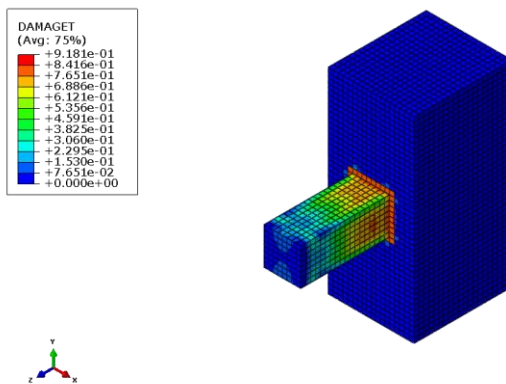


Figure D - 78: Tensile damage: ECFRP, loose sand, medium span.

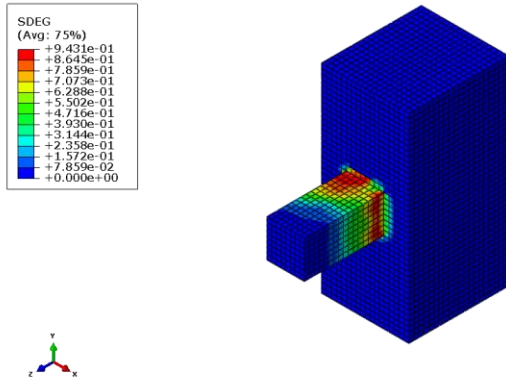


Figure D - 79: Stiffness degradation: control, loose sand, medium span.

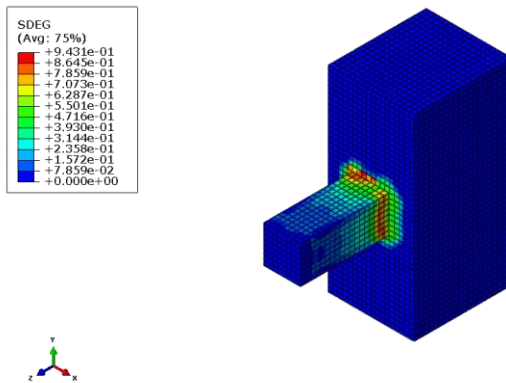


Figure D - 80: Stiffness degradation: CFRP, loose sand, medium span.

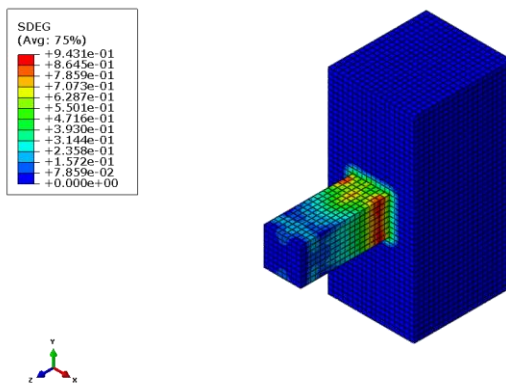


Figure D - 81: Stiffness degradation: ECFRP, loose sand, medium span.

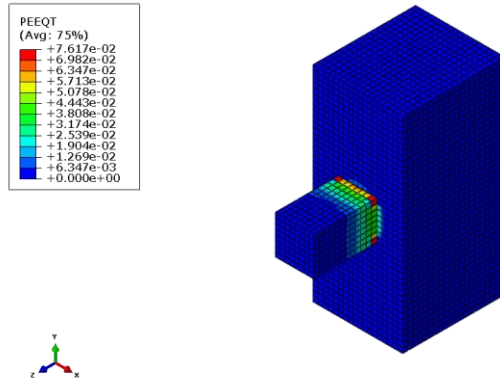


Figure D - 82: Tensile plastic strain: control, stiff clay, medium span.

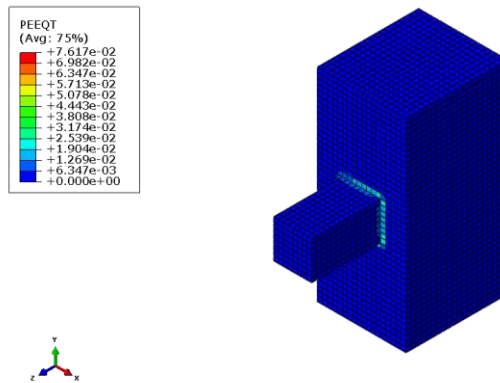


Figure D - 83: Tensile plastic strain: CFRP, stiff clay, medium span.

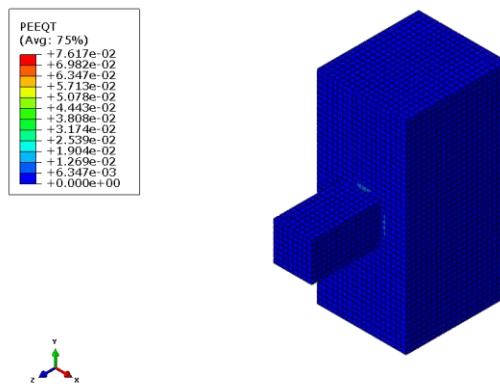


Figure D - 84: Tensile plastic strain: ECFRP, stiff clay, medium span.

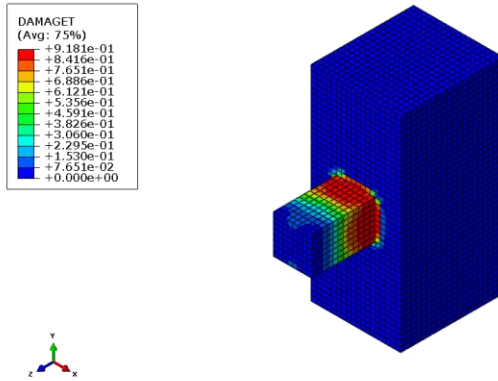


Figure D - 85: Tensile damage: control, stiff clay, medium span.

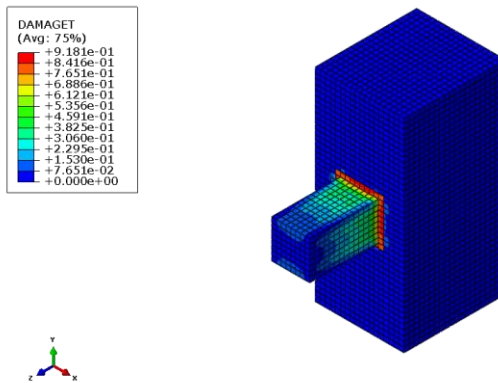


Figure D - 86: Tensile damage: CFRP, stiff clay, medium span.

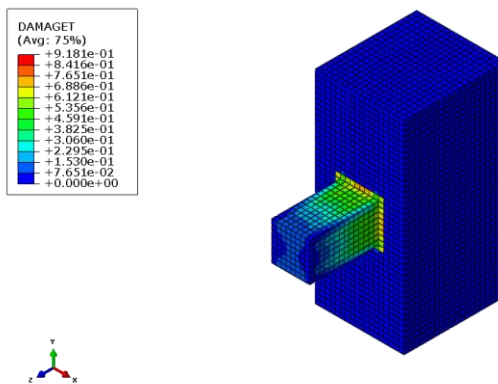


Figure D - 87: Tensile damage: ECFRP, stiff clay, medium span.

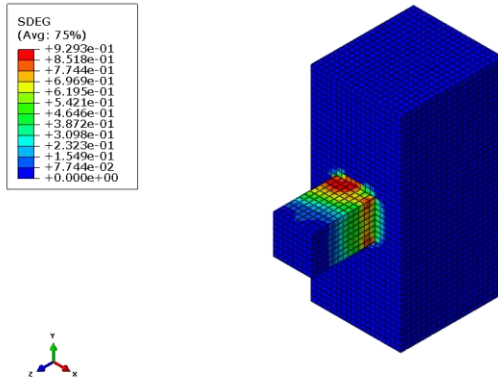


Figure D - 88: Stiffness degradation: control, stiff clay, medium span.

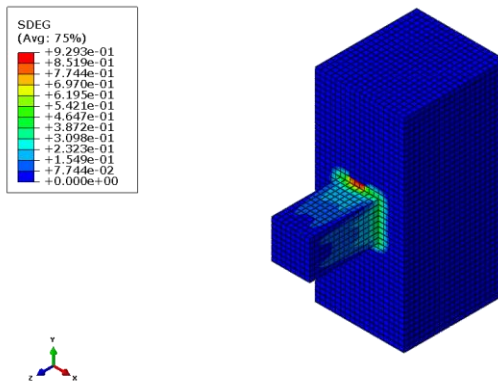


Figure D - 89: Stiffness degradation: CFRP, stiff clay, medium span.

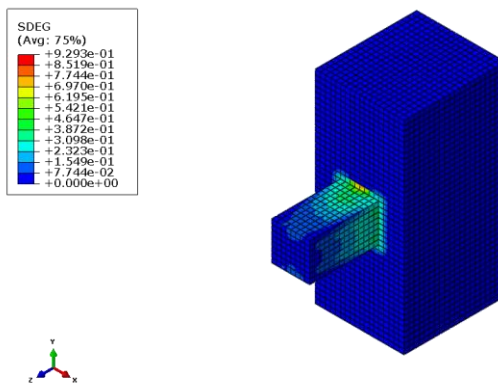


Figure D - 90: Stiffness degradation: ECFRP, stiff clay, medium span.

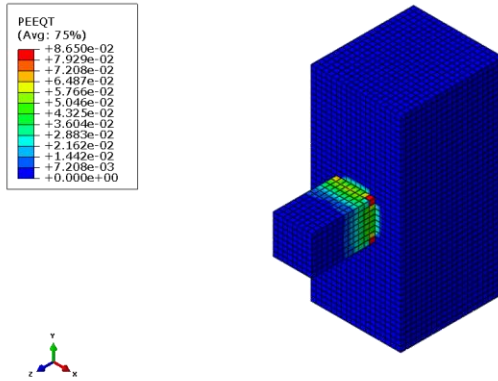


Figure D - 91: Tensile plastic strain: control, medium clay, medium span.

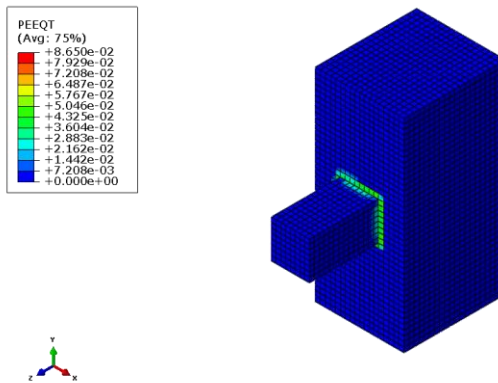


Figure D - 92: Tensile plastic strain: CFRP, medium clay, medium span.

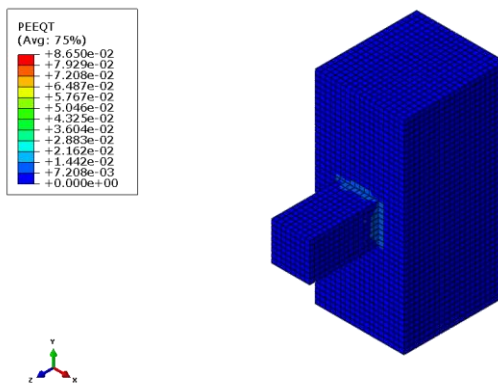


Figure D - 93: Tensile plastic strain: ECFRP, medium clay, medium span.

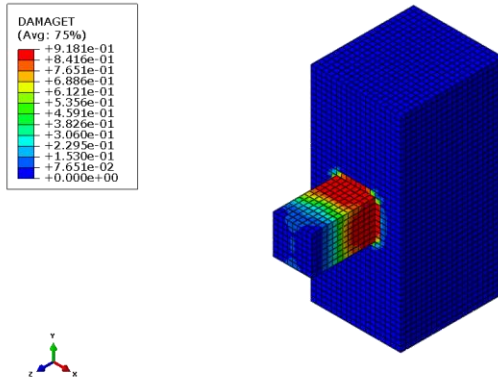


Figure D - 94: Tensile damage: control, medium clay, medium span.

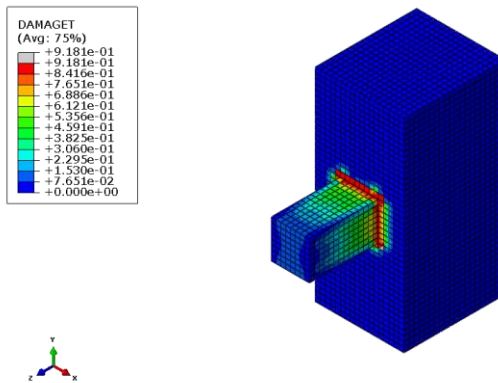


Figure D - 95: Tensile damage: CFRP, medium clay, medium span.

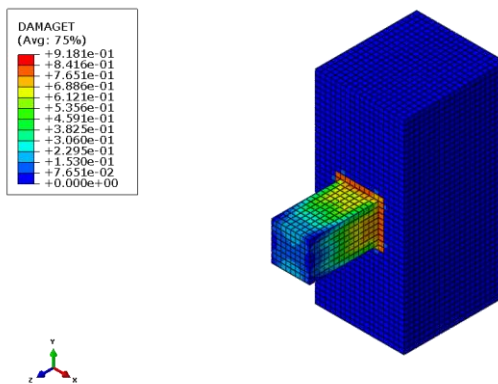


Figure D - 96: Tensile damage: ECFRP, medium clay, medium span.

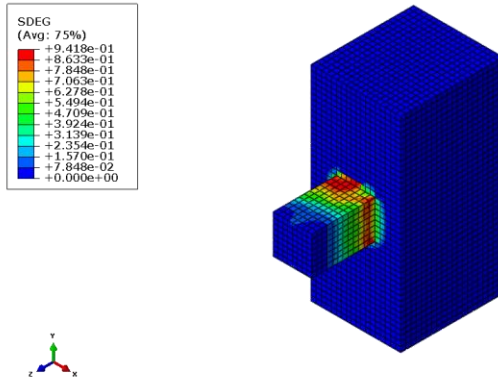


Figure D - 97: Stiffness degradation: control, medium clay, medium span.

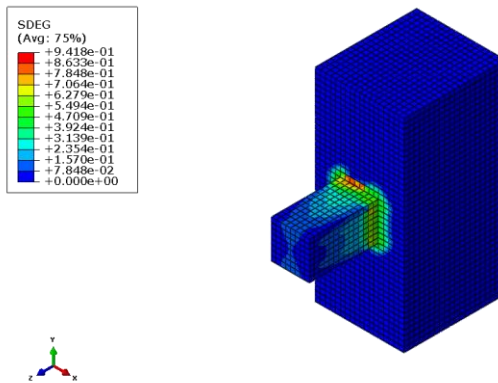


Figure D - 98: Stiffness degradation: CFRP, medium clay, medium span.

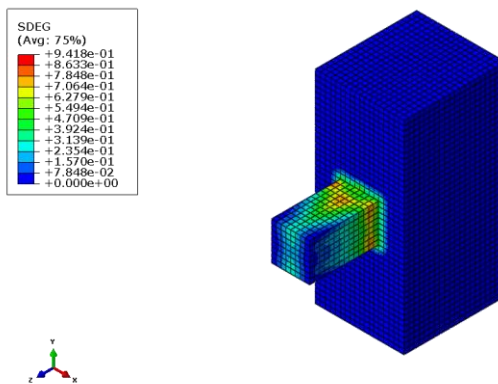


Figure D - 99: Stiffness degradation: ECFRP, medium clay, medium span.

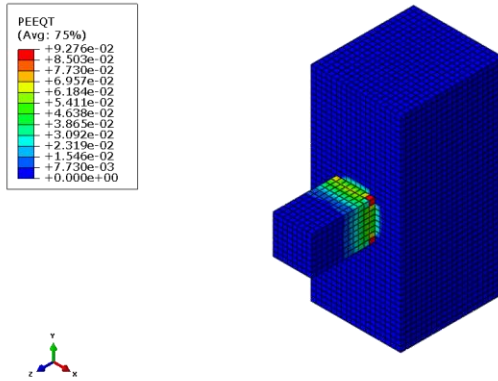


Figure D - 100: Tensile plastic strain: control, soft clay, medium span.

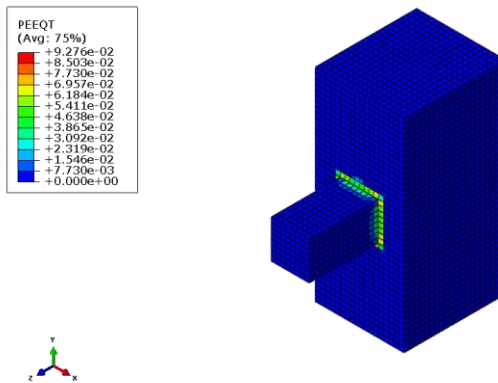


Figure D - 101: Tensile plastic strain: CFRP, soft clay, medium span.

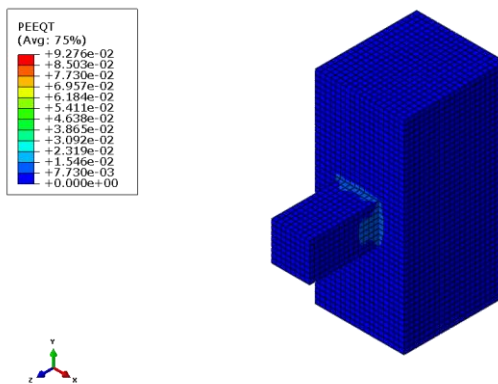


Figure D - 102: Tensile plastic strain: ECFRP, soft clay, medium span.

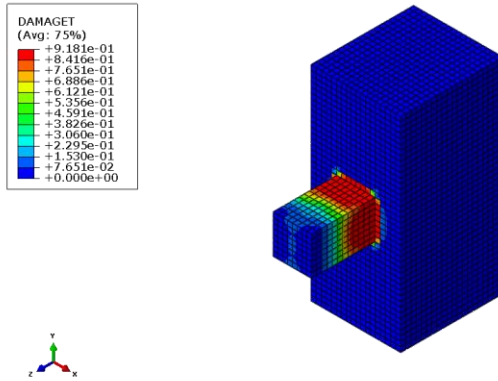


Figure D - 103: Tensile damage: control, soft clay, medium span.

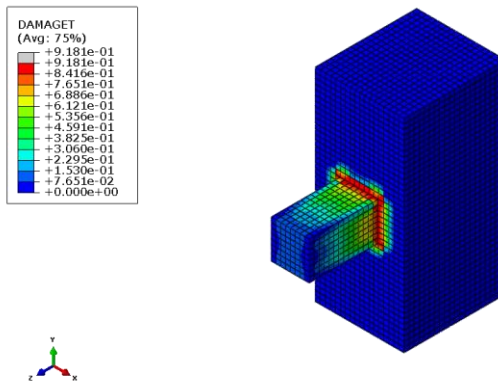


Figure D - 104: Tensile damage: CFRP, soft clay, medium span.

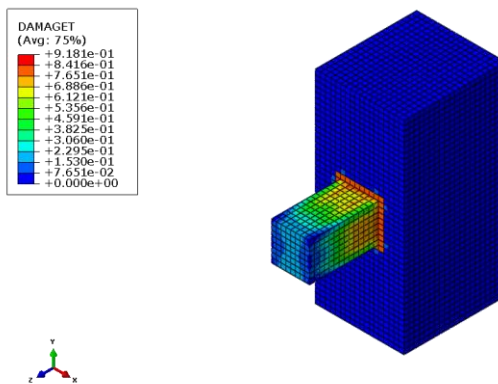


Figure D - 105: Tensile damage: ECFRP, soft clay, medium span.

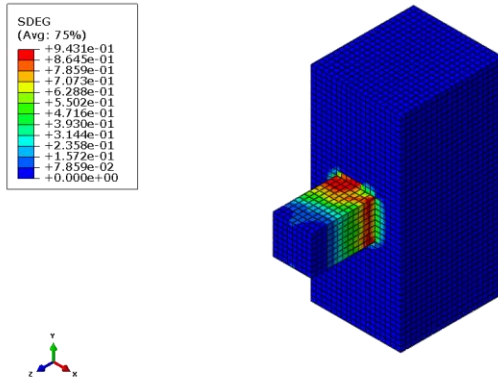


Figure D - 106: Stiffness degradation: control, soft clay, medium span.

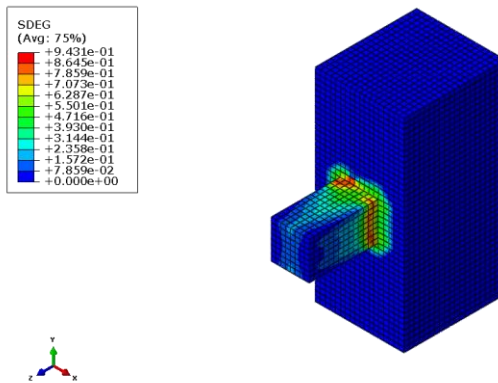


Figure D - 107: Stiffness degradation: CFRP, soft clay, medium span.

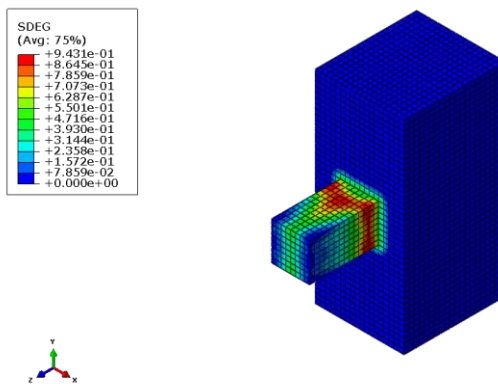


Figure D - 108: Stiffness degradation: ECFRP, soft clay, medium span.

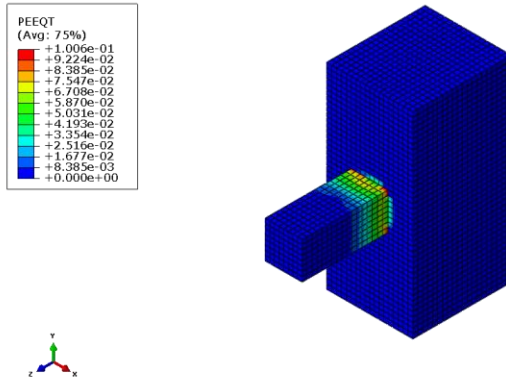


Figure D - 109: Tensile plastic strain: control, dense sand, long span.

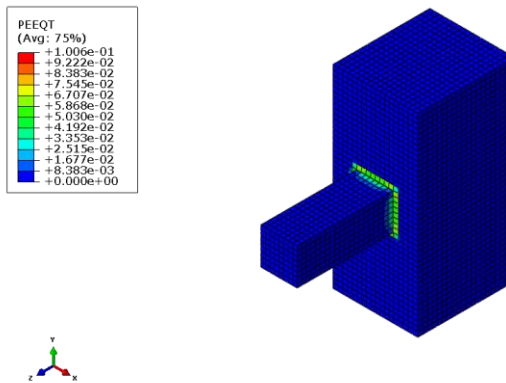


Figure D - 110: Tensile plastic strain: CFRP, dense sand, long span.

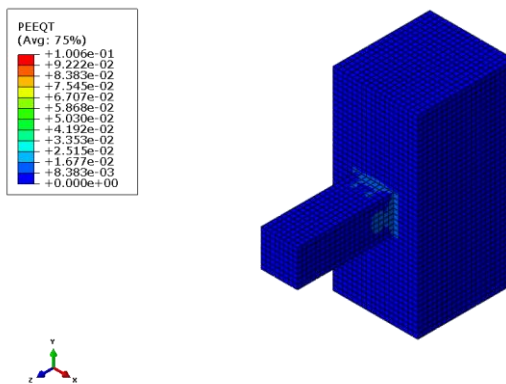


Figure D - 111: Tensile plastic strain: ECFRP, dense sand, long span.

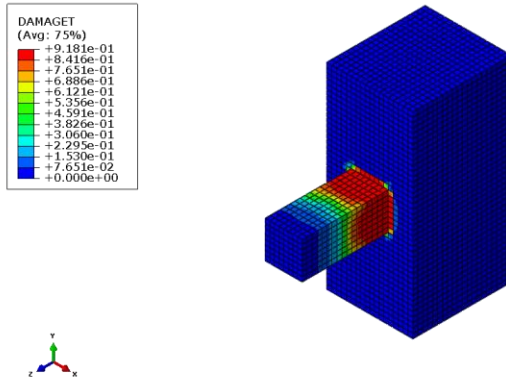


Figure D - 112: Tensile damage: control, dense sand, long span.

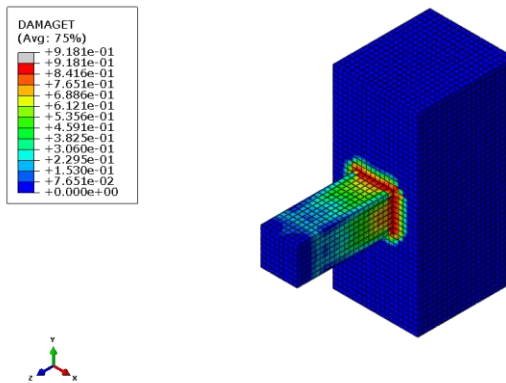


Figure D - 113: Tensile damage: CFRP, dense sand, long span.

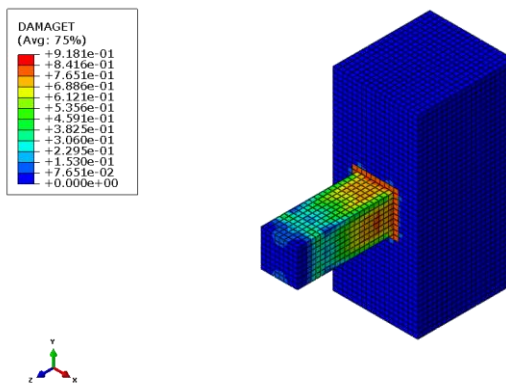


Figure D - 114: Tensile damage: ECFRP, dense sand, long span.

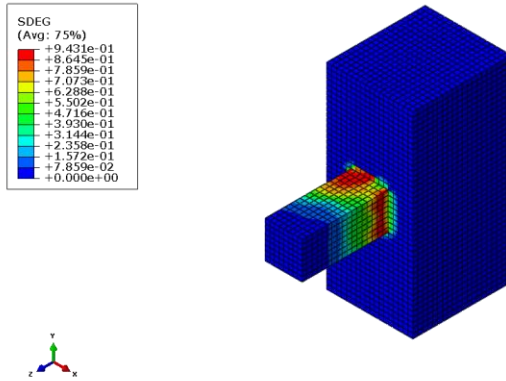


Figure D - 115: Stiffness degradation: control, dense sand, long span.

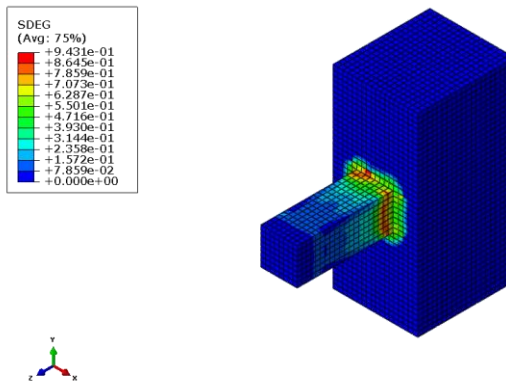


Figure D - 116: Stiffness degradation: CFRP, dense sand, long span.

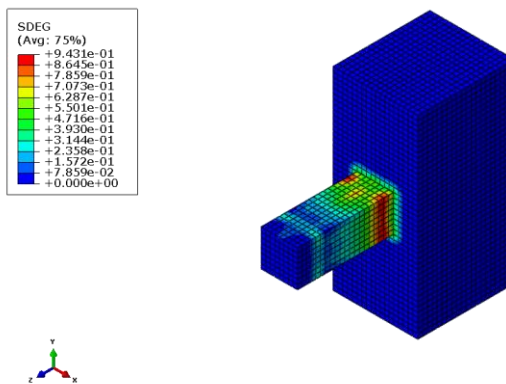


Figure D - 117: Stiffness degradation: ECFRP, dense sand, long span.

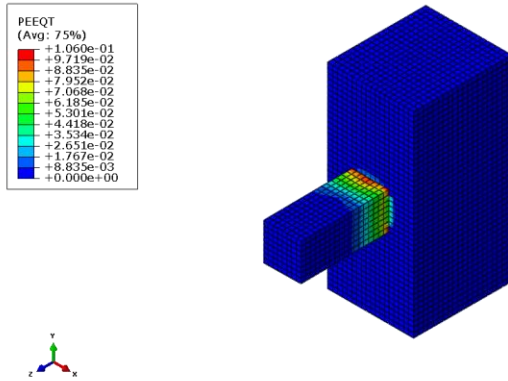


Figure D - 118: Tensile plastic strain: control, medium sand, long span.

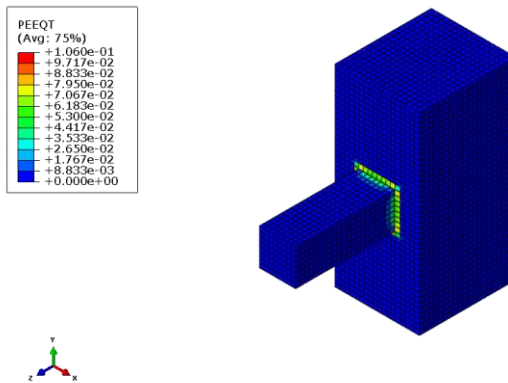


Figure D - 119: Tensile plastic strain: CFRP, medium sand, long span.

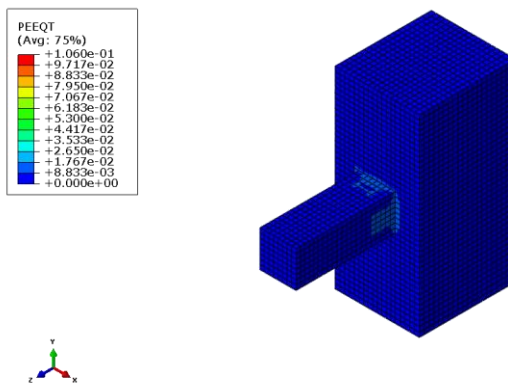


Figure D - 120: Tensile plastic strain: ECFRP, medium sand, long span.

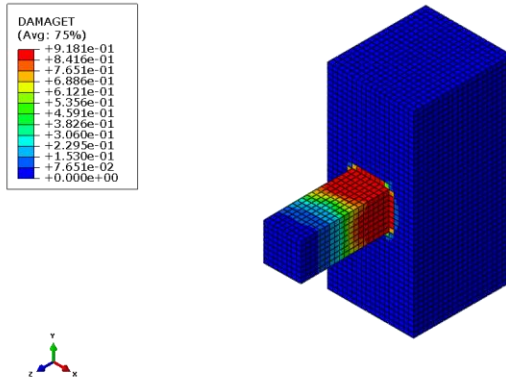


Figure D - 121: Tensile damage: control, medium sand, long span.

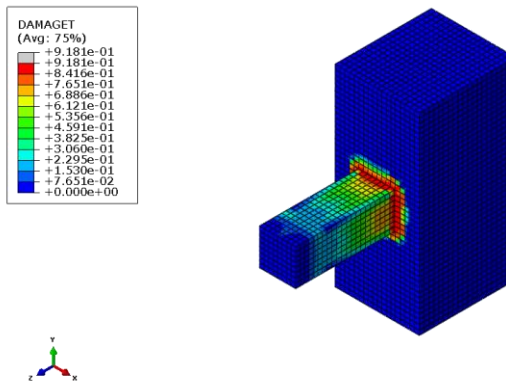


Figure D - 122: Tensile damage: CFRP, medium sand, long span.

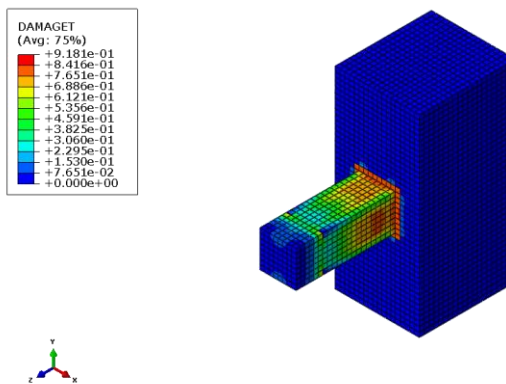


Figure D - 123: Tensile damage: ECFRP, medium sand, long span.

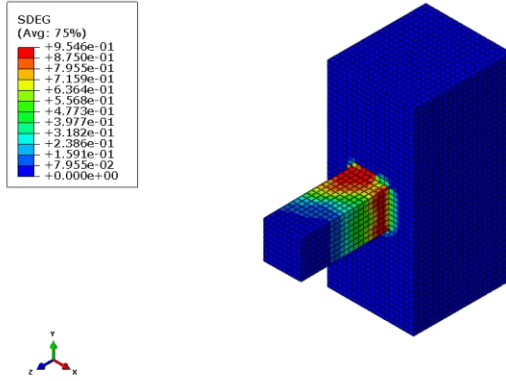


Figure D - 124: Stiffness degradation: control, medium sand, long span.

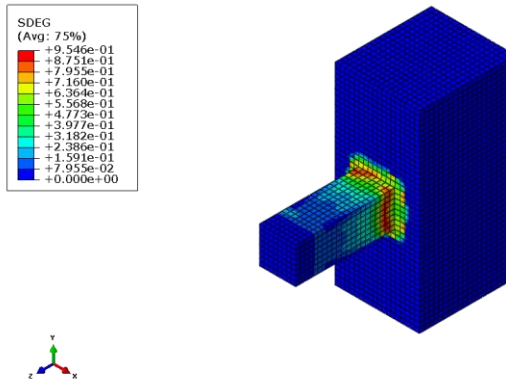


Figure D - 125: Stiffness degradation: CFRP, medium sand, long span.

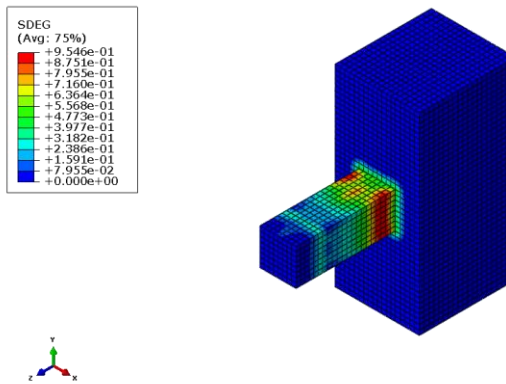


Figure D - 126: Stiffness degradation: ECFRP, medium sand, long span.

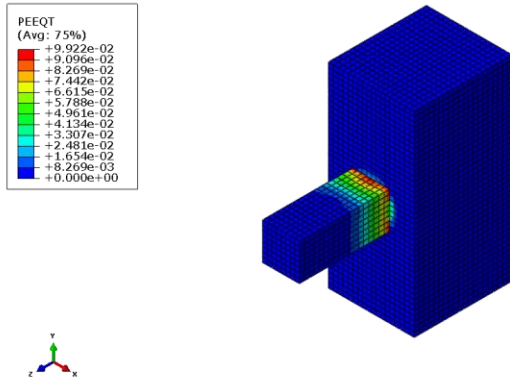


Figure D - 127: Tensile plastic strain: control, loose sand, long span.

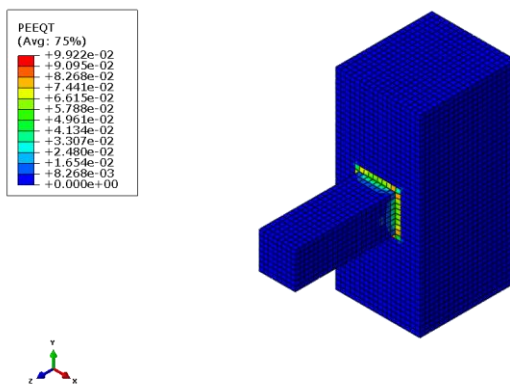


Figure D - 128: Tensile plastic strain: CFRP, loose sand, long span.

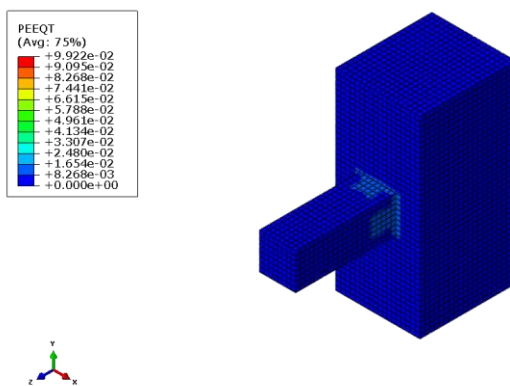


Figure D - 129: Tensile plastic strain: ECFRP, loose sand, long span.

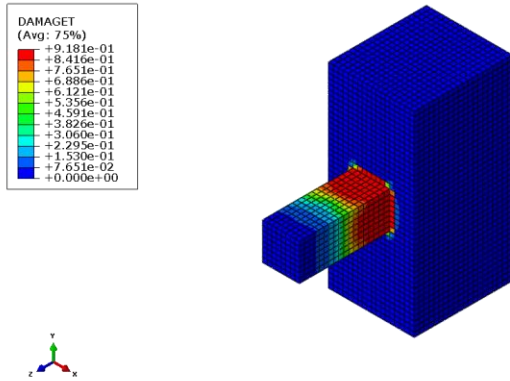


Figure D - 130: Tensile damage: control, loose sand, long span.

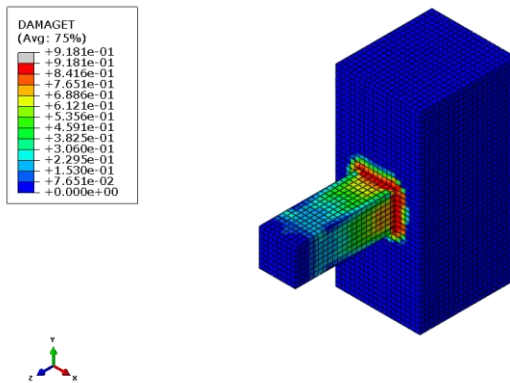


Figure D - 131: Tensile damage: CFRP, loose sand, long span.

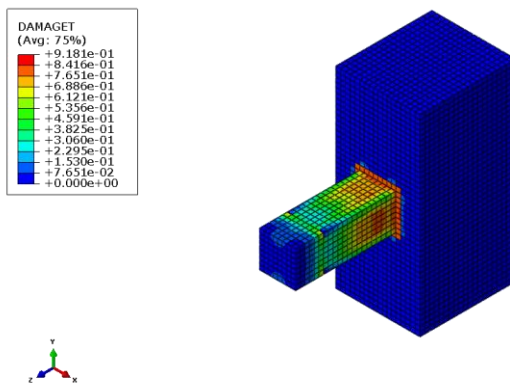


Figure D - 132: Tensile damage: ECFRP, loose sand, long span.

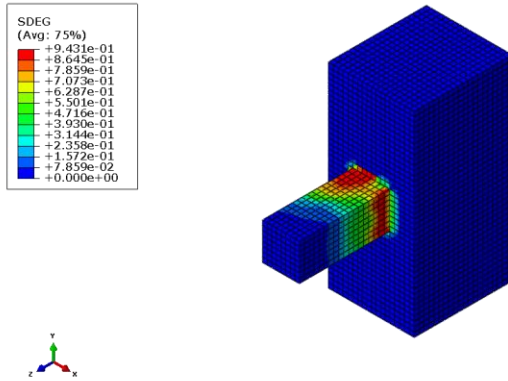


Figure D - 133: Stiffness degradation: control, loose sand, long span.

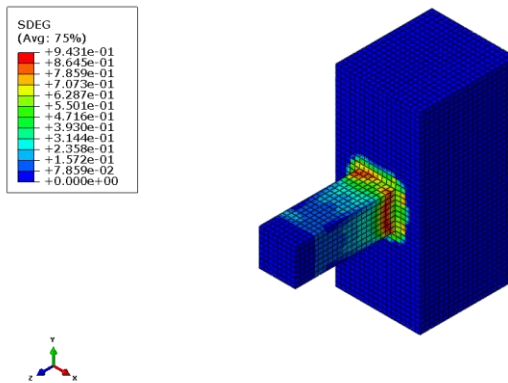


Figure D - 134: Stiffness degradation: CFRP, loose sand, long span.

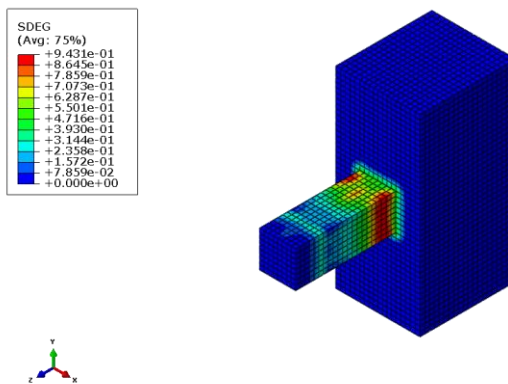


Figure D - 135: Stiffness degradation: ECFRP, loose sand, long span.

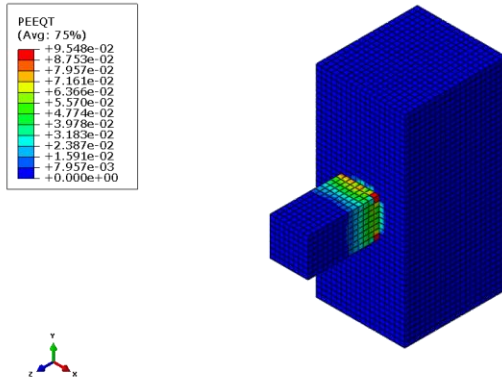


Figure D - 136: Tensile plastic strain: control, stiff clay, long span.

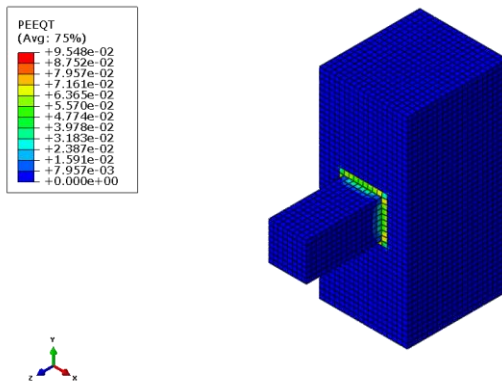


Figure D - 137: Tensile plastic strain: CFRP, stiff clay, long span.

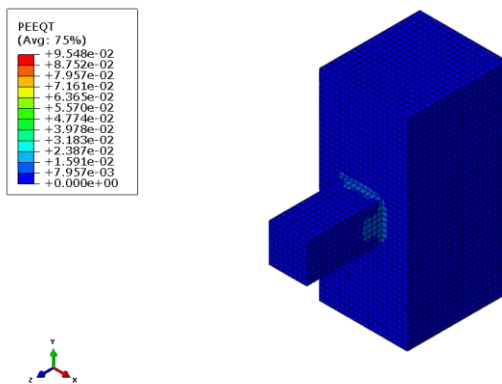


Figure D - 138: Tensile plastic strain: ECFRP, stiff clay, long span.

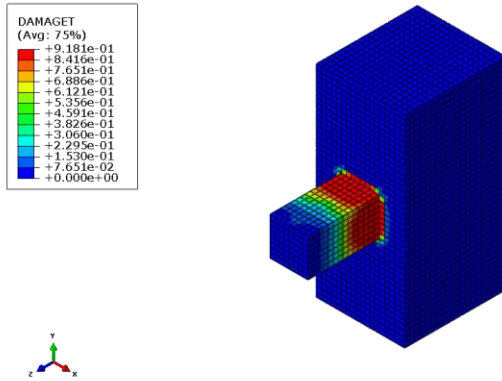


Figure D - 139: Tensile damage: control, stiff clay, long span.

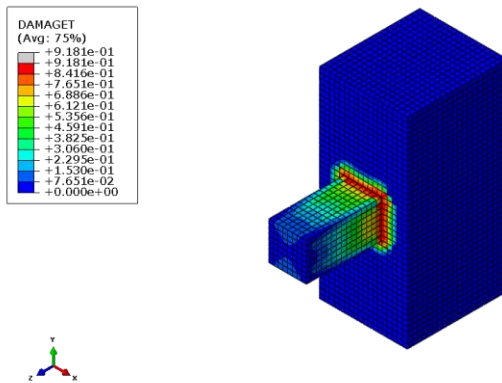


Figure D - 140: Tensile damage: CFRP, stiff clay, long span.

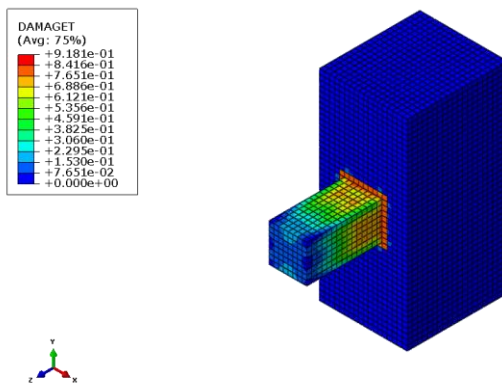


Figure D - 141: Tensile damage: ECFRP, stiff clay, long span.

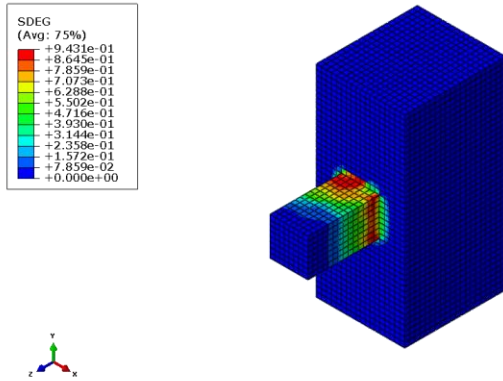


Figure D - 142: Stiffness degradation: control, stiff clay, long span.

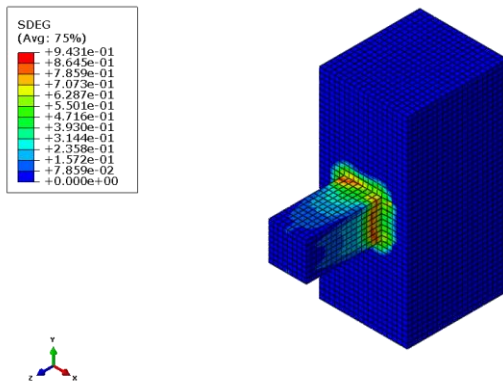


Figure D - 143: Stiffness degradation: CFRP, stiff clay, long span.

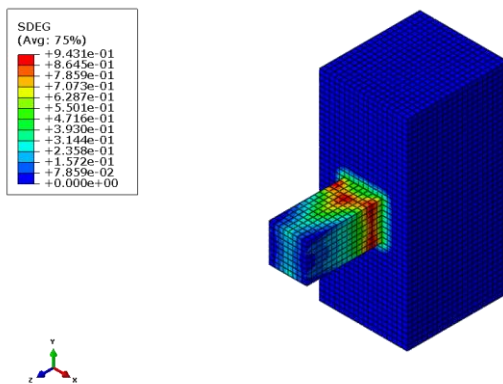


Figure D - 144: Stiffness degradation: ECFRP, stiff clay, long span.

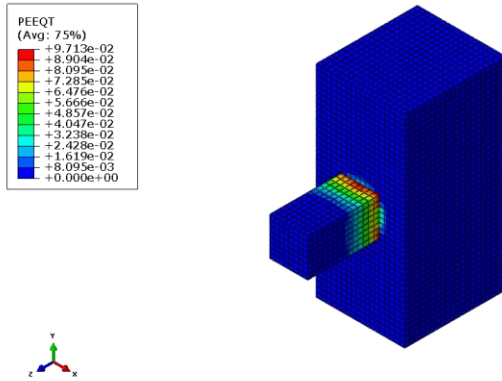


Figure D - 145: Tensile plastic strain: control, medium clay, long span.

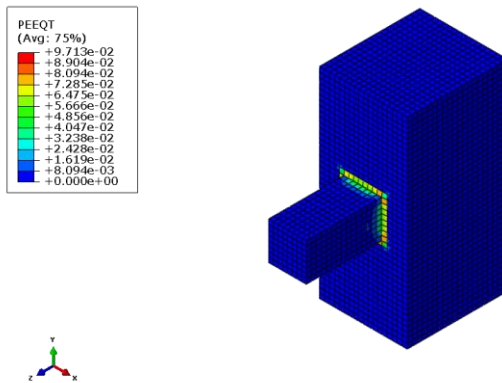


Figure D - 146: Tensile plastic strain: CFRP, medium clay, long span.

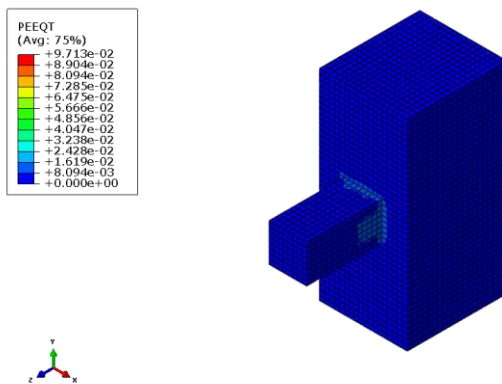


Figure D - 147: Tensile plastic strain: ECFRP, medium clay, long span.

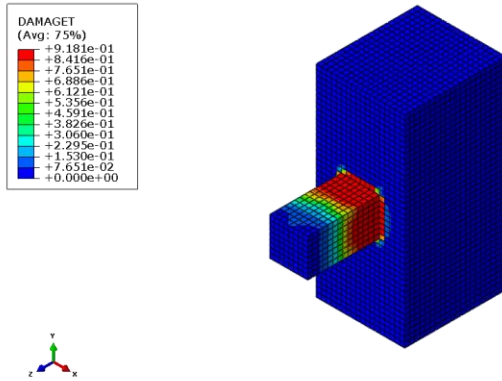


Figure D - 148: Tensile damage: control, medium clay, long span.

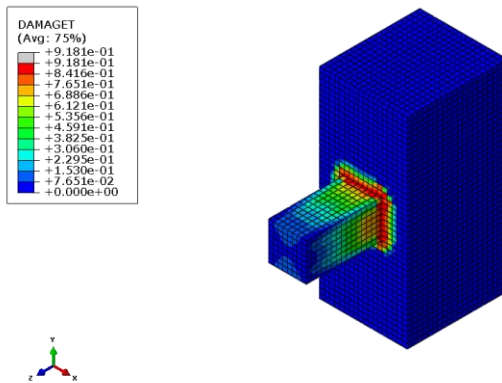


Figure D - 149: Tensile damage: CFRP, medium clay, long span.

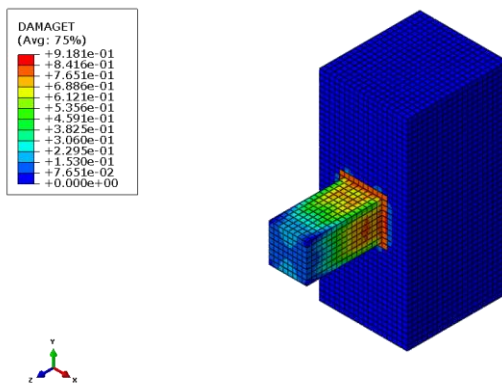


Figure D - 150: Tensile damage: ECFRP, medium clay, long span.

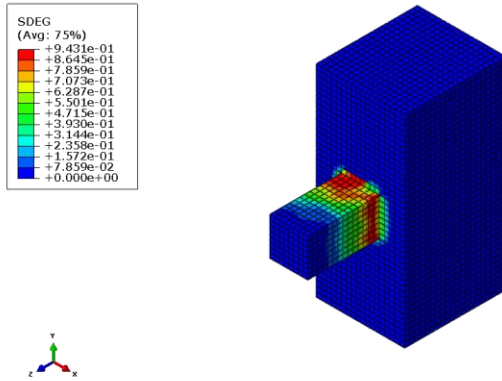


Figure D - 151: Stiffness degradation: control, medium clay, long span.

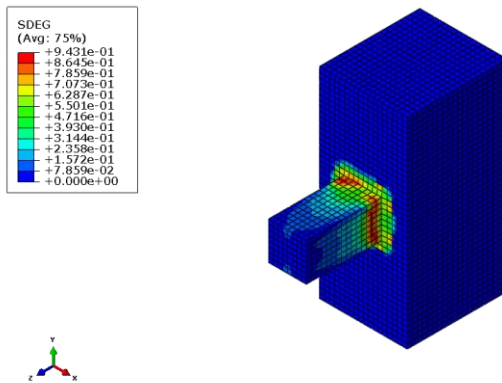


Figure D - 152: Stiffness degradation: CFRP, medium clay, long span.

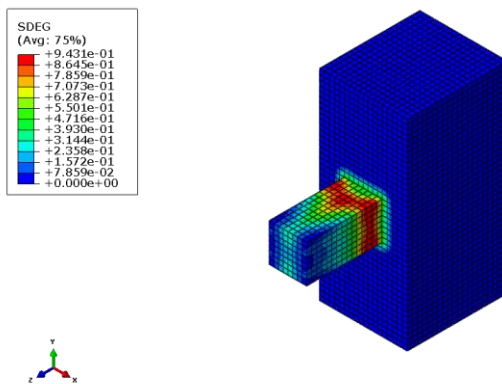


Figure D - 153: Stiffness degradation: ECFRP, medium clay, long span.

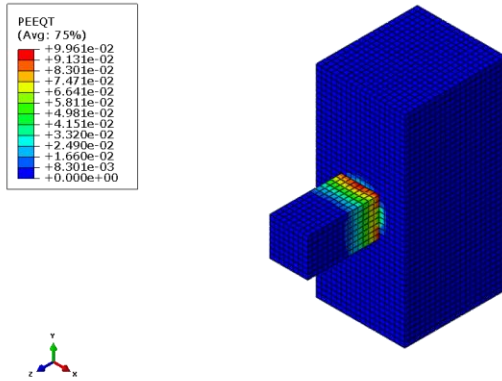


Figure D - 154: Tensile plastic strain: control, soft clay, long span.

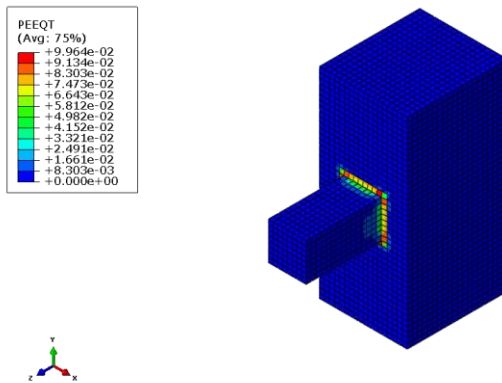


Figure D - 155: Tensile plastic strain: CFRP, soft clay, long span.

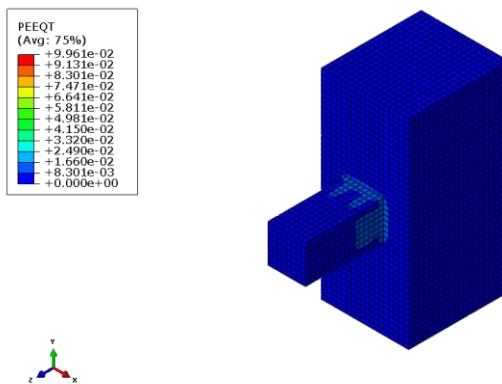


Figure D - 156: Tensile plastic strain: ECFRP, soft clay, long span.

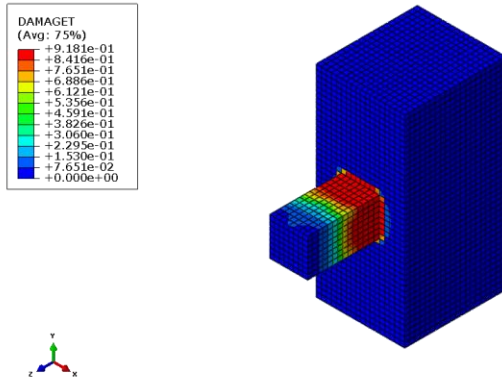


Figure D - 157: Tensile damage: control, soft clay, long span.

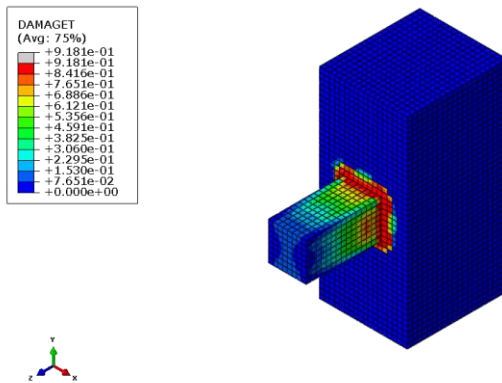


Figure D - 158: Tensile damage: CFRP, soft clay, long span.

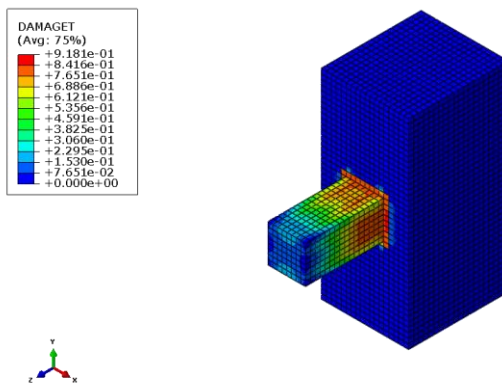


Figure D - 159: Tensile damage: ECFRP, soft clay, long span.

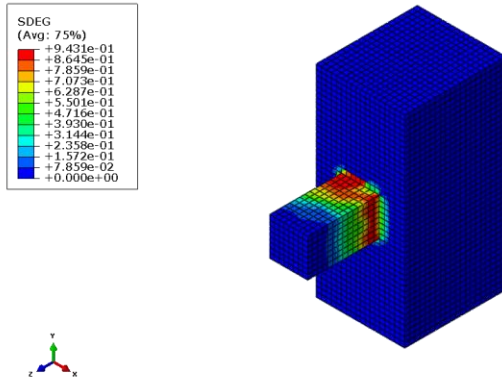


Figure D - 160: Stiffness degradation: control, soft clay, long span.

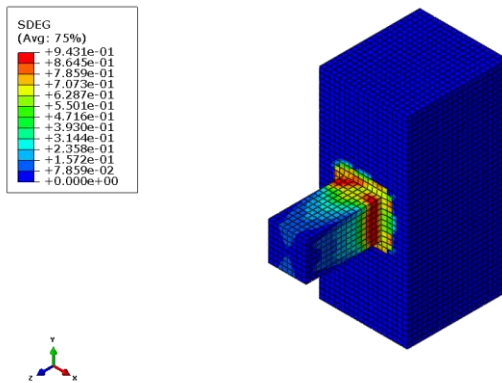


Figure D - 161: Stiffness degradation: CFRP, soft clay, long span.

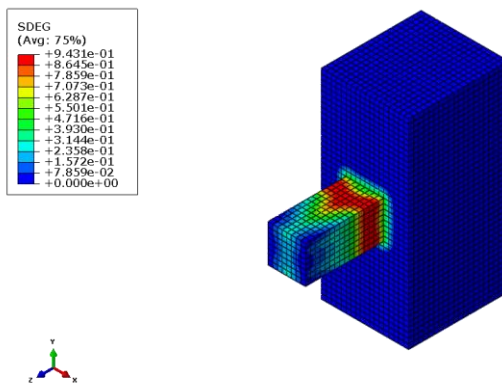


Figure D - 162: Stiffness degradation: ECFRP, soft clay, long span.

CURRICULUM VITAE

Hassan Mohammed Magbool

Place of birth: Jazan, Saudi Arabia

Education

Bachelor, King Abdulaziz University
Major: Landscape Architecture

Master of Science, Idaho State University
Major: Civil Engineering

Dissertation Title: Analysis of FRP-Wrapped Concrete Piles in Integral Abutment Bridges
Subjected to Axial and Cyclic Lateral Loads